Experimental and Numerical Studies of Cavities, Flows, and Waves in Arched Flux Ropes

Thesis by
Magnus Albert Haw

In Partial Fulfillment of the Requirements for the
degree of
Doctor of Philosophy

Caltech

CALIFORNIA INSTITUTE OF TECHNOLOGY
Pasadena, California

2018
Defended May 18, 2018

ORCID: 0000-0001-5739-5160

ACKNOWLEDGEMENTS

apparatuses and so forth. Bao's training was so successful I ended up working on all three experiments. I must also thank Bao for his positive attitude and encouraging me to continue pursuing swing dance and Toastmasters. Vernon was the only brave soul to take on the challenge of organizing a weekly journal club. From his single-handed efforts in this area, I learned a great deal of plasma physics. Xiang was an invaluable troubleshooter for many of my experimental woes in my early years, a fellow maker, and fellow raider of the unusually impressive Caltech e-waste. Finally, I must thank Zach for passing on his double loop experiment in mint condition.

I thank Dr. Hui Li at Los Alamos National Labs for his mentorship, career advice, and his patience with me and Pakorn after telling him for the nth time that we nearly had simulation results but not quite.

Thank you Connie Rodriguez, Jennifer Blankenship, and Christy Jenstad for your support, and all the emails about events and deadlines. You are the best administrative team I have had the privilege to work with. I cannot remember a single time I hit an administrative roadblock.

Outside of research, there are a number of other people that made my time at Caltech truly special. First, Amanda, my partner and girlfriend, thank you so much, I'm so lucky to have found you.

A big thank you to my Applied Physics class for being awesome people and getting me through classes and beyond.

To my friends: Jeremy Brouillet, Hannah Allen, Zofii Anna, Heidi Klumpe, Georgia Papadakis, Yu-Hung Lai, Teddy Albertson, BG, and Tal Einav, thank you for all the good times and I hope to stay in touch.

I am so grateful to everyone in the Caltech dance community, especially swing, for being so welcoming and so passionate. There are too many to name but special thanks to Neil Haleilamien for teaching both of my left feet, and to my students who have since surpassed me.

To all the people in TSF, SEPAC, TACIT, and the Caltech Y, who have dedicated so much time to making a difference on and off campus, thank you for enriching my time outside of lab. Special thanks to my co-founder of TSF, Lina Bird, the tireless founder of SEPAC, Kat Saad, and to Jeremy Brouillet who dragged me into theater lighting.

A special thank you to Ernie's food truck and Chandler's mongolian grill for pro-

viding a significant fraction of calories during my grad school career.

Also thank you to all the Caltech sports groups that I was able to participate in: afternoon pickup frisbee, Fighting Pinecones softball, Fighting Pinecones volleyball, Fighting Pinecones basketball, and the SOPs soccer team. Such activities were vitally necessary given my penchant for unreasonably large lunches.

ABSTRACT

This dissertation details various studies of arched flux ropes using both scalable laboratory experiments and numerical simulations. This work can be divided into three major classes: studies of flux rope motion and shape, development of supporting simulations, and development of new experimental diagnostics.

The primary scientific results in this work are the characterization of new mechanisms for flux rope motion and morphology. These studies are done on two separate experiments, the single loop and double loop, which produce arched flux ropes with non-dimensional evolution equivalent to solar prominences. Measurements taken on these experiments characterize three flux rope mechanisms: (1) how variation in a flux rope minor radius can drive axial flows and collimation, (2) how non-uniform axial density can perturb flux rope shape and inhibit the kink instability, and (3) how changing flux rope current can repel background plasma and form density cavities around the flux rope. These mechanisms are each relevant to a different aspect of solar prominences: the collimation mechansim (1) can explain why solar loops are denser and more collimated than expected, the work on density perturbations (2) puts a higher limit on prominence stability, and the cavity mechanism (3) provides the first model to explain why coronal mass ejections (CMEs) are observed to have a three part structure.

Two numerical simulations were developed in support of the experiments: a 3D magnetohydrodynamic (MHD) simulation of the single loop experiment and a 3D spline model simulating flux ropes as interacting current carrying wires. The MHD simulation uses the solver module from the Los Alamos COMPutational Astrophysics Simulation Suite (LA-COMPASS) to evolve $\mathbf{B}$, $\mathbf{v}$, ρ, and P on a 96^3 Cartesian grid using the dimensionless ideal MHD equations. The resulting simulation has excellent agreement with experimental observations in shape, velocity, and magnetic field and quantitatively reproduces the mechanisms (2,3) observed in the single loop experiment. The spline simulation models the flux ropes experiments as plasma systems of thin current paths in a 3D space with no background plasma. This model is shown to be useful for reproducing flux rope evolution, testing new experimental configurations, evaluating the magnetic fields generated from complex 3D current paths, and testing the robustness of analytic flux rope models.

The last body of work concerns the development of two novel diagnostics: a high

frequency (1-100 MHz) wave probe designed to measure both the magnetic field $\mathbf{B}$, and current density $\mathbf{J}$, of passing waves and a high frequency (100 MHz) 1D coded aperture camera. The wave probe consists of four 3-axis $\dot{B}$-probes arranged in a tetrahedron. This additional spatial resolution allows the calculation of both $\mathbf{J}$ and the wavevector $\mathbf{k}$. Measurements taken by this probe on the plasma jet experiment identify short whistler wave pulses emitted from magnetic reconnection events. These waves are identified by measurements of the background conditions, the wave polarization, and comparisons with the theoretical whistler dispersion relation. The pulses also occur simultaneously with bursts of X-ray emissions, indicating that non-MHD physics (i.e. two-fluid or kinetic effects) are important during the reconnection event. The coded aperture camera is a fast (100MHz) 1D visible light system developed as a prototype for imaging plasma experiments in the EUV/X-ray bands. In the low signal limit, the system demonstrates 40-fold increase in throughput and a signal-to-noise gain of ≈ 7 over that of a pinhole camera of equivalent parameters.

PUBLISHED CONTENT AND CONTRIBUTIONS

[1] Magnus Haw and Paul Bellan. "1D fast coded aperture camera". In: *Review of Scientific Instruments* 86.4 (2015), p. 043506. DOI: 10.1063/1.4917345.
M.A.H designed and built the coded aperture camera, wrote the ray tracing simulation, carried out the experimental measurements, and wrote the manuscript.

[2] Pakorn Wongwaitayakornkul et al. "Apex Dips of Experimental Flux Ropes: Helix or Cusp?" In: *The Astrophysical Journal* 848.2 (2017), p. 89. DOI: 10.3847/1538-4357/aa8990.
M.A.H developed the theoretical model, collaborated with P.W on the simulation, and lead the writing of the manuscript. P.W carried out all of the experimental measurements.

[3] Magnus A. Haw and Paul M. Bellan. "MHD Collimation Mechanism in Arched Flux Ropes Characterized Using Volumetric, Time-Dependent B-Vector Measurements". In: *Geophysical Research Letters* 44.19 (2017), pp. 9525–9531. DOI: 10.1002/2017GL074505.
M.A.H designed and built the magnetic probe array, carried out the experimental measurements, did the numerical analysis, and wrote the manuscript.

[4] Magnus A. Haw et al. "Reverse Current Model for Coronal Mass Ejection Cavity Formation". (under review). 2018.
M.A.H developed the theoretical model, collaborated with P.W on the simulation, and lead the writing of the manuscript. P.W carried out all of the experimental measurements.

[5] Magnus A. Haw, Byoung-Hoon Seo, and Paul M. Bellan. "Measurement of Whistler Wave Pulse from Fast Magnetic Reconnection". (in preparation). 2018.
M.A.H contributed to the design of the wave probe, built the wave probe, conducted the experimental measurements with B.S, and lead the writing of the manuscript.

[6] Magnus A. Haw and Paul M. Bellan. "Reduced physics model for simulating flux ropes as current carrying wires". (in preparation). 2018.
M.A.H developed the theory, implemented the simulation, analyzed the results, and wrote the manuscript.

TABLE OF CONTENTS

LIST OF ILLUSTRATIONS

LIST OF TABLES

C h a p t e r   1

INTRODUCTION

Plasma physics is the study of ionized gases which are classified as a fourth state of matter. This relatively new field began in the 1920's with the advent of vacuum chambers, made possible by Irving Langmuir's improved diffusion pump. Subsequent studies applying high voltage to low pressure gases discovered a surprising effect: the gases would glow and move about in strange ways. Langmuir named this new substance "plasma" and ever since, plasma physicists have been trying to understand these glowing gases and why they move about in strange ways.

Plasmas are different from other classical materials because they have strong, non-local interactions. For most gases, liquids, and solids, microscopic motion is dominated by collisions with other nearby particles. For plasmas, individual particles have net electric charge and motion is instead dominated by long-range electric and magnetic fields. This strong, long-range coupling makes numerical simulations of macroscopic numbers ($\sim 10^{23}$) of charged particles prohibitively expensive, even on modern supercomputers [1].

Consequently, there are still a number of frontiers in plasma physics. Many of these problems are concerned with a particular magnetic configuration called a flux rope, a twisted bundle of magnetic field lines which can resemble a rope. These structures contain electric current and their dynamics are generally dominated by the magnetic force ($\mathbf{J} \times \mathbf{B}$). Several important flux rope problems are listed below:

1. **Solar eruptions**: the eruption of solar prominences into space, also known as a coronal mass ejection (CME). Models of solar eruptions still fail to provide sufficient predictability for potentially disastrous Earth-impacting events.

2. **Magnetic reconnection**: this is a process whereby magnetic energy can be converted to kinetic energy through topological changes in the magnetic field. This process is responsible for fast, turbulent transfers of energy which cause solar eruptions and fusion reactor disruptions.

3. **Fusion reactors**: a potentially large source of carbon & radiation-free energy. Plasma instabilities have prevented the realization of fusion reactors with net energy production since the 1950's.
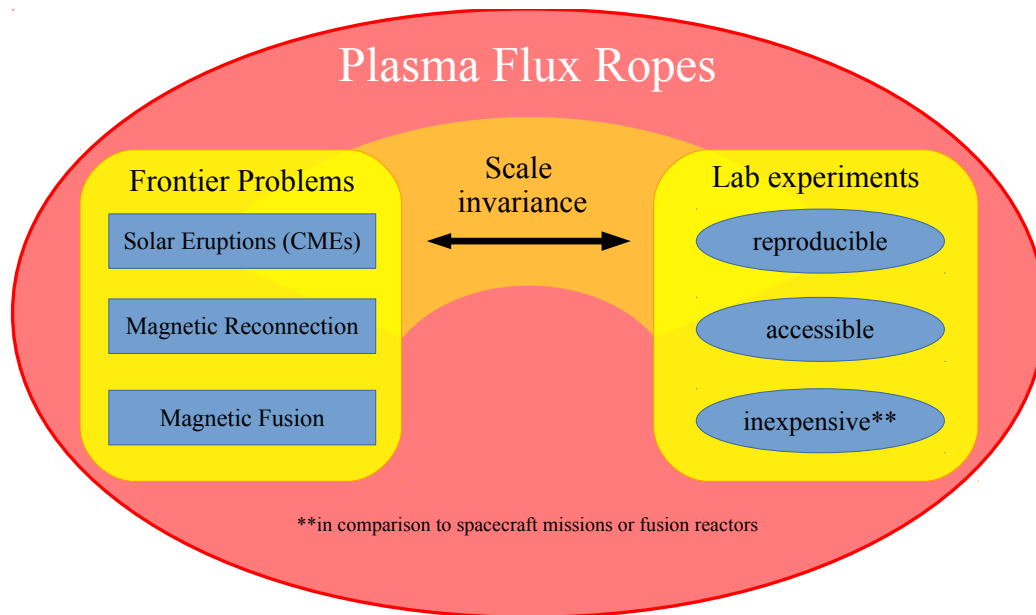
Figure 1.1: Diagram showing how laboratory flux rope experiments are relevant to many frontier problems in plasma physics.

This work studies the motion, morphology, and waves of laboratory flux rope experiments. These experiments are relevant to the above problems because of the scale invariance of the plasma equations. This property allows scaled experiments to model inaccessible systems such as solar prominences, fusion plasmas, and astrophysical jets. Section 1.2 provides a more detailed description of the scaling procedure and caveats. These scaled experiments are reproducible, accessible, and resolve more physics than numerical simulations.

Readers unfamiliar with plasma physics can review basic topics in Appendix A. This review includes the three plasma descriptions (particle, two-fluid, single-fluid), and several aspects of the single-fluid description also known as magnetohydrodynamics (MHD).

1.1   Thesis overview

This dissertation covers work on three different flux rope experiments (single loop, double loop and jet experiments), each with multiple sub-projects. The parameters and apparatus for each of these experiments are described in Chapter 2. The results can be divided into three categories: flux rope motion and morphology (Chapters 3-7), construction of a new wave diagnostic (Chapter 8) and the development of a coded aperture camera (Chapter 9). Figure 1.2 displays a minimal summary of the

Single loop	Double loop	Jet experiment
New theories for (1) CME cavity formation (2) Apex dip in experiment Relevant to: • Solar prominence stability • Solar prominence shape **Chapters 5, 6**	**3D time-dependent measurements of axial flow/collimation mechanism** Relevant to: • Pressure scale heights of solar loops • Astrophysical jets • Fusion instabilities **Chapter 3**	**Measuring whistler waves from magnetic reconnection** Relevant to: • Non-MHD reconnection • Solar flares • Magnetospheric reconnection **Chapter 8**
3D MHD Simulation	Flux rope wire simulation	Coded aperture camera
3D MHD simulation of single loop experiment • Quantitative agreement with experiment • Full compressional description **Chapter 4**	**Reduced physics model of flux ropes as 1D current paths** • Fast simulation for testing 3D geometries • Can reproduce loop evolution • Can visualize B-fields for 3D current paths **Chapter 7**	**Prototype camera for imaging X-rays from jet reconnection** • Superior signal to noise as compared with pinhole • High frequency (100 MHz) **Chapter 9**

Figure 1.2: Visual outline of the different thesis chapters

different chapters.

Flux rope motion and morphology

The majority of this thesis is concerned with dynamic mechanisms in flux ropes. Due to the scale invariance of MHD, the variety of mechanisms measured in the experiments (e.g., flows, collimation, density cavities, density pileups) can be directly scaled to solar prominences. Chapter 3 describes volumetric measurements of $\mathbf{B}(\mathbf{x}, t)$ on the double loop experiment which confirm a proposed magnetic collimation mechanism for arched flux ropes. This mechanism explains why coronal loops are thinner and denser than expected at large heights. Chapter 4 details the de-

velopment of a 3D MHD simulation of the single loop experiment. This simulation provides an important tool used in Chapters 5 & 6 to support and interpret experimental measurements. Chapter 5 explains a new mechanism, based on non-uniform axial density, for the characteristic dip at the apex of the single loop experiment. This supplants the previous theory that the dip is caused by a helical magnetic instability, the kink instability, and demonstrates that non-uniform density can play an important role in shaping solar prominences. Chapter 6 presents a new model for formation of density cavities around flux ropes. The model is supported by experiment, numerical simulation, and spacecraft observations. This model also provides an explanation for the three-part structure of CMEs and identifies the prominence cavity size as an observable metric for the likelihood of eruption. Last, but not least, Chapter 7 details the development and implementation of a reduced physics model for simulating flux ropes as interacting wires. This reduces a 3D domain to a set of 1D splines in 3D space, making the implementation extremely fast. Such a model is useful for testing new electrode topologies, investigating system scale instabilities, evaluating the magnetic fields generated from complex 3D current paths, and testing the robustness of analytic flux rope models.

Quadruple wave probe

Chapter 8 covers the construction and measurements of a new wave diagnostic. The quadruple wave probe was built to measure high frequency (1-100 MHz) magnetized waves emitted from magnetic reconnection on the jet experiment. This new diagnostic consists of four 3-axis $\dot{B}$-probes arranged in a tetrahedron, capable of simultaneously measuring both the magnetic field and current density of passing waves. Measurements using this new diagnostic identified short pulses of whistler waves emitted from magnetic reconnection. These pulses are observed synchronously with production of X-rays indicating the importance of two-fluid or kinetic physics in these events.

Coded aperture imaging

Coded aperture imaging is a ray-imaging technique originally developed for high energy X-ray telescopes. The technique is essentially a multiplexed pinhole camera (i.e., more than one pinhole in the mask) which projects a superposition of images onto the detector. With the proper arrangement of pinholes (i.e., the "coded" aperture), the detected superposition can be inverted to acquire the desired image with much higher signal to noise than a single pinhole. Chapter 9 details the

adaptation of this technique to high frequency (100 MHz) and near-field for use as a laboratory diagnostic. The constructed visible light prototype demonstrated a signal-to-noise improvement by a factor of ≈ 7 over an equivalent pinhole camera.

1.2 Laboratory astrophysics

Ideal magnetohydrodynamics, like hydrodynamics, has the peculiar property of having no intrinsic scale. In other words, systems with certain ratios will have equivalent behavior over a vast range of scales. For plasmas, these ratios are the following dimensionless parameters:

- **Plasma beta** β, the ratio of thermal pressure to magnetic pressure,

$$\beta = \frac{n\kappa T}{B^2/2\mu_0} \tag{1.1}$$

- **Lundquist number** S, the ratio of magnetic convection to magnetic diffusion,

$$S = \frac{\mu_0 v_A L}{\eta} \tag{1.2}$$

where η is the resistivity, $v_A = \frac{B}{\sqrt{\mu_0 \rho}}$ is the Alfvén speed, and L is a characteristic length.

Due to this scale invariance, it is possible to develop an equivalent system at the laboratory scale for any astrophysical plasma described by ideal MHD [2]. Laboratory experiments can use this scalability to study small versions of astrophysical plasmas, such as protostellar jets and solar prominences, in a reproducible, controlled, and accessible laboratory environment.

Completely scalable behavior requires that dissipative effects (resistivity, viscosity, etc.) are small because these introduce a dissipative length scale. However, for most astrophysical plasmas, ignoring dissipation is an excellent assumption as both the Reynolds and Lundquist numbers are enormous ($R, S \ggg 10^3$). Consequently, the minimum constraints on accessing the correct plasma regime in the lab are $\beta \sim \beta'$ and $S, S' \gg 1$. To achieve one-to-one correspondence between laboratory and astrophysical scales, the following invariant transformations must be applied:

$$
\begin{array}{c|c|c}
\begin{aligned}
L_0/a_1 &\to L' \\
P_0/a_3 &\to P' \\
\tfrac{a_1 a_2}{a_3} g &\to g'
\end{aligned}
&
\begin{aligned}
\rho_0/a_2 &\to \rho' \\
\tfrac{1}{a_1}\sqrt{\tfrac{a_3}{a_2}} t_0 &\to t' \\
\beta &\to \beta'
\end{aligned}
&
\begin{aligned}
B_0/\sqrt{a_3} &\to B' \\
\sqrt{\tfrac{a_2}{a_3}} v_0 &\to v'
\end{aligned}
\end{array}
$$

Laboratory Plasma		Solar Prominence	
$B = 3000$ G	$L = 0.5$ m	$B = 50$ G	$L = 2\times10^7$ m
$\rho = 10^{-4}$ kg m^{-3}	$\tau = 17$ μs	$\rho = 10^{-12}$ kg m^{-3}	$\tau = 5$ s
$g = 10$ m s^{-2}	$P = 300$ Pa	$g = 300$ m s^{-2}	$P = 0.01$ Pa
$v_A = 3\cdot10^4$ m s^{-1}	$\beta = 0.01$	$v_A = 4\cdot10^6$ m s^{-1}	$\beta = 0.002$

Scaled up to Solar Corona		Scaled down to Laboratory	
$B = 30$ G	$L = 2\times10^7$ m	$B = 5000$ G	$L = 0.5$ m
$\rho = 10^{-12}$ kg m^{-3}	$\tau = 7$ s	$\rho = 10^{-4}$ kg m^{-3}	$\tau = 13$ μs
$g = 3\cdot10^{-3}$ m s^{-2}	$P = 0.03$ Pa	$g = 10^6$ m s^{-2}	$P = 100$ Pa
$v_A = 3\cdot10^6$ m s^{-1}	$\beta = 0.01$	$v_A = 4\cdot10^4$ m s^{-1}	$\beta = 0.002$
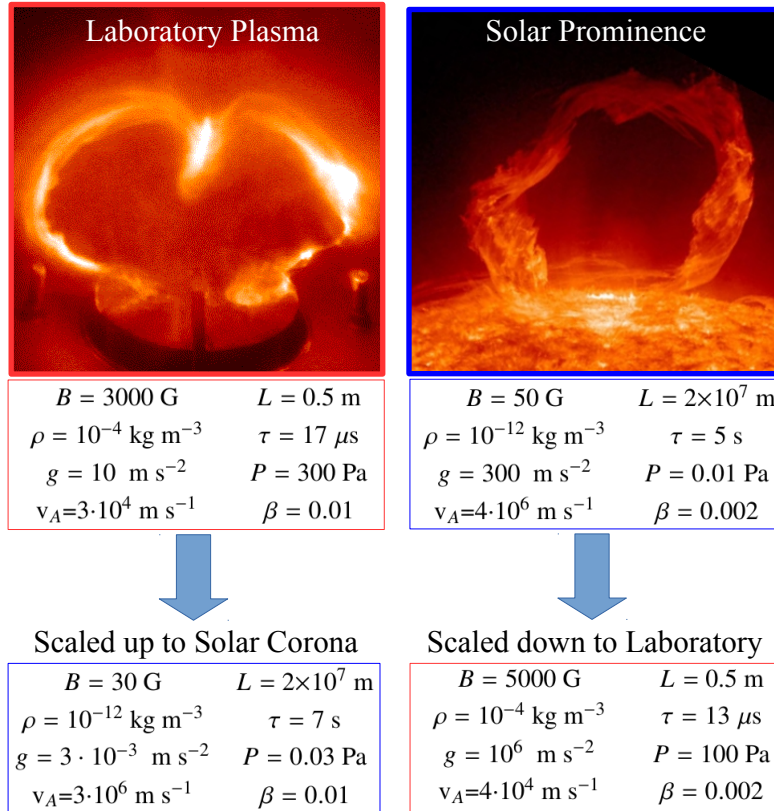
Figure 1.3: Scaling of single loop experiment to solar scale and vice versa. Following the convention described in this section, the scaling ratios are, $a_1 = 2.5 \cdot 10^{-8}$, $a_2 = 10^8$ and $a_3 = 3 \cdot 10^4$.

where a_1, a_2, a_3 are free parameters [2]. These transformations give directly comparable parameters for systems at different scales.

Figure 1.3 shows the characteristic parameters of the single loop experiment, typical solar prominence parameters, and equivalent scaled parameters using $a_1 = 2.5\cdot10^{-8}$, $a_2 = 10^8$ and $a_3 = 3 \cdot 10^4$. With the notable exception of gravity, the experimental parameters scale well to the solar case. It is important to note that the listed timescale, τ_A, is the Alfvén crossing time ($\tau_A = L/v_A$) and not the feature lifetime, which for solar loops is typically $\sim 10^2\tau_A$-$10^3\tau_A$.

Some other notable labs doing laboratory astrophysics include the magnetic reconnection experiment (MRX) at Princeton Plasma Physics Lab, the large plasma device (LAPD) at UCLA, FlareLab at Ruhr-Universität Bochum, the mega-ampere generator for plasma implosion experiments (MAGPIE) facility at Imperial College London, and the big red ball (BRB) facility at University of Wisconsin Madison.

1.3 Solar physics: background and motivation

Most of the interesting plasma physics problems have one or more applications in our local star. Magnetic reconnection is of critical importance in eruptive events and solar flares, the solar dynamo is still not well understood, and solar prominences exhibit many of the same instabilities as fusion reactors. Of more practical importance to government funding agencies are the potentially disastrous consequences of a large solar eruption also known as a coronal mass ejection (CME) hitting Earth. A variety of studies have concluded that a direct impact from a large event could bring down most of the United States electric grid (see Figure 1.4b) for several years [3, 4, 5]. It is difficult to imagine the full impact on modern society of months to years without electric power. The probability of such an event is about 10% per decade and should occur, on average, every 100-150 years [6]. The "Carrington event" of 1859 was the last large event to impact Earth but had few consequences, besides a near-global aurora, as the only electronics present were telegraph lines. Given the reasonably high probability and the risk to society, there is significant interest in understanding and predicting solar eruptions.

Solar structure

The following is a brief introduction to solar structure and terminology to provide some context for solar eruptions. The sun is composed of several layers: a core 0-0.25 $R_\odot$, a radiative zone 0.25-0.7 $R_\odot$, a convection zone 0.7-1 $R_\odot$, and the solar atmosphere 1-30 $R_\odot$, where the solar radius $R_\odot$=695.5 Mm. The solar atmosphere is itself composed of three layers:

1. **Photosphere**: the layer of the sun that emits most of the visible light that we see. It is an optically thick, relatively thin (0.5 Mm) layer with the occasional sunspot, a visibly dark patch. These dark patches are cooler regions with strong radial magnetic fields.

2. **Chromosphere**: a thicker (~2.5 Mm), optically thin layer above the photosphere which is hotter and less dense. It is imaged principally via the Hα line.

3. **Corona**: a diffuse, magnetically dominated region which extends for many solar radii characterized by a sharp increase in temperature relative to the chromosphere. It is in this region where solar prominences (also called solar filaments) can be observed.
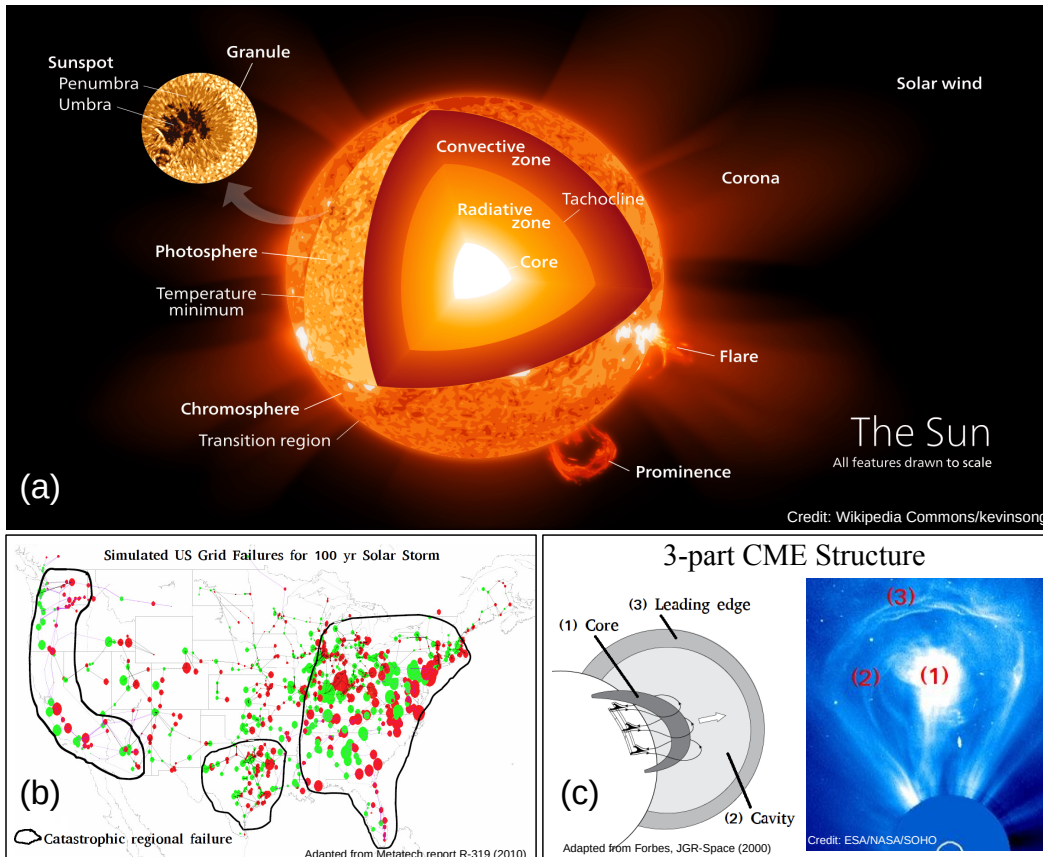
Figure 1.4: (a) Representation of the different layers and features of the sun. Credit: Wikipedia Commons/kelvinsong (b) Simulated US grid response to 100-yr solar storm from [4]. Green and red circles indicate strength of induced currents and black outlines indicate catastrophic regional failures. (c) Depiction of the typical three-part structure of coronal mass ejections (CMEs) and image of CME on Feb. 27, 2000 from the Solar and Heliospheric Observatory spacecraft (SOHO).

The corona is of particular interest since it is where solar eruptions occur. Most CMEs are associated with arched flux-rope structures (solar prominences) emerging from pairs of sunspots. As a result, the precise magnetic structure of these prominences and the processes which lead to their eruption are a major area of solar research.

The force-free paradigm

Due to the potentially catastrophic effects of large Earth-directed CMEs, there have been a slew of ever more complex methods to determine the 3D magnetic fields of prominences [7, 8, 9]. However, direct measurements of the optically thin corona are nearly impossible against the background solar disk, most of these methods use

spatial maps of the radial magnetic field at the photosphere (magnetograms).

1. **Potential field extrapolation**: the earliest attempts used a potential field approximation $\nabla \times \mathbf{B} = 0$, $R > R_{\odot}$, to extrapolate the field from the photosphere. This assumes that there are no currents present above the photosphere, where the B-field can be represented as the gradient of a scalar potential, $\mathbf{B} = \nabla \phi$.

2. **Force-free extrapolation**: an assumption that the magnetic field is parallel to the current density, $\nabla \times \mathbf{B} = \lambda \mathbf{B}$, where λ is constant. This assumption does permit current above the photosphere but only in force-free configurations.

3. **Non-linear force-free extrapolation**: a more complicated solution where λ is allowed to vary, $\nabla \times \mathbf{B} = \lambda(\mathbf{x})\mathbf{B}$.

These extrapolations form the basis of what is known in solar physics as the force-free paradigm. This view interprets prominences as quasi-equilibrium systems which slowly move between equilibrium states until reaching an unstable equilibria. Pressure and gravity forces are also ignored as negligible perturbations. This force-free paradigm is convenient in many ways but has not held up in comparisons with observations. Even the most advanced non-linear extrapolations, with a free parameter at each point in space, cannot adequately reproduce observations of stationary coronal loops [10, 11, 12].

The various mechanisms measured by this dissertation (i.e., flows, collimation, density cavities, cusps) violate the force-free assumption and demonstrate the importance of non-force-free physics in arched flux ropes.

1.4 Notation and units

The units will follow the SI convention with two exceptions: temperature will be given in eV (1 eV = $1.16 \cdot 10^4$ K) and magnetic field values will occasionally be listed in terms of Gauss instead of Tesla (1 T = 10,000 G).

The following notation is used to throughout the rest of the thesis,

- **Vectors**: vectors are denoted by bold-face font and vector operations use the conventional dot and cross products.

$$\mathbf{a} \cdot \mathbf{b} = c, \; \mathbf{a} \times \mathbf{b} = \mathbf{d}$$

- **Convective derivative**: a capital "D" in a time derivative indicates a convec-
  tive derivative, the rate of change measured by an observer moving with the
  local fluid frame.

$$\frac{\mathrm{D}}{\mathrm{Dt}} = (\frac{\partial}{\partial t} + \mathbf{U} \cdot \nabla)$$

- **Normalized quantities**: normalization will be indicated by a bar above the
  quantity.

$$\bar{\rho} = \rho/\rho_0$$

C h a p t e r   2

NUTS AND BOLTS: THE CALTECH PLASMA GUNS

The practical implementation of the Caltech plasma guns is quite remarkable and significant credit should be given to my advisor and the many grad students and post-docs who brought them to life. These custom systems, constructed in-house, access a unique plasma regime due to their fast timescales ($10\ \mu$s) and high magnetic fields (≤ 0.3 T). However, there are correspondingly fewer resources available when they do not work and many of the unwritten hours of this dissertation went into trouble-shooting unexpected problems. This chapter is dedicated to those many hours of frustration and to that special satisfaction of experimental success.
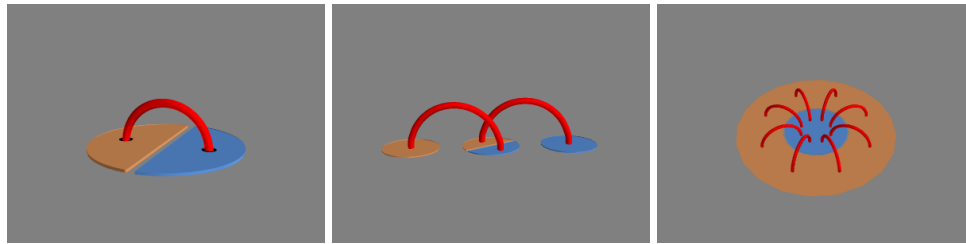
Figure 2.1: Graphical representation of the three plasma guns (left to right): single-loop, double-loop and jet/spheromak. Positive electrodes are colored copper and negative electrodes are colored in blue. Red loops represent the plasma flux ropes which form during electrode discharges.

There are three plasma experiments relevant to this thesis. They are the single loop, double loop, and jet experiments (Fig. 2.1). Each of these experiments has a different magnetic topology and accesses a novel plasma regime. However, despite these differences, these experiments all have certain subsystems: a fast gas-supply, solenoids to generate background magnetic field, capacitor banks to provide current, and a microsecond timing system. Plasmas are formed by a particular activation sequence of the various systems. The solenoid systems are triggered first to provide a background magnetic field. Second, the fast gas valves are triggered to provide localized gas density from nozzles in the electrodes. Finally, the main capacitors are switched across the electrodes. This ionizes the neutral gas and drives current along the background magnetic field, generating a flux rope, a twisted bundle of magnetic field lines. This sequence is shown in Figure 2.2 for the single loop experiment.

The plasma lifetime ranges from 10-20 μs, significantly shorter than either the gas diffusion or background solenoid timescales (5 ms). This timescale separation allows the background field to be treated as constant and ensures the velocity of the neutral gas (~200 m/s) is negligible compared to the plasma motion (10^4 m/s).
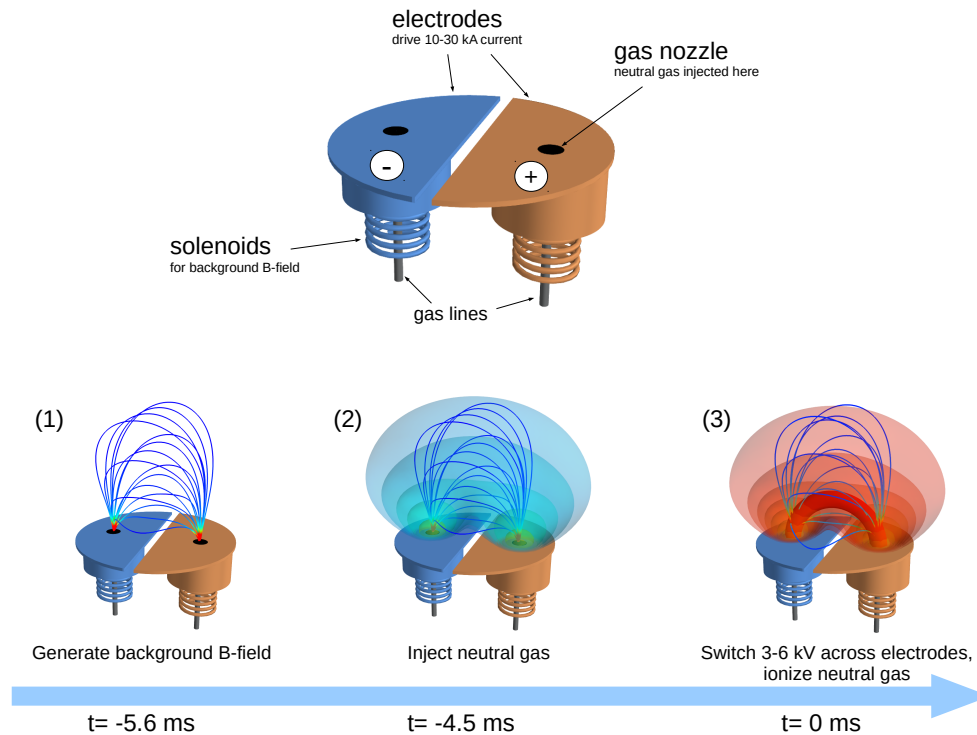
Figure 2.2: Diagram of the single loop apparatus showing the primary steps to generate a flux rope (1) generate arched background magnetic field (2) puff in neutral gas (3) switch capacitor bank across electrodes.

The following sections provide a description of each experiment and its associated diagnostics. For the reader principally interested in the plasma parameters rather than the nuts and bolts, Table 2.1 provides a range of parameters for each experiment.

2.1 Shared diagnostics and vacuum chambers

Vacuum chambers

The experiments are housed within two separate vacuum chambers. The double loop and jet experiments are located in the alpha chamber and the single loop experiment is in the slightly smaller bravo chamber (Figure 2.3). As can be seen from the chamber figure, the experiments are mounted horizontally. However, since

	Single Loop	Double Loop	Jet
L (m)	0.2	0.5	0.7
$|B|$ (T)	0.01-0.1	0.01-0.3	0.01-0.3
n (m^{-3})	10^{19}-10^{21}	10^{19}-10^{22}	10^{19}-10^{23}
v (m/s)	10^4	10^3	$8 \cdot 10^5$
T (eV)	1-2	1-2	2-10
ρ (kg/m^3)	$2 \cdot 10^{-8}$-$7 \cdot 10^{-5}$	$2 \cdot 10^{-8}$-$7 \cdot 10^{-4}$	$2 \cdot 10^{-8}$-$7 \cdot 10^{-3}$
P (N/m^2)	10-10^3	10-10^4	10-10^5
β	0.01-1	0.01-3	0.01-3

Table 2.1: Shows characteristic parameters of different experiments. Density range encompasses both hydrogen and argon. Values for the Lundquist number, S, are calculated using the Spitzer resistivity.

Alpha chamber
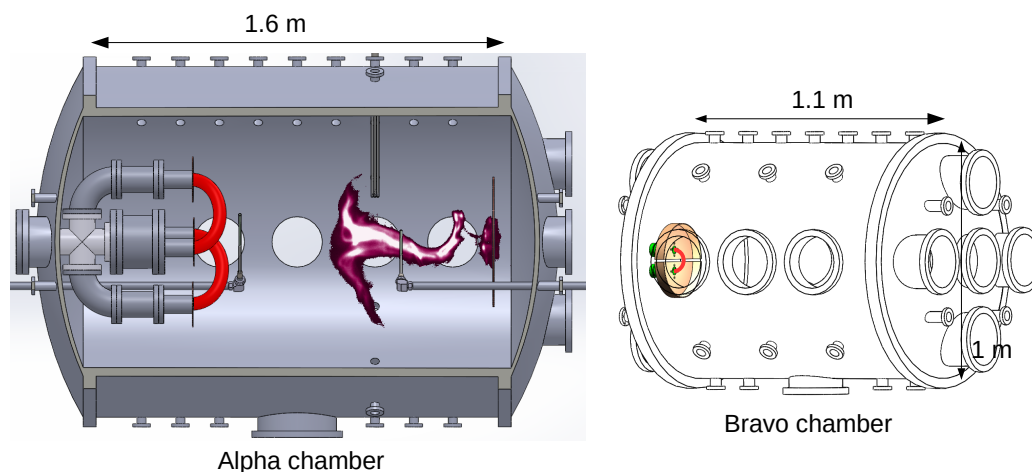
Bravo chamber

Figure 2.3: Diagram of both chambers showing the position of the different experiments. The Alpha chamber houses both the jet and double loop experiments. The Bravo chamber contains the single loop experiment.

gravitational acceleration ($|g| = 9.8$ m/s^2) on the plasma is negligible compared to magnetic accelerations ($10^9 - 10^{11}$ m/s^2), many images are rotated to display the propagation direction as vertical, to provide a more intuitive picture.

ICCD Camera (Imacon)

The intensified CCD camera (Imacon 200) is the star diagnostic of the Bellan lab. This enviable piece of equipment can take 14 individual frames (1200×980 pixels, 16-bit resolution) at nearly arbitrary time resolution. This camera provides instant feedback on the global plasma behavior and greatly shortens trouble-shooting time.
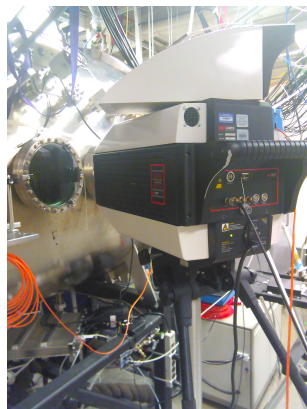
Figure 2.4: ICCD ultra-fast camera, model: Imacon200

The system is mobile and can interchange different lenses and filters. Consequently, it is often moved between the two chambers to image the different experiments in different wavelengths.

Spectrometer

The experiments also share a JY Horiba 1000M spectrometer with a 1 meter focal length, 3600 grooves/mm diffraction grating. Spectra are recorded using an Andor iStar ICCD camera (single frame). The spectral resolution of the system (3.6 pm/pixel at λ=500 nm to 6.7 pm/pixel at λ=250 nm) is sufficient to resolve line profiles and Doppler shifts.

Digitizer

The primary digitizer for the myriad of diagnostics is a 96-channel crate consisting of eight 12-channel DAQ boards (SiS GmbH SIS3300) with a Versa Module Europa (VME) interface. Each channel is digitized at 12 bits at a frequency of 100 MHz.

2.2 Single Loop Apparatus

The single loop system has gone through a number of iterations ([13, 14, 15, 16]) over the years. The latest incarnation was built by Bao Ha and is well documented in his thesis ([16]). The apparatus consists of a single pair of electrodes, with associated gas nozzles and solenoids. The firing sequence is shown in Fig. 2.2 and Figure 2.5 shows the position of various diagnostics.
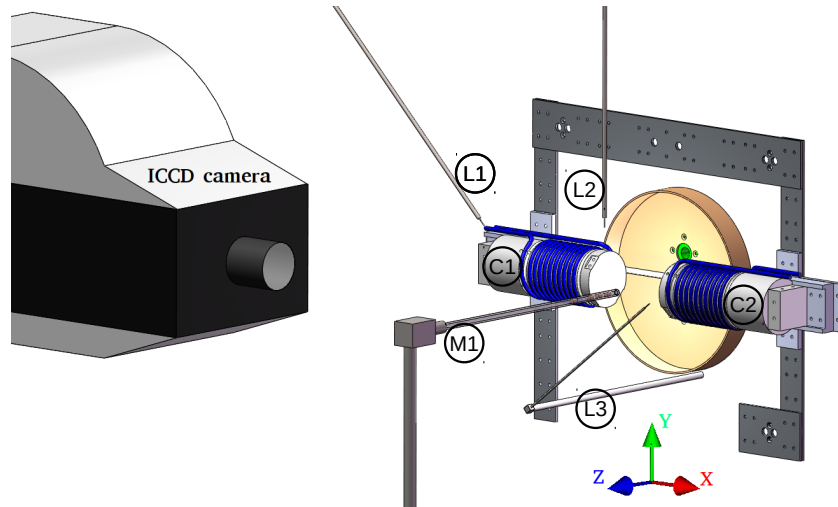
Figure 2.5: Mechanical drawing of single loop experiment showing the primary diagnostics. (M1) is the magnetic probe, (L1-L3) are Langmuir probes, and (C1,C2) are additional coils for producing background magnetic fields. Loop is formed in the YZ plane and the standard ICCD camera position is shown to the left.

Power Supply

The power supply for the experiment is provided by a high-voltage 59 μF capacitor. This is charged to 2.5-6 kV and is discharged using a two-stage, low-inductance trigger. This corresponds to 0.2-1.1 kJ discharged over 20 μs giving an average power input of 10-55 MW. For comparison, the City of Pasadena uses around 150 MW of power. This high power output is made possible by extensive inductance minimization in the transmission cables and connectors.

Background magnetic field

The arched background magnetic field is produced by two solenoids of opposite polarity situated behind the electrodes. These solenoids are pulsed to produce a peak field of 0.3 T at the loop footpoints (0.025 T at the loop apex), 6 ms after activation.

Gas supply

Gas is supplied by a pair of fast-gas-valves which are connected to nozzles in the electrodes. This system provides dense (10^{21}-10^{22}) neutral gas in the vicinity of the electrodes to facilitate plasma breakdown into a coherent flux rope. Measurements from [17, 18] indicate that the gas emerging from the nozzles forms exponential

cones with a density of $\sim 10^{22}$ at the footpoints,

$$n = n_0 \frac{1}{z^2} \exp(-\frac{r^2}{(z/M)^2}),$$

where z is the distance above the electrode plane, r is the radial position relative to the nozzle, and $M \sim 1$ is the mach number of the expanding gas.

Voltage measurements

Measurement of the time dependent voltage is done using a high-voltage capacitive divider. The capacitive divider is suitable for measuring high voltage at high frequency and the system avoids electrical noise issues via optical triggers and optical data transmission. The full design by Xiang Zhai can be found in [19].

Current measurement

Current is measured using a Rogowski coil, a type of low-inductance current transformer suitable for high-frequency current measurements.

B-field measurements

The primary magnetic diagnostic is a 12-channel B-dot probe array. These 12 channels are arranged into four 3-axis cluster to measure the vector magnetic field at four locations located 17.5, 19.5, 21.5 and 25.5 cm from the electrode plane.

Density/temperature measurements

Several Langmuir probes built by Pakorn Wongwaitayakornkul are also present in the experiment to measure plasma density and temperature. The probes consists of a small wire inserted into the plasma and biased at a large negative voltage to measure a local ion flux.

2.3 Double Loop Apparatus

The first version of the double loop experiment was much smaller with two parallel loops of similar dimensions (R=4 cm) to the single loop experiment [14, 15]. The new geometry of two offset loops (R=12 cm) was motivated by observations of solar arcades in which similar geometries are unstable to magnetic reconnection. Much of the power, gas, and B-field supply systems was built by former grad student Zachary Tobin. A movie of the evolving flux ropes is linked here and a movie of the firing sequence is linked here.
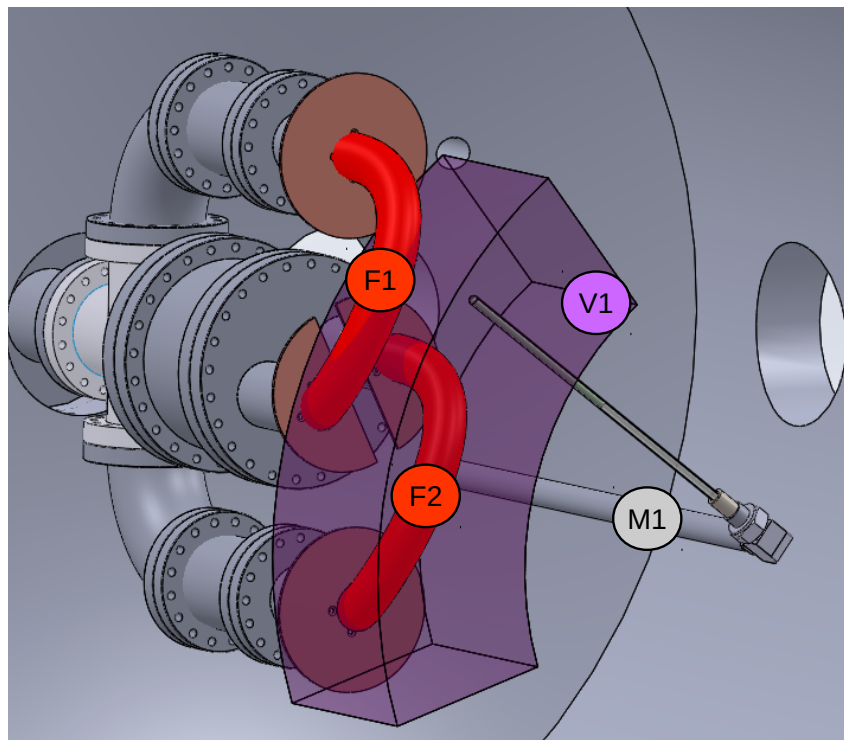
Figure 2.6: Mechanical drawing of double loop experiment showing the primary features. (F1,F2) are the two flux ropes, (M1) is the magnetic probe, and (V1) is the volume in which the probe can measure magnetic field.

Power Supply

The power supply for the double loop is essentially double that of the single loop experiment. Each loop has its own 59 μF capacitor which is typically charged from 3-6 kV. The charging circuitry and triggering systems are also independent.

Background magnetic field

The magnetic background field is generated by four separately controlled solenoids, one behind each electrode. The power supplies allow the magnitude and polarity of the field to be controlled from -0.1 to 0.1 T at the electrode footpoints.

Gas supply

The gas supply system is again double that of the single loop. Four fast gas valves are used to provide gas at the four electrodes. Each loop can be supplied with a different gas.

Voltage measurements

Two high-voltage capacitive probes are used to measure the voltages of both loops. The full probe design by Xiang Zhai can be found in [19].

Current measurements

As with the single loop, the current of each loop is measured with a Rogowski coil.

Magnetic measurements

Volumetric B-field is measured using a rotatable B-dot probe array. This array consisted of fifty-four, 5.6 μH surface-mount inductors in a linear array of 18 three-axis clusters (1 cm spacing). Rotating and translating the probe can access a volume containing most of the lower loop and a portion of the upper loop (Figure 2.6).

2.4   Jet Apparatus

Last, but not least, is the jet experiment. This venerable piece of equipment has undergone 16 years of operation without significant changes, and continues to provide a range of unexpected plasma phenomena to study. The current scientific focus has shifted to smaller length scales and non-MHD phenomena (e.g. X-rays, wave pulses) associated with fast magnetic reconnection.

Power Supplies

The 120 μF capacitor bank consists of two 60 μF Aerovox Industries, Inc., capacitors, each switched by a GL-7703 size A mercury-vapor ignitron. Four Belden YK-198 low-inductance coaxial cables connect the capacitor bank to the electrodes. The capacitor bank provides a sinusoidal current trace, with a peak current of $\sim$ 100 kA and period of 30 μs for a 5 kV charging voltage.

Background magnetic field

The background poloidal field is generated by a coil behind the electrodes ($R = 9.55$ cm, 110 turns).

Gas supply

The gas supply consists of four fast gas valves, two for the outer 8 nozzles (e.g. outer left, outer right) and two for the inner 8 nozzles. Each fast gas valve can be triggered separately. An additional gas input nozzle (see Figure 2.7) can add a target gas cloud in front of the jet.
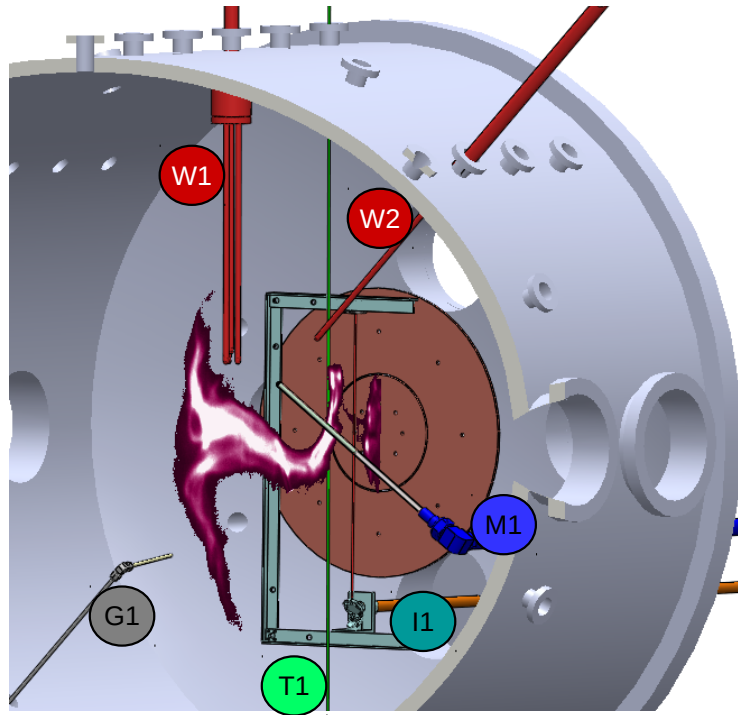
Figure 2.7: Mechanical drawing of jet experiment and relevant diagnostics. (W1) is the quadruple wave probe and (W2) is a single wave probe. (M1) is a 60 channel B-dot probe array. (I1) is a movable interferometer arm and (T1) is a Thompson scattering beam path. (G1) is an additional gas input nozzle for gas collision experiments.

Voltage probe

Voltage is measured using a Tektronix P6013A high voltage probe. This probe has a rise time of 7 ns and a range of 0-12 kV.

Rogowski coil

Total current is measured using a Rogowski coil. The output of the coil is passed through a passive RC integrator ($R = 86 \ \Omega$, $C = 2 \ \mu F$, $RC = 172 \ \mu s$) instead of using digital integration.

Magnetic probe

The magnetic probe has sixty channels organized into twenty 3-axis clusters with 2 cm spacing. The probe can translate and rotate to access different parts of the jet. Each channel is attached to a 5±0.1 μH chip inductor (Coilcraft Inc., model 1008CS-472XGBB).

Interferometer

A heterodyne He-Ne laser interferometer, originally built by Deepak Kumar, has recently been upgraded by Byounghoon Seo to use a fiber for most of one the interferometer arms. The upgraded interferometer can now translate and rotate to give a much more detailed density measurements of the jet.

Thompson scattering

Thompson scattering setup built by Byounghoon Seo using a Nd:YAG (532 nm, neodymium-doped yttrium aluminum garnet) laser. Due to the presence of ion lines near the 532 nm wavelength in other gas species, the setup is only able to measure hydrogen plasmas. Temperature measurements (2-4 eV) agree with spectroscopic line ratios.

Wave probes

Based on the design by Xiang Zhai [20], several wave probes have been built to measure high-frequency magnetic oscillations. These probes are sensitive up to GHz frequencies and are significantly better shielded from electrostatic oscillations than the other magnetic probes. More details on the probe designs and specifications are given in Chapter 6.

Chapter 3

VERIFYING AXIAL FLOW MECHANISM IN FLUX ROPES

Laboratory measurements of $\mathbf{B}(\mathbf{x}, t)$ in a volume enclosing portions of two arched flux ropes show flux rope collimation driven by gradients in axial current density. These measurements verify the three predictions of a proposed MHD collimation mechanism [21]: (1) axial magnetic forces exist in current channels with spatially varying minor radius, (2) these forces can drive counterpropagating axial flows, and (3) this process collimates the flux rope. This mechanism may explain the axial uniformity of solar loops and is relevant to other systems with current channels of varying minor radius such as solar prominences and astrophysical jets.

3.1 Introduction

For many years models of arched magnetic structures in the solar corona have assumed a magneto-hydrodynamic (MHD) force-free equilibrium ($\mu_0 \mathbf{J} = \lambda \mathbf{B}$, $\mathbf{J} \times \mathbf{B} = 0$) where pressure and gravity forces are assumed to be negligible ($|\nabla P|/|\mathbf{J} \times \mathbf{B}| \approx 0, |\rho\mathbf{g}|/|\mathbf{J} \times \mathbf{B}| \approx 0$) [9, 8]. These force-free models are an advancement over potential magnetic field models ($\mathbf{B} = \nabla\Psi$, $\mathbf{J} = 0$) but still have difficulty fully matching observations [10, 11, 12]. Outstanding discrepancies between force-free models and observation include the unexpectedly strong collimation of coronal loops [22, 23, 24] and why large loops have significantly higher density than expected from a hydrostatic equilibrium [25, 26]. Other proposed mechanisms to explain overdense loops [27, 28, 29] or loop collimation [30] treat these two problems separately.

The mechanism proposed in Bellan [21] observes that both collimation and over-dense loops could be explained by net current flowing along the flux rope axis (Fig 3.1). This theory observes that current channels with changing minor radius, ($J_r, J_z \neq 0$) have an unbalanced component of the magnetic force along the flux rope axis:

$$f_{\hat{s}}[N/m^3] = J_r B_\theta \approx -\frac{\partial}{\partial s}(\frac{B_\theta^2}{2\mu_0}),\tag{3.1}$$

where "s" is the distance along the loop axis from the footpoint. Such forces could increase the equilibrium density of loops by providing a force opposing gravity along the loop axis. Furthermore, if these forces exceed gravity, they will drive counter-propagating flows from both loop footpoints which convect poloidal flux to the loop

apex, leading to loop collimation. This mechanism is relevant to the collimation and equilibrium of coronal loops [31], vertical upflows in solar prominences [32, 33, 34, 35, 8], the fast counter-streaming flows observed along prominence and loop axes [34, 36, 35, 37, 38] and the persistent collimation of astrophysical jets [39, 40, 41].

This chapter presents measurements of the time-dependent vector magnetic field $\mathbf{B}(\mathbf{x}, t)$ in an annular volume containing portions of two experimental plasma flux ropes (Fig. 3.2a). Analysis of these measurements provides experimental verification of the three key predictions of the collimation theory: 1) axial magnetic forces exist in widening current channels, 2) these forces can drive counter-propagating axial flows, and 3) the process drives loop collimation. These measurements of experimental flux ropes are relevant to other MHD plasmas because the ideal MHD equations have no intrinsic length scale and can be written in a non-dimensional form.

3.2 Apparatus

The double-loop apparatus is similar to previous loop experiments done at Caltech [42, 43]. The plasma formation sequence begins by energizing solenoids below each electrode, producing an arched background magnetic field between each electrode pair. Then, Argon neutral gas is injected by fast gas valves [44] from nozzles in each electrode and a capacitor is discharged across each electrode pair. The high voltage ionizes the gas cloud, driving current along the background B-field, forming flux ropes. This initial configuration is shown in Fig. 3.2a. These two flux ropes collide and merge, eventually forming a single collimated flux rope (Fig. 3.1). The experiment operates inside a 1.6-meter-long, 1.4-meter-diameter vacuum chamber (base pressure $\sim 10^{-7}$ Torr), as described in Hansen, Tripathi, and Bellan [43].

B-dot Probe Array

The volumetric B-field data was acquired using a rotatable B-dot probe array. This array consisted of fifty-four, 5.6 μH surface-mount inductors in a linear array of 18 three-axis clusters. Each channel is digitized at 12 bits at a frequency of 100 MHz. By rotating and translating the probe through 750 shots, the array maps out the time-dependent vector field $\mathbf{B}(\mathbf{x}, t)$ in a volume containing most of Loop b and part of Loop a (Fig. 3.2a). Fig. 3.2b demonstrates the high reproducibility (shot variation $\sim$1%-5%, $\pm 10^{-3}$ T) of the magnetic field that makes this 3D scan possible. The combined B-vector measurements have a spacing of 1-2 cm, a temporal resolution
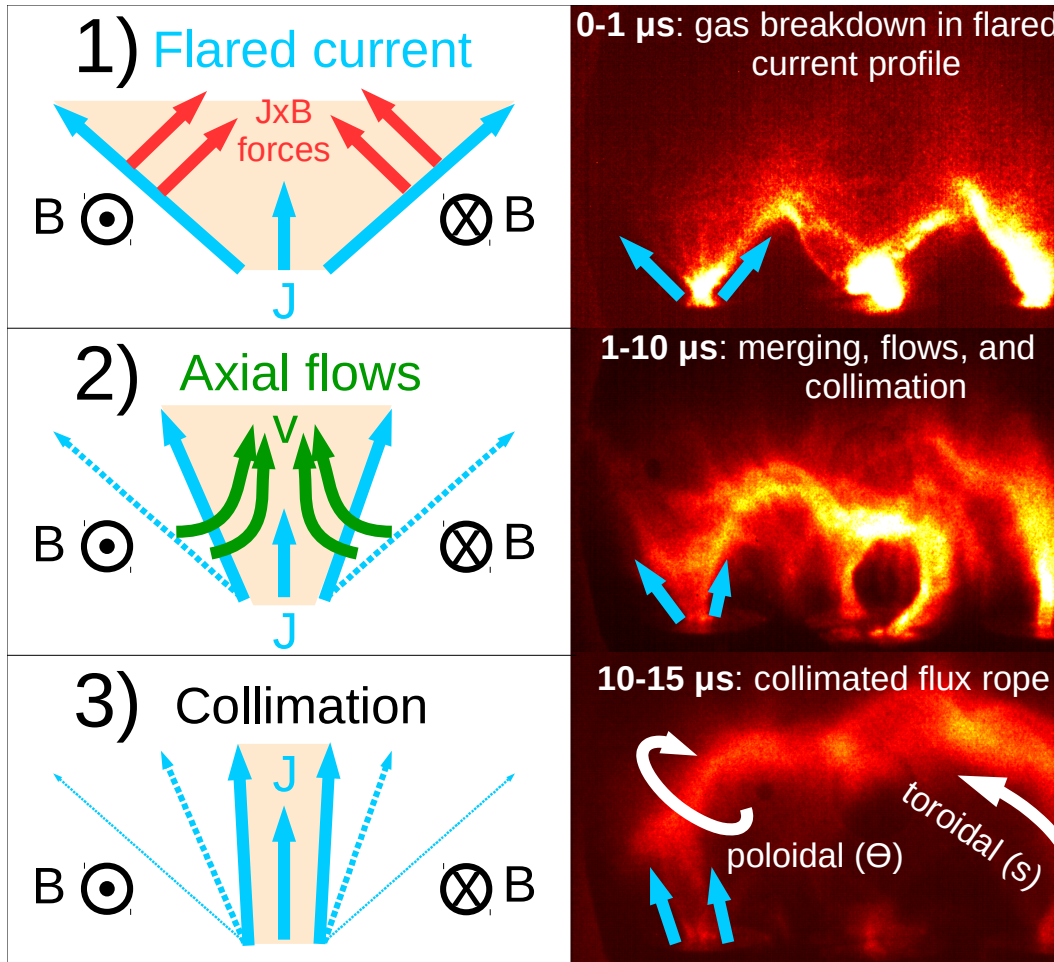
Figure 3.1: Figure displays collimation theory stages on left and fast-camera images of the double loop experiment in these stages on the right. Blue arrows at footpoint highlight the initially diverging current collimating over time.

of 0.1 μs, and extend from 4.5 cm to 22.7 cm above the electrode surface.

Magnetohydrodynamic (MHD) interpretation

MHD provides an appropriate description of the experiment since the length (0.5 m) and time scales (20 μs) are large compared to particle scales (plasma frequency: $f_{pe} = 10^{12}$ s^{-1}, Larmor radius: $r_{L_i} = 10^{-3}$ m, mean free path: $l_{\mathrm{mfp}} = 10^{-4}$ m) and the characteristic velocities are not relativistic ($v \ll c$). In this limit, the plasma can be treated as a single conducting fluid which obeys the following equation of motion:

$$\rho \frac{D\mathbf{U}}{Dt} = \mathbf{J} \times \mathbf{B} - \nabla P + \rho \mathbf{g}. \tag{3.2}$$
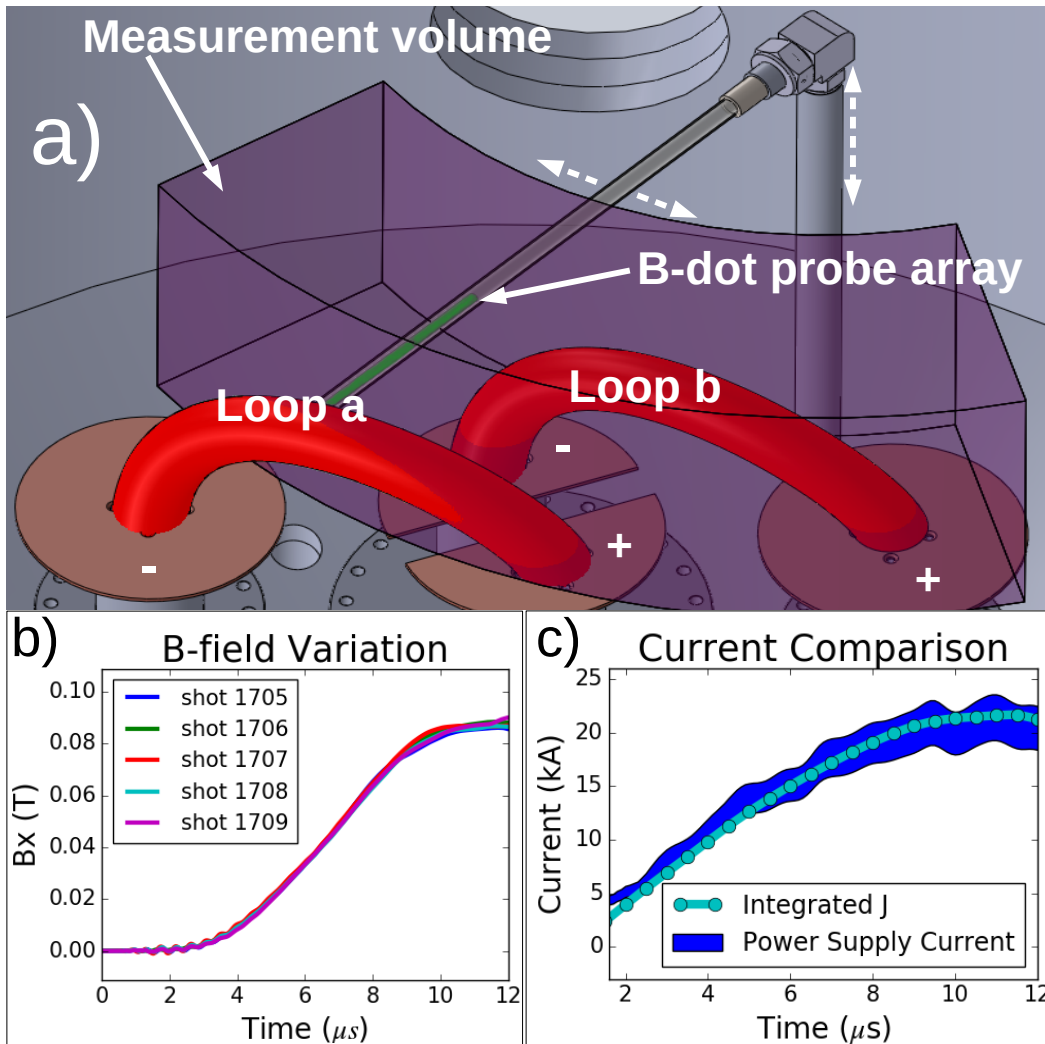
Figure 3.2: a) Diagram of double loop apparatus showing positioning of electrodes (copper), initial plasma loops (red), the annular measurement volume (purple) and the magnetic probe array (green). b) Representative plot of B-field variation for single direction at single location over sample of 5 shots. c) Comparison of Loop b power supply current and the calculated 3D current density: $\mathbf{J} = \nabla \times \mathbf{B}$. The power supply trace (dark blue) represents $\pm 1\sigma$ errorbars for the sample of 750 shots, the other line (light blue) plots the integrated current density through a Loop b cross section ($\int \mathbf{J} \cdot \mathbf{dA}$, this cross-section is plotted in Fig. 3.3).

This equation can be non-dimensionalized to allow for comparisons between different scales. The MHD form of Ampére's Law is also used, $\mathbf{J} = \nabla \times \mathbf{B}/\mu_0$, since the displacement current is ignorable for characteristic velocities much slower than the speed of light ($|\frac{1}{c^2}\frac{\partial \mathbf{E}}{\partial t}| \ / \ |\nabla \times \mathbf{B}| \sim (v/c)^2$). It also ensures that the current density is divergenceless $\nabla \cdot \mathbf{J} = 0$. Comparing the measured B-field with independent current measurements validates this assumption: integrating $\nabla \times \mathbf{B}/\mu_0$ over a

flux rope cross-section gives total current in good agreement with Rogowski-coil measurements of the power-supply current (Fig. 3.2c). The experimental Lundquist number is $S \sim 100 \gg 1$ ensuring that magnetic diffusion remains small ($\eta = 3 \cdot 10^{-4}$ Ω·m) and the magnetic evolution is governed by the induction equation:

$$\frac{\partial \mathbf{B}}{\partial t} = \nabla \times (\mathbf{U} \times \mathbf{B}). \tag{3.3}$$

Assuming a plasma can be described by ideal MHD ($S \gg 1$), its behavior can be scaled to a dimensionless form. This lack of an intrinsic length scale provides a one-to-one correspondence between systems with the same dimensionless form. The following invariant transformations provide scaling between equivalent systems: $L_0/a_1 \rightarrow L'$, $\rho_0/a_2 \rightarrow \rho'$, $B_0/\sqrt{a_3} \rightarrow B'$, $P_0/a_3 \rightarrow P'$, $\frac{1}{a_1}\sqrt{\frac{a_3}{a_2}}t_0 \rightarrow t'$, $\sqrt{\frac{a_2}{a_3}}v_0 \rightarrow v'$, $\frac{a_1 a_2}{a_3}g \rightarrow g'$, where a_1, a_2, a_3 are free parameters [2]. Table 3.1 shows the characteristic parameters of the experiment, typical coronal loop parameters, and experimental parameters scaled to the solar environment using $a_1 = 2.5 \cdot 10^{-8}$, $a_2 = 10^8$ and $a_3 = 10^4$. With the notable exception of gravity, the experimental parameters scale well to the solar case. It is important to note that the listed timescale, τ_A, is the Alfvén crossing time ($\tau_A = L/v_A$) and not the loop lifetime, which for solar loops is typically $\sim 10^2\tau_A$-$10^3\tau_A$. The experimental plasma lifetime $\approx 2\tau_A$ is limited due to the power supply duration; however, this lifetime is sufficiently long to resolve the collimation timescale ($< \tau_A$).

Table 3.1: Dimensionless scaling of Caltech parameters to solar loops

Experimental Parameters	$B = 3000$ G	$L = 0.5$ m	$\rho = 10^{-4}\frac{\text{kg}}{\text{m}^3}$	$\tau_A = 20~\mu$s
	$g = 10~\frac{\text{m}}{\text{s}^2}$	$P = 300$ Pa	$v_A=3\cdot10^4\frac{\text{m}}{\text{s}}$	$\beta = 0.01$
Scaled Exp. Parameters	$B = 30$ G	$L = 2\cdot10^7$ m	$\rho = 10^{-12}\frac{\text{kg}}{\text{m}^3}$	$\tau_A = 7$ s
	$g = 3\cdot10^{-3}~\frac{\text{m}}{\text{s}^2}$	$P = 3\cdot10^{-2}$ Pa	$v_A=3\cdot10^6\frac{\text{m}}{\text{s}}$	$\beta = 0.01$
Typical Coronal Loop	$B = 50$ G	$L = 2\cdot10^7$ m	$\rho = 10^{-12}\frac{\text{kg}}{\text{m}^3}$	$\tau_A = 5$ s
T= 1.5 MK	$g = 300~\frac{\text{m}}{\text{s}^2}$	$P = 1\cdot10^{-2}$ Pa	$v_A=4\cdot10^6\frac{\text{m}}{\text{s}}$	$\beta = 0.002$

3.3 Results

The analysis of the data is limited to the first 12 μs of evolution when the flux ropes are still within the measurement volume and the shot-to-shot variation is minimal (Figure 3.2). Within these constraints, the current density $\mathbf{J}(t)$, and magnetic force density, $\mathbf{J}(t) \times \mathbf{B}(t)$, can be calculated at each point in the measurement volume. Figure 3.3 plots several representations of this data set at t=4.5μs including magnetic field lines, current density isosurfaces, vectors of the magnetic force density ($\mathbf{J}\times\mathbf{B}$),

and 2D cross-sections. A movie of the 3D B-field evolution is available here and a movie of the current density evolution is available here.

Axial Magnetic Forces

As expected from the visible light images of the plasma, the total current has a funnel-like profile: narrower at the footpoints ($r_{\mathrm{minor}} \sim 3$ cm), and wider at the apex ($r_{\mathrm{minor}} \sim 6$ cm). The $|J|$ isosurfaces in Figure 3.3 show larger current density at the footpoints ($\sim 2.8 \times 10^6$ A/m^2) than at the apex ($\sim 0.7 \times 10^6$ A/m^2). These values are consistent with the earlier assumption that current density is divergenceless $\nabla \cdot \mathbf{J} = 0$ (i.e. the net current through each cross-section should be the same). This flaring can also be observed in the $\mathbf{J}$ cross-section (Fig. 3.3, lower right) in which there is a diverging radial component.

The $\mathbf{J} \times \mathbf{B}$ force density given by this flared current has a significant axial component. This axial component can be seen in the 3D vectors plotted in the upper half of Fig. 3.3 and in the $\mathbf{J} \times \mathbf{B}$ cross-section in lower left, where the colormap corresponds to the axial component. This axial component is vertical at both footpoints and reverses direction at the apex of the loop. Figure 3.4 plots this axial component for 22 cross-sections along loop b. This figure demonstrates the existence of axial magnetic forces directed from both footpoints towards the apex, independent of the current direction. The magnitude of these values are consistent with Eq. 3.1 and a more detailed quantitative comparison is included in Appendix C. These symmetric axial forces directed towards the apex are the primary result.

Axial Pressure and Density

Since the flux rope minor radius does not immediately collapse, the magnetic forces must be partially balanced by the internal pressure of the flux rope. The slight imbalance of these forces leads to the observed expansion of the major radius. Consequently, the magnetic forces on the interior edge of the loop must be greater than the pressure forces: $|\mathbf{J} \times \mathbf{B}|_{(R-\Delta)} > |\frac{\partial P}{\partial R}|_{(R-\Delta)}$, and the magnetic forces on the exterior edge must be less than the pressure forces: $|\mathbf{J} \times \mathbf{B}|_{(R+\Delta)} < |\frac{\partial P}{\partial R}|_{(R+\Delta)}$. Integrating this force asymmetry gives strong bounds on the internal pressure of the flux rope:

$$\int_{\infty}^{R} \hat{\mathbf{R}} \cdot (\mathbf{J} \times \mathbf{B}) \, dR' < P(r) < \int_{0}^{R} \hat{\mathbf{R}} \cdot (\mathbf{J} \times \mathbf{B}) \, dR'. \tag{3.4}$$

These measurements show that the axial pressure gradients (10^3-$10^5 \frac{\mathrm{N}}{\mathrm{m}^3}$) are comparable to the axial magnetic force-density (10^4-$10^6 \frac{\mathrm{N}}{\mathrm{m}^3}$). More detailed analysis of the
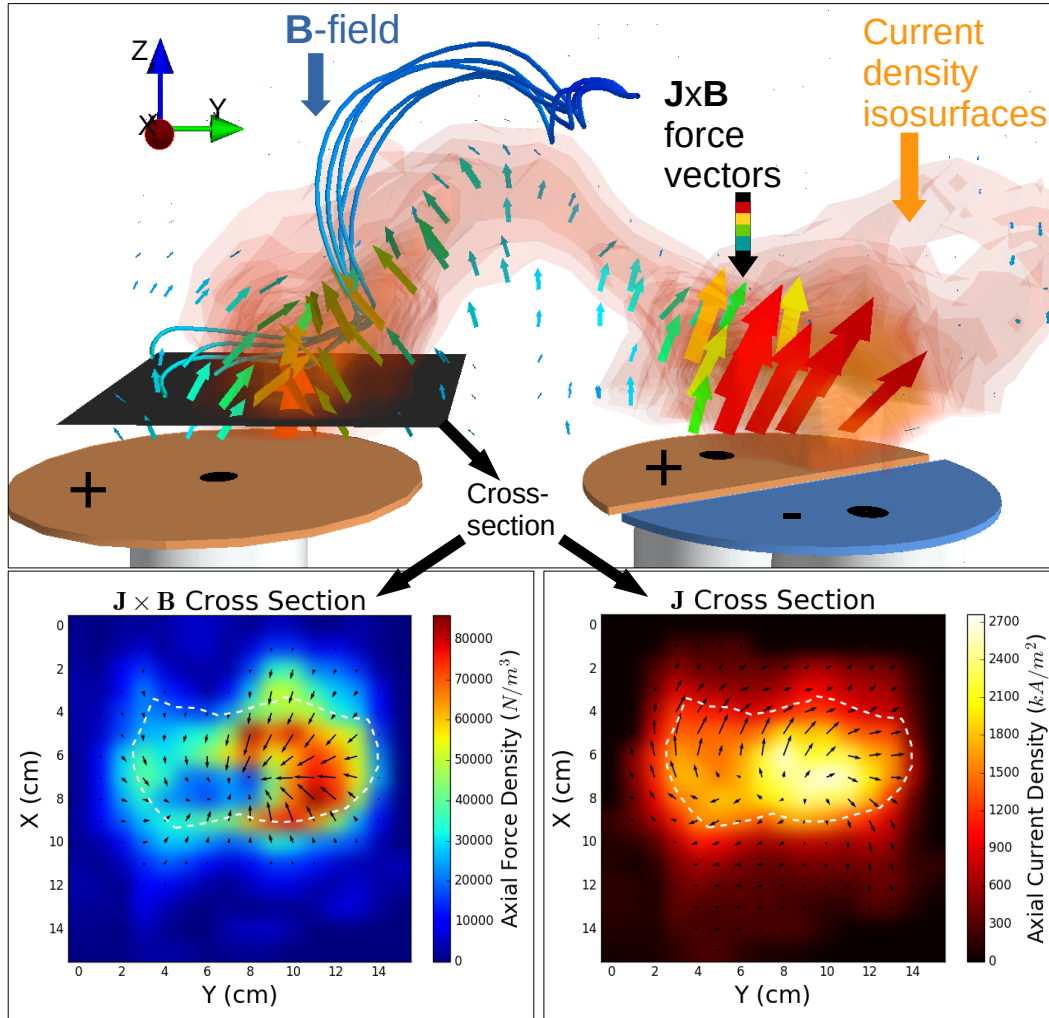
Figure 3.3: Plot of 3D B-field measurements viewed from B-dot probe axis of rotation at t=4.5μs: B-field streamlines are shown in blue, current density isosurfaces are shown in orange and colored vectors represent the $\mathbf{J} \times \mathbf{B}$ force density. 2D slices of $\mathbf{J} \times \mathbf{B}$ and $\mathbf{J}$ are shown for the black cross-section where arrows represent the in-plane components and colors represent the out of plane component. The dotted white line represents the 50% current contour.

relative contributions of pressure and magnetic forces is included in Appendix C.

Since the temperature of the plasma is fairly uniform and nearly constant in time (1.92-2.02 eV, from spectroscopic line ratios [45], see supporting information), the density is proportional to the pressure: $n(r) = P(r)/\kappa T$. Figure 3.5 shows a plot of this inferred number density at the footpoints and apex as a function of time. There is a two-hundredfold increase in density from t=1μs (10^{19} m^{-3}) to t=10μs (2×10^{21} m^{-3}) at the apex. This large increase in density suggests large flows from
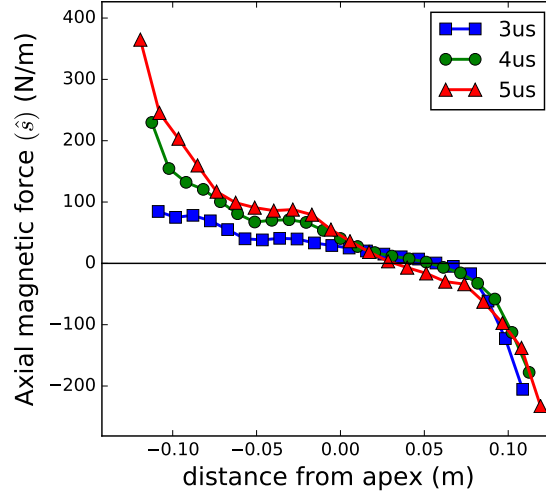
Figure 3.4: Plot of magnetic-force-per-length ($\int_S (\mathbf{J} \times \mathbf{B}) \cdot d\mathbf{S}$) through loop cross sections along the full loop axis at three times. The $\mathbf{J} \times \mathbf{B}$ axial component is directed towards the apex independent of the current direction.

the footpoints as there is insufficient background gas present to account for such a large increase.

Axial Flows

From the density evolution, the axial flow velocity is inferred from the continuity equation, assuming flow is primarily in the axial direction ($\hat{s}$):

$$\frac{\partial \rho}{\partial t} = -\nabla \cdot (\rho \mathbf{u}) \approx -\left(\frac{\partial \rho}{\partial s} u_s + \frac{\partial u_s}{\partial s} \rho \right). \tag{3.5}$$

Axial velocity at the footpoints is estimated, assuming the compressible term, $(\partial u_s / \partial s)\rho$, is small, as:

$$u_0 \approx -\left(\frac{\partial \rho}{\partial t} \left(\frac{\partial \rho}{\partial s} \right)^{-1} \right)\Big|_{s=0}. \tag{3.6}$$

The inferred axial velocities (10^4-10^5 m/s) are consistent with the flows imaged in other experiments [42, 46] for similar currents (20 kA). For comparison, the ion sound speed is $\sim 10^3$ m/s and the Alfvén velocity is $\sim 10^5$ m/s, so the observed flows are supersonic but sub-Alfvènic. The total axial force divided by the inferred density (10^{-6}-10^{-3} kg/m^3), $\hat{s} \cdot (\mathbf{J} \times \mathbf{B} - \nabla P)/\rho$, gives axial accelerations in the range (10^9-$10^{11} \frac{m}{s^2}$). These accelerations are consistent with the inferred velocities (10^4-10^5 m/s), distances (0.1-0.2 m), and times (1-10 μs).
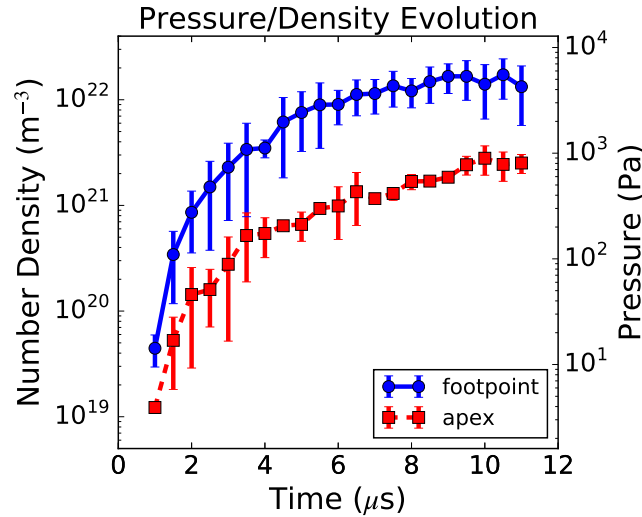
Figure 3.5: Logarithmic plot of pressure and number density as a function of time. Density is estimated from pressure bounds, assuming a uniform temperature of 2 eV: $n = P/\kappa T$.

Flux Collimation

The total axial flux, Ψ, of each loop can be considered constant since the solenoids generating the background axial field have a much longer decay timescale ($\tau \approx 40$ ms) than the experiment lifetime ($\Delta t \approx 30$ μs). Consequently, the collimation is proportional to the magnitude of the axial B-field. In this sense, collimation is any compression of the initial background field.

Figure 3.6 plots the magnitude of the axial field at the b+ footpoint and at the loop b apex as a function of time. The axial field strength at both locations increases by an order of magnitude demonstrating significant collimation (e.g. minor radius decreases by factor of 3). If the flows were primarily in the radial direction, the density would only increase by one order of magnitude. Since the density increases by nearly three orders of magnitude, the mass flux must come mainly from the footpoints.

3.4 Discussion

The experimental measurements verify the three predictions of Bellan [21]: that a flux rope with changing minor radius has axial magnetic forces, that these axial forces can drive counter-propagating flows from both footpoints, and that this process increases collimation of the axial field.
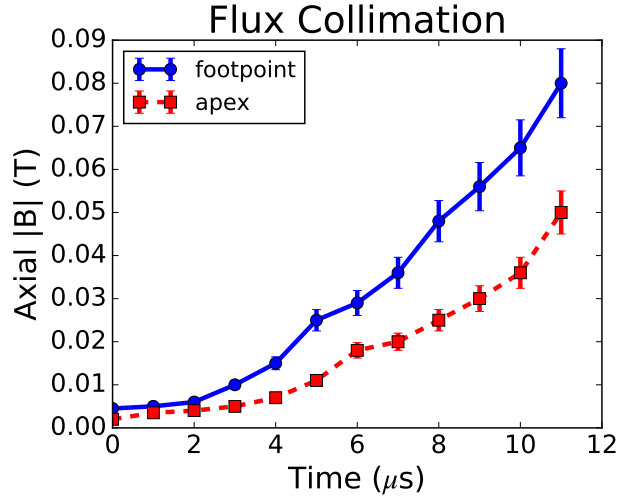
Figure 3.6: Comparison of axial magnetic field strength at loop apex and footpoint as a function of time. The magnitude increases by more than a factor of ten for both locations corresponding to a factor of 3 compression in minor radius.

In the solar corona, even small deviations from the force-free paradigm, (i.e. $\mathbf{J} \times \mathbf{B} \neq 0$) can result in significant changes to loop equilibria [12]. For this reason, the collimation mechanism could be significant in explaining observations of solar loop collimation, equilibrium density profiles and counter-streaming flows.

For example, a typical coronal loop ($T = 1\text{-}3 \cdot 10^6$ K, $g = 200\text{-}273$ m/s^2, $m = 1.67 \cdot 10^{-27}$ kg, $\rho = 10^{-12}$ kg/m^3) has a pressure scale height of, $H_P = P_0/\rho g = \kappa T/mg = 30\text{-}123$ Mm. The equivalent scale height for the collimation mechanism is, $H_B = B_\theta^2/(\mu_0 \rho g)$. If a flux rope's poloidal field at a footpoint is $B_\theta = 1$ G, the magnetic scale height is: $H_B = 30$ Mm. Since such poloidal fields are routinely observed in coronal loops [11, 47], this mechanism could explain the discrepancy between measured scale heights (45-60 Mm) and hydrostatic scale heights (17 Mm) in some loops [31].

For flux ropes with larger poloidal fields (1-10 G), the mechanism could generate counter-propagating flows along the loop axis. This could explain the recent observations of widespread counter-streaming flows in both solar prominences and solar loops [34, 36, 37, 48, 35, 8].

Chapter 4

3D MHD NUMERICAL SIMULATION OF SINGLE LOOP EXPERIMENT

This chapter covers the development and first results of a 3D MHD simulation for the single loop experiment. The simulation quantitatively reproduces the experimental loop expansion, shape, and magnetic field. In addition to validating the simulation, this agreement with experiment gives confidence that the essential physics of the experiment is well characterized. Since non-uniform initial density and various boundary fluxes (e.g. mass, helicity) are critical to accurately modeling the experiment, it is likely that similar detail is necessary for modeling solar loops and solar eruptions. This simulation is used in Chapters 5 and 6 to supplement the experimental results.

The key innovation of this simulation is a new method for constructing low aspect ratio (fat/broad etc.) arched current channels. This method allows study of flux rope compression which is essential to the mechanisms in Chapters 3 and Chapter 6.

4.1   3D MHD Simulation

The work on the simulation was done in collaboration with Pakorn Wongwait-ayakornkul and was co-advised by Hui Li at Los Alamos. The simulation uses a modified version of the Los Alamos COMPutational Astrophysics Simulation Suite (LA-COMPASS) and was run on the Turquoise supercomputing cluster [49]. The original code was used to simulate astrophysical jets in the intra-cluster medium [40] and the Caltech plasma jet experiment [41].

Simulating a measureable experiment provided great physical insight since the simulation gave clearly incorrect results with the initial hand-waving assumptions. This initial disagreement led to a better understanding of the experimental initial conditions and the most important factors in the loop evolution.

Comparison with previous work

There have been several simulations of the single loop experiment over the years which have mirrored the evolution of the larger simulation community. The first simulation of the single loop was a code which solved for force-free magnetic

Hansen and Bellan 1998 — Force free Incompressible

Tokman and Bellan 2002 — Dynamic Incompressible

2018 — Dynamic Compressible
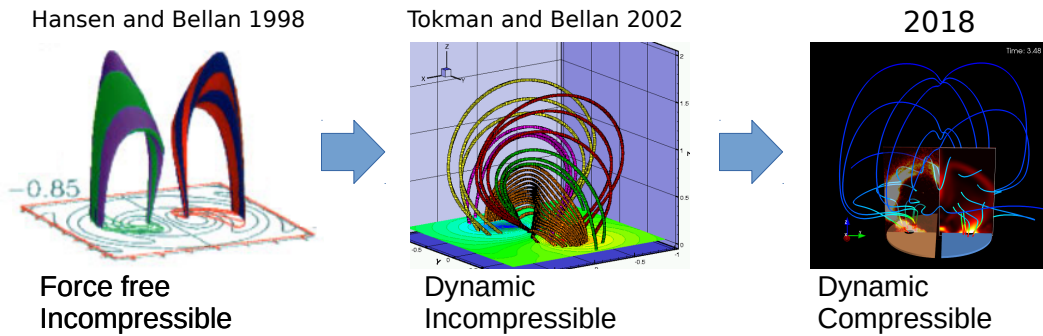
Figure 4.1: Simulation history of the single loop experiment

equilibria [13]. The next iteration was the PhD thesis of Mayya Tokman [50], a fully dynamic simulation using exponential propagation techniques, but assumed incompressible flow (ρ =const).

This new simulation has several unique features which set it apart from previous work,

- Compressible evolution: density is not constant, ($\nabla \cdot v \neq 0$)

- Low aspect ratio flux rope: the initial current density profile is extremely broad/fat.

- Fully dynamic: both magnetic and pressure forces are fully dynamic

These three factors are necessary to properly model the evolution of the flux rope minor radius and are crucial to the results presented in Chapters 5 and 6.

Numerical methods

The spatial domain is a Cartesian mesh cube with 96 grid points in each dimension simulating a cube of 36^3 cm^3 and outflow (Neumann) boundary conditions. The code evolves a set of two 3D vectors (velocity, magnetic field) and two scalars (density, pressure) at each grid point through the conservative form of the ideal MHD equations:

$$\frac{\partial \bar{\rho}}{\partial \bar{t}} = -\nabla \cdot (\bar{\rho} \bar{\mathbf{v}}) \tag{4.1}$$

$$\frac{\partial (\bar{\rho} \bar{\mathbf{v}})}{\partial \bar{t}} = -\nabla \cdot (\bar{\rho} \bar{\mathbf{v}} \bar{\mathbf{v}} + (\bar{P} + \bar{B}^2/2) \overleftrightarrow{\mathbf{I}} - \bar{\mathbf{B}} \bar{\mathbf{B}}) \tag{4.2}$$

$$\frac{\partial \bar{e}}{\partial \bar{t}} = -\nabla \cdot \left[(\bar{e} + \bar{P} + \bar{B}^2/2) \bar{\mathbf{v}} - \bar{\mathbf{B}} (\bar{\mathbf{v}} \cdot \bar{\mathbf{B}}) \right] + \dot{\bar{e}}_{\text{inj}} \tag{4.3}$$

$$\frac{\partial \bar{\mathbf{B}}}{\partial \bar{t}} = -\nabla (\bar{\mathbf{v}} \bar{\mathbf{B}} - \bar{\mathbf{B}} \bar{\mathbf{v}}) + \dot{\bar{B}}_{\text{inj}}. \tag{4.4}$$

These equations characterize the four primary conservation laws in ideal MHD: conservation of mass (4.1), momentum (4.2), energy (4.3), and magnetic flux (4.4). Equations 4.3, 4.4 both have an injection term which is used to model the flux injection from the electrodes. The total energy $\bar{e}$ is defined by $\bar{e} \equiv \bar{\rho} \bar{v}^2/2 + \bar{P}/(\gamma - 1) + \bar{B}^2/2$, $\gamma = 5/3$. The simulation evolves with a timestep of $0.01 t_0$, where t_0 is the normalized simulation unit for time, for 34 time steps.

The solver is a conservative Godunov-type finite volume method using a constrained transport scheme (face-centered grid for B-field) to preserve $\nabla \cdot \mathbf{B} = 0$. Further details on the numerical methods can be found in [49, 40].

Concerns about using ideal MHD

Despite the many more accurate descriptions of plasma behavior, MHD is used because it is usually sufficient to capture the bulk behavior of the plasma. In the case of the single loop experiment, the phenomena of interest are in this large length scale/slow timescale regime.

The following tables provide a description of the relevant length and time scales for argon and hydrogen for a characteristic magnetic field |B|= 0.06 T, and density n=10^{21} m^{-3}.

Length Scales (m)	Symbol	Hydrogen	Argon
Electron skin depth	d_e	1.7×10^{-4}	1.7×10^{-4}
Electron Larmor radius	r_{l_e}	6×10^{-5}	6×10^{-5}
Ion skin depth	d_i	0.007	0.05
Ion Larmor radius	r_{l_i}	0.0024	0.015
Distance between the electrodes	L	0.08	
Simulation length	D	0.36	
Chamber radius	R	0.70	

Time Scales (s)	Symbol	Hydrogen	Argon
Electron plasma frequency	$2\pi/\omega_{pe}$	4×10^{-12}	4×10^{-12}
Electron cyclotron period	$2\pi/\omega_{ce}$	6×10^{-10}	6×10^{-10}
Ion plasma frequency	$2\pi/\omega_{pi}$	2×10^{-10}	1×10^{-9}
Ion cyclotron period	$2\pi/\omega_{ci}$	1×10^{-6}	4×10^{-5}
Alfvén time	$\tau_A = L/v_A$	2×10^{-6}	
Simulation duration	T_{sim}	2×10^{-5}	

However due to the good agreement of the simulated loop with the experiment, the non-MHD effects are not expected to provide significant corrections to the bulk behavior, even for Argon plasmas.

Normalization

Length, number density and speed units are normalized to nominal values. This reduces parameters of interest to order unity and prevents issues with roundoff error. All other quantities are normalized to reference values derived from these three nominal values and ion mass (m_i). These values are shown in Table 4.1),

Boundary Conditions

At the boundaries ($x, y, z = \pm R_0$), Neumann outflow conditions ($\partial f/\partial x = 0$) were imposed. These boundary conditions allow flow through the boundary by using a set of ghost cells with values equal to the edge cells. These conditions do still generate reflections of wave modes.

Initial Conditions

The simulation uses the initial density profile shown in Figure 4.2. In addition to the two gas cones, a high density wall region is added below the footpoints ($z < 0$) to simulate the conductive boundary provided by the electrodes.

The initial background magnetic field (bias field) is generated by specifying a set of loop currents in a half-circle configuration below the electrode plane. This ensures that all field lines emerge and terminate at the footpoints. This topology is closer to that of the experimental field (i.e. where B_z does not change sign on a given electrode) than a simple dipole and is scaled to match the measured field strength (600 G) at the loop apex. The resulting initial bias field is shown in Figure 4.2.

Table 4.1: Normalization constants for simulation

Quantity Unit	Quantity Symbols	Ar ($\mu = 40$)	Solar
Length	R_0	0.18 m	2×10^7 m
Number density	n_0	10^{21} m^{-3}	1.2×10^{15} m^{-3}
Speed	C_{s0}	3.1×10^3 m s^{-1}	300 km s^{-1}
Ion Weight	$\mu = m_i/m_H$	40	1
Time	$t_0 = R_0/C_{s0}$	58 μs	67 s
Mass Density	$\rho_0 = n_0 m_i/2$	3.3×10^{-6} kg m^{-3}	1.0×10^{-12} kg m^{-3}
Mass	$M_0 = \rho_0 R_0^3$	1.92×10^{-8} kg	
Pressure	$p_0 = \rho_0 C_{s0}^2$	32 Pa	90 mPa
Temperature	$k_B T = m_i C_{s0}^2/2$	2 eV	5.4×10^6 K
Energy	$E_0 = p_0 R_0^3$	0.187 J	
Power	$P_0 = E_0/t_0$	3.21×10^3 Watt	
Magnetic Field	$B_0 = \sqrt{\mu_0 p_0}$	190.2 G	3.4 G
Magnetic Flux	$\Psi_0 = B_0 R_0^2$	205.4 μWb	
Current Density	$J_0 = B_0/(\mu_0 R_0)$	84.1 kA m^{-2}	13.5 μA m^{-2}
Current	$I_0 = J_0 R_0^2$	9.08×10^2 A	
Voltage	$V_0 = P_0/I_0$	3.53 V	
Magnetic Moment	$m_0 = B_0 R_0^3/\mu_0$	29.4 A m^2	
Force Density	$F_0 = B_0 J_0$	178 N/m^3	
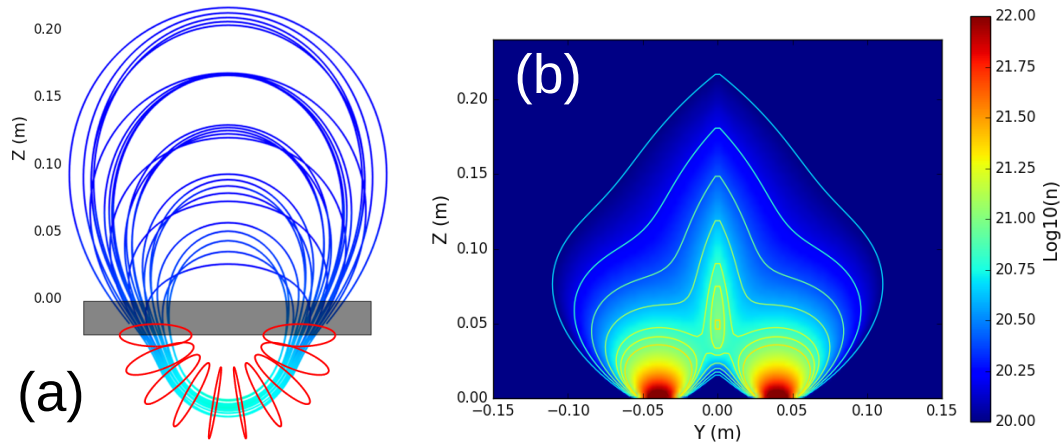
Figure 4.2: Plots of the initial conditions for the simulation. (a) Plot of background magnetic field. Field lines are shown in blue, source currents for this field are shown in red (i.e. 10 thin loops arranged in a semi-circle), and the high density plasma wall at the footpoints is shown in grey. (b) Initial number density profile above the high density wall. The origin of the density pileup at the center of this profile is explained in Chapter 5.

Components of Density Distribution

Background Density The MHD solver cannot process regions of high vacuum (e.g. density must be greater than 10^{-10} kg/m^{-3} everywhere in the simulation volume). Therefore, a small uniform background density 3.3×10^{-10} kg/m^{-3} is added prevent code errors while not affecting the morphology of the flux rope evolution.

High Density Wall The density below the footpoint level is set to be extremely high, relative to the plasma density, to simulate the conductive, stationary boundary provided by the copper electrodes,

$$\rho_{\text{wall}}(z) = \rho_{\text{large}} H(z_{\text{wall}} - z), \tag{4.5}$$

where $\rho_{\text{large}} =$ and $z_{\text{wall}} = 1$ cm from the bottom boundary ($y = -R_0$). The wall was also initialized with zero pressure such that there would be no motion from pressure gradients.

Single Gas Valve The Caltech experiment has detailed measurements of the neutral density profile emerging from a single footpoint. This measured profile is that of an exponential cone:

$$\rho_n(r, z) = \rho_0 \left(\frac{z_0}{|z| + z_0} \right)^2 \exp\left[-\left(\frac{Kr}{|z| + z_0} \right)^2 \right] \tag{4.6}$$

where $K = \tan\alpha \sqrt{\log 2} = 1.1$ and $\alpha \approx 54°$ is the half cone angle. $z_0 = 0.01$ m is an offset distance in the z direction. $\rho_0 = 2 \times 10^{-3}$ kg m^{-3} is the density at the footpoints. All the parameters are chosen to match the measurements made by fast ion gauge [17, 18]. The use of two adjacent nozzles results in a pileup region between the two cones due to the finite mean free path. This effect is further explained in Chapter 5.

Initial Velocity

Since the sound speed of neutral gas (1 km/s) is 10 times smaller than the speed of the plasma expansion ($\sim$ 10 km/s), we can assume that the plasma is initially stationary throughout the whole spatial domain.

Initial Pressure

The initial pressure scales with initial plasma density, assuming the system is isothermal (except for the wall region which has zero pressure). Several measurements [51] imply a reasonably uniform temperature of 2 eV in our plasma.

Background Magnetic Field

The background magnetic field is generated by a set of 10 loop currents equally spaced along a 4 cm radius half circle beneath the loop footpoints. Each of these loops is given a current of 6.31×10^5 A. The expression for the vector potential of each loop is given by,

$$A_\phi(r, \theta) = \frac{\mu_0}{4\pi} \frac{4Ia}{\sqrt{a^2 + r^2 + 2ar \sin \theta}} \left[\frac{(2 - k^2)K(k) - 2E(k)}{k^2} \right], \qquad (4.7)$$

$$K(k) = \frac{\pi}{2} \sum_{n=0}^{\infty} \left[\frac{(2n)!}{2^{2n}(n!)^2} \right]^2 k^{2n} \qquad (4.8)$$

$$E(k) = \frac{\pi}{2} \sum_{n=0}^{\infty} \left[\frac{(2n)!}{2^{2n}(n!)^2} \right]^2 \frac{k^{2n}}{1 - 2n} \qquad (4.9)$$

$$k^2 = \frac{4ar \sin \theta}{a^2 + r^2 + 2ar \sin \theta}. \qquad (4.10)$$

where r, θ, and ϕ are the usual spherical coordinates. This expression is taken from [52].

The more terms that are used in the series, the thinner the current profile. Conversely, truncating this particular series results in a finite radius current loop. The loops used in the simulation were truncated at $N = 80$, where the aspect ratio $R/r \geq 3$.

Current Injection

Diffuse poloidal flux is continuously injected into the simulation domain corresponding to the electric current measured in the experiment. The diffuse current profile is constructed from the superposition of 110 thin circular current loops, where each loop has the analytic magnetic field expression from Eq. 4.7. The loops heights and radii are adjusted such that all loops pass through the footpoints,

$$d^2 + (\Delta z)^2 = R^2 \qquad (4.11)$$

where Δz is the vertical offset, R is the radius, and $d = \pm 4$ cm are the footpoint locations. To avoid singularities, the elliptic integrals are approximately evaluated using truncated power series, $N = 80$. This injected distribution, shown in Figure

4.3a, is physically motivated by experimental current density measurements which indicate that the current profile begins as a flared diffuse structure and maintains this outer diffuse current during helicity injection. Figure 4.3c shows the current path of 10 loops in yz-plane with apexes equally spaced from $1.2y_0$ to $2.6y_0$. Figure 4.3b shows another view of the profile in xz-plane with 11 sets of 10 current loops distributed over $\theta_{yz} \in [-54°, 54°]$ respect to the yz-plane. The injected current profile is stationary throughout the simulation. Since we are principally interested in the formation phase, we do not attempt to model the helicity extraction or the decreasing current after t_{off}=20 μs. The experimentally measured current undergoes a damped oscillation with the period $T = 40$ μs, so we model the temporal dependence of the injection as

$$\frac{d}{dt}B(t) = \dot{B}_0 \cos\left(\frac{2\pi t}{T}\right) H(t_{\text{off}} - t),$$

(4.12)

where $\dot{B}_0$ has only spatial dependency and H is the Heaviside step function. This injection method allows us to better match the injection of magnetic helicity and energy in the experiment. Several alternate schemes and their corresponding issues are described in the next section.

Alternate Injection Schemes

A number of other injection schemes were tried before settling on the final version and the following sections briefly outline these other schemes and their associated problems.

Boundary Injection Region

The previous use of the LA-COMPASS code simulated the Caltech astrophysical jet [41]. This code injected axisymmetric flux in a localized "engine region" near the $z = 0$ plane. This method was the first candidate to provide helicity injection for the single loop. To adapt this method for the loop geometry, the equivalent of two jets were injected, one at each footpoint and with opposite currents. It was expected that the current would follow the arched background magnetic field, giving a loop geometry. This was a poor assumption. The resulting simulation produced two jets which did not merge to form a coherent flux rope.
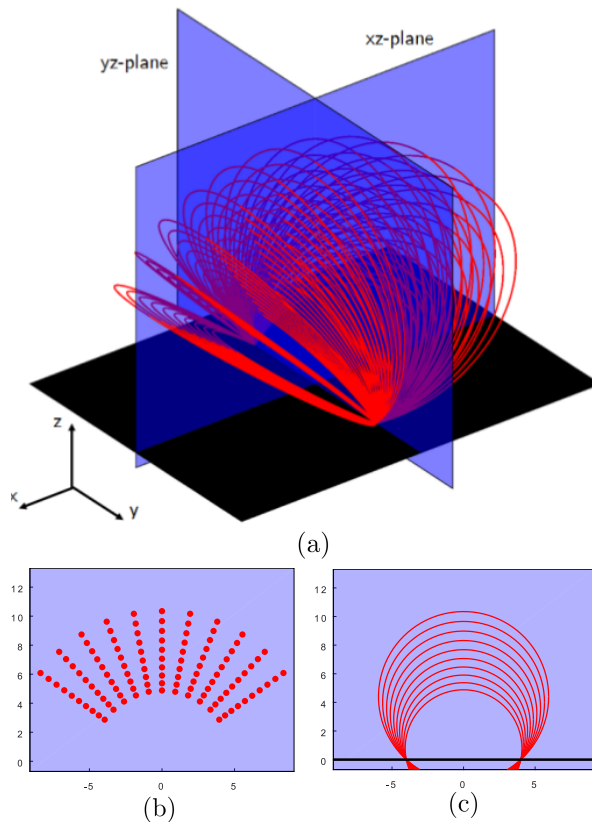
Figure 4.3: Illustration of spatial profile of the current injection. Each red circle represents a thin circular current loop. (a) The 3 dimensional view showing all 110 loops. (b) The 2 dimensional cross section in xz-plane. (c) The 2 dimensional cross section in yz-plane. The spatial units are in centimeters.

Footpoint Rotation

The next scheme involved rotating the footpoints. This local rotation injects a co-axial current distribution by twisting the axial field at each footpoint.

There are a number of other issues which made this scheme difficult to apply to the experiment:

- The velocity forcing at the footpoints prevents self-consistent evolution of loop collimation.

- The net current is zero since rotation injects coaxial current.

- The magnetic twist from the footpoint rotation propagates/changes slowly compared to the near-instantaneous changes in experimental current.

- The current profile is entirely determined by the background magnetic field where in the experiment the current is heavily restricted by the gas distribution.

- The scheme conflicts with the presence of the high density wall since wall motion guarantees finite wall pressure, leading to large pressure gradients and flows in the vertical direction.

Flared Initial Current Profile with no Injection

Another set of initial conditions used an initially flared profile with no injection. Since diffuse current at large radius does not significantly affect the dynamics at small radii, this scheme allowed the loop to sweep up additional current as it expanded, giving an effectively increasing current in the primary loop structure. This was reasonable as a first approximation but could not be precisely matched to the experiment.

4.2 First Results

Morphology and Velocity

The simulation reproduces the shape and major radial expansion of the experiment. Figure 4.4 compares a sequence of images from the experiment and an equivalent sequence of synthetic images from the simulation. The characteristic cusp shape is the result of the density pileup region between the two gas valves. This gives the simulation a very similar shape to the experimental images.
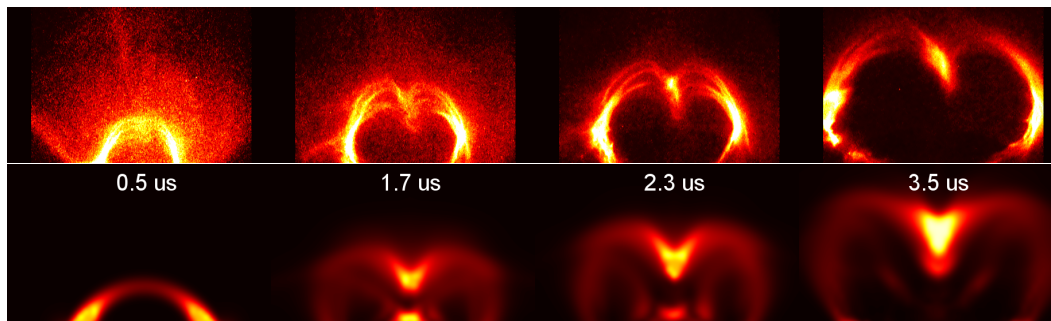
Figure 4.4: Image sequences of loop evolution comparing white light images of the experiment (upper panel) with synthetic images of the experiment (lower panel). The synthetic images plot the line integrated $J \cdot P^2$.

Furthermore, Figure 4.4 shows that the apex position and velocity are well matched to the experiment. This quantitative matching gives reasonable confidence that the simulation captures the first order dynamics present in the experiment.

Magnetic Field

The magnetic field of the simulated loop quickly evolves from the broad current injection profile to a well collimated flux rope. The interior of the flux rope ($r_{minor} < 2$ cm) remains highly twisted (5-10 turns) while the outer portion ($2 < r_{minor} < 8$ cm) is only slightly sheared (< 1 turn). Consequently, the edge safety factor (where the edge is defined to enclose 95% of the current) is quite large and the plasma should be stable against global sausage and kink modes. Figure 4.5 shows the global magnetic field profile as well as the region accessible to the magnetic probes.
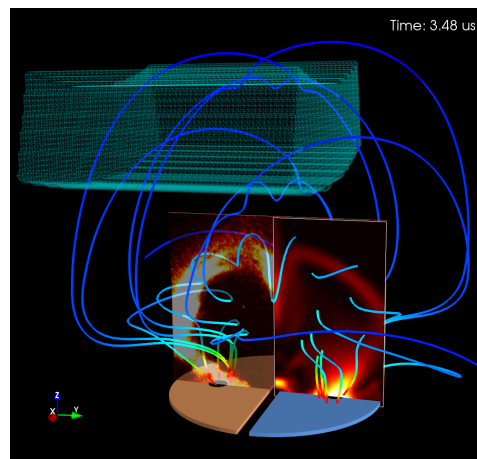
Figure 4.5: Figure shows the global magnetic field structure of the loop at t=3.48 μs after breakdown. The loop is visualized using an image on the left and the simulated current density on the right. The blue annulus above the loop represents the volume accessible to the magnetic probe and the electrodes are depicted below the footpoints (copper electrode +, blue electrode -).
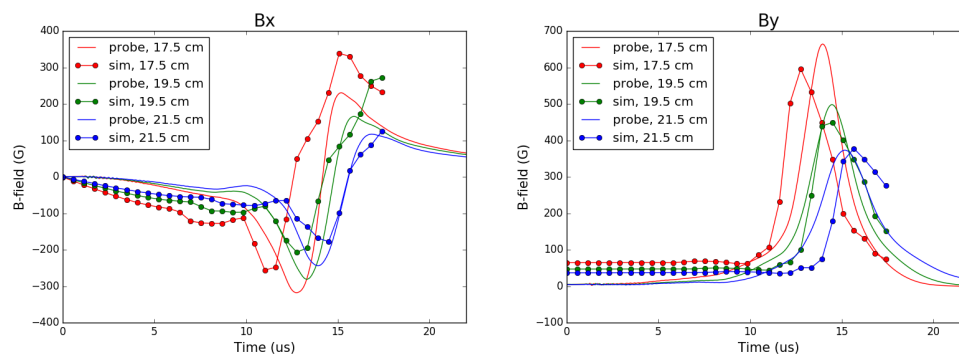
Figure 4.6: Plot of experimental B-field from magnetic probes and equivalent measurements at probe locations in simulation.

Flows and collimation

The simulation also shows evidence for the collimation mechanism described in Chapter 3. As the broad injected current profile from Figure 4.3 rises and collimates, axial flows from both footpoints are generated. Figure 4.7 (left) shows the axial mass flow (dm/dt) 3 cm above a loop footpoint as a function of time. To illustrate the effect of these flows on the density profile, a simulation was run with an initial density profile that did not have a pileup region (Figure 4.7, right). This plot shows the axial density of the loop at different times starting with a smooth initial density profile (no initial pileup region). The axial profiles at later times demonstrate that the relative density increases at the loop apex from the counter-propagating flows.
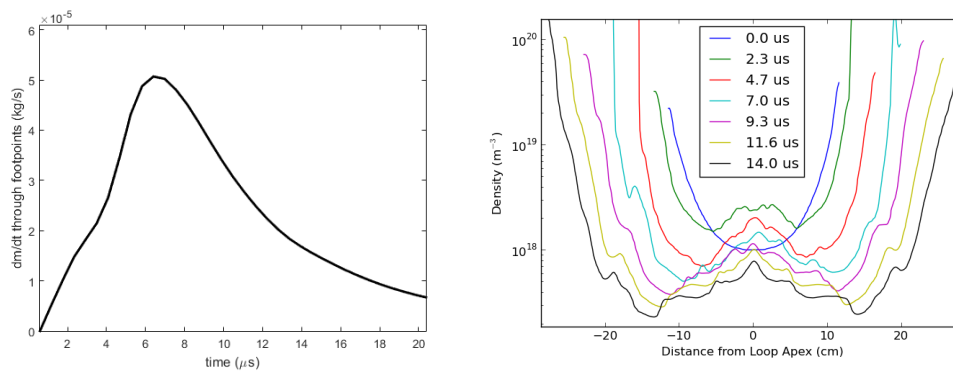
Figure 4.7: Plot of axial flow at the footpoint (left) and evolution of the axial density profile (right).

C h a p t e r   5

HELIX OR CUSP?

5.1   Introduction

The downward dip feature present in the single-loop experiment [53, 42, 54] has remained poorly understood for almost two decades. This feature is extremely reproducible and happpens every experiment. A typical image of this dip is shown in Fig. 5.1a. The interpretation until now has been that the dip seen in images is the projection of a helical loop axis generated by the kink instability [53, 42, 55]. However, there are several problems with this interpretation. First, the observed dip is always downwards, whereas the kink instability should generate both upward and downward helical perturbations. Second, images from other angles show little evidence for helical structure in the third dimension (Fig. 5.1b). Third, kink modes should grow but the dip remains a constant size. Lastly, the dip feature also appears in the FlareLab flux rope experiment [55], but not in other similar flux rope experiments [56, 57]. Alternative to the helical interpretation is that the dip is a sharp downward cusp, but this interpretation has no obvious formation mechanism and has consequently not been considered until now.
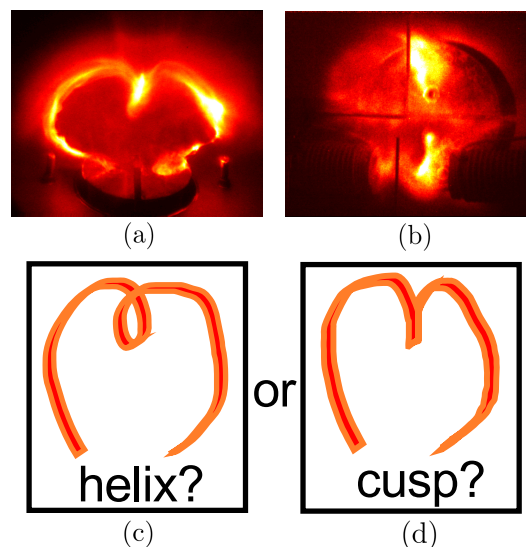
Figure 5.1: (a) Side view of lab experiment flux rope showing dip at apex, (b) top view of lab flux rope showing little evidence of helical shape, (c) sketch of side view for helix interpretation, (d) sketch of side view for downward cusp interpretation

This chapter identifies a formation mechanism for the cusp shape sketched in Figure 5.1d and provides detailed evidence from theory, experiment, and simulation supporting the cusp interpretation. The proposed mechanism is that neutral gas, injected from fast-gas valves at both footpoints, collides at the loop midplane creating a density pileup region. This causes the loop apex to have a greater linear mass density than the rest of the loop and, since the apex and the rest of the loop experience equivalent forces, the apex will have a slower acceleration, leading to the formation of a downward cusp during expansion. This theory explains why the dip is always downward, why there is no helical structure or dip growth, and why the feature only appears in experiments with gas injection from both footpoints. The results indicate that density perturbations can greatly distort the shape of an erupting flux rope and that introducing such perturbations may suppress external kink modes. These results are applicable to all MHD flux ropes with density perturbations (solar prominences, tokamaks, astrophysical jets etc.) and are especially relevant to the morphology of solar eruptions. Furthermore, other plasma experiments which use fast-gas valves [58, 59, 60, 61, 62, 53, 42, 54, 63] should be aware of the potential for non-linear interaction between multiple gas valves.

5.2 Experimental Apparatus

The primary experiments of interest are the different iterations [53, 42, 54] of the Caltech single-loop experiment. All of these experiments exhibit the apex dip feature and have similar designs. The experimental apparatus is the latest incarnation of the Caltech single loop experiment. This apparatus was described in Chapter 2 and more detail can be found in Ref. [54], but a brief review is provided here. The experiment has a single pair of electrodes with internal solenoids and fast-gas valves [64]. The system is mounted at the end of a 1.5 m long, 0.92 m diameter vacuum chamber with 10^{-7} Torr base pressure. The solenoids, located behind the electrodes, generate an arched background magnetic field (< 0.1 T). Fast valves then release cones of neutral particles over 5 ms [18] through holes in the electrodes into the vacuum chamber. High voltage applied to the electrodes by a 59 μF capacitor ionizes the gas to form an arched plasma of density $n \sim 10^{21}$ m^{-3}. The capacitor is typically charged to 2.5-5 kV driving 30 kA of current for 10 μs. Schematic diagrams of the experiment and start sequence are shown in Figure 5.2.
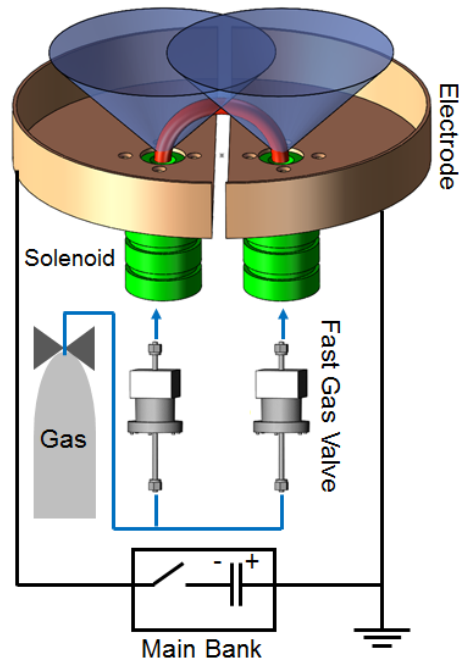
Figure 5.2: Schematic diagram of the experimental setup showing cones of neutral gas (blue) ejected from holes in electrodes (copper), plasma loop (red), solenoids (green) for providing background magnetic field, and gas injection system

Other Experiments

The FlareLab experiment at Ruhr University Bochum was designed based on the Caltech apparatus and has similar gas supply, timescales, electrodes, and magnetic fields [63]. This experiment also observes a downward apex dip.

The PPPL apparatus is located in the MRX facility [56]. It uses uniform background gas injection as well as fast-gas valve injection at a single footpoint. Plasma is also generated via high voltage breakdown from the electrodes. However, the timescale for this experiment is ~ 1 ms, 100 times longer than the Caltech loop, and is comparable to the gas diffusion time. This experiment does not observe apex dips.

The UCLA single loop experiment [57] is generated in a uniform pre-ionized plasma and utilizes LaB_6 electrodes with much lower currents (600 A). Additional density is added from laser ablation of targets at the footpoints to trigger eruptions. No apex dips are observed in this experiment either.

For comparison, Figure 5.3 shows the white light images for the solar flux rope in all 4 experiments.

(a) Caltech Single-loop	(b) FlareLab

adapted with permission from
Tenfelde et al. (2012)

FGV at both footpoints · FGV at both footpoints

(c) PPPL MRX	(d) UCLA SPD

provided by Clayton Myers

adapted with permission from
Tripathi & Gekelman (2010)

neutral pre-fill and FGV
at single footpoint · background plasma
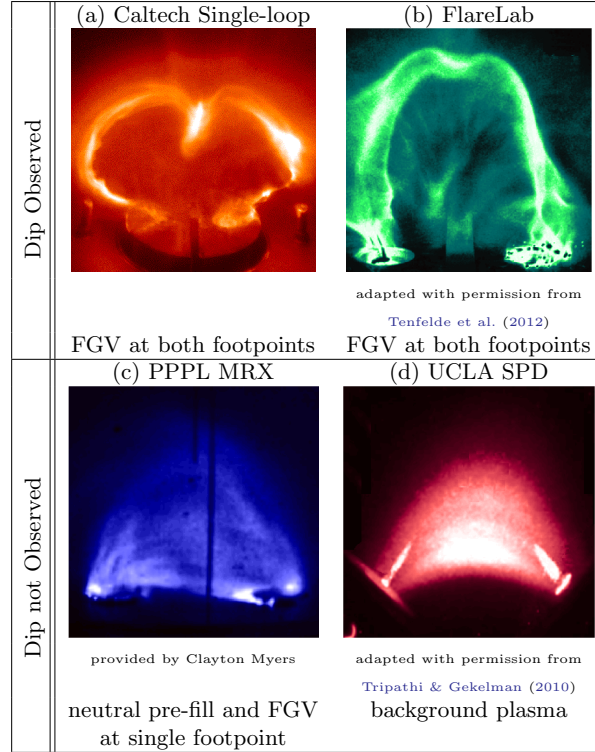
Figure 5.3: Comparison of white light images for arched flux rope experiments with their gas supply. Only experiments with fast-gas valves (FGV) at both footpoints observe dip feature

5.3 Theory

Single Gas Valve

The Caltech experiment has detailed measurements of the neutral density profile emerging from a single footpoint [18, 17]. This measured profile is that of an exponential cone:

$$\rho(x, y, z) = \rho_0 \left(\frac{z_0}{|z| + z_0} \right)^2 \exp\left[-\frac{K(x^2 + y^2)}{(|z| + z_0)^2} \right],$$

(5.1)

where $K = \tan\alpha\sqrt{\log 2} = 1.1$, $\alpha \approx 54°$ is the half cone angle, $z_0 = 0.01$ m, and $\rho_0 = 2 \times 10^{-3}$ kg m^{-3} is the density at the footpoints.

Two Gas Nozzles

The two gas nozzles (1 cm apertures) are equally spaced in the y direction ($y_0 = \pm 4$ cm) and point in the z direction. This gas injection from both nozzles creates overlapping gas cones. If the mean free path is large, the neutral gas in the two cones will not interact and the final distribution is simply a linear superposition of

two cones (Figure 5.4a). However, if the neutral gas has a mean free path comparable to the system size ($\sim$ 10 cm), the gases will interact and a density pileup will form between the two cones. The mean free path is defined as: $\ell_{\mathrm{mfp}} = (\sigma n)^{-1}$ where σ is the cross-section and n is the number density. Calculations of ℓ_{mfp} for the three main gases used in the experiment are shown in Table 5.1.

Under standard experimental conditions all three gases have a mean free path less than 3 mm. Since the overlap region is several centimeters wide, there should be significant interaction between the two cones.

	H_2	He	N_2
n (m^{-3})	10^{20}-10^{21}	10^{20}-10^{21}	10^{20}-10^{21}
σ (10^{-19} m^2)	2.62	2.35	4.16
ℓ_{mfp}(m)	0.0027-0.027	0.003-0.03	0.0017-0.017

Table 5.1: Parameters for Density Pileup. Densities are from [17] and cross-section data from [65, 66]

Pileup Region Model

Estimating the extent and magnitude of the pileup involves evaluating how the density from cone 1 penetrates into cone 2. To first order, this pileup should be confined to the scale of the mean free path, ℓ_{mfp} and conserve mass. To satisfy these basic constraints, the pileup model is constructed such that the interpenetrating density is compressed to an exponential profile with local characteristic length, $\ell_{\mathrm{mfp}}(z)$:

$$\rho_{\mathrm{pileup}}(x, y, z) = M(x, z)\frac{e^{-|y|/\ell_{\mathrm{mfp}}}}{\ell_{\mathrm{mfp}}} \tag{5.2}$$

$$M(x, z) = \int_0^\infty \rho(x, y'+\mathbf{y_0}, z)\, dy'. \tag{5.3}$$

This corresponds to integrating the density from cone 1 (e.g. left cone at $y = -y_0$) that penetrates the XZ-plane at each height, and redistributing it in an exponential profile with characteristic length, $\ell_{\mathrm{mfp}}(x, 0, z)$. The process is mirrored for cone 2.

The estimated density pileup from this exponential profile increases the apex density by a factor of 1.6 relative to the non-interacting case. Figure 5.4 highlights the difference between the case of no interaction $\ell_{\mathrm{mfp}} > 0.1$ m, and the pileup region model, $\ell_{\mathrm{mfp}} \ll 0.1$ m: a pileup region creates peaked density contours as distinct from the flat profile of a direct superposition. For the gas cones and densities
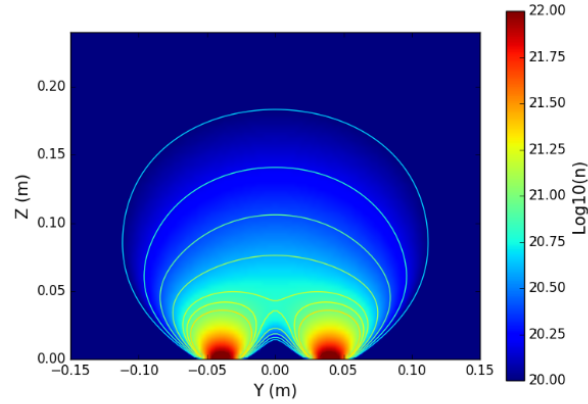
(a) with no interaction, $\ell_{\mathrm{mfp}} > 0.1$ m
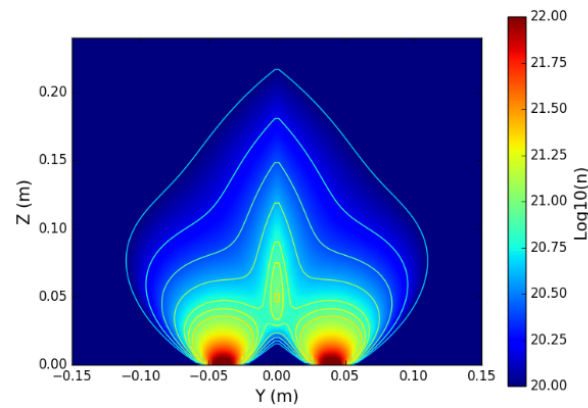
(b) with interaction, $\ell_{\mathrm{mfp}} \ll 0.1$ m.

Figure 5.4: Density profiles for (a) direct superposition of two gas cone profiles and (b) modeled gas profile with finite neutral mean free path (Eq. 5.2)

described here, this model predicts that the pileup effect is only significant for valve separation distances less than 12 cm.

Although this is an ad hoc model, 2D measurements of the FlareLab initial density profile [67, 68, 69] show a peaked density distribution, with contours very similar to Figure 5.4b, indicating a comparable pileup region at the loop apex. This pileup model is used in Section 5.5 for the initial conditions of a 3D MHD simulation of the experiment.

Hoop Force

The hoop force is an outward radial force present in all curved current channels. This force exists because the internal magnetic pressure of a current loop is greater than the exterior magnetic pressure. The equation of motion for an infinitesimal segment of a circular current (length ds, major radius R, minor radius a, and average

mass density $\bar{\rho}$) is given by:

$$F_{\text{hoop}} \, ds = \ddot{R} \, \bar{\rho} \pi a^2 \, ds \tag{5.4}$$

$$F_{\text{hoop}} = \frac{\mu_0 I^2}{4\pi R} \left[\ln\left(\frac{8R}{a}\right) - 2 + \frac{l_i}{2} \right], \tag{5.5}$$

where I is the current flowing through the plasma loop, and l_i is a constant of order unity related to the internal current distribution [54, 42]. Approximating the term in square brackets in Eq. 5.5 as constant and assuming a linearly rising current, the major radius expands quadratically with time: $R(t) \propto t^2/\sqrt{\bar{\rho}}$ [42]. However, sections of the loop with higher density will accelerate more slowly and lag behind the global expansion.

5.4 Experimental Results

Several observed features on the Caltech experiment indicate the presence of a density pileup at the loop apex. The first of these is the presence of a localized bright region at the loop apex; this bright region can be detected from fast camera images as early as 500 ns after the breakdown. Since the apex is 6 cm away from each footpoint, the plasma at the footpoints does not have time to travel to the apex in 500 ns ($v_A = 3 \cdot 10^4$ m/s, 6 cm/$v_A = 2$ μs). Consequently, this feature must already be present in the neutral density. Figure 5.5 shows an image of this bright apex feature for a Nitrogen loop 1.5 μs after breakdown. This bright feature at the loop apex extends beyond the major radius in an expanding cone. This expansion of the pileup region width at greater heights is consistent with the increasing mean-free path further away from the fast-gas nozzles.

The second observation is that the loop apex always lags behind during expansion, forming a heart-shaped dip. This expansion is driven by the hoop force described in Section 5.3. This dip is unusual as it is a large, extremely reproducible feature. It is always pointed downward, remains a similar size, and appears consistently for all gases used (H_2, He, Ar, N_2). The dip moves slower than the leading edge of the loop and creates a significant deformation from circular expansion. Figure 5.6a shows the evolution of this apex dip for a N_2 loop.

We can also control the shape and location of this apex dip by varying the gas output of each fast-gas valve. For the symmetric gas output, the dip appears to be sharper and larger when the gas density output is higher, as shown in Figure 5.7. If the output of the fast-gas valves differ significantly, the pileup region is shifted away from the footpoint with greater gas output and towards the footpoint with weaker
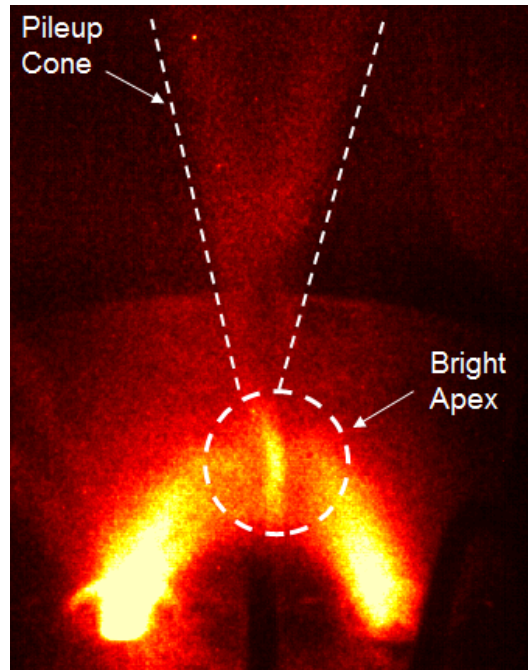
Figure 5.5: Photograph of the loop at 1.5 μs after breakdown. The white dashes mark the bright feature at the loop's apex and pileup cone at the midplane

gas output. Figure 5.8 shows superimposed images of a shot with higher gas output on the right footpoint (red) and a shot with higher gas output on the left footpoint (cyan). The shift of the bright apex feature is about 3 cm and highly reproducible.

Lastly, when creating plasma loops from a uniform gas backfill, both the bright apex feature and the heart shape are not observed. Figure 5.6b shows the evolution of a loop created with uniform Hydrogen backfill.

These observations demonstrate that the apex dip depends strongly on the initial neutral gas profile.

5.5 Ideal MHD Simulation

The 3D MHD simulation described in Chapter 4 was used to test if the calculated pileup region could produce the observed dip shape. Using an initial density distribution with a pileup region, the simulation replicates the shape and expansion velocity of the loop. Figure 5.9a shows the image of the loop with the dip at the apex and Figure 5.9b shows a synthetic image from the simulation where intensity is proportional to current density and number density squared ($I \propto J\rho^2$). There were no other set of initial or driving conditions which reproduced the characteristic dip

(a) Using fast-gas valves (Gas = N)

(b) Using uniform background gas (Gas = H)
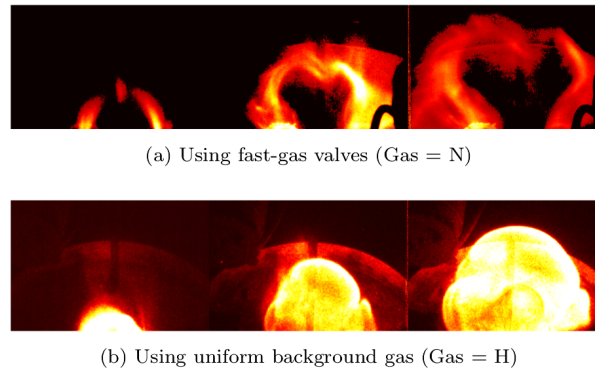
Figure 5.6: Plot shows the evolution of two different initial density profiles. (a) Standard initial conditions with two colliding cones of gas supplied by nozzles in electrodes. (b) Non-standard conditions with uniform background gas supplied from sources on opposite side of chamber. Without the gas cones from the nozzles, the apex dip feature disappears

(a) Smooth dip from low gas density output

(b) Sharp dip from high gas density output
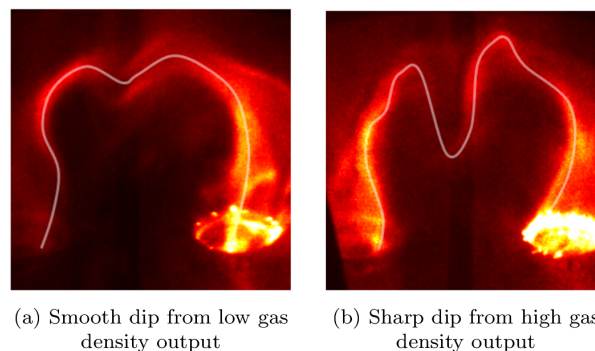
Figure 5.7: Comparison of dip shape for two different gas outputs. Loop axis is manually traced with white lines to highlight differences (Gas = H)

shape seen in the experiment.

Figure 5.10 shows that the apex position of the simulated loop also closely matches that of the experiment. The evolution comprises of three stages. First, after the initial brightening of neutral gas as shown in Figure 5.5, magnetic forces generate axial flow and pinch to form a collimated loop [21], resulting in the initial decrease in apex height. Subsequently, the apex is accelerated by the hoop force [42], colliding with the neutral pileup region. Lastly, the apex is accelerated to its terminal velocity from the high magnetic curvature forces, illustrated in Figure 5.11, present in the cusp.

Given the good match in shape and velocity, the simulation demonstrates that a pileup region is consistent with the observed loop evolution.
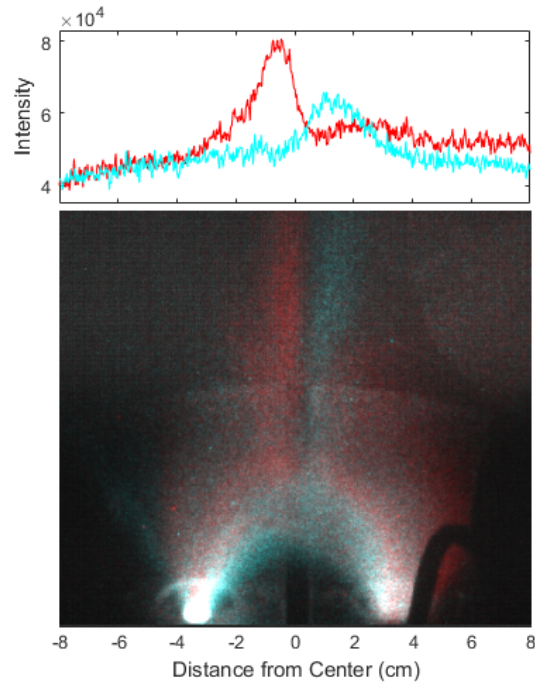
Figure 5.8: (top) Plot of vertically integrated pixel values. (bottom) Superimposed images of a shot with higher gas output on the right footpoint (red) and a shot with higher gas output on the left footpoint (cyan) (Gas = He)

(a) Photograph of experimental loop

(b) Synthetic image from simulation
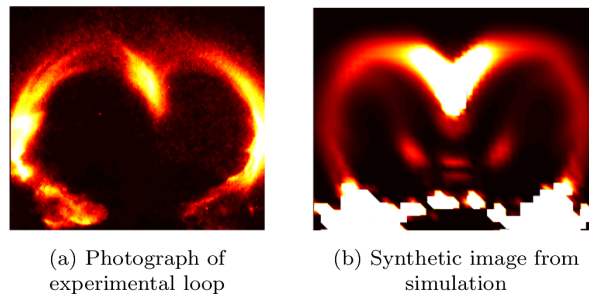
Figure 5.9: Comparison of the cusp shape between experiment (left) and simulation (right)

5.6   Discussion

The data presented provide strong evidence that the dip feature is in fact a cusp rather than a helix. The proposed cusp formation mechanism, a neutral pileup region, resolves all of the inconsistencies with the helical interpretation and achieves excellent agreement with observation and simulation. This new understanding of the experiment has implications for both future experiments and solar flux ropes.
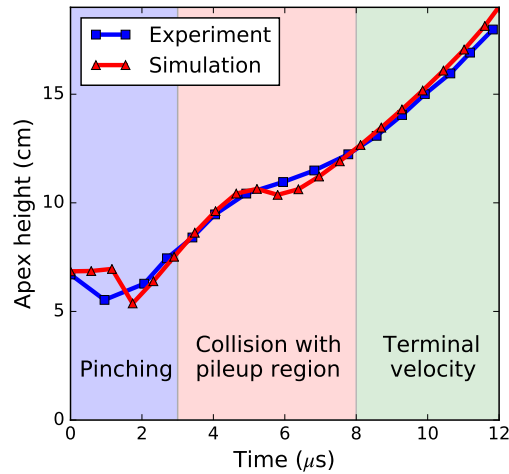
Figure 5.10: Evolution of the loop apex position in 3 stages: (i) the minor radius undergoes pinching before expansion (ii) the loop collides with the pileup region temporarily slowing down (iii) the magnetic curvature forces of the cusp re-accelerate the apex to a terminal velocity

Neutral Pileup Regions

Most other experiments with fast-gas valves do not have the appropriate densities or length scales necessary to create density pileup regions. However, as in our experiments, such an effect can greatly perturb the initial conditions and should be considered in the design of future plasma experiments. The high reproducibility and simple control of the feature suggests that future experiments could utilize such pileup regions to study the effect of density perturbations, instabilities, or localized collisions between plasma and neutral gas.

Relevance of Dip Feature in Solar Context

Since the plasma loop can be described by ideal MHD, its behavior can be scaled. This scaling allows for three free parameters a_1, a_2, a_3 with the following invariant transformations: $L_0/a_1 \rightarrow L'$, $\rho_0/a_2 \rightarrow \rho'$, $B_0/\sqrt{a_3} \rightarrow B'$, $P_0/a_3 \rightarrow P'$, $\frac{1}{a_1}\sqrt{\frac{a_3}{a_2}}t_0 \rightarrow t'$, $\sqrt{\frac{a_2}{a_3}}v_0 \rightarrow v'$, $\frac{a_1 a_2}{a_3}g \rightarrow g'$ [2]. These transformations provide a one-to-one correspondence between systems allowing simulated and experimental plasmas to be scaled to an equivalent system at the space plasma scale. Table 5.2 shows the characteristic parameters of the experiment, typical coronal loop parameters, and experimental parameters scaled to the solar environment using $a_1 = 2.5 \cdot 10^{-8}$, $a_2 = 10^8$ and $a_3 = 10^4$. With the notable exception of gravity, the
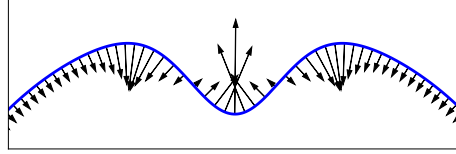
Figure 5.11: Magnetic tension forces ($\mathbf{B} \cdot \nabla \mathbf{B}$, arrows) plotted for an apex dip of a thin flux rope (blue line). Central cusp area has strong vertical magnetic forces because of the high curvature

experimental parameters scale well to the solar case. However, the effective gravity associated with the acceleration provides useful insight into gravitational effects.

Experiment	B = 3000 G	L = 0.5 m
	$\rho = 10^{-4}$ kg m^{-3}	τ = 20 μs
	$g = 10$ m s^{-2}	P = 300 Pa
	v_A=3×10^4 m s^{-1}	β = 0.01
Scaled Exp.	B = 30 G	L = 2×10^7 m
	$\rho = 10^{-12}$ kg m^{-3}	τ = 7 s
	$g = 3 \times 10^{-3}$ m s^{-2}	P = 0.03 Pa
	v_A=3×10^6 m s^{-1}	β = 0.01
Coronal Loop	B = 50 G	L = 2×10^7 m
T= 1.5 MK	$\rho = 10^{-12}$ kg m^{-3}	τ = 5 s
	$g = 300$ m s^{-2}	P = 0.01 Pa
	v_A=4×10^6 m s^{-1}	β = 0.002

Table 5.2: Dimensionless scaling of Caltech parameters to solar loops

The presence of a dense, cusp feature in the experimental flux rope is similar to common features of solar prominences. It is well established that solar prominences have inhomogeneous density along their axis and that the highest density is localized near the apex [70, 71, 72]. Despite these measurements of density modulation, many models of coronal structures assume constant density [50, 55, 9, 73, 74]. The experimental results indicate that density perturbations can result in large distortions of an erupting flux rope, even in the absence of significant pressure or gravity forces. Consequently, a more realistic density profile should be considered when attempting to precisely model erupting flux ropes or CME's.

Furthermore, this denser apex material is thought to sit in a shallow magnetic dip [75, 76], a similar but less extreme version of the experimental cusp. Many of the models

simulating this apex density are purely hydrodynamic [77] and ignore magnetic effects from changes in minor radius. In future experiments, these theories could be tested by appropriate acceleration of the loop apex, imposing an effective gravity with appropriate scaling to solar gravity. The acceleration from loop expansion with current parameters ($5 \cdot 10^7$ m/s^2) scales to an effective gravity of 10^4 m/s^2 at the coronal scale, 40 times larger than solar gravity (270 m/s^2).

Suppression of Kink Instability

The last mechanism of interest is the effect of the pileup region on the kink instability. The kink instability is a current-driven instability which drives exponential growth of long-wavelength helical perturbations. The instability threshold is reached when the magnetic field lines complete more than one twist around the major axis. The kink stability is usually defined with respect to the safety factor, q:

$$q = \frac{2\pi a B_\phi}{L B_\theta},$$

(5.6)

where L is the length of the major axis, a is the minor radius, B_ϕ is the toroidal field, and B_θ is the poloidal field. Full toroids and other line-tied flux-rope experiments, become unstable for $q < 1$. B-field measurements of the loop from $t = 10 - 14$ μs give $B_\phi(a) = 250 - 560$ G, $B_\theta(a) = 200 - 350$ G, $a = 2 - 4$ cm. From images we know that the length of the loop is between 40-56 cm in this time-frame. These values imply an unstable safety factor, $q \approx 0.5$. Consequently, it is surprising that the loop does not exhibit more violent kinking behavior.

We propose that the high density region at the loop apex suppresses the kink since the unstable kink mode has an anti-node at the apex and the high density region acts like a stationary node. This effectively halves the axial length available to kink and doubles the safety factor. Similar suppression of the longest wavelength kink modes by high density regions has been seen before in astrophysical jet simulations [78] and experiments [79].

Chapter 6

MODEL FOR FLUX ROPE CAVITY FORMATION

This chapter details a new model for the cavity portion of the three-part structure of coronal mass ejections (CMEs). The model proposes that the cavity in a CME forms because a rising electric current in the core prominence induces an oppositely directed electric current in the background plasma; this eddy current is required to satisfy the frozen-in magnetic flux condition in the background plasma. The magnetic force between the inner core electric current and the oppositely directed induced eddy current propels the background plasma away from the core creating a cavity and a density pileup at the cavity edge. The cavity radius saturates when an inward restoring force from magnetic and hydrodynamic pressure in the region outside the cavity edge balances the outward magnetic force. The model is supported by (i) laboratory experiments showing development of a cavity as a result of the repulsion of an induced reverse current by a rising inner core flux rope current, (ii) 3D numerical MHD simulations that reproduce the laboratory experiments in quantitative detail, and (iii) an analytic model that describes cavity formation as a result of the plasma containing the induced reverse current being repelled from the inner core. This analytic model has broad applicability because the predicted cavity widths are relatively independent of both the current injection mechanism and the injection timescale.

6.1 Introduction

Coronal mass ejections (CMEs) are energetic solar eruptions that occur every few days, launching millions of tons of magnetized plasma into space. Understanding and predicting these events is of increasing importance given the potential danger they pose to spacecraft, aircraft communications, and the electrical grid. However, reliable prediction of CMEs is difficult because the three dimensional magnetic structures driving these eruptions in the solar corona cannot yet be measured. Despite the limited magnetic data, there are extensive white light observations of CMEs from satellite coronographs. These images consistently display a three-part structure: (1) a bright shock-like leading edge followed by (2) a dark, croissant-shaped density cavity with (3) a bright core corresponding to an erupting prominence [80, 81, 82, 83]. The second frame of Figure 6.1a identifies these parts on a typical CME.

Prior work has focused on developing models and simulations that are consistent with the magnetic data and still reproduce this observed structure. These models all propose some form of flux rope (i.e. a twisted bundle of magnetic field lines) as the fundamental magnetic structure but have different eruption mechanisms [84, 85, 86]. Remote magnetic measurements and various imaging bands suggest that these three parts are contained within a magnetic flux rope, a twisted bundle of helical magnetic field lines [87, 82].

Despite some success of these models in reproducing eruption speeds, it is still unclear how and why the three-part structure forms [88]. The formation of the density cavity is of particular interest because it is an observable feature which is linked to the large-scale structure of the magnetic field. These density cavities can form during a CME or up to several days in advance around an eruptive prominence [89]. Existing theories of cavity formation use 1D hydrostatic models along fixed magnetic field lines [90, 91]. These theories are limited to specific magnetic equilibria and are characterized by hydrostatic scaling resulting from stratification in the presence of a gravitational field. However, measurements of cavity density have shown that the density depletion relative to the background is greatest at lower heights and minimum, or zero, at the top of the cavity [92, 93, 94]. This implies that a mechanism independent of gravitational stratification is likely responsible for cavity formation.

This chapter presents a dynamic, magnetically driven mechanism for cavity formation, equilibrium, and evolution. The model describing this mechanism is motivated by experimental measurements and 3D MHD simulations. This new model provides a detailed interpretation of the three-part CME structure in terms of current densities. The model explains several observed trends including why cavity density depletion is greatest at lower heights and why prominences with larger cavities are more likely to erupt [95].

The experimental measurements were done on the Caltech single-loop apparatus [13, 42, 54]. This apparatus produces a flux rope with dimensionless scaling similar to solar flux ropes and erupts due to flux injection [54, 96, 97]. The rapidly expanding flux rope collides with background plasma, forming a distinctive three-part structure with a core, cavity, and leading edge (Figure 6.1b). Magnetic B-dot probe measurements indicate that the leading edge is a reverse current layer, i.e., a layer with current propagating anti-parallel to the main current. Examination of the bulk magnetic forces in the system shows that the cavity is formed by the mutual

repulsion of the anti-parallel main and reverse currents.

A three-dimensional MHD simulation [96] reproduces the observed experimental features and provides further insight into the origin of the reverse current layer. From the simulation, we are able to identify that the reverse current layer is diamagnetically induced by increasing magnetic flux from the core current channel. This is simply the frozen-in flux condition of MHD: the increasing field from the current channel necessarily induces an equal and opposite current in the background plasma such that magnetic flux in the background plasma does not change. Since anti-parallel currents repel, the reverse current layer is driven away from the flux rope, forming a cavity. The evolution of the simulated flux rope is shown in Figure 6.1c.

The formation and propagation of reverse current layers has been documented in experiments dating back to the 1960's [98, 99, 100] and was a technique used to generate MHD shocks in the laboratory. However, this effect has not been studied in an arched geometry and, to the best of the authors' knowledge, has not previously been used to interpret the three-part structure of CMEs [101, 81, 9]. This work extends the analytic cylindrical shock solution of Ref. [100] to a current layer of finite width, δ. This model is then shown to be in good agreement with the experiment, simulation, and CME observations.

6.2 Experiment

The experiment generates an expanding flux rope (argon) which collides with a background plasma (hydrogen). The apparatus consists of a magnetized plasma gun mounted at the end of a 1.6 meter-long, 0.92 meter-diameter vacuum chamber [13, 42, 54, 96]. Figure 6.2 shows the apparatus and Cartesian coordinate system. Two solenoids, one beneath each electrode, are pulsed to produce an arched magnetic field, similar to a horseshoe magnet. This background field ranges from 0.3 T at the footpoints to 0.06 T at the loop apex. Above each solenoid there are gas nozzles connected to fast-gas valves. These valves are pulsed, releasing diverging flows of argon neutral gas in two expanding cones with number density $10^{19} - 10^{22}$ m^{-3}. A neutral hydrogen prefill, $n = 3 \times 10^{21}$ m^{-3}, is added to provide a background gas. Finally, a 59 μF capacitor charged to 3.6 kV is discharged across the electrodes, ionizing the neutral gas and driving up to 30 kA for ~ 10 μs through the plasma. Less than 2 kA is carried by the bright collimated loop structure with the remainder of the current traveling in a broad, diffuse outer envelope. The collimated loop has $\beta = 2\mu_0 n_i \kappa T / B^2 \sim 0.1$, for $n_i = 5 \times 10^{19}$ m^{-3}, $\kappa T = 2$ eV, and $B = 200$ G.
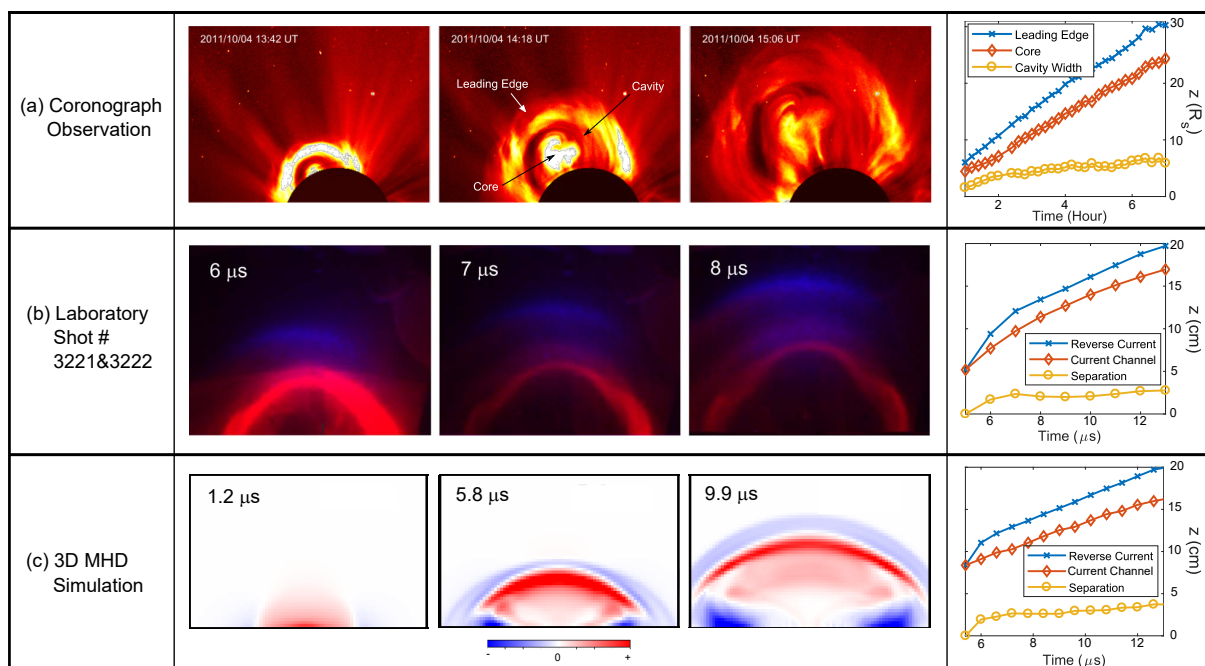
Figure 6.1: (a) Image sequence of the three-part CME captured by LASCO-C3 on October 4th, 2011. This sequence shows a nearly edge on view of the current channel instead of the perpendicular views shown from the experiment. (b) Image sequence of composite multiwavelength fast camera images of laboratory experiment. Each image consists of two bandwidths: filtered H_α (blue) and visible light (red). (c) Cross-sectional plots of simulated current density in the horizontal direction (J_y) showing the propagation of the main current (red) and an induced reverse current layer (blue). For each case, the height evolution of leading edge/reverse current (blue), core/current channel (red) and cavity width/separation (yellow) are plotted in the last column.

The dynamics of the current channel and the reverse current are captured by correlating a sequence of visible light images using a multiple-frame fast camera with measurements made by magnetic probes. The false color images are superimposed with filtered Hα in blue (H-dominated) and visible light in red (Ar-dominated). Using hydrogen gas for the expanding flux rope produced equivalent cavity structures (e.g. ~2 cm separation) but argon was chosen due to its slower expansion speed and better imaging properties. Figure 6.1b shows the formation and subsequent separation of the reverse current layer from the driving current channel. Magnetic measurements from B-dot probes show that the blue feature in Figure 6.1b contains a current oppositely directed to that of the primary injected current channel (red feature). The time dependence of apex positions of the current channel and reverse current layer are tracked from the images and plotted in the far right of Figure 6.1b
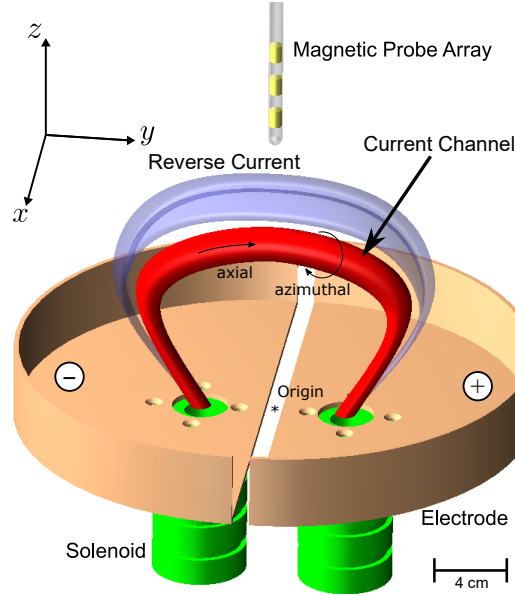
Figure 6.2: Schematic diagram of the experimental setup showing the primary current channel (red), the induced reverse current layer (blue), electrodes (copper), solenoid (green), and magnetic probe array (yellow)

and are labelled as current channel (i.e., core as in Fig. 6.1a) and reverse current (i.e., leading edge as in Fig. 6.1a). Since these features have a non-negligible thickness, the locations of the apexes are chosen to be at the center of the feature on the z-axis. The separation (i.e., cavity width as in Fig. 6.1a) between the two features is also plotted. The cavity width defined by the distance between the two apexes, grows quickly and reaches the asymptotic value of 2 cm. The projected emission in the yz-plane shows that the curvature of the reverse current layer is similar to that of the current channel. The following paragraph describes the method used to identify the reverse current from magnetic probe data.

The time dependence of $\boldsymbol{B}$ seen by the probe is from convection rather than diffusion and images show little change in the different features as they move by the probes, i.e., $\partial/\partial z \leftrightarrow v_z^{-1}\partial/\partial t$. The horizontal current density can therefore be estimated from the time dependence of the magnetic field, i.e., $J_y = (\boldsymbol{\nabla}\times\boldsymbol{B}) \cdot \hat{y}/\mu_0 = (\partial_z B_x - \partial_x B_z)/\mu_0 \approx (\partial_t B_x)/(\mu_0 v_z)$ where $v_z \approx 13 - 15$ km s^{-1} as measured from feature tracking in fast camera images. Additional magnetic measurements in the xz-plane confirm that the center of the flux rope has spatial variation principally in the z-direction with much less variation in the x-direction ($\partial_x B_z \ll \partial_z B_x$). Figure 6.3 shows experimental J_y profiles calculated from $B_x(t)$ measurements at 3 locations ($x, y = 0$, $z = 17.5$, 19.5, and 21.5 cm); the inset shows a zoomed-in view of the

reverse current, and indicates that this reverse current layer appears spatially ahead of the main current. The spatial distribution and motion of the primary and reverse currents match the features observed in the fast camera images.

The current channel in the experiment expands due to the hoop force, a consequence of greater magnetic pressure on the inboard side of the loop than on the outside [42]. During this expansion, the current channel collides with the background gas, inducing a reverse current layer of ionized hydrogen.
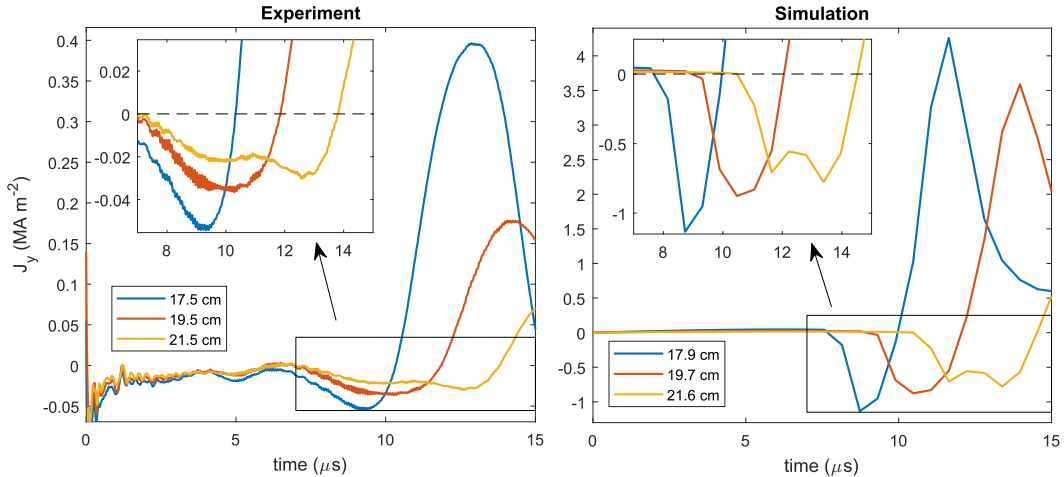
Figure 6.3: (Left) Calculated $J_y(t)$ profiles at three locations show the distribution and propagation of the reverse current and the current channel in the experiment. Inset shows a reverse currents in more detail. (Right) The equivalent plot of J_y obtained from the simulation at the 3 locations close to those in the experiment.

6.3 Simulation

To gain further insight into this reverse current layer, the experimental setup was simulated using a 3D MHD equation solver code, a subset of the Los Alamos COMPutational Astrophysics Simulation Suite (LA-COMPASS) [49]. This code is described in previous papers simulating the Caltech plasma jet experiment [41] and the arched flux rope experiment [96]. The ideal MHD code evolves a set of dimensionless parameters: density ρ, pressure P, magnetic field $\boldsymbol{B}$, and velocity $\boldsymbol{v}$ on a Cartesian grid with non-reflecting outflow boundary conditions.

The initial density profile consists of (i) exponential cones emerging from the gas nozzles at each footpoint[1], (ii) a uniform background gas $\rho_b = 1.0 \times 10^{-5}$ kg m^{-3},

---

[1]Without background gas, cone density decays as z^{-2}. Addition of background gas constrains gas cones such that density decays as z^{-3}

and (iii) a high density region below $z = 0$ to simulate the anchoring effect of the electrode boundary. The neutral density in the $z > 0$ region is

$$\rho(x, y, z) = \rho_0 \left(\frac{z_0}{z + z_0}\right)^3 \left(\exp\left[-\frac{K(x^2 + (y - y_0)^2)}{(z + z_0)^2}\right] + \exp\left[-\frac{K(x^2 + (y + y_0)^2)}{(z + z_0)^2}\right]\right) + \rho_b,$$

(6.1)

where $\rho_0 = 4.8 \times 10^{-3}$ kg m^{-3} is the density at the footpoint, $K = \tan \alpha \sqrt{\log 2} = 1.1$, $\alpha \approx 54°$ is a half cone angle, $y_0 = 0.04$ m is the footpoint location, $z_0 = 0.01$ m is an offset to avoid singularities, and $\rho_b = 1.0 \times 10^{-5}$ kg m^{-3} is the background density. Initial pressure is defined such that $P = (\rho - \rho_b)\kappa T / m_i$ where $m_i = $ mass of hydrogen ion, and $\kappa T = 2$ eV. The ρ_b is subtracted because the background is cold. The plasma is assumed to be initially at rest $v = 0$.

The background magnetic field is constructed from a set of 10 current loops arranged in a half-circle below the footpoints, each with a current of $I = 631$ kA. This arrangement produces a horseshoe-magnet field topology with a magnitude ranging from 0.2 T at the footpoints to 10^{-3} T at the upper edge of the simulation. The field from each current loop is calculated from a truncated series approximation for the vector potential of an infinitely thin loop [52]. This truncation gives an analytic expression for a current loop which is non-singular and divergence-free.

From $t = 0$ to $t = 10$ μs, azimuthal flux is added to the domain to match the rising experimental current, $I_{\exp}(t) \approx I_0 \sin(2\pi t / T)$ where $T = 40$ μs and $I_0 = 30$ kA. This azimuthal magnetic field corresponds to a diffuse arched current constructed from the superposition of 110 current loops and conforms roughly to the shape of the gas cones (i.e., a 54° flared angle at the footpoints). About 5-10% of this diffuse injected current condenses into a collimated core current channel as observed in the experiment. A more detailed description of this injection scheme can be found in Wongwaitayakornkul et al. [96].

This setup simulates a flux rope with increasing current that expands into a background plasma. As observed in the experiment, the simulated current channel produces a reverse current layer as the current channel collimates and expands outward. Figure 6.1c plots a time series of J_y from the numerical simulation in the yz-plane, showing a reverse current layer propagating in front of the main current. The shape and position of the main current and reverse current layer are in reasonable agreement with the experiment ($\pm 20\%$) as can be seen by comparing Figure 6.1b and 6.1c. Figure 6.3 compares the current density J_y in the simulation and in the experiment at the three magnetic probe locations. The experimental current density

J_y (left) is broader than in the simulation (right) because of magnetic diffusion from finite resistivity in the experiment. However, the morphology of the profiles are quite similar, as both show a reverse current layer propagating ahead of the core current channel.

Reverse Current Formation Mechanisms

The reverse currents in the simulation are generated by a locally increasing B-field between the current channel and background field. This occurs via two mechanisms: flux injection and flux compression. Flux injection relies on addition of azimuthal flux from increasing current to the interior of the current channel, where the azimuthal direction is defined relative to the current channel axis. This necessarily creates a reverse current at the boundary since the added flux from increasing current is confined to a finite volume. It should be noted that previous simulations which employ current injection [50, 102, 103], also see the production of reverse current layers but did not identify them as such.
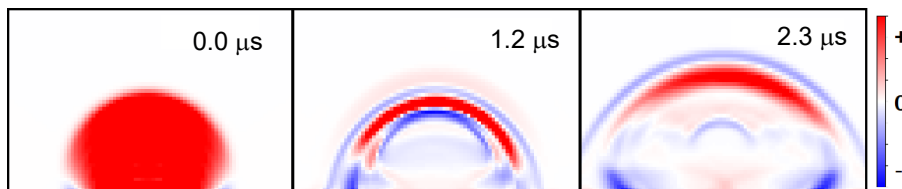
Figure 6.4: Sequence of simulated J_y evolution showing reverse current generation from the pinch effect without flux injection.

Reverse currents are in addition induced by compression of the current channel. One simple demonstration of this effect is the evolution of a diffuse arched current similar to the popular flux cancellation model [85, 104, 105]. Figure 6.4 shows the evolution of this system: the interior edge of the current expands faster than the outer edge, collimating and compressing the current channel. This similarly increases the azimuthal field (relative to the current channel axis) at the current channel edges, inducing reverse currents around the primary current. In fact, any flux rope with an azimuthal field that decays faster than $1/r$ will have a reverse current layer.

Consequently, reverse current layers are commonly observed in compressible plasmas and/or plasmas with flux injection [106, 104, 50, 102, 103]. We believe both compression and injection are responsible for the reverse current layer observed in the laboratory experiment described in Section 6.2.

6.4 Snowplow Model for Reverse Current

This model extends the infinitely thin snowplow analysis from Greifinger and Cole [107] to a finite-width reverse current layer and has three key features: an increasing current channel, an expanding reverse current layer, and a density cavity between the current channel and the reverse current layer.

Figure 6.5 illustrates the model. The configuration consists of a vertical ($\hat{y}$) cylindrical current channel with finite radius a and increasing total current $I(t)$ in a uniform plasma of density ρ_0, magnetic field $B_0 \hat{y}$, and pressure P_0. The current channel is surrounded by a shell/layer of induced reverse current at position $b(t)$, corresponding to the shielding effect of the background plasma. The inner radius of this shell of reverse current is initially at position $b(0) = a$ and the shell is assumed to have a constant thickness δ and a uniform current density $J_y = -I/\sigma$ across its width, where $\sigma = \pi(2\delta b + \delta^2)$ is the cross-sectional area of the shell. The motion of the reverse current shell is governed by an expansive force resulting from the mutual repulsion of the oppositely directed currents competing with a restoring force from the background pressure and background magnetic field external to the shell.

The total expansive force-per-length f_e is obtained by integrating $-J_y B_\phi$ over the reverse current layer:

$$
\begin{aligned}
f_e &= -\int_{r=b}^{r=b+\delta} J_y B_\phi 2\pi r \, dr \\
&= -\frac{2\pi}{\mu_0} \int_{r=b}^{r=b+\delta} B_\phi \frac{\partial}{\partial r} \left(r B_\phi \right) dr \\
&= \frac{\mu_0 I^2}{\sigma} \int_{r=b}^{r=b+\delta} \left(1 - \frac{\pi(r^2 - b^2)}{\sigma} \right) dr \\
&= \frac{\mu_0 I^2}{3\pi} \frac{3b + 2\delta}{(2b + \delta)^2}.
\end{aligned}
\tag{6.2}
$$

Taking the limit $\delta \to 0$ recovers the expression from Greifinger and Cole [107], i.e.,

$$
\lim_{\delta \to 0} f_e = \frac{\mu_0 I^2}{4\pi b}.
\tag{6.3}
$$

The total confining force f_c is calculated as the product of the background pressure and the shell outer perimeter:

$$
f_c = 2\pi(b + \delta) \left[\frac{B_0^2}{2\mu_0} + P_0 \right].
\tag{6.4}
$$
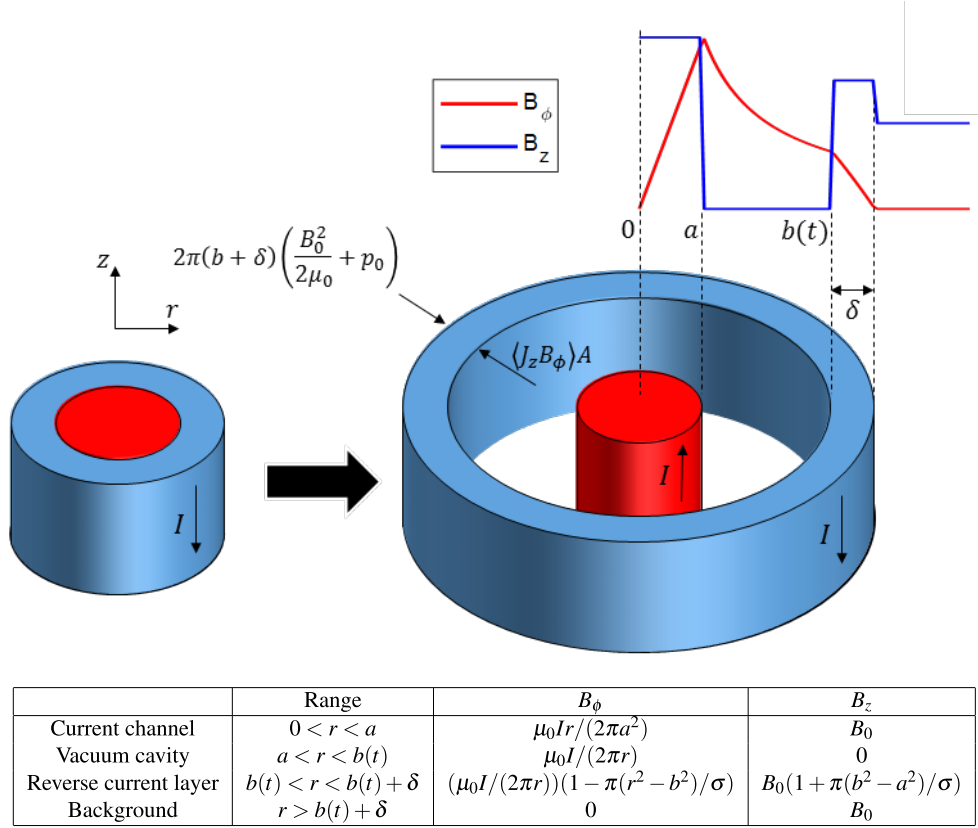
Figure 6.5: Illustration of the model. The current I is in the $+z$-direction in the main current channel (red) and in the $-z$ direction in the reverse current shell (blue). The reverse current layer of thickness δ expands radially forming a cavity region in between them (left to right). The plot shows the radial dependence of the normalized axial field (B_z, blue) and azimuthal field (B_ϕ, red). The table lists model regions with their corresponding magnetic fields.

This gives the equation of motion for the expansion of the current layer to be

$$\frac{d}{dt}\left(M\frac{db}{dt}\right) = f_e - f_c. \tag{6.5}$$

Using the "snowplow" assumption, the mass-per-length M scales with the swept area, so

$$M = \rho_0 \pi \left((b(t) + \delta)^2 - a^2\right). \tag{6.6}$$

The full equation of motion for the current layer can therefore be written as

$$M\ddot{b} = \frac{\mu_0 I(t)^2}{3\pi}\frac{3b + 2\delta}{(2b + \delta)^2} - 2\pi(b + \delta)\left[\frac{B_0^2}{2\mu_0} + P_0\right] - \dot{M}\dot{b}. \tag{6.7}$$

The last term on the right hand side is a consequence of momentum conservation from the increasing mass of the layer.

Non-Dimensional Form and Equilibrium

Equation 6.7 can be put in dimensionless form to compare plasmas having different scales. The characteristic velocity is chosen to be the Alfvén speed $v_A = B_0/\sqrt{\mu_0 \rho_0}$ and the characteristic time is chosen to be the Alfvén crossing time $\tau = a/v_A$. This choice of normalization has three free parameters: B_0, a, and ρ_0 so Eq. 6.7 becomes

$$\bar{M}\ddot{\bar{b}} = \frac{\bar{I}^2}{3\pi} \frac{3\bar{b} + 2\bar{\delta}}{(2\bar{b} + \bar{\delta})^2} - \pi(\bar{b} + \bar{\delta})\left[1 + \beta\right] - \dot{\bar{M}}\dot{\bar{b}}, \tag{6.8}$$

where normalized values are indicated with a bar, (e.g. $\bar{I} = I/I_0 = I\mu_0/(B_0 a)$, $\bar{M} = M/(\rho_0 a^2)$) and $\beta = 2\mu_0 P_0/B_0^2$). In both the experiment and the simulation, the evolution prescribed by Eq. 6.8 reaches equilibrium within a few Alfvén crossing times (i.e., $t \sim 5a/v_A$). This fast equilibration time implies that the observed cavity widths are relatively independent of the current injection timescale. Solving for this equilibrium ($\dot{b} = 0$, $\ddot{b} = 0$) gives:

$$\pi(\bar{b}_{eq} + \bar{\delta})\left[1 + \beta\right] = \frac{\bar{I}^2}{3\pi} \frac{3\bar{b}_{eq} + 2\bar{\delta}}{(2\bar{b}_{eq} + \bar{\delta})^2}, \tag{6.9}$$

$$\bar{b}_{eq} = \frac{\bar{I}}{2\pi\sqrt{1 + \beta}} - \frac{2}{3}\bar{\delta} + \left(\frac{\pi\sqrt{1 + \beta}}{12\bar{I}}\right)\bar{\delta}^2 + O[\bar{\delta}^3]. \tag{6.10}$$

For $\delta \ll b_{eq}$, the solution is a simple pressure balance where $B_\phi(b_{eq}) = B_0\sqrt{1 + \beta}$. In dimensioned quantities, the equilibrium cavity size is $b_{eq} = \mu_0 I/(2\pi B_0\sqrt{1 + \beta})$ where I is the main current and B_0 is the background field. Since the dependence on plasma β is weak, and the mechanism is independent of the collisional mean free path, the effects should be similar across a wide range of plasma parameters.

Core Acceleration

The effects of an accelerating frame can be quantified by substituting $[b(t) - h(t)]$ for $b(t)$ in the expansive term, where $h(t)$ represents the height of the loop apex as a function of time, so Eq. 6.2 becomes

$$f_e = \frac{\mu_0 I^2}{3\pi} \frac{3[b(t) - h(t)] + 2\delta}{(2[b(t) - h(t)] + \delta)^2}. \tag{6.11}$$

This substitution effectively shifts the central current channel (the red cylinder in Figure 6.5) off-axis with speed $\partial_t h(t)$. However, for speeds $\partial_t h(t) \ll v_A$, the cavity width is not significantly affected and the cavity again reaches an equilibrium width within a few Alfvén crossing times. Equivalently, the system reaches a similar

equilibrium width in a moving frame if the momentum conservation term $\ddot{M}\ddot{b}$ is small compared to the magnetic terms. This limit is a reasonable approximation for the cases of interest and the next section will show that the cavity widths predicted by the stationary model agree well with the experiment, simulation, and CME observations. Consequently, the model can be used to infer the internal current $I \approx 2\pi b_{eq} B_0 \sqrt{1 + \beta}/\mu_0$ from cavity width for both stationary flux ropes and flux ropes moving at sub-Alfvénic speeds.

6.5 Scaling to CMEs

The understanding gained from the experiment, simulation, and theory provide new insights for interpreting the three-part structure of CMEs. The leading edge, cavity, and core elements of a CME respectively correspond to the reverse current layer, the cavity and the central current channel of the model. This new interpretation is still a flux rope structure but the interpretation identifies where the currents are flowing: the main current channel is the core, the cavity is a region of expanding azimuthal flux around the main current channel, and the leading edge corresponds to a compressed reverse current layer between the core current and background plasma.

It is important to evaluate how the experiment and simulation scale to the solar situation. To do this, we follow the MHD scaling method in Ryutov, Drake, and Remington [2] and so normalize each system using a reference length a, a reference magnetic field B_0, and a reference density ρ_0. The reference time for normalization is then given by $\tau_0 = a\sqrt{\mu_0 \rho_0}/B_0$. The reference parameters for both the simulation and experiment are $a = 5.0 \times 10^{-3}$ m, $B_0 = 0.01$ T, $\rho_0 = 2 \times 10^{-7}$ kg m^{-3}, $\tau_0 = 2.5 \times 10^{-7}$ s. The reference parameters for the 2011 October 4 CME event are $a = 1.0 \times 10^9$ m, $B_0 = 1.0 \times 10^{-5}$ T [108, 109], $\rho_0 = 3.0 \times 10^{-17}$ kg m^{-3}, $\tau_0 = 710$ s. The density is estimated from a typical CME mass $M = 10^{12}$ kg [110] divided by the core volume, $\pi a^2 \pi R$, using $R = 5a$. The laboratory, simulation and CME event can then all be expressed in terms of the same dimensionless variables.

Figure 6.6 compares the scaled height and time of the leading edge and core, as well as the separation between the leading edge and core, for theory, simulation, experiment, and CME observations. Separation is defined as the center-to-center distance between the main current channel and the reverse current shell. The center of the reverse current shell is at $\bar{b} + \bar{\delta}/2$. The theoretical black line is calculated by solving Equation 6.8 with $\bar{\delta} = 0.25$, $\bar{b}(\bar{t} = 0) = 1$, $\dot{\bar{b}}(\bar{t} = 0) = 0$, and a sinusoidal

ramping current, $\bar{I} = [\bar{I}_0 + 20\sin(\pi\bar{t}/60)]$ where $\bar{I}_0 \sim 2\pi\sqrt{1+\beta}$ is set such that the system is initially at equilibrium. This dimensionless current corresponds to an experimental current of 1 kA and a solar current of $\sim 5 \times 10^{12}$ A. This agreement of normalized parameters in Figure 6.6 indicates that the reverse current mechanism can reproduce the observed three-part structure at the solar scale.
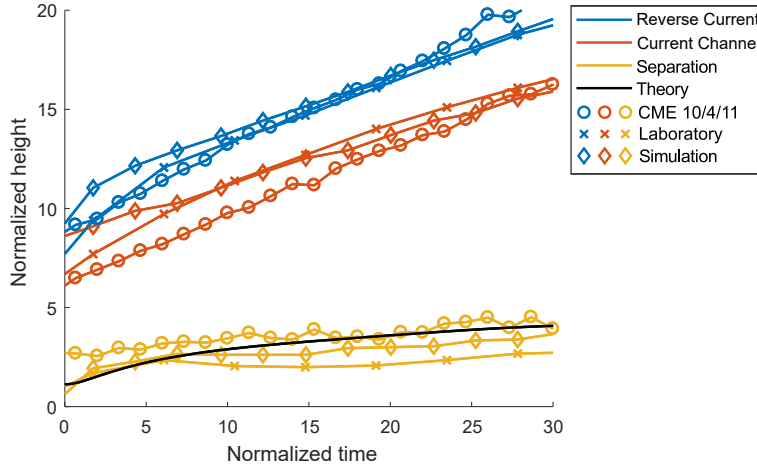
Figure 6.6: Comparison of the cavity width for all the different scenarios, taken from the right column of Figure 6.1. Color: (blue) Reverse current, (red) current channel, (yellow) separation, and (black) theory $(\bar{b}(t) + \bar{\delta}/2)$. Style: (o) CME on 2011 October 4, (x) laboratory, and (⋄) simulation. In this plot, the separation is defined as the center-to-center distance between the main current and the reverse current layer. Vertical errorbars are ±0.5 for all traces. The black line represents a numerical solution to Eq. 6.8 with $\bar{\delta} = 0.25$ and $\bar{I} = [\bar{I}_0 + 20\sin(\pi\bar{t}/60)]$.

Cavity magnetic fields

The model is also consistent with the much higher twist (> 10 turns) of cavity magnetic fields as compared with the dense prominence structures (< 3 turns). Ubiquitous observations of spinning vorticies [111, 112], twisting "horn" features from 171 Å observations [113], and forward-calculations of polarimetric measurements [114, 115] all indicate a highly twisted magnetic field inside cavities. Such a highly twisted field must be supported by a core current and, furthermore, the cavity must have a paucity of axial field. This twist corresponds to B_ϕ/B_y in Fig. 6.5: a central current (low twist) surrounded by a cavity filled with azimuthal flux and negligible B_y (high twist).

Cavity density profiles

The model also provides an explanation for observations of maximum density depletion near the core prominence [92, 93]. If the snowplow assumption is relaxed, the compressional leading edge will continuously diffuse with some decay profile, resulting in a non-empty cavity region with maximum depletion near the core and rising density towards the reverse current layer. This profile is the opposite of what is predicted by cavity models assuming gravitational stratification.

Consequences for flux rope stability

The model also has implications for flux rope stability. Since the equilibrium cavity size $b_{eq} = \mu_0 I/(2\pi B_0 \sqrt{1+\beta})$ is proportional to the ratio of expansive and confining forces, prominences with larger cavities should be more likely to erupt. This inverse relation between cavity size and stability is consistent observations [95]. Furthermore, the model predicts that cavity width should vary according to the background field as observed in experiments with spatial variation of the strapping field. Consequently, the cavity width along the prominence axis as a function of height implies a particular decay profile of the background field. This could determine whether a particular flux rope is torus unstable [97]. The model can also be used to measure the time dependent internal current of a prominence, $I(t) = (2\pi b_{eq} B_0 \sqrt{1+\beta})/\mu_0$ and resolve questions about helicity injection rates before and during eruptions [116, 83].

6.6 Discussion

We have reported experimental measurements of a reverse current front in advance of an expanding flux rope. Simulations indicate that this reverse current is induced so as to conserve flux in the background plasma as the current density of the core flux rope increases. To explain this phenomenon, we presented an analytic model describing the formation and propagation of the reverse current layer. The model provides a simple mechanism for cavity formation above a flux rope: anti-parallel currents repel, which drives the reverse current layer away from the core flux rope forming a density cavity between the forward and reverse currents. Since the model has a weak β-dependence, the laboratory results are eminently scalable to the solar corona. Dimensionless comparisons show quantitative agreement between experiment, simulation, theory, and coronagraph observations. The model is also relevant to other observed trends including why cavity density depletion is greatest at lower heights [93], why cavity magnetic fields are significantly more twisted than

their core prominences [90], and why prominences with larger cavities are more likely to erupt [95].

C h a p t e r 7

WIRE SIMULATION

In the process of working on the single and double loop experiments, a simulation was developed to model each arched flux rope as a current carrying wire. This reduced physics model gives a computationally fast description which can characterize 3D flux rope motion to first order. This description is particularly well-suited to model the experimental flux ropes because the loop current is an easily specified boundary condition.

The simulation was constructed to provide a simple method of testing different experimental configurations. However, it has also proved useful in evaluating various phenomenological theories and mapping the magnetic fields and forces of complex 3D flux rope shapes.

The following sections describe the basic model, how the simulation is implemented, and several useful applications of the simulation on different experiments.

7.1   Reduced physics model

The wire model uses several parameters to characterize each loop,

1. 1D Path $\mathbf{R}(x, y, z, t)$

2. Current $I(t)$

3. Minor radius a

4. Axial magnetic flux Φ

5. Total mass M

These parameters fully define the state of each loop at a given time. This loop state is modified by two forces: the hoop force associated with the poloidal magnetic field due to the loop current and the tension force associated with stretching of the axial magnetic flux, Φ.

The hoop force is calculated as the magnetic force on a wire,

$$\mathbf{f}_{\text{hoop}}(\mathbf{r}) = I d\vec{\ell} \times \mathbf{B}(\mathbf{r}) \tag{7.1}$$

where $d\vec{\ell}$ is a vector representing the length and direction of a wire segment. This captures the driving expansive forces from the imposed currents.

The tension force is a reactive restoring force from inductive currents. To approximate this effect, the expression for the tension force is constructed to conform to two limits of the loop length, L: the initial conditions $L = L_0$ where the tension force is zero and the large expansion limit $L \gg L_0$ where the force should be proportional to the curvature of the magnetic field. This gives,

$$\mathbf{f}_{\text{tension}} = -\left(\frac{\Phi^2}{2\mu_0\pi a^2}\right)\left(\frac{L^2 - L_0^2}{L^2}\right)|d\vec{\ell}|\frac{\hat{r}}{R_c},\tag{7.2}$$

where $\vec{\kappa} = \hat{r}/R_c$ is the curvature vector.

This model assumes there is no background plasma and that the loops are thin (i.e., large aspect ratio $R/a \gg 1$). The axial flux is assumed to convect with the loop and, since there is no background plasma, the B-fields exterior to the loop minor radius are potential magnetic fields.

7.2 Implementation

The implementation of this model represents each loop path as a 3D cubic spline. This continuous representation gives a well defined length parameterization, smooth derivatives, and arbitrary linear resolution for calculations of the magnetic field. Simulations are typically run with $n = 100\text{-}200$ spline knots which is sufficient to resolve the lengths scales (0.02-1 m) of interest.

The magnetic field at position $\mathbf{r}$ is calculated using the Biot-Savart Law and summing over all loops,

$$\mathbf{B}(\mathbf{r}) = \frac{\mu_0}{4\pi}\sum_i \int_{C_i} \frac{I_i(t)\,d\vec{\ell} \times (\mathbf{r} - \mathbf{R_i})}{|(\mathbf{r} - \mathbf{R_i})|^3}\tag{7.3}$$

where i is the loop index, $I_i(t)$ is the loop current, $d\vec{\ell}$ is in the direction of the loop current, and R_i is a position along loop path i. Although the number of calculations for Biot-Savart scales quadratically with the number of points, the B-field only needs to be calculated along the 1D spline to evaluate the magnetic forces. This reduction to 1D makes the model computationally fast for small numbers of loops.

Each spline knot is assigned a mass $m = M/n$ associated with a constant linear mass density of the loop. The points are advanced with explicit time steps by updating
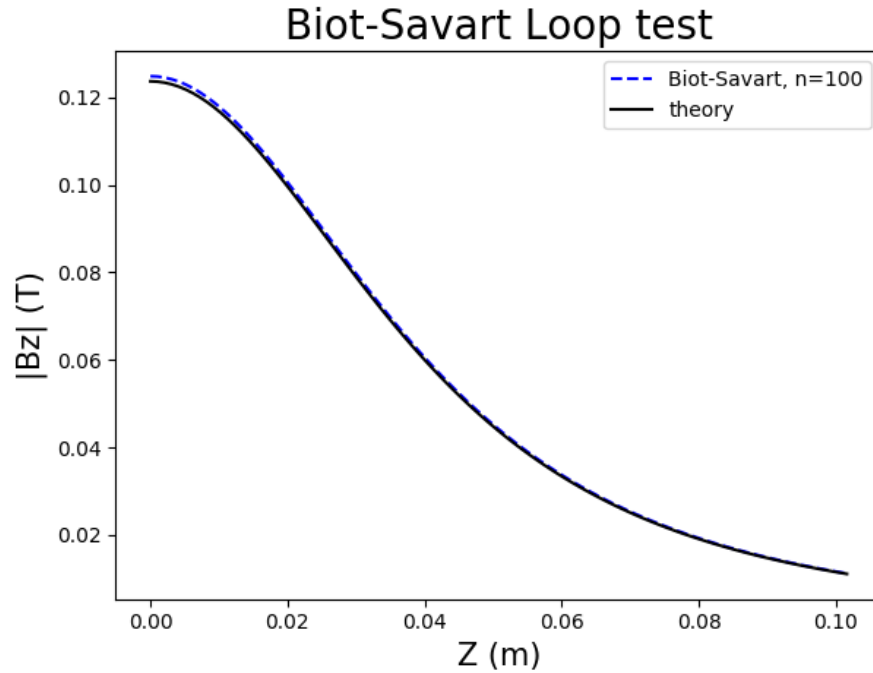
Figure 7.1: Plot of magnetic field along the center axis of a current loop (R = 5.1cm, a = 0.5 cm, I = 10 kA) for theory and simulation (n=100). This demonstrates that the numerical implementation works as expected.

the velocity and position at each time step,

$$\mathbf{v}_{j+1} = \mathbf{v}_j + \frac{\mathbf{f}_{\text{hoop}} + \mathbf{f}_{\text{tension}}}{m}\Delta t$$

$$\mathbf{R}_{j+1} = \mathbf{R}_j + \mathbf{v}_j\Delta t$$

These time steps are adaptively constrained such that $\Delta t < \frac{a}{u_{\text{max}}}$, where a is the minor radius and u_{max} is the maximum velocity. Spline points are re-interpolated each time step to maintain equal spacing.

The lower boundary is made impervious ($u_z|^{z=0} = 0$) to approximate the copper electrodes. Loop footpoints are also anchored to their initial positions.

7.3   Comparisons with analytic models

The model reproduces magnetic fields and forces from known analytic expressions. Figure 7.1 shows a plot comparing the analytic and numerical calculations for the B-field along the axis of a current loop.

The code also agrees with the analytic expression for the hoop force-per-length of a circular current loop with constant current density,

$$F_{\text{hoop}} = \frac{\mu_0 I^2}{4\pi R} \left[\ln\left(\frac{8R}{a}\right) - \frac{3}{4} \right].$$

(7.4)

Table 7.1 shows comparisons of Eq. 7.4 with numerical calculations using the simulation. The numerically calculated forces are within a few percent error for a range of aspect ratios.

Table 7.1: Hoop force comparison: ratios of numerical force over analytic hoop force

	R/a=5	R/a=7	R/a=10	R/a=20
n=50	1.13	1.03	1.20	1.01
n=100	1.03	1.06	1.10	1.16
n=200	1.03	1.07	1.03	1.08

These sanity checks confirm that the simulation works as expected.

7.4 Applications

This model turned out to have a number of useful applications for a variety of experiments. The following sections will classify the various insights from using the simulation into several categories: loop shape and motion, distribution of different magnetic forces, the effects of density variations, and modeling magnetic field topologies.

Non-dimensionalization

Since the simulation uses MHD forces, the entire system can be non-dimensionalized as described in Section 1.2 giving a characteristic time scale $\tau = \frac{4\pi^2 R a \sqrt{\mu_0 \rho}}{I \mu_0}$. This means that any linear scaling of mass density, B-field, or length will simply scale the time dependence. For example, if the mass density is changed by a factor of 4, it will take twice as long to reach the same positions. Similarly, if the current is increased by a factor of 2, the loop will evolve twice as fast. Consequently, all sets of parameters (I, ρ, L) produce the same shape, just on different timescales and it is not necessary to employ parameter scans.

This scaling is incredibly useful. One application is determining the relative number densities of different gases. It is known that for the same fast-gas valve settings, hydrogen gas has a much higher number density than the other gases. Figure 7.2 shows the relative evolution of a hydrogen and argon loop. Since the current
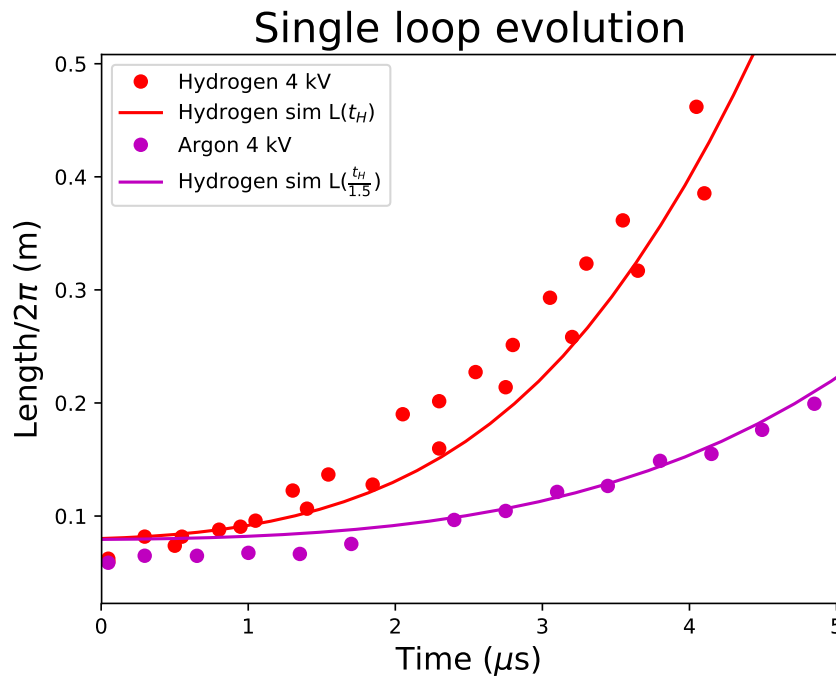
Figure 7.2: Plot of loop length for experiment and simulation. The argon evolution is 1.5 times slower than the hydrogen loop which implies the Argon loop is 2.25 times heavier.

and length scales remain roughly the same, the difference in timing ($t_{Ar} \approx 1.5t_H$) indicates $\rho_{Ar} = 2.25\rho_H$ and that $n_{Ar} \approx n_H/18$.

Reproducing loop shape

The simulation can reproduce the shape and evolution of the different experiments. Figure 7.3 shows a time series of wire simulations of each experiment.

This gives a 3D time-dependent picture of the important driving forces and how they produce the observed shapes. Dimensionless scaling gives a simple method for evaluating how the experiments scale with density, magnetic field, and current. However, the simulations are not identical to the experimental evolution and these differences identify where additional parameters (i.e., minor radius, axial density gradients) are important.

Magnetic forces

Another useful application of the model is the evaluation of magnetic forces on complex 3D current paths.
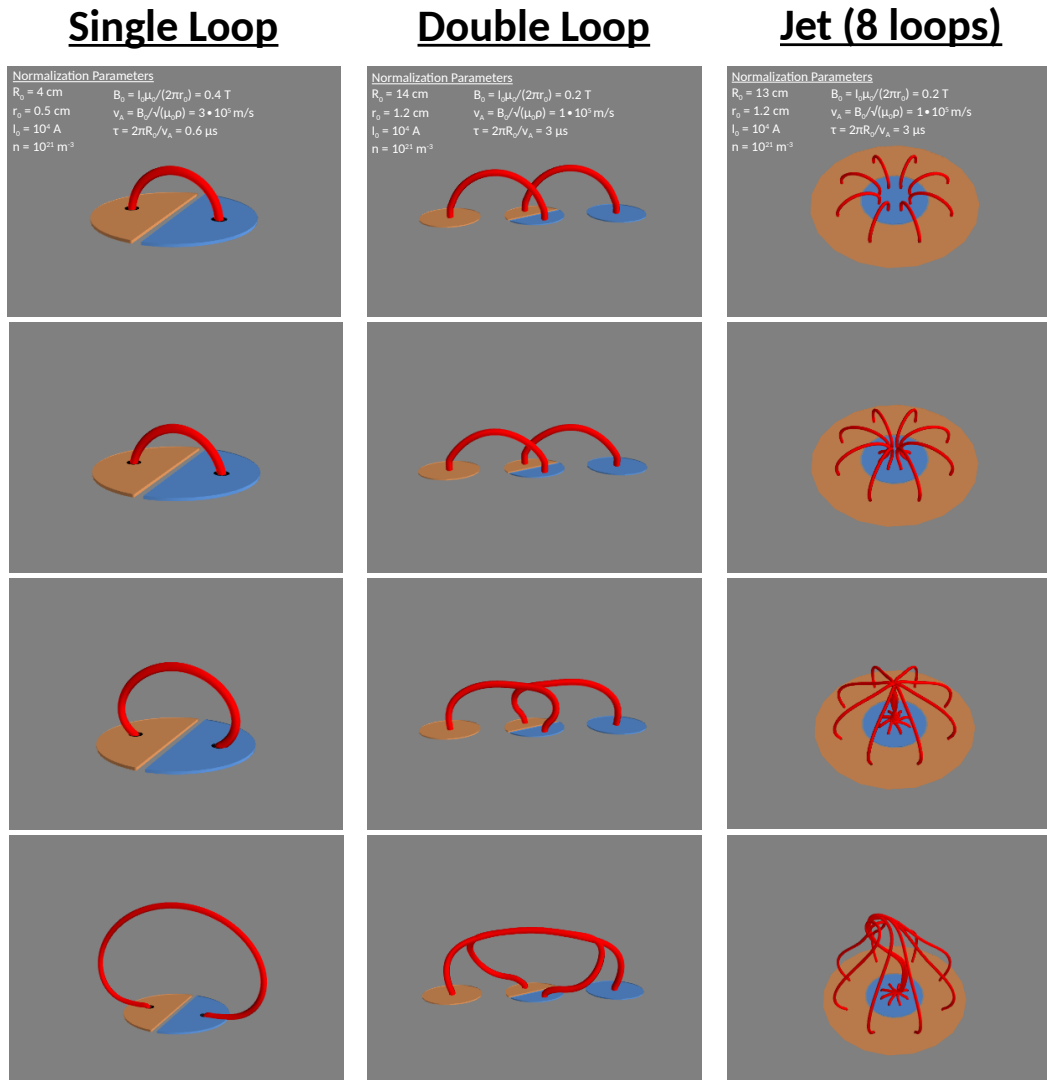
Figure 7.3: Plots showing that the wire simulation can reproduce the large scale evolution of the single loop, double loop, and jet experiments.

The first use of this feature was to evaluate the relative magnitudes of the hoop and tension forces for the single loop experiment. As expected, the tension forces are only significant within a couple centimeters of the footpoints. Since all of the experiments are far from equilibrium, the inclusion of the tension force contributes relatively little to the global evolution and can generally be ignored.

Density variation

As highlighted in Chapter 5, the density profile of a flux rope can have significant effects on its shape. However, the current implementation of the wire simulation
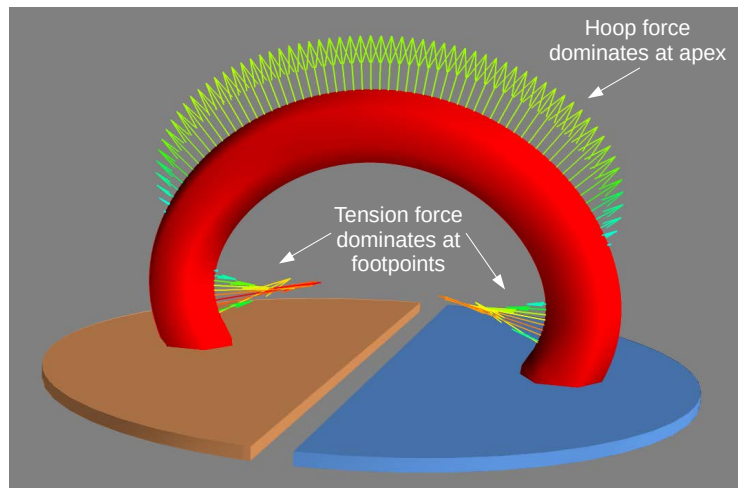
Figure 7.4: Plot of single loop with magnetic force vectors. The hoop force dominates the expansion and the tension forces are only significant near the footpoints.

maintains a uniform linear density. Consequently, the effect mediated by non-uniform density in the experiment are not seen in the simulation. This is especially evident for the jet experiment which has an extremely high density front, quickly decaying density along the axis, and low density in the outer return currents. These differences are highlighted in Figure 7.5.
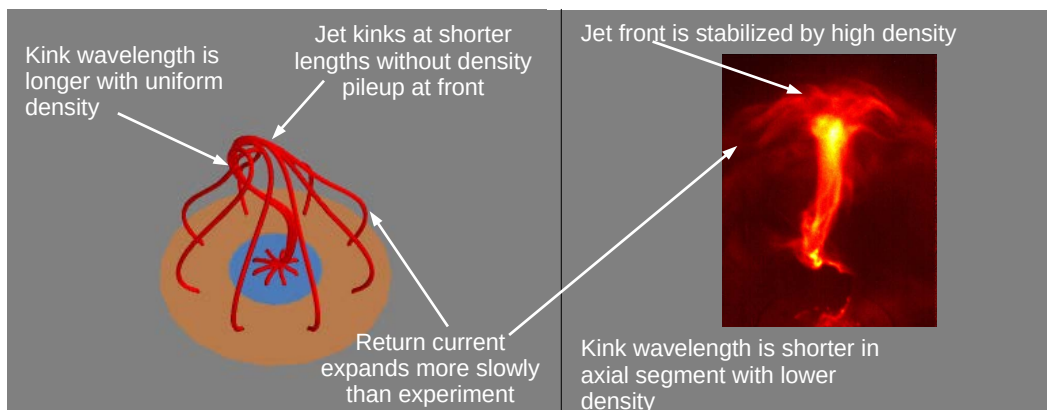
Figure 7.5: Plot of simulated jet and experimental jet. Key differences in morphology of the kink instability imply that the density variation in the jet is crucial to its particular shape.
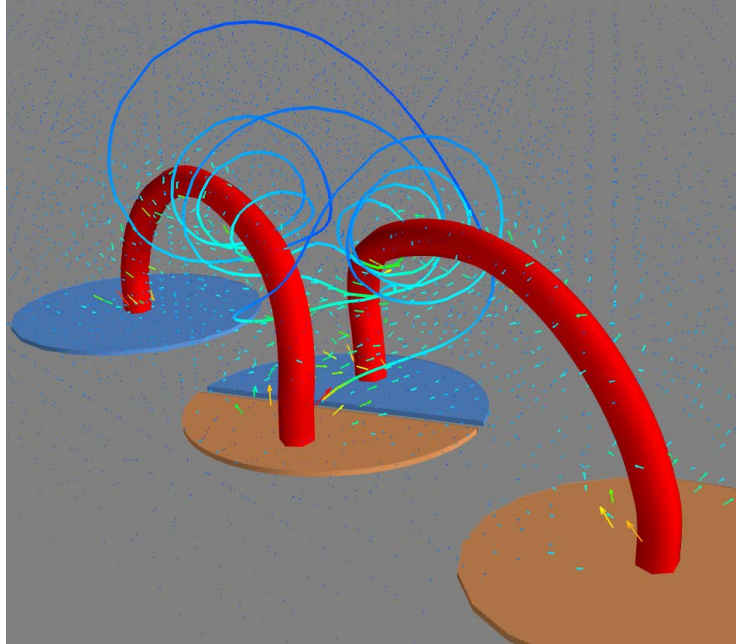
Figure 7.6: Plot of single field line in double loop experiment. This field line demonstrates that a complex topology encircling both loops, then each loop individually before terminating at the adjacent footpoint.

Magnetic field topologies

Due to the complex shapes formed by the various loop experiments, the shape of the magnetic field is often difficult to determine. This is especially problematic when interpreting data from magnetic probes. The simulation provides a simple way to predict what the magnetic field should look like for a particular loop shape. This is also useful for generating synthetic magnetic probe data which can be used to better interpret real measurements. Figure 7.6 shows a plot of the complicated fields that can arise from only two loops.

7.5   Future work

There are several potential extensions of the model,

- Variable axial mass density

- Variable minor radius

- Comparison of wire forces with 3D $\mathbf{J} \times \mathbf{B}$ measurements on double loop experiment

Chapter 8

QUADRUPLE WAVE PROBE

This chapter details the construction and first results of several high frequency (1-20 MHz) $\dot{B}$-probes, designed to measure magnetized plasma waves in the jet experiment. The construction of the probes is motivated by observations of fast magnetic reconnection events on the jet experiment (Figure 8.1). These events are interesting because the reconnection is both spontaneous (i.e., not forced by external conditions) and fast ($\omega \gg \omega_{ci}$). These characteristics are indicative of two-fluid or kinetic processes (i.e., effects which are not present in MHD).

Since fast magnetic reconnection is still poorly understood, there is no comprehensive understanding of what waves should be observed during and after such an event. Consequently, detailed measurements of associated waves can be used to constrain theoretical and numerical models of magnetic reconnection. Several spacecraft, including the current Magnetospheric Multi-Scale mission (MMS), are attempting to measure similar reconnection events in the Earth's magnetosphere for precisely this reason.

The wave probe consists of a set of four 3-axis b-dot probes arranged in a tetrahedron. This tetrahedral arrangement, or quadprobe, is designed to obtain the 3D spatial variation of **B** and thereby also calculate the current density **J** of the wave.
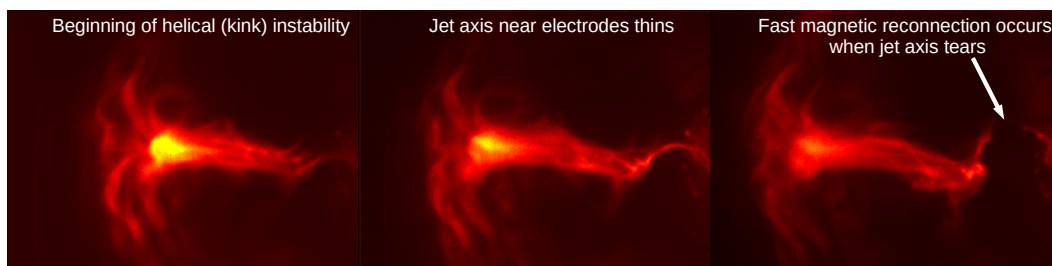
Figure 8.1: Image sequence of hydrogen jet with kink instability. Jet length in these images is ~0.3 m

The chapter will first describe the different wave modes present in the experiment, then describe the probe design. The remaining sections discuss the major result: measurements of a whistler wave pulse generated by magnetic reconnection.

8.1 Classifying plasma waves
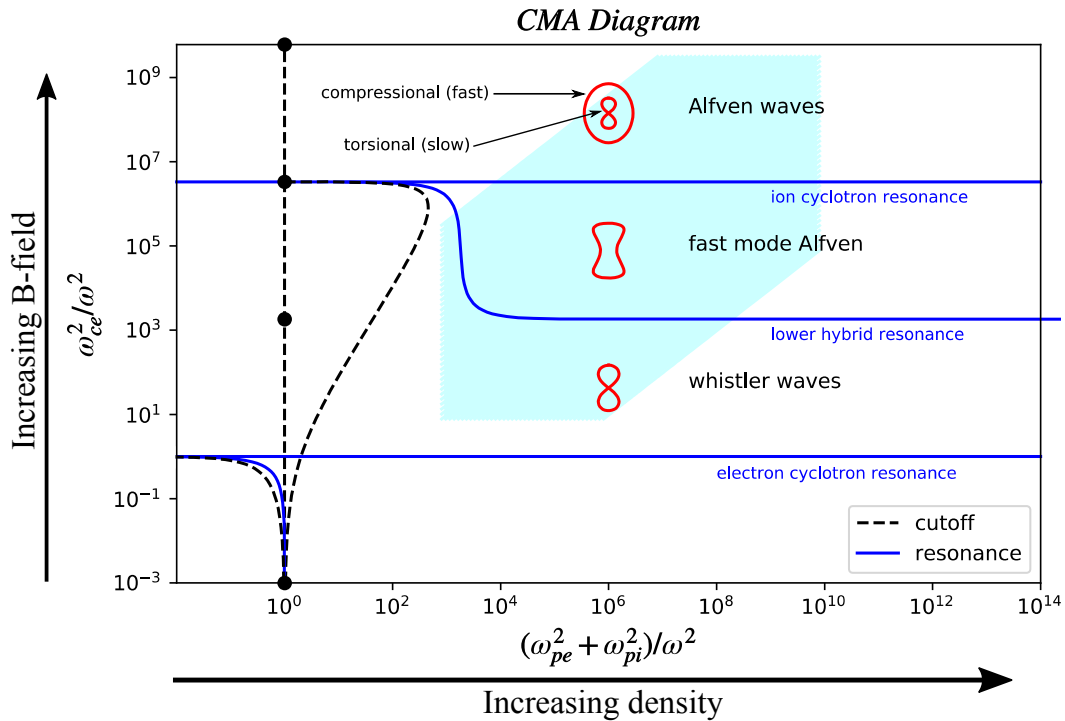
Figure 8.2: CMA diagram showing the relevant resonances, cutoffs and wave modes. The blue region represents the accessible parameter space in the jet experiment: B(10-2000 G), n(10^{15},10^{22} m^{-3}), f(0.1-10.0 MHz). Resonances are plotted as blue lines and cutoffs are shown as dotted lines. The red figures represent wave normal surfaces (i.e., vertical dumbbell shapes indicate propagation mainly parallel to the background magnetic field, ellipsoids represent modes which do not have a preferred direction). There are three possible wave modes in the experiment, the two Alfvén wave modes and the whistler wave mode. These waves modes are defined by regions bounded by resonances and cutoffs.

The Caltech jet experiment has a large range of plasma parameters ranging from |**B**|= 0.001 T, $n_e = 10^{16}$ m^{-3} at the outer edges of the jet to |**B**|= 0.3 T, $n_e = 10^{22}$ m^{-3} along the jet axis. In this highly non-uniform plasma, there are multiple plasma modes in the frequency range of interest.

The modes are described here in the "cold plasma wave" limit where any temperature dependence of the dispersion relations is ignored. For the nearly isothermal experimental plasmas, this is a good approximation. The modes are mapped in parameter space using the Clemmow-Mullaly-Allis (CMA) diagram, a normalized representation of the different wave modes as a function of density and magnetic field (Figure 8.2). The wave modes in the CMA diagram are divided by resonances

(solid blue lines) and cutoffs (dotted lines). Resonances ($n^2 \to \infty$, $\lambda \to 0$) tend to absorb waves and cutoffs ($n^2 = 0$) tend to reflect waves.

Since most observed waves are at higher frequency than the ion cyclotron frequency, the two dominant modes are the fast Alfvén wave and the whistler wave.

The fast Alfvén mode is characteristic of compressional perturbations, is right-hand circularly polarized and has the following dispersion relation,

$$\omega^2 = k^2 v_A^2 + k_\perp^2 c_s^2 \tag{8.1}$$

where $v_A = B/\sqrt{\mu_0 \rho}$ is the Alfvén speed, $k_\perp$ is the component of the wavevector perpendicular to the background magnetic field, and $c_s = \sqrt{\gamma \kappa \frac{T_e + T_i}{m_i}}$ is the sound speed.

The whistler wave is the fundamental mode of the two-fluid plasma description, is also right-hand circularly polarized and is characterized by dispersive propagation (i.e., higher frequencies travel faster). Whistler waves travel mainly parallel to the background magnetic field and in this quasi-longitudinal limit ($\theta \sim 0$), the dispersion can be written as,

$$\omega = \frac{k^2 c^2}{\omega_{pe}^2} |\omega_{ce} \cos(\theta)| \tag{8.2}$$

The presence of whistler waves is an indication that two-fluid effects are important.

8.2 Previous work

The probe design is based off of the thesis work of Xiang Zhai, a previous grad student in the Bellan group who built a single high frequency, 3-axis $\dot{B}$-probe (Figure 8.3). This work extends this single cluster design to a set of four clusters arranged in a tetrahedron.

The single cluster design uses single turn loops constructed from 0.047" semi-rigid coaxial cable (Figure 8.3a). The center conductor is soldered to the outer conductor at the completion of the loop to complete the circuit. Loops are paired with another loop of the opposite orientation to provide a differential signal which reduces common mode noise (Figure 8.3b). Three of these differential pairs are then arranged along perpendicular axes to create a 3D cluster (Figure 8.3c). This loop design provides significant electrostatic shielding and linear frequency response up to several hundred MHz.

Measurements by this single cluster probe of circularly polarized magnetic oscillations were published in [117]. However, it is now believed that these measurements

(a) Single loop design

0.047" semi-rigid coax with copper jack

¼ in

to data acquisition

Very small gap (≤0.02")
- No eddy current allowed
- Noise minimized

Center conductor soldered
on outer conductor

(b) Differential pair design

$$V_1 = A\frac{dB}{dt} + V_{common}$$

$$V_2 = -A\frac{dB}{dt} + V_{common}$$

3-axis cluster

(c)
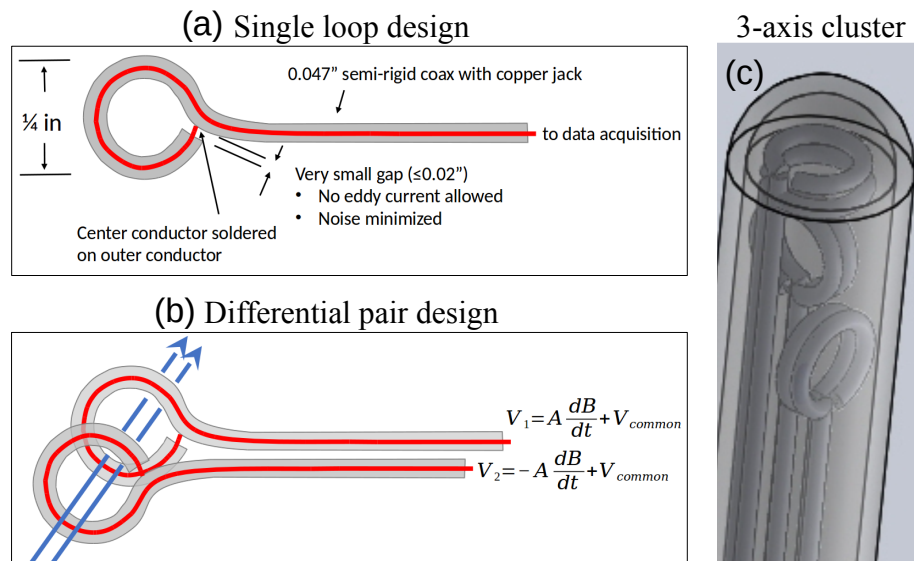
Figure 8.3: Single cluster $\dot{B}$-probe design from [20]. The coaxial design provides electrostatic shielding, loops are paired with opposite orientations to give differential signals, and a 3D cluster is formed from 3 perpendicular pairs of loops.

of circular polarization are an artifact of narrow band filtering and significant common mode noise. This review of the previous measurements is detailed in Appendix section F.1.

8.3 Quadprobe version 1

The first version of the quadprobe (Figure 8.4a) was built with the same techniques as the probe from [20]: loops were manually bent into shape using planar pliers and kept in place using thin strips of painters tape. In this design, the center probe is longer than the surrounding probes.

Vacuum design

The vacuum mounting of the probe was designed by my advisor, Paul M. Bellan. The design encases each probe in a 10 mm outer diameter quartz tubes which are attached to a 2-3/4" conflat (CF) flange using vacuum resin (Torr-Seal). This flange mounts to a 2-3/4" CF spacer flange (3 in length). The other end of the spacer flange connects to another 2-3/4" conflat (CF) flange which is welded to a 1 in diameter steel tube. The whole assembly is attached to the vacuum chamber using a 1 in diameter feedthrough for the steel pipe. The assembly can translate along and rotate about the tube axis. Figure 8.5 shows a diagram of vacuum mounting.
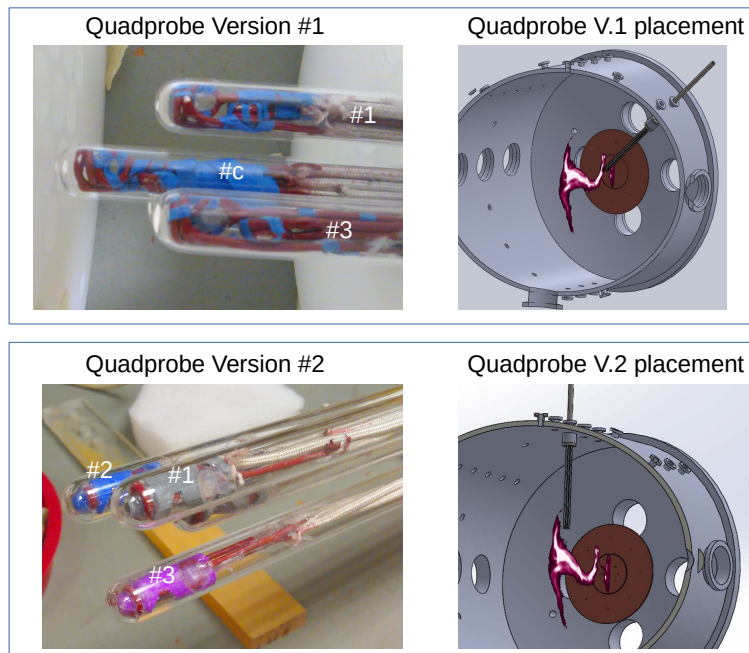
Figure 8.4: Images of the quadruple wave probe and placement relative to jet experiment. The probe consists of four 3-axis high-frequency $\dot{B}$-probes arranged in a tetrahedron. Each cluster is encased in an 8mm outer diameter quartz tube. Probes are labeled with their respective number. Probe #1 is aligned along the x-axis. Version 1 was located in the first port 15.8 cm from the electrode plane and version 2 was located in the third port, 46.2 cm from the electrode plane.

This design sets the probe spacing where the distance between any two probes is 2.2 cm. For the first version of the probe, the center quartz tube was 1.8 cm longer than the surrounding probes and where in the second version, the center probe is shorter than the surrounding probes by 1.8 cm. The quartz tubes for the surrounding probes remained 42 cm long.

Calibration

Calibration is conducted using a Helmholtz coil assembly with special mounting holes arranged in a honeycomb pattern for central placement of each of the four 3-axis probes (Figure 8.6). The honeycomb pattern on the two non-axial plates were rotated 90° relative to each other for calibration of X and Y directions.

The Helmholtz coils each have N=6 turns, with a radius of $r = 3$ in = 7.62 cm. The coils used AWG 30 magnet wire and were secured using hot glue. Coil #1 had an inductance of 17.7 μH, Coil #2 had an inductance of 17.6 μH; both coils are linked
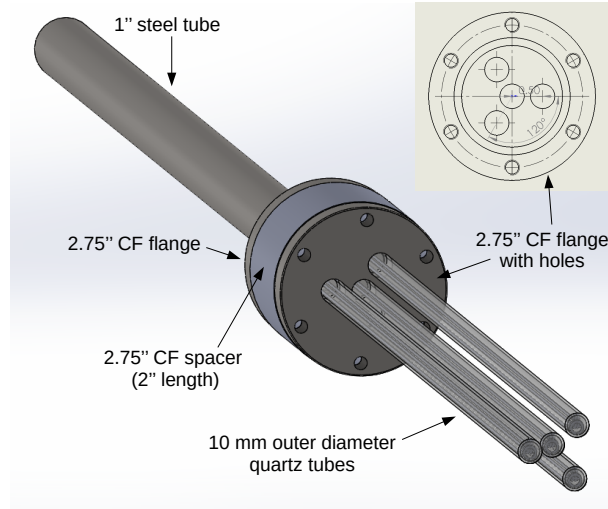
Figure 8.5: Quadprobe vacuum design

in series with coil #1 on the positive side. Coil current was measured using a fast Ion Physics transformer.

A capacitor, $C = 1.37$ nF was also placed in series with the coils, giving a resonant frequency of:

$$f = \omega/2\pi = \frac{1}{2\pi\sqrt{LC}} = \frac{1}{2\pi\sqrt{(17.7 + 17.6) * 1.37 * 10^{-15}}} = 0.72\text{MHz} \quad (8.3)$$

This resonance was necessary to generate a sufficiently large magnetic field to calibrate the probes. Signal from single loop probe at 50Ω termination gives a ± 1.5 mV signal at maximum gain from the signal generator with a coil current of ± 240 mA.

Using the expression for the B-field of a Helmholtz coil,

$$B = \left(\frac{4}{5}\right)^{\frac{3}{2}} \frac{\mu_0 N I}{r}, \quad (8.4)$$

the calibration B-field has an amplitude of 0.17 G, where r is the radius, I is the current, and N is the number of turn per coil. This gives a nominal probe sensitivity of 8156 T/V·s at 0.72 MHz.

The calibration was implemented for each cluster by applying a field in each Cartesian direction, measuring the probe response, and then inverting the transformation matrix. This calibration assumes that the B-field does not significantly change direction across the length scale of a given cluster. The x-direction for the calibration

was chosen to be in the direction of probe #1, the z-direction was chosen to be along the probe axis pointing into the chamber, and the y-direction is defined as $\hat{z} \times \hat{x}$ to maintain a right handed coordinate system.
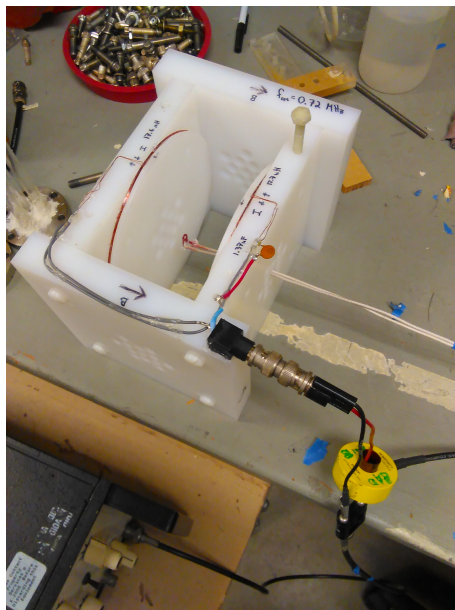
Figure 8.6: Image of Helmholtz coil assembly

Ferrites

Ferrite beads are a convenient way to eliminate high frequency, common mode noise without compromising the original signal. The beads increase the inductance, and therefore the impedance, of common mode oscillations because the common mode currents produce an external B-field. The differential signal of the coaxial cable does not produce an external B-field and is therefore unaffected by the beads.

Cabling consists of semi-rigid cables (RG-402) each 12m long with SMA connectors. Some of these cables were assembled by Jonah Philion, a volunteer summer student. These bridge the distance from the semirigid probe cables to the data acquisition device. Two bead ferrites were used on each connecting cable, the larger (12.8 mm inner diameter) had 4 turns of the cable and the smaller one (9.5 mm inner diameter) had two turns. The ferrite material chosen was mix type 31 (MnZn), which is appropriate for the range of noise frequencies (1-300 MHz) present in the experiment (Fig. 8.7). This ferrite material was found to be significantly more effective at reducing common mode noise than the ferrite material used on the previous single-cluster probe (type 3C90, designed for low-frequency power applications < 200 kHz).
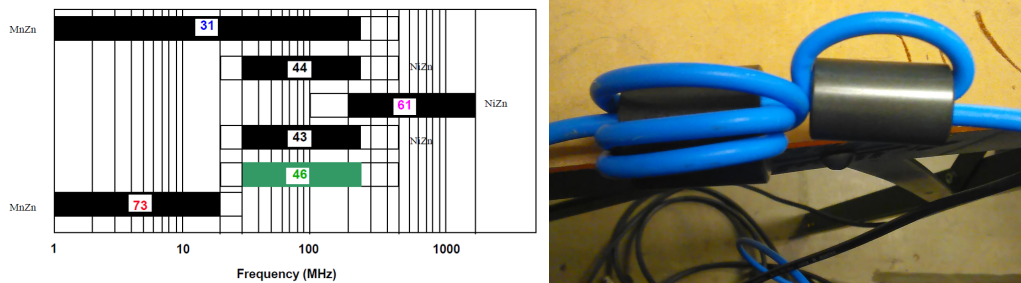
Figure 8.7: **Left**: plot of the frequency ranges for different EMI suppression ferrite materials. Type 31 material is the most effective for the noise spectrum present in the experiment. **Right**: image of ferrite beads on single semi-rigid cable. Cable passes through the large bead 4 times and through the small bead 2 times.
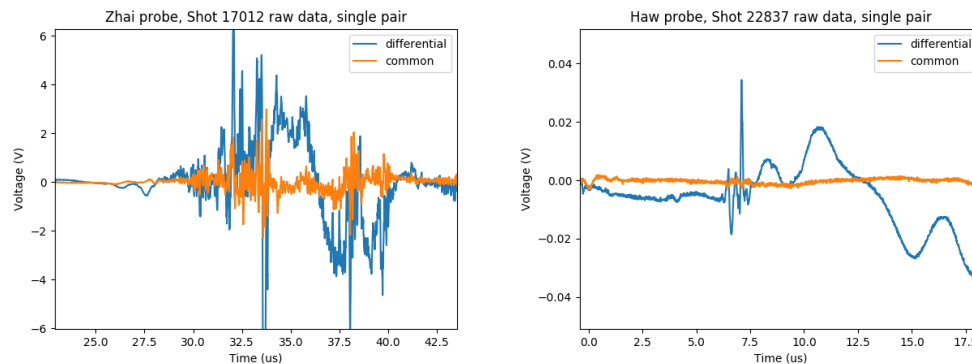
Figure 8.8: (Left) Single pair data from [20] showing differential:blue and common mode:orange signal (Right) Single pair signal from new probe showing differential:blue and common mode:orange signal. New probe shows significantly reduced common mode noise, especially at high frequency, compared to previous version.

The new ferrites provided substantially improved common mode noise rejection compared to previous versions. Figure 8.8 shows the differential and common mode signals of the old probe (left) and the new probe (right). This reduction of common mode noise is critically important to distinguish wave fields in the experiment from electrostatic noise generated outside the vacuum chamber.

8.4 Quadprobe version 2

Unfortunately, one of the quartz tubes in quadprobe version 1 exploded unexpectedly while inside the vacuum chamber, likely due to a small defect which grew over time.

This provided the opportunity to redesign the probe. Since the ferrites eliminated

issues with common mode noise, the second version of the quadprobe used single loops instead of paired loops. This reduced the complexity of re-assembly and provided spare parts for use in a revised single-cluster probe.

The vacuum structure was also altered to have the center probe shorter instead of longer than the surrounding probes. This reduced the perturbation of the center probe in the tetrahedral volume.

Improved fabrication techniques

In the process of rebuilding the quadprobe, new manufacturing aids/techniques were developed to make the loops more consistent.
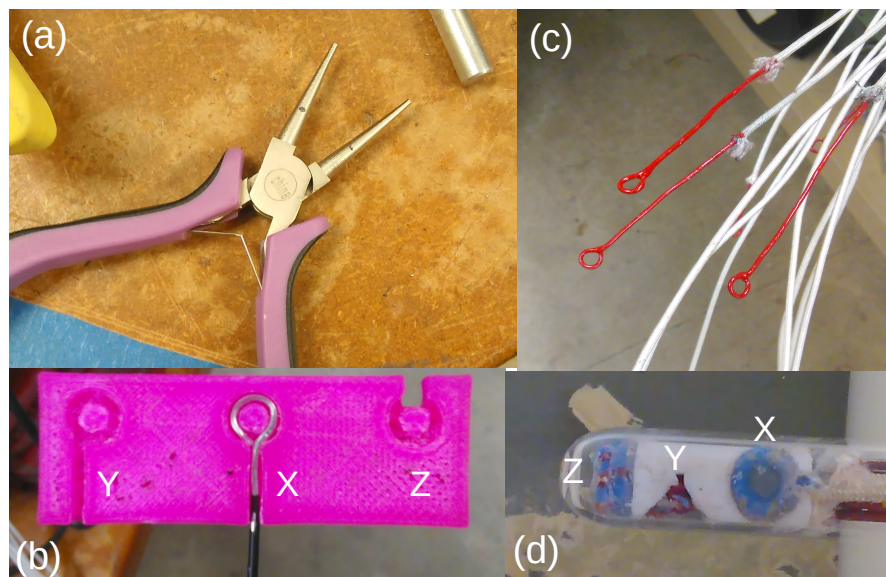
Figure 8.9: Improvements to probe manufacturing: (a) pliers with conical jaws, can bend loops without tearing outer conductor, (b) 3D printed molds for shaping loops for different axes, (c) image of several loops after addition of red high-dielectric spray paint to prevent shorts between loops (d) 3D printed alignment structure for loop clusters.

The previous loop manufacturing process involved manually bending the loops around a 10-32 screw with regular pliers and a vise. This process required both significant force and dexterity to prevent tearing of the outer conductor at the small radius of curvature (r=3 mm). Loop manufacturing was made substantially easier via the purchase of a pair of pliers with conical jaws (Figure 8.9a). These pliers could grip and wrap the loops at the correct radius without tearing the outer conductor.

A 3D printed mold was also made to form each of the different probe axes (X,Y,Z) (Figure 8.9b). This mold made the loops for each axis a consistent shape.

After forming, the probes were coated using a red high-dielectric spray paint (Figure 8.9c) previously used in [14]. This paint prevented shorts between the probes and dried substantially faster (1 hr) than the glyptal varnish (6 days) used in previous versions.

The last improvement was the use of 3D printed mounts to secure the perpendicular orientation of the loops in each cluster (Figure 8.9). This addition was a substantially more reliable than the previous method of taping the clusters together.

Single probe version 2

Since the new quadprobe used only half of the previous cables, another single-cluster probe was built and placed in the vacuum mounting from [20]. This probe retains the paired cluster design (6 channels) and provides another position for time of flight measurements (Figure 8.4).
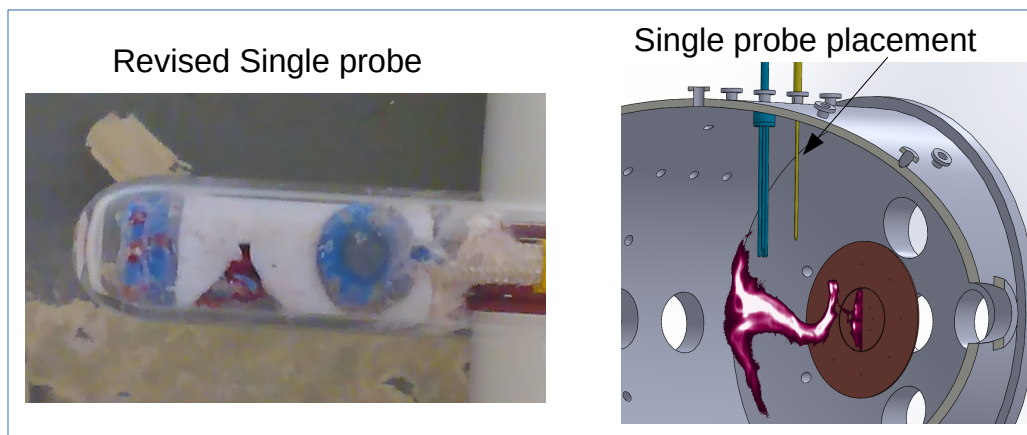
Figure 8.10: Images of single cluster probe and placement in chamber.

Wavelength limit

A simulation was constructed to sample arbitrary plane wave data at the four points of a tetrahedron (side length = 2.2 cm). This was used to test the reconstruction of **B** and **J** at the center of the four probes and to determine which wavelengths could be accurately measured. Calculation of **B** and **J** at the tetrahedron center is done using a first order Taylor expansion; details can be found in Appendix F.
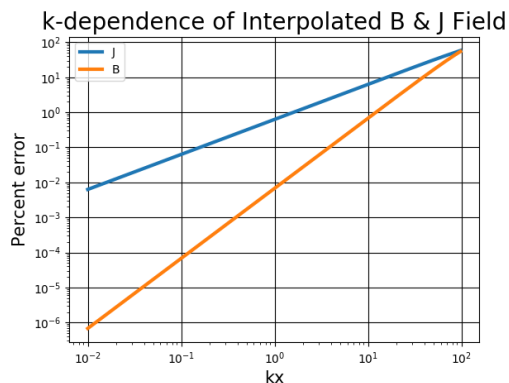
Figure 8.11: Error for simulated k-vectors: limit for reasonable interpolation is $\lambda = 20$ cm, k=31 m^{-1} where error is $\sim 10\%$.

As expected, the reconstruction works well for wavelengths much greater than the probe spacing, $\lambda \gg 2cm$ and can reasonably interpolate wavelengths larger than 20 cm. The percent error in the reconstructed **B** and **J** is shown in Figure 8.11 as a function of wavenumber k.

These calculations motivated the placement of the second version of the probe (Figure 8.4) further from the jet into a region of lower B-field and density. Figure 8.12 shows a contour plot of whistler wavelengths as a function of B and n at 7 MHz. This plot indicates that quadprobe version 1 could not properly measure the current density of whistler waves and that quadprobe version 2 should be at the limit of measuring the whistler wave current.

8.5 Whistler wave pulse from fast magnetic reconnection

A high frequency wave pulse is observed by the quadprobe concurrently with fast magnetic reconnection events in hydrogen jets. These pulses are reproducibly observed every time the jet undergoes a fast reconnection event. The pulse is determined to be a whistler wave by measurements of the background parameters, the wave polarization, and comparisons with the whistler dispersion relation.

Figure 8.13 shows the raw signal from the quadprobe x-channels for a wave pulse observed in shot #22600.

Background parameters

The background magnetic field during the wave pulses is between 10 and 20 G, and points mainly in the negative x-z direction, $\hat{B} \approx [-0.6\hat{x}-0.1\hat{y}-0.8\hat{z}]$ (see Figure 8.14).
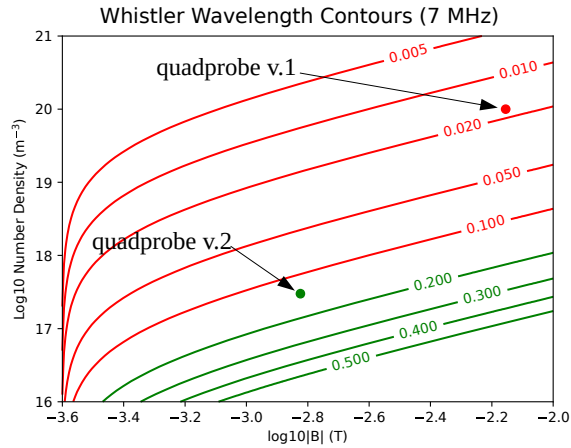
Figure 8.12: Contour plot of whistler wavelengths for a typical wave pulse frequency of 7 MHz. Red contours indicate wavelengths too short for the quadprobe to properly calculate **J**, green contours indicate wavelength is long enough to calculate the wave current.
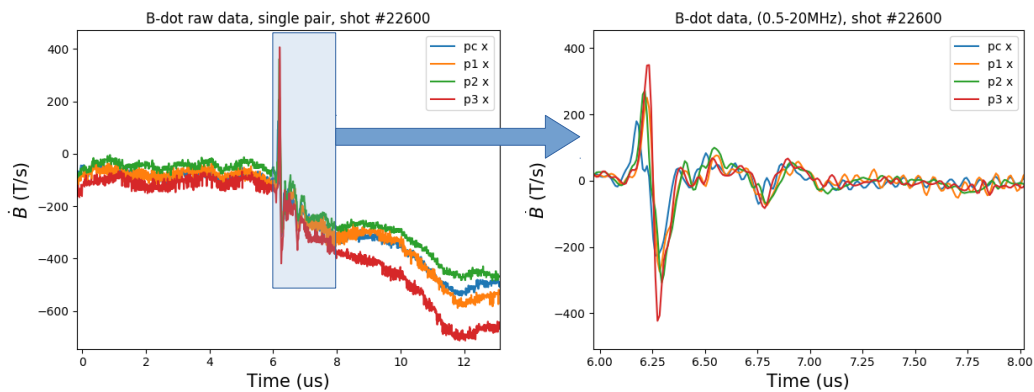
Figure 8.13: Plot of signal from the four x-direction channels from the quadprobe for shot 22600. High frequency pulse is visible in the raw data without filtering (left) and the filtered data (right).

The number density is not well characterized at the probe location but should be within the range of 10^{15}-10^{20} m^{-3}.

As described earlier in Section 8.1, waves can be classified based on the background plasma parameters of density and magnetic field. The measured wave pulses are consistently measured within a certain range of parameters: |B|=[.001-.002] T, n=[10^{15}-10^{20}] m^{-3}, f=[3-10] MHz. This parameter space is entirely within the whistler regime of the CMA diagram (Figure 8.15). Consequently, the only
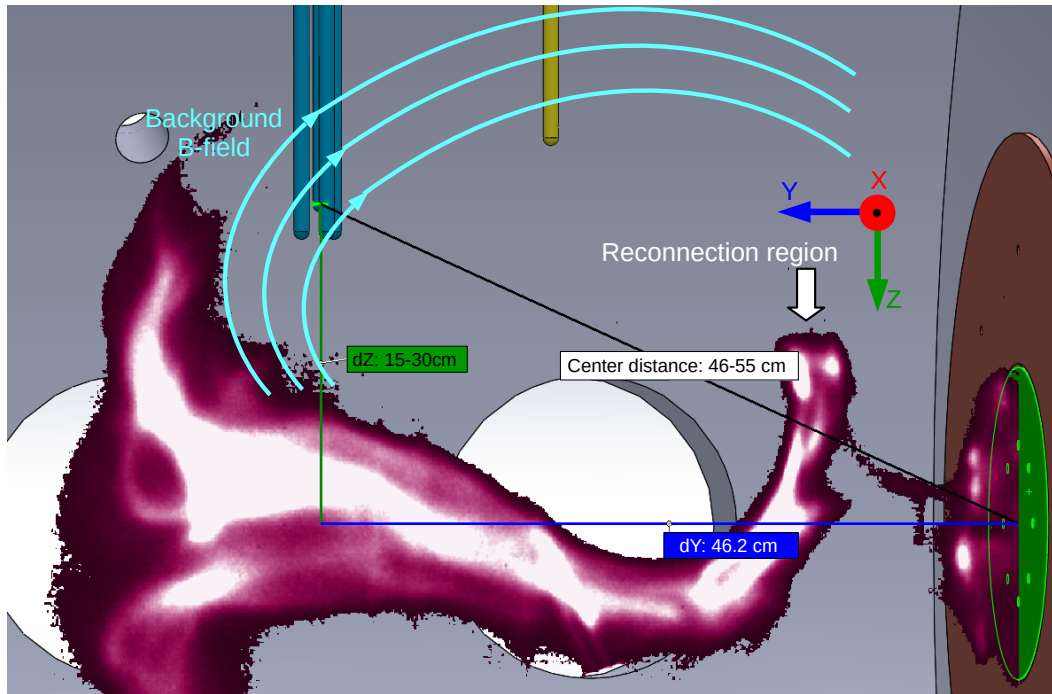
Figure 8.14: (Plot showing both quadprobe and the single probe locations relative to the background B-field. Axes are defined such that $\hat{y}$ is the axial direction, $\hat{z}$ is vertically down, and $\hat{x}$ is out of the page.

propagating wave mode should be the whistler mode.

Polarization

The polarization of the wave can be visualized using a plot called a hodogram. This plots the B-vector as a path in 3D space as a function of time. Helical or circular motion of these hodogram paths indicate circular polarization. Figure 8.16 plots hodograms for shot #22600 for a single probe (left) and for all four probes (right). These hodogram plots correspond to a right-handed circular polarization for a wave moving parallel to the magentic field.

Wavevector

Two complementary types of analysis were used to estimate the wavevector. The first is a simple time of flight calculation and the second involves a new technique developed by my advisor [118]. The time of flight method is appropriate for wavelengths smaller than the probe spacing and the second method is only valid for wavelengths larger than the probe spacing.
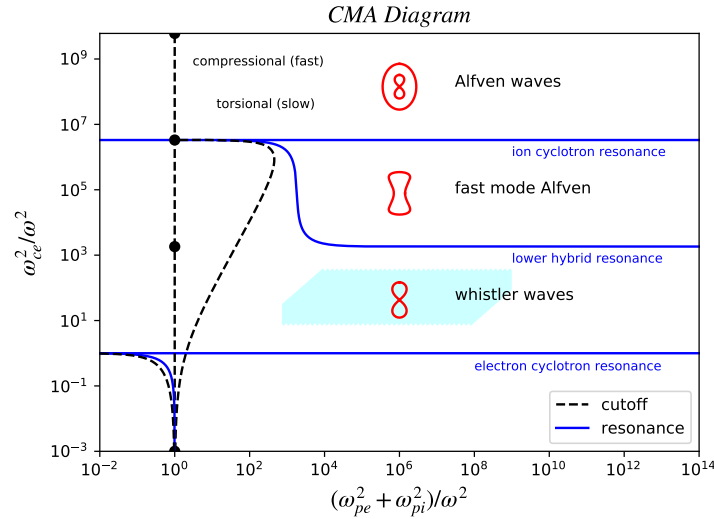
Figure 8.15: Plot of wave pulse parameter space (light blue region, B [.001-.002] T, n [10^{15},10^{20}] m^{-3}, f [3-10] MHz) on the CMA diagram. This indicates that the observed waves should be whistler waves.

Time of flight

The time of flight calculation estimates the wavevector by calculating the propagation velocity of the pulse and then inferring the spatial variation from temporal measurements.

The wave velocity was estimated by assuming a plane wavefront moving through the quadprode with a constant uniform velocity. In this limit, the time delays between the different probes determine the velocity of the wavefront,

$$\mathbf{v} \cdot \hat{r}_{ij} = \frac{|\mathbf{r}_{ij}|}{\Delta t_{ij}} \tag{8.5}$$

where i and j subscripts indicate different probes, $\mathbf{v}$ is the wavefront velocity, and $|\mathbf{r}_{ij}| = 2.2$ cm is the inter-probe distance. These three equations can be inverted to solve for the three-dimensional velocity vector, $\mathbf{v}$. This technique only works when the wavefronts passing each probe are of similar shape and have measurable time delays.

Unfortunately, the shape of the pulse at the four probe locations is not self-similar enough to accurately measure delay timescales less than 50 ns. Consequently, the delay times could not be accurately measured.
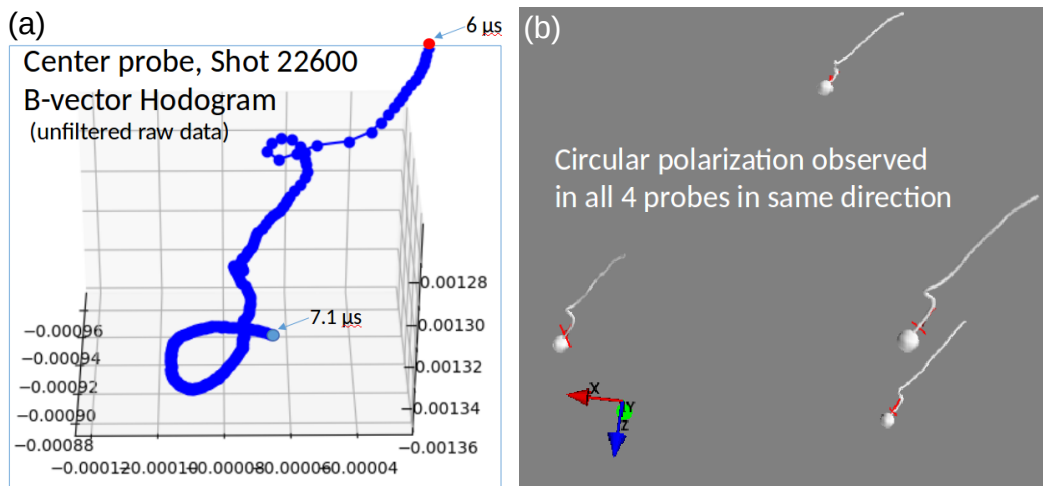
Figure 8.16: (a) detailed hodogram of center probe for shot #22600. This time frame can be compared with the x-component plotted in Figure 8.13. (b) plot of hodograms for all four probes where each path is started at the respective probe position indicated by a white sphere. The observed polarization is consistent across all four probes.

However, the technique does impose a lower limit on the wavelength of the pulse. Since the difference in arrival times of the front are small compared to the period of the oscillations, the wavelength of the pulse must be significantly longer than the probe spacing. Figure 8.17 shows a plot of a high frequency pulse (Bx channels) measured with a fast (5 GHz) oscilloscope. The time delay is difficult to determine since the pulse widths/strengths/shapes vary between the different probes. However, the plot does demonstrate that the pulse width is ~5x larger than the maximum delay time. This implies the wavelength $\lambda \geq 5 \times a = 5 \times 2$ cm = 10 cm, where a is the probe spacing. This also implies that the probe can reasonably calculate the wave current for these pulses.

Calculation from cospatial J and B

The other method of calculating the wavevector takes advantage of the quadprobe's ability to calculate the current density. [118] demonstrated that the wave-vector **k** can be inferred in a quasi-neutral plasma from time series measurements of **J** and **B** at the same point.

The following is an overview of the k-vector solution which assumes the displacement current is negligable (i.e., quasi-neutral plasma),

$$\mu_0 \mathbf{J} = \nabla \times \mathbf{B} = i\mathbf{k} \times \mathbf{B}. \tag{8.6}$$
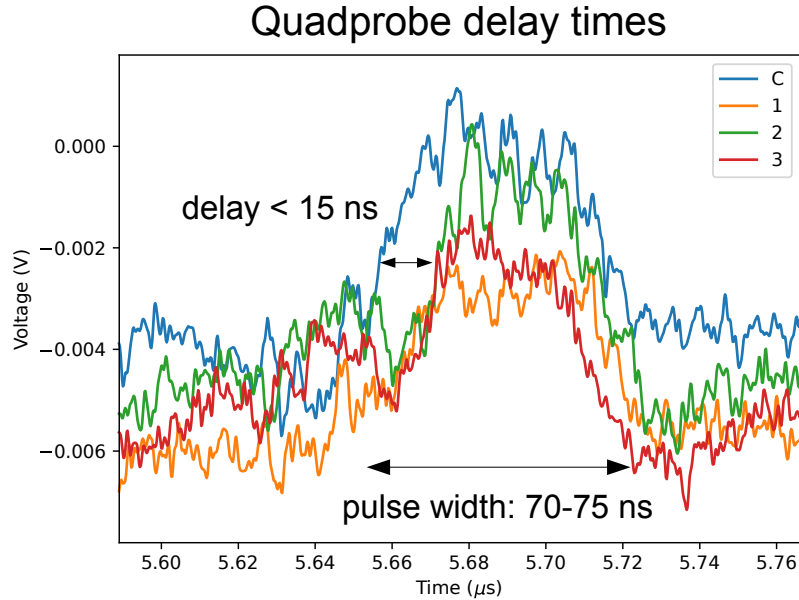
Figure 8.17: Plot of the wavefront timing for the four B_x components of the quad-probe for shot #22717. The pulse width is significantly longer than the difference in arrival times. This data was taken with a 5 GHz sampling rate oscilloscope.

This implies $\mathbf{J} \perp \mathbf{k}, \mathbf{B}$ and since $\nabla \cdot \mathbf{B} = i\mathbf{k} \cdot \mathbf{B} = 0$, the three vectors form an orthogonal basis. To solve for $\mathbf{k}$, we have:

$$\mathbf{k}(\omega) = i\mu_0 \frac{\mathbf{J}(\omega) \times \mathbf{B}^*(\omega)}{\mathbf{B}(\omega) \cdot \mathbf{B}^*(\omega)}. \tag{8.7}$$

This method has recently been successfully used by the MMS spacecraft ([119]) to measure wavevectors in the solar wind.

Applying the technique to the wave pulses gives results in good agreement with the theoretical whistler wave dispersion. Figure 8.18 shows a plot of the calculated wavevector as a function of frequency for shot #22600. For the dominant frequencies in the wavepulse (5-10 MHz), the wavevector magnitude is 40-50 m^{-1} corresponding to a wavelength of 12-16 cm. The wavevector is mainly in the negative $\hat{z}$ direction, indicating mostly parallel propagation ($\theta < 45°$) relative to the background magentic field.

Shots #22588, 22601, 22602 have similar dispersion relations; plots of these can be found in Appendix F.
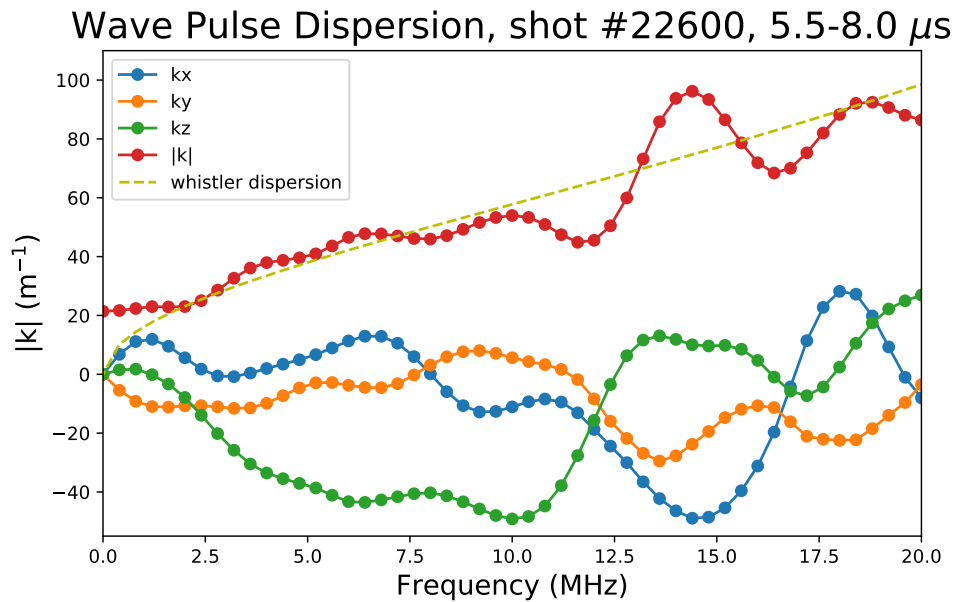
Figure 8.18: Plot of wavevector components calculated from wave pulse in shot #22600. Theoretical whistler dispersion is plotted for background parameters $|\mathbf{B}| = 0.0015$ T, $n = 3 \cdot 10^{17}$ m^{-3}. The calculation indicates that the dominant 6-9 MHz frequencies are mainly in the $-\hat{z}$ direction.

Timing

The observed wave pulses are also concurrent with voltage spikes on the electrodes, current spikes, and bursts of X-rays from the reconnecting plasma. The X-ray bursts were measured with a new X-ray scintillator diagnostic built by fellow grad student Ryan Marshall. Figure 8.19 shows the similar timing for all of these effects associated with the jet reconnection event.

The high temporal correlation between all these signals indicates that they are all related to the magnetic reconnection of the jet. The simultaneous emission of both X-rays and whistler waves during the reconnection indicates that this particular type of reconnection cannot be explained by MHD.

Next steps

The wavevector, direction of propagation, and spatial distribution can be better established. The following are potential next steps for better characterization of these quantities,

- Modify jet settings to determine how waves vary with density, background B-field, etc.
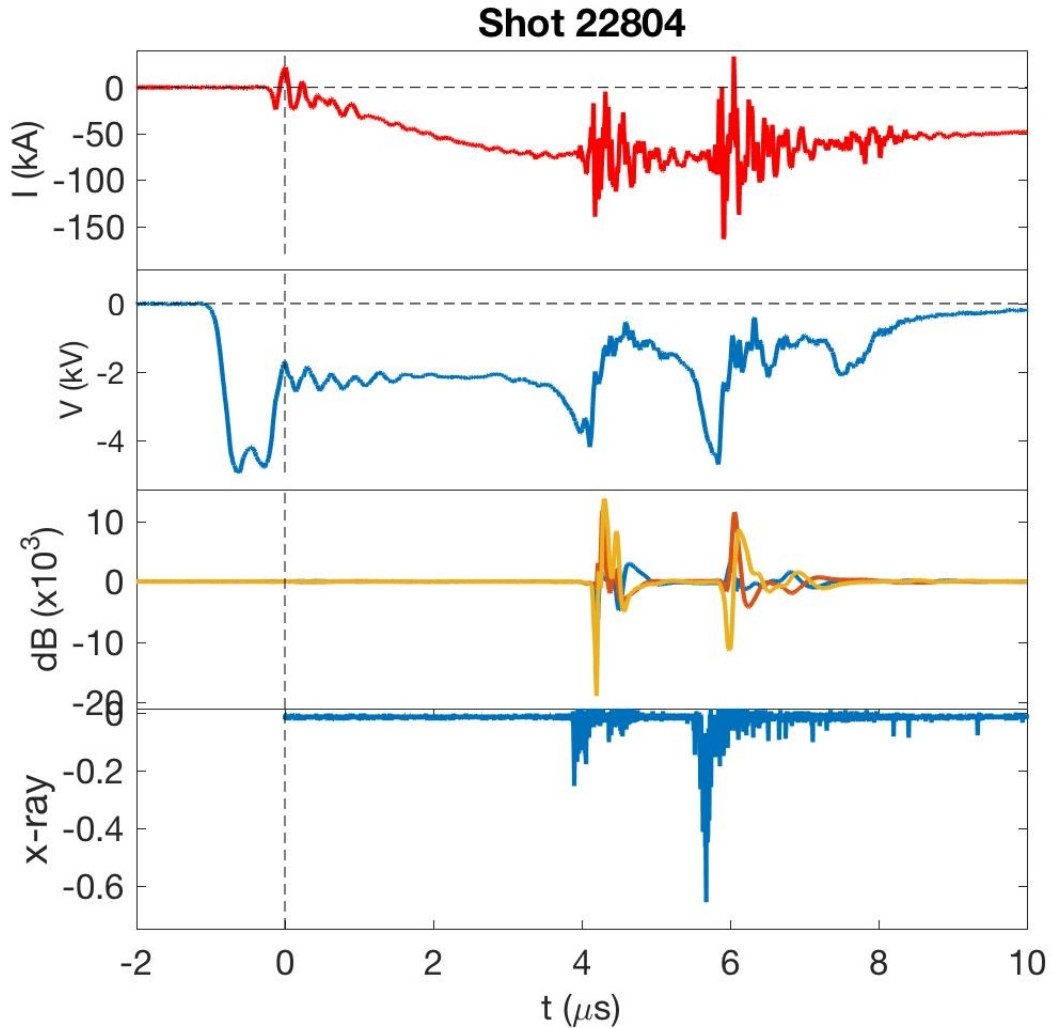
Figure 8.19: Plot of various diagnostics during reconnection event. Shown in order of top to bottom are the power supply current, the electrode voltage, the B_x-components of the quadprobe, and signal from the X-ray scintillator detector.

- Move quadprobe and single probe vertically to determine time of arrival at different radial positions.

- Assemble another single cluster probe out of the spare parts from quadprobe version 1 and place in additional location.

- Calibrate quadprobe and analysis techniques in uniform plasma with known waves.

8.6 Conclusions

This chapter detailed the construction and first application of a quadruple magnetic probe designed to measure the high frequency magnetic field and current density of waves emitted from magnetic reconnection in the jet experiment. Use of new ferrite bead material reduced common mode noise by orders of magnitude and the probe was placed in a location with more constant background field, where the wave oscillations could be easily distinguished.

Measurements of the quadprobe reveal a short ($\sim 2\mu$s) whistler wave pulse emitted during reconnection events. The whistler character of the pulse is confirmed by measurements of the background field, frequency, polarization, and dispersion relation. The dispersion relation is extracted from the measurements using a new method outlined in [118]. These wave pulses also occur simultaneously with X-ray emission and perturbations of current and voltage. This provides a new diagnostic for fast, spontaneous magnetic reconnection events.

Chapter 9

CODED APERTURE IMAGING

9.1 Introduction

Measuring high energy radiation (>100 eV) is challenging because it cannot be focused by conventional lenses or mirrors. As a result, the most common imaging techniques for high energy radiation are pinhole and collimation. Unfortunately, both of these techniques rely on blocking the majority of incident radiation to form an image.

Coded or masked apertures are an alternative high energy imaging technique with much better signal to noise ratio (SNR) than pinhole or collimation imaging [120]. They were initially developed for X-ray astronomy in the 1970's [121, 122] and have since been applied in medical imaging [123], high energy particle imaging [124], and chemical spectroscopy [125]. Despite the vast advantage in SNR offered by coded apertures, the technique has been slow to catch on, perhaps due to the lack of computational power when it was first suggested. However, all computational hurdles have long been surpassed and, for any diagnostic using a pinhole camera that suffers from low signal, this technique can be used to great effect.

Coded apertures consist of a 1 or 2 dimensional mask, composed of transparent and opaque elements, which is placed in front of a detector. Each transparent element acts like a pinhole camera, projecting an image on the detector. Given an appropriate pattern of these transparent elements, the detected superposition of pinhole images can be inverted to recover the original image. The advantage in signal scales like N, where N is the number of transparent elements [123, 126]. If the dominant source of noise is shot noise (i.e., discretization noise where the number of detected counts is small), then the noise scales like $\sqrt{N}$ and the corresponding signal-to-noise ratio scales like $\sqrt{N}$ as well.

In this chapter, part 9.2 will cover theory, part 9.3 will cover design and construction, part 9.4 will discuss simulation and perturbations, and part 9.5 will cover results.

9.2 Theory

Coded aperture imaging relies on projecting incident light through a mask pattern into an invertible superposition of shadow patterns on a detector. This results in a two step imaging process: projecting the source light through a mask pattern to encode the image and the decoding scheme for the detected image.

Image projection

For an arbitrary mask pattern, the detected image, D, will be the source intensity modulated by the mask transmission characteristics. In the far-field approximation (i.e., the intensity from a point source is approximately uniform across the detector [123]) the projected image can be represented as a convolution of the mask transmission, M, and the source intensity distribution, S:

$$D = S * M. \tag{9.1}$$

Due to issues with mask construction, most coded apertures are composed of discrete opaque or transparent elements (transmission of 0 or 1) [120, 126].

For these discrete systems, the simplest scheme is for each resolved source to project a single mask element onto a single detector; this resolves any ambiguities produced by edge effects of partial illumination and greatly simplifies the convolution. With this constraint in mind, we can derive the spacings and field of view for a given system.

To achieve 1-to-1 projection of mask elements onto detector elements, the placement of the mask (see Figure 9.1) is constrained by the ratio of detector element size, d, to mask element size, m:

$$\frac{d}{m} = \frac{a+b}{a} = \frac{z}{a}, \tag{9.2}$$

where z is the source-detector distance, a is the source-mask distance, and b is the mask-detector distance. In this case, the magnification of the mask pattern, $\frac{d}{m} \in [1, \infty]$, constrains the system spacing. The source-detector distance, z is then:

$$z = \frac{d}{m}a = \frac{b}{1 - \frac{m}{d}}. \tag{9.3}$$

We can also solve for the field of view (FOV) for a detector of n elements. By design, each source projects n mask elements onto the detector. This means we must have $2n - 1$ individual mask elements: the first source requires n mask elements and the

remaining $n - 1$ sources each require an additional mask element (See Figure 9.1). Solving for the FOV,

$$FOV = nd + \frac{(2n - 1)m - nd}{b} z = \frac{n - 1}{\frac{1}{m} - \frac{1}{d}}, \tag{9.4}$$

we find that the FOV depends on the detector element size, mask element size, and the number of detector elements.
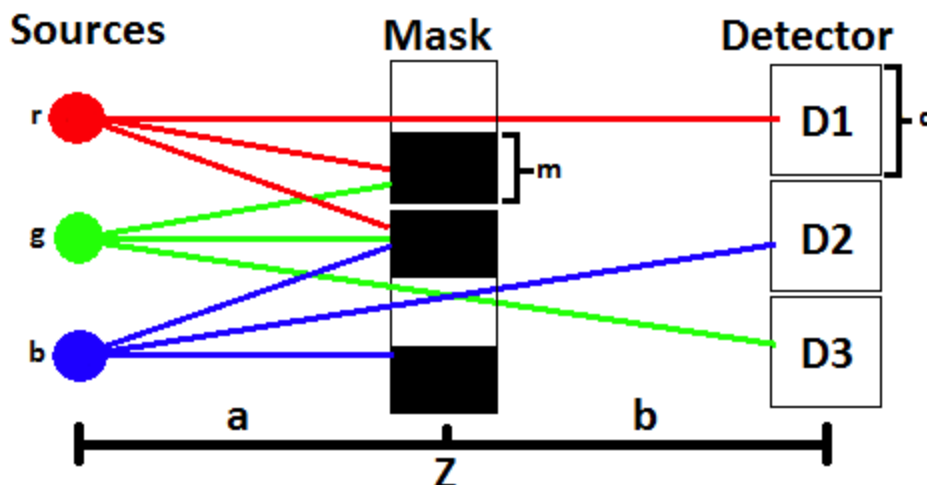
Figure 9.1: Example of coded aperture with 3 detector elements. The source-mask distance is a, the mask-detector distance is b, and the total distance is z. The mask element length is m and the detector element length is d. A more realistically scaled version of this mask-detector pair is shown in Figure 9.9.

Inverting the image in 1D

Inverting the detected image first requires an invertible mask pattern. The condition that determines whether a mask is invertible is that each point source projects a unique, linearly independent pattern on the detector. In the case where the far-field approximation is valid, we can discretize the source distribution into n resolved pixels, where n is the number of detectors; in this approximation, the projection calculation becomes a matrix multiplication. Each subsequence of n mask elements projected onto the detector corresponds to a row of the projection matrix; if all rows are linearly independent, the projection of the mask is invertible.

Figure 9.1 demonstrates this for the case of three detectors: the top source projects the top 3 mask elements (1,0,0) giving the first row of the projection matrix. The other two sources project linearly independent subsequences of three (0,0,1), (0,1,0) giving an invertible transformation matrix, M:

$$D \quad = \quad M \quad * \quad S$$

$$\begin{pmatrix} D_1 \\ D_2 \\ D_3 \end{pmatrix} = \begin{pmatrix} 1 & 0 & 0 \\ 0 & 0 & 1 \\ 0 & 1 & 0 \end{pmatrix} * \begin{pmatrix} r \\ g \\ b \end{pmatrix}$$

To recover the initial image, one simply multiplies the detected array, D, by the inverse of the projection matrix.

Mask Patterns

The next question is how to find invertible mask patterns of length $2n - 1$. The simplest method is to guess and check with random sequences. The advantage of this method is that one can choose any open fraction of the mask (percentage of mask that is transparent); the disadvantage is that there is no guarantee of finding an invertible pattern.

However, there are also classes of invertible analytic sequences. The most popular of these classes are the cyclic difference sets. There are many names and classifications for cyclic difference sets: Singer sets, pseudo-noise sequences, Paley sets, Hadamard sets, m-sequences, quadratic residues, twin prime sets, etc.; however, they all share the same property: each register shift of the sequence is linearly independent of every other. To make a 1D mask of length $(2n - 1)$ from a cyclic difference sequence (CDS) of length (n), one concatenates two periods of the CDS with the last element of the second period omitted. This procedure was used in the mask shown in Figure 9.1: the CDS sequence in this case is (1,0,0) and the mask sequence is (1,0,0,1,0). This ensures that each resolved position projects a different register shift of the CDS on the detector, resulting in an invertible transform. Another useful property of these sequences is that the negative image of any CDS (i.e., exchanging 1's and 0's) is also a CDS.

There are a myriad of construction formulae for different cyclic difference sets which can be found in references: [123, 127, 128]. In this work we present only a single construction method for sequences of length $2^k - 1$ that relies on the coefficients (mod 2) of primitive polynomials of degree k. This method is taken from Nelson and Fredman [128].

We construct the fundamental sequence of length $2^k - 1$ by arbitrarily choosing the

first k elements, $\{e_i ; i = 1...k\}$ and finding the remaining elements as follows:

$$e_{j+k} = \text{mod2}\left(\sum_{i=0}^{k-1} a_i e_{j+i}\right), \qquad (9.5)$$

where a_i is the coefficient of a primitive polynomial of degree k. An example for a 15-element sequence: we use one of the two primitive polynomials of degree 4, $P(x) = 1 + x + x^4$; $a_0 = 1$, $a_1 = 1$, $a_2 = 0$, $a_3 = 0$, and choose the first four elements to be 1. This gives the following sequence of length 15: [1,1,1,1,0,0,0,1,0,0,1,1,0,1,0].

Signal to noise ratio

Coded apertures were designed to minimize shot noise by more efficient use of the detector and thus improve the signal to noise ratio (SNR) by $\sim \sqrt{N}$. Accorsi [129] derives an expression for SNR on a pixel-by-pixel basis. This derivation assumes Poisson counting statistics and defines several parameters: fraction of counts from background ξ, finite transparency of opaque elements t, open mask fraction ρ, total number of pixels N_T, total intensity I_T, and the fraction of total intensity emitted by pixel ij, ψ_{ij}:

$$SNR_{ij} = \frac{\sqrt{N_T I_T}\sqrt{\rho(1-\rho)}(1-t)\psi_{ij}}{\sqrt{(1-t)[\rho + (1-2\rho)\psi_{ij}] + t + \xi}} \qquad (9.6)$$

Using this expression, one can optimize the mask for SNR based on the parameters of one's setup. For the case of imaging a single point source with a perfect mask and no background ($\psi_{ij} = 1$, $\xi = 0$, $t = 0$) the expression reduces to $\sqrt{\rho N_T I_T} = \sqrt{N I_T}$ where N is the number of transparent elements in the mask. Hence we recover the basic $\sqrt{N}$ scaling for the case of a point source. For this case, the optimal mask, with respect to SNR, is the anti-pinhole mask with only one opaque element, $\rho = \frac{N_T - 1}{N_T}$. However, for more distributed sources, $\psi_{ij} \ll 1$, the optimal open fraction is reduced and the SNR gains are smaller. For these more distributed sources it useful to define some global figure of merit such as: $FOM = \Sigma_{ij} SNR_{ij}$.

For the Caltech jet experiment, background interference (e.g., electromagnetic interference, EMI) is large and in this large background limit ($\xi \gg 1$), Eq. 9.6 gives an optimal open fraction around 50%.

Moving to 2D

For most applications, with the notable exception of spectroscopy, it is desirable to have a 2D coded aperture. Conveniently, the only requirement is folding an invertible

1D sequence into 2D. The same principle applies for invertibility: each resolved source must project a linearly independent shadow pattern. Figure 9.2 demonstrates folding a 9-element cyclic difference sequence into a 2D mask: every sub-square of 9 mask elements projects a different register shift of the original sequence.
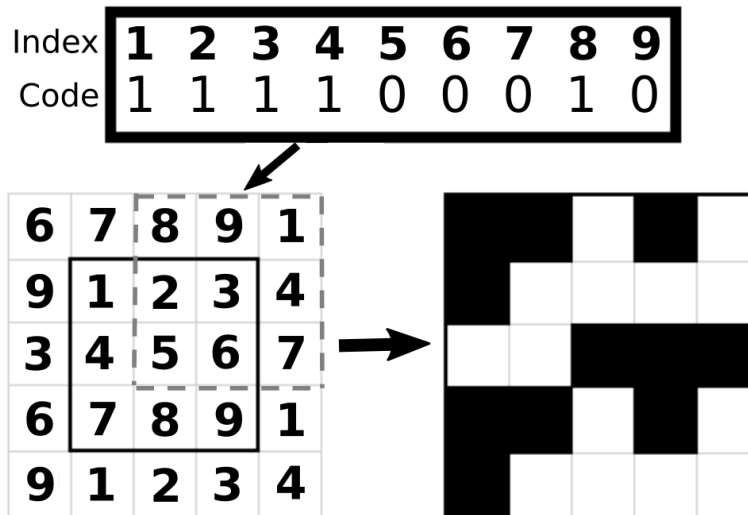
Figure 9.2: This figure depicts folding a 2D sequence into a 2D invertible mask. Start with a 1D cyclic difference sequence (shown at top with associated indices). Next fold sequence such that every sub-square of 9 mask elements projects a register shift of the original sequence: solid sub-square has zero register shift, dotted sub-square has 2 element register shift. Lastly, fill in sequence to obtain 2D pattern.
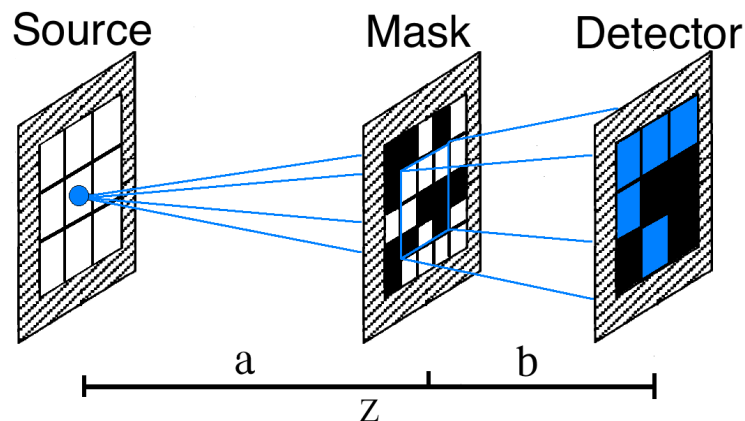
Figure 9.3: Canonical representation of 2D coded aperture system: a light source, S, a coded aperture or mask, M, and the detector, D. A source at the center of the field of view projects the central sub-square of 9 mask elements onto the 9 detector elements.

The projection matrix of the 2D mask is similar to that of the 1D mask: a 2D matrix with rows corresponding to the shadows cast by particular source positions. Each matrix row will correspond to the register shift of a CDS given by the projected sub-rectangle (Figures 9.2,9.3).

9.3 Design

The initial motivation for the project was to image EUV/X-ray bursts from fast ($\sim 1\mu s$) magnetic reconnection events in the Caltech plasma jet experiment [39, 130]. Imaging these events requires very fast time resolution and high sensitivity. The visible light prototype was designed within these constraints with portability to an EUV/X-ray system in mind.
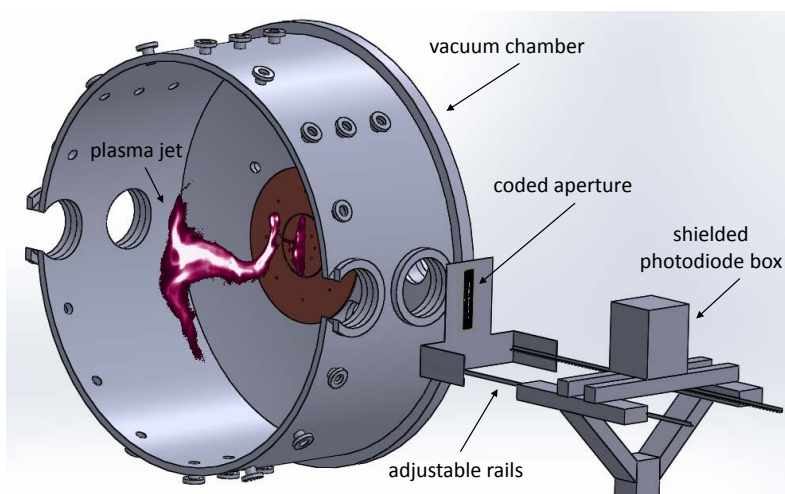
Figure 9.4: Drawing depicting the coded aperture camera in relation to the plasma jet.

Detector

Due to the constraints of the EUV bursts, namely 1-2 μs events occurring over a $30\mu s$ plasma lifetime, the system must be sensitive on a μs timescale. To satisfy this timescale, a photodiode array was chosen as the detector. Photodiodes of small size under reverse bias have much faster response time as compared with CMOS and CCD detectors. Reverse biasing the photodiode arrays greatly increases their dynamic range and prevents saturation at high light intensity. Five 16-element photodiode arrays (A2V-16) from OSI Optoelectronics Inc. were chosen as the detectors because their mechanical design allows for continuous linear mounting. The arrays are mounted in sockets on a printed circuit board and placed inside a shielded box with a slit aperture. BNC cables connect each channel to the digitizer

and all five arrays are reversed biased by four 9V batteries in parallel; no amplifiers were needed.

The digitizer is a 96-channel (e.g., twelve 8-channel 3300 Versa Module Europa panels) system from Struck Innovative Systems. Each channel has a sampling rate of 100 MHz, 12-bit dynamic range, 50 Ω input impedance, 32 kB memory, and an input range of -512 to 512 mV with continuously adjustable offset.
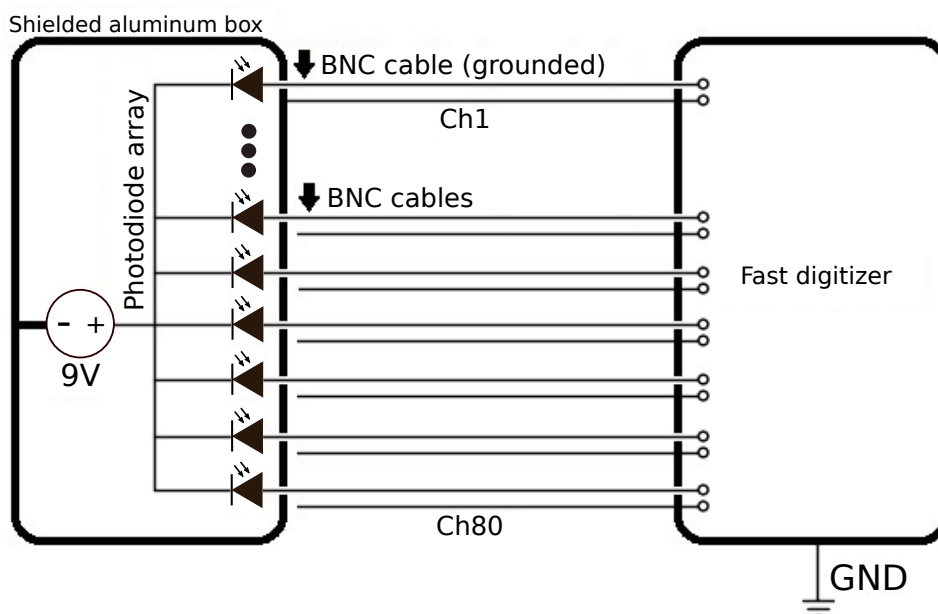
Figure 9.5: Circuit diagram of coded aperture detector system. Shielded box for photodiode array is grounded through a single BNC cable to eliminate ground loops.

Mask

The mask was made by printing out appropriate patterns on standard transparency paper. This made fabrication accessible, inexpensive, and fast, which was essential in testing different mask patterns. New mask patterns could be generated, printed on the office printer, and tested on the experiment within 15 minutes. Two copies of a printed pattern were stacked together to increase the optical density of the opaque elements. Mask element dimensions ranged from $m = 1.5875$ mm (1/16") to $m = 0.79375$ mm (1/32"). Mask patterns were translated into JPEG images using a Python script and printed to scale by setting the pixels per inch (PPI) resolution.

Mounting

The mounting for the system is important as the system relies on geometric optics: placement of the mask and detector determines the focal length and field of view
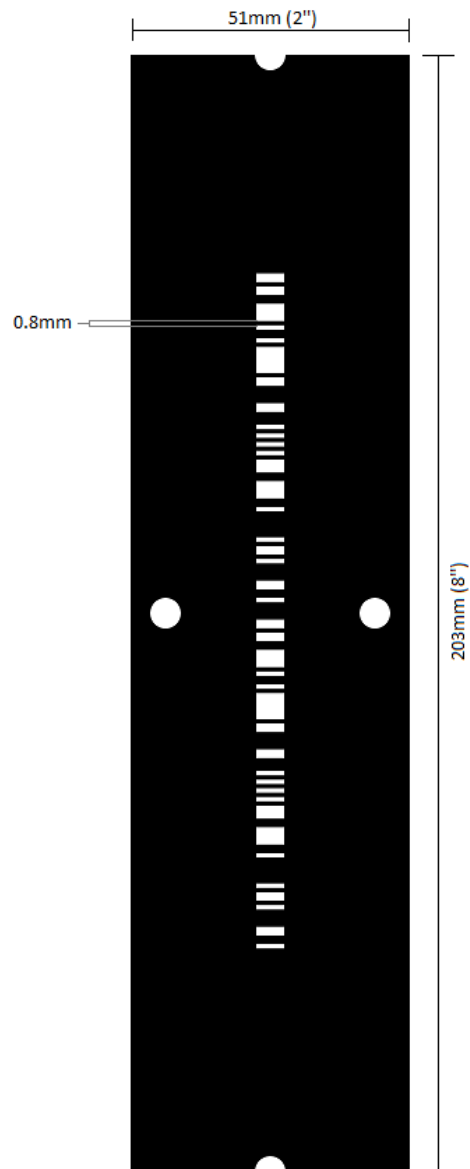
Figure 9.6: Image showing mask dimensions for mask with element size 0.8mm (1/32 "). Additional circular holes are for mounting and alignment purposes.

(FOV) [Eq. 9.3,9.4]. The photodiode array was mounted inside a shielded box with a slit aperture. The mask was mounted on adjustable rails attached to the main stand. This allowed the focal length to be adjusted by sliding the rails while maintaining vertical alignment. For imaging through a given window on the vacuum chamber, the distance to the plasma was measured, the focal length was adjusted accordingly, and the FOV, relative to the chamber, was found by shining a laser array from the detector through the mask. To prevent light from outside the field of view from entering the detector, horizontal baffles were required along the length of the rails.
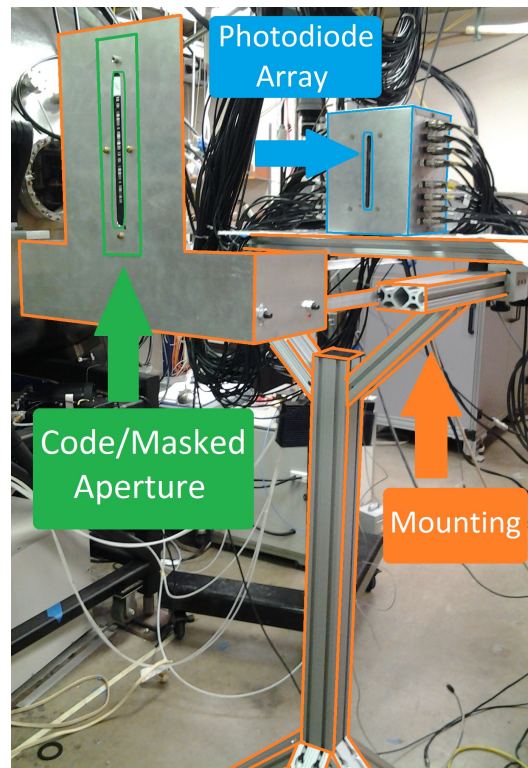
Figure 9.7: Image of coded aperture apparatus

9.4 Simulation and perturbations

In addition to the physical apparatus, a 3D coded aperture simulation was developed in Python to determine the severity of potential perturbations. The simulation inputs are the positions and orientations of light sources, mask elements, and detecter elements. Single light sources are represented as point sources and distributed sources are formed by using a high density of point sources. Light projection from sources to detector is accomplished via ray tracing from each point source. Rays that pass through mask elements are deleted and the remaining rays passing through each detector element are counted. Rays were distributed uniformly spherically and it was found that convergence was achieved with > 20 rays per source per detector. This ray formulation allows for testing of perturbations in 3D as well as accounting for the inverse square intensity of light sources.

Using this simple simulation, several perturbations to the system were examined: misalignment of mask, partially coded sources, and out of focus sources (depth sensitivity).

Mask alignment

Several different misalignments of the mask were tested using the simulation: vertical and horizontal offsets, tilt towards sources, and rotation around axis of sight. For these comparisons, the simulation test setup used a 15 element 1D detector array using a 29 element mask, imaging an off-center Gaussian peak, $\sigma = 6\%$ FOV. A smaller detector array was chosen for these benchmark tests to reduce simulation time.

For vertical (along the FOV dimension) perturbations, the FOV will shift by the number of mask elements displaced. Horizontal perturbations for a one-dimensional detectors only shift the field of view but in 2D will have the same issues as the vertical perturbations in 1D. It was found that tilting the mask towards or away from the detector has little effect for angles less than $10°$. Rotations of the mask along the axis of sight were not significant until mask elements were rotated out of the source-detector plane (in general, $\omega_{max} < \sin^{-1}(h/(mn))/2$ where h is the horizontal width of a mask element). Consequently, for long thin arrays and 2D arrays, the rotational alignment must be fairly accurate.

Depth sensitivity

Since the coded aperture technique relies on proper projection of patterns, the sources must be at the correct distance for crisp images. To determine the depth sensitivity of the apparatus, the full 80 channel system was simulated using appropriate distances for a mask spacing, $m = 0.8$mm and a detector element length, $d = 1.6$mm. To estimate the depth of field, a single point source was used and the signal to noise ratio was calculated as the ratio of the single peak to the RMS of the remaining FOV. It was found that the system has a depth of field of 1-2 cm.

Tomography using coded coded apertures has been of interest for some time[123, 131]. However, this requires resolving small changes in the size of shadow projections, effectively requiring heavy oversampling. In general, one can expect the depth resolution to be at least 5 times worse than the spatial resolution [123].

Partially coded field of view

The partially coded field of view is defined as those areas adjacent to the field of view which can still project light through the mask onto the detector. This region extends a distance as large as the original field of view on all sides. Sources in this region will project an incomplete pattern on the detector that will be inverted as some arbitrary superposition of values (positive and/or negative) over the entire field

Depth of Field for Coded Aperture
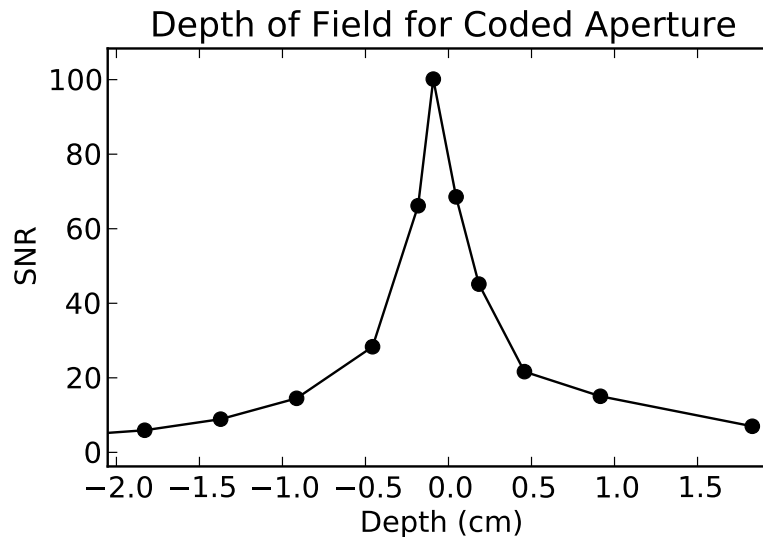
Figure 9.8: Simulated depth of field for coded aperture system. The system can accurately reconstruct source distributions in a depth range of 1-2cm. Outside of this range, sources will be out of focus and contribute noise.

of view. Since the resulting superposition is non-physical, the relative magnitude of the perturbation in a reconstructed image can be much larger than the relative signal intensity of the partially coded source. If strong negative intensities are visible in the inverted image, it may be an indication that partially coded sources are present. To prevent light from partially coded regions from reaching the detector, one must extend baffles from the detector to the source plane. Unfortunately, extending baffles to the source plane is impractical in many cases (e.g., astronomy) and, in these situations, the coded aperture cannot image subsections of bright objects.

9.5 Results

The camera has been used to image a radial cross-section of the Caltech plasma jet experiment [39, 130, 17]. We present here basic tests confirming that the coded aperture performs as expected.

Image Reconstruction

Several data reduction steps were taken before image reconstruction. First, the initial data (Figure 9.10) was smoothed using a 200 ns Gaussian window to remove high frequency EMI ($>$15MHz) from the raw signal. Second, the calibration of the photodiode array was applied (accounting for background levels and relative sensitivity of each element). Last, any negative voltages (due to noise) still present in the raw
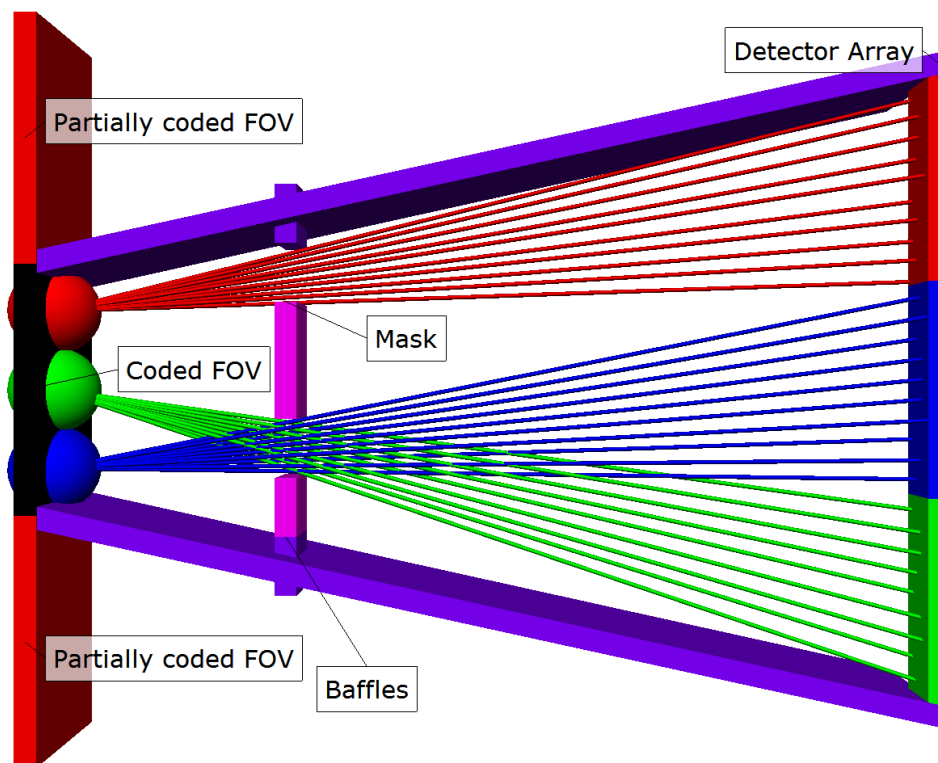
Figure 9.9: The coded and partially coded fields of view are shown with respect to the mask-detector pair in Figure 9.1. Extended baffles are displayed, blocking light from partially coded regions.

data were set to zero. From this reduced raw data, the coded aperture inversion was applied, yielding physical images.

A typical reconstructed image is shown in Figure 9.11. 2D images of the plasma jet taken with an ICCD camera (Imacon 200) are shown in Figure 9.12 for comparison. The major features visible in the coded aperture image are the jet front and the kinking of the jet axis [132, 39]. The relative intensities of the jet front and the jet axis differ by a factor of 20-50. The jet axis undergoes a kink instability where the axis accelerates into an expanding spiral. This spiral shape is projected in the coded aperture image as sinusoidal motion of the axis center.

Comparing each of these features with the 2D camera images, we find quantitative agreement in position, intensity ratios, and timing. The dynamic range of the coded aperture is greater than that of the ICCD, (ICCD pixels are 10-bit, coded-aperture pixels are 12-bit) and this aids in resolving the large range in plasma light intensity.
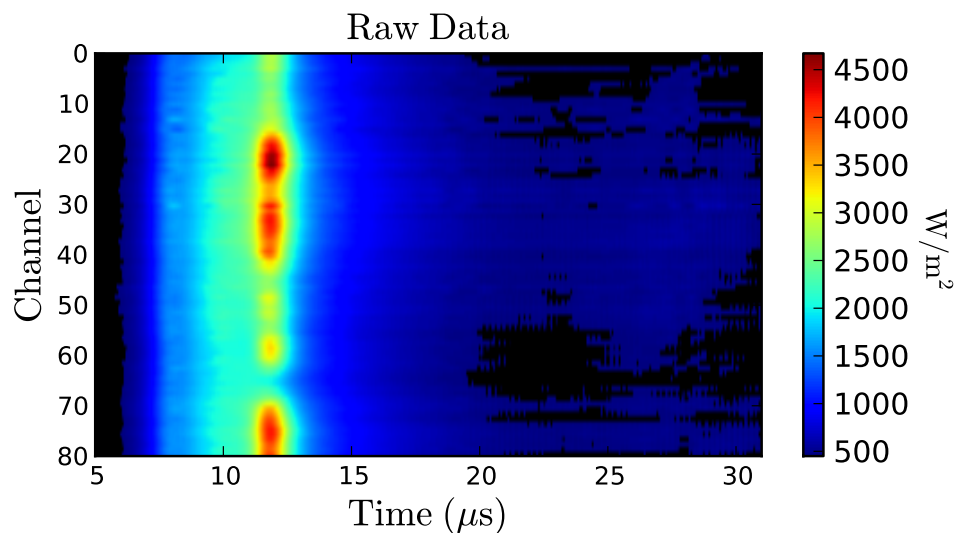
Figure 9.10: Typical raw voltage data collected by the photodiode array.

Given this agreement, we are confident that the coded aperture reconstructions are valid images.
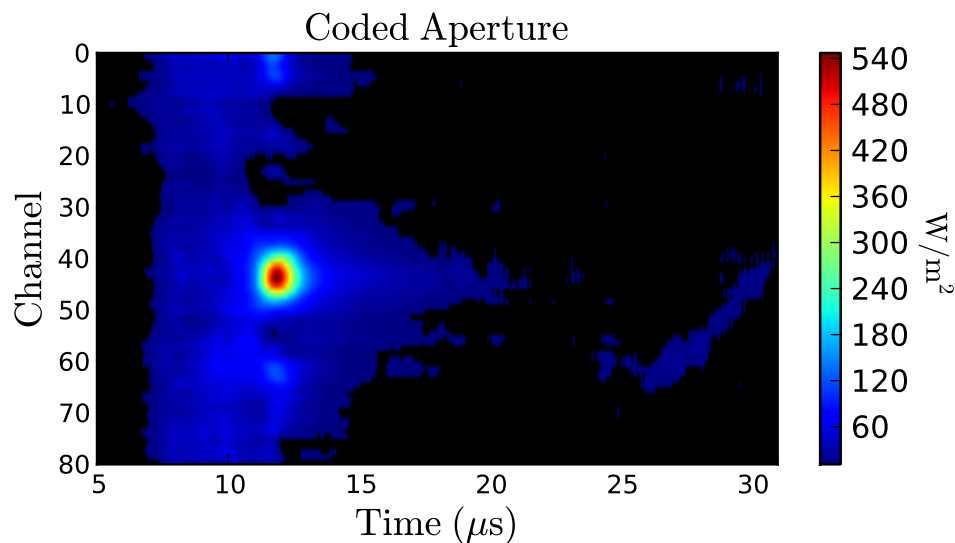
Figure 9.11: Typical coded aperture image of plasma jet cross-section obtained after decoding. Resolution is 2.8mm/channel. Scale bar on the right ranges from 10 to 540 W/m^2.

Comparison with pinhole camera

To benchmark the coded aperture images, they were compared with images taken using an equivalent pinhole mask on the same apparatus (i.e., a pinhole mask with same resolution and FOV as the coded aperture). For this instrument, the coded
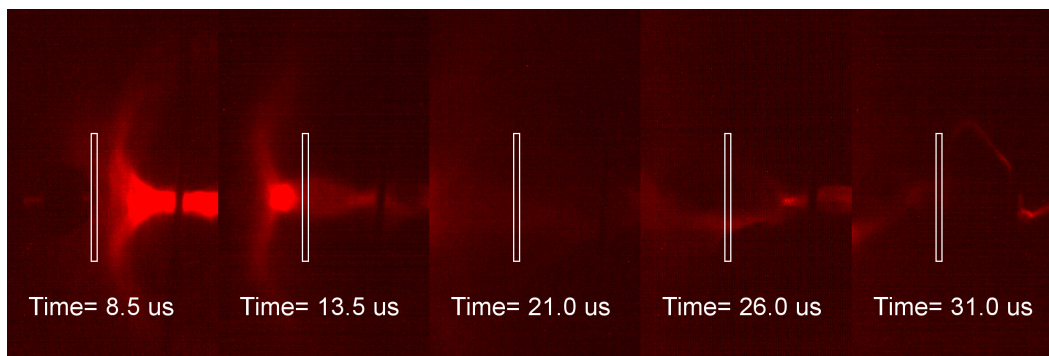
Figure 9.12: Sequence of images of plasma jet taken with fast ICCD camera (Imacon 200). The FOV of the coded aperture camera is outlined in white.
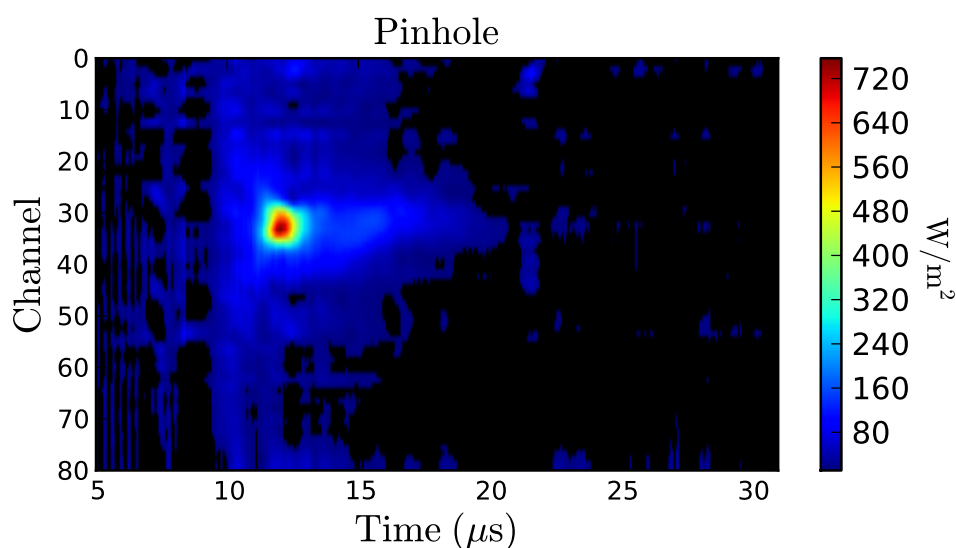
Figure 9.13: Image of plasma jet taken with pinhole mask. This was an especially bright shot ($\approx 40\%$ brighter than average) chosen to illustrate the limited sensitivity of the pinhole configuration. The jet axis disappears at an intensity of 100 W/m^2. Scale bar ranges from 10 to 760 W/m^2. Resolution is 2.8mm/channel.

aperture mask gives an integrated raw signal roughly 40 times greater than that of the pinhole mask (Figures 9.10,9.13). This meets the expectation for a 50% open mask: a given source will illuminate approximately half of the detectors giving an $n/2$ increase in signal relative to a pinhole, where $n = 80$ is the number of detectors. The coded aperture camera can resolve features down to 10 W/m^2 whereas the pinhole camera can only resolve features down to 100 W/m^2. Even for an especially bright plasma shot, such as the one shown in Figure 9.13, the pinhole camera is unable to resolve the kinking of the jet axis.

If we define the signal to noise ratio as the intensity ratio of the brightest versus the dimmest identifiable feature, then the coded aperture image has about an order of magnitude better SNR as compared with the pinhole camera. This matches the expectation of square-root scaling of SNR.

	Brightest feature (W/m^2)	Dimmest feature (W/m^2)	SNR
Coded aperture	540	10	54
Pinhole camera	760	100	7.6

Table 9.1: Comparison of SNR for coded aperture and pinhole.

Measurement of kink instability

Since the jet axis motion is visible in the coded aperture images, we can use this to estimate the acceleration present during the kink instability. To obtain an estimate of radial acceleration, we account for projection effects by inferring the angular position at the points where the kink crosses the initial axis position. From these points we linearly interpolate the angular position from 16-30μs. Then the angular projection of a constant radial acceleration is fit to the image data. For the plasma shot shown in Figure 9.14, the constant acceleration model of the radial motion fits quite well from 16-30μs. Other plasma shots also exhibited constant accelerations in the range [6e8,1e10]m/s^2. This range of accelerations is consistent with previous measurements taken with the fast camera [132]. [80]

9.6 Discussion

We have presented the design and first results of a fast (100MHz) 1D coded aperture system for visible light. First tests show that the system properly reconstructs 1D cross-sections and scales linearly with incident light intensity. Further measurements show that the system has ~ 7 times larger signal to noise ratio than an equivalent pinhole camera. A simulation was written to test various perturbations and it was found that the most significant perturbations were: rotation of the mask around the axis of sight and light sources in the partially coded regions.

In addition to fulfilling its role as a prototype for an EUV/X-ray system, the system was able to provide high resolution measurement of the radial motion of the Caltech plasma jet as it goes kink-unstable.

Now that the technology has been demosntrated to work with visible light in 1D, the next step is to replace the photodiodes with EUV/X-ray diodes and repeat the
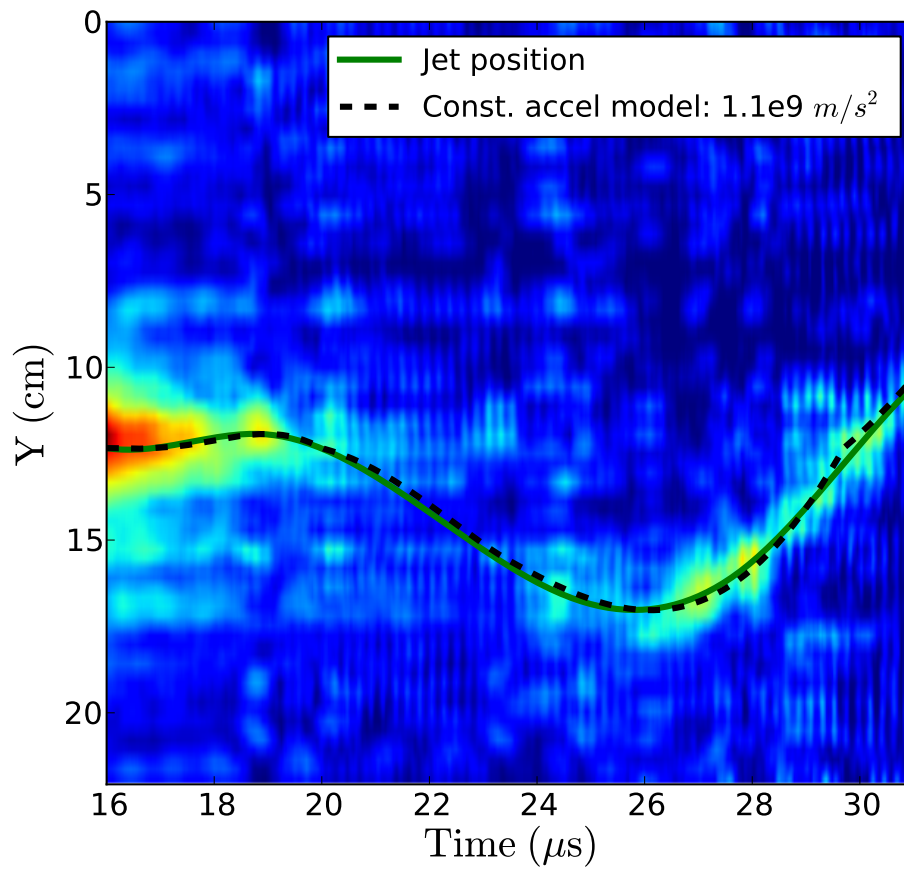
Figure 9.14: Plot showing jet intensity over time, fit to jet axis as function of time, and a constant radial acceleration model. Fit to jet position is done by fitting a Gaussian profile at each time step and smoothing the resulting positions.

measurements for high energy bands.

C h a p t e r   10

SUMMARY

This dissertation describes investigations of laboratory flux ropes with non-dimensional scaling to solar prominences using a combination of experiments and numerical simulations. The major experimental results are,

1. A new model for the formation of flux rope density cavities driven by increasing flux rope current

2. Characterization of magnetically driven axial flow/collimation in arched flux ropes

3. A new mechanism for the suppression of the kink instability by non-uniform density

4. Measurements of short, coherent whistler wave pulses from fast magnetic reconnection induced by tearing of a flux rope

In parallel with the experiments, two numerical simulations were developed to support and interpret the experimental results,

1. A 3D MHD simulation of the single loop experiment.

2. A new reduced physics model for simulating flux rope motion that assumes each flux rope can be treated as a thin, 1D current path in 3D space.

All of these results are the consequence of an asymmetric or 3D perturbation: density cavities will only form if the increasing current is localized in space, the axial flows and collimation only occur in flux ropes with non-uniform minor radius, the kink instability is suppressed by non-uniform density, and the fast reconnection from tearing is an asymmetric process. The following paragraphs briefly summarize each result.

The new model for cavity formation (Chapter 6) is perhaps the most exciting result. This model identifies a new mechanism for why density cavities form around flux ropes with increasing current. The central idea is that a flux rope with increasing

current will induce a shell of reverse current in the background plasma to satisfy the frozen-in flux condition. Since oppositely directed currents repel, the shell of reverse current is pushed away from the main current, creating a density cavity. The model was motivated by observations of cavities forming on the single loop apparatus in experiments with a background gas. Probe measurements of the structure showed that the outer boundary of the cavity contained a layer of reverse current. This same reverse current feature was also seen in the 3D MHD simulation. The primary application of this model is to explain the density cavities observed around stable and erupting solar prominences. This model also has relevance to space weather prediction because it connects a visible feature, cavity size, with the magnetic stability of solar prominences.

The 3D B-field measurements detailed in Chapter 3 are important for several reasons. First and foremost, they confirm the three predictions of a longstanding theory [21]: (1) axial magnetic forces exist in current channels with spatially varying minor radius, (2) these forces can drive counterpropagating axial flows, and (3) this process collimates the flux rope. This mechanism can explain the significant discrepancy between observed densities in solar loops and the predictions of hydrodynamic models. The other important consequence is that this work developed the necessary diagnostics, procedures, visualization tools, and analysis tools to do further 3D investigations on other experiments.

The work investigating the apex dip feature of the single loop experiment upended a decades old phenomenology (Chapter 5). These experiments and simulations demonstrated that the dip feature was created by a non-uniform density distribution rather than a current driven kink instability. This identified a key non-linear interaction of gas supply in the experiment and was a critical discovery for quantitative numerical simulation. Furthermore, these results indicate that such density perturbations in flux ropes can inhibit the kink instability which was intially proposed to explain the dip feature. This implies that the kink instability threshold for solar prominences, which are known to have high density at the apex, should be modified to include the effect of non-uniform density.

A new type of wave diagnostic was successful in measuring high frequency whistler wave pulses emitted during fast magnetic reconnection events in the hydrogen jet experiment. The wave character was confirmed by measurements of the background parameters, the wave polarization, and comparisons with the whistler dispersion relation. These observed wave pulses are observed concurrently with voltage spikes

on the electrodes, current spikes, and bursts of X-rays from the reconnecting plasma. These additional effects indicate the importance of two-fluid or kinetic physics during the reconnection events. This work also improved previous noise reduction schemes by an order of magnitude which was necessary to identify the weak wave signal.

To supplement the single loop experiment, a numerical 3D MHD simulation was developed from the Los Alamos COMPutational Astrophysics Simulation Suite (LA-COMPASS). The process of developing this simulation demonstrated that previous assumptions about the experimental initial density distribution, current density, and background magnetic fields were not quite correct. Correcting these misconceptions resulted in excellent agreement between experiment and simulation. The most useful technique to emerge from this work is a method for constructing low aspect ratio (fat/broad etc.) arched current channels. This method allows study of the effects of flux rope compression which are essential to the mechanisms in Chapters 3 and Chapter 6.

The wire simulation was developed as a simple way to predict the 3D motion of the experimental flux ropes. This is a reduced physics model that treats each flux rope as a current carrying wire and evolves each wire path based on magnetic forces. This reduces the 3D system to a set of 1D paths in 3D space, making the model computationally fast. The resulting simulation can characterize the motion and shape of the single loop, double loop, and jet experiments. The model was used to test different experimental configurations, plot magnetic fields from complex 3D current paths, and evaluate limits of simple analytic models.

10.1   Outlook

In my humble opinion, the venerable Bellan flux rope experiments still have substantially more interesting physics to reveal. In particular, this thesis has opened several new avenues of investigation related to 3D effects, quantitative comparisons with numerical simulations, and measurements of wave phenomena.

Much of this thesis was devoted to developing diagnostics and procedures for 3D measurements, 3D visualizations, and 3D numerical simulations of the various flux rope experiments. This expansion into fully 3D characterization is a new and likely fruitful direction for the Bellan lab. Few other experiments are as reproducible as ours and those that are have highly symmetric setups with few, if any, fully 3D effects. With these new tools, additional 3D studies and measurements are already

being carried out on the jet and single loop experiments.

At the same time, we now also have 3D numerical simulations with which to directly compare and contrast the 3D measurements. In this dissertation, the immediate access and fast iteration time of both experiment and simulation greatly accelerated understanding of the physical mechanisms. It is likely that future joint efforts will be similarly enhanced.

The last new frontier for the lab is the study of magnetized plasma waves. Prior to the current work, wave measurements at high frequency were difficult due to limited probe sensitivity and significant noise. These limitations have been overcome and the new quad probe diagnostic has demonstrated the ability to measure and characterize waves from single plasma shots. This provides a new range of analysis and measurement techniques for characterizing both the bulk plasma parameters as well as fast reconnection, shocks and other time-dependent phenomena.

In conclusion, I look forward to the future research that these new avenues and approaches lead to in future years.

BIBLIOGRAPHY

[1] J P Verboncoeur. "Particle simulation of plasmas: review and advances". In: *Plasma Physics and Controlled Fusion* 47.5A (2005), A231. DOI: 10.1088/0741-3335/47/5A/017.

[2] D. D. Ryutov, R. P. Drake, and B. A. Remington. "Criteria for Scaled Laboratory Simulations of Astrophysical MHD Phenomena". In: *Astrophysical Journal Supplement* 127 (Apr. 2000), pp. 465–468. DOI: 10.1086/313320.

[3] National Research Council. *Severe Space Weather Events: Understanding Societal and Economic Impacts: A Workshop Report*. Washington, DC: The National Academies Press, 2008. ISBN: 978-0-309-12769-1. DOI: 10.17226/12507.

[4] John Kappenman. *Geomagnetic Storms and Their Impacts on the U.S. Power Grid*. Tech. rep. Metatech Corporation, Jan. 2010.

[5] Nicole Homeier and Lisa Wei. *Solar Storm Risk to the North American Electric Grid*. Tech. rep. Lloyds, Jan. 2013.

[6] Jeffrey J. Love. "Credible occurrence probabilities for extreme geophysical events: Earthquakes, volcanic eruptions, magnetic storms". In: *Geophysical Research Letters* 39.10 (2012). L10301, n/a–n/a. ISSN: 1944-8007. DOI: 10.1029/2012GL051431.

[7] G. Allen Gary. "Plasma Beta above a Solar Active Region: Rethinking the Paradigm". In: *Solar Physics* 203.1 (2001), pp. 71–86. ISSN: 1573-093X. DOI: 10.1023/A:1012722021820.

[8] D. H. Mackay et al. "Physics of Solar Prominences: II- Magnetic Structure and Dynamics". In: *Space Science Reviews* 151 (Apr. 2010), pp. 333–399. DOI: 10.1007/s11214-010-9628-0. arXiv: 1001.1635 [astro-ph.SR].

[9] Thomas Wiegelmann and Takashi Sakurai. "Solar Force-free Magnetic Fields". In: *Living Reviews in Solar Physics* 9.1 (2012), p. 5. ISSN: 1614-4961. DOI: 10.12942/lrsp-2012-5.

[10] Marc L. DeRosa et al. "A Critical Assessment of Nonlinear Force-Free Field Modeling of the Solar Corona for Active Region 10953". In: *The Astrophysical Journal* 696.2 (2009), p. 1780. URL: http://stacks.iop.org/0004-637X/696/i=2/a=1780.

[11] M. J. Aschwanden et al. "First Three-dimensional Reconstructions of Coronal Loops with the STEREO A+B Spacecraft. IV. Magnetic Modeling with Twisted Force-free Fields". In: *The Astrophysical Journal* 756, 124 (Sept. 2012), p. 124. DOI: 10.1088/0004-637X/756/2/124. arXiv: 1207.2790 [astro-ph.SR].

[12] Linda E. Sugiyama and M. Asgari-Targhi. "Gravitational steady states of solar coronal loops". In: *Physics of Plasmas* 24.2 (2017), p. 022904. DOI: 10.1063/1.4975311.

[13] Paul M. Bellan and John F. Hansen. "Laboratory simulations of solar prominence eruptions". In: *Physics of Plasmas* 5.5 (1998), pp. 1991–2000. DOI: 10.1063/1.872870.

[14] Rory James Perkins. "Experimental and analytical studies of merging plasma loops on the Caltech solar loop experiment". PhD thesis. Caltech, 2011. URL: http://resolver.caltech.edu/CaltechTHESIS:05252011-110433288.

[15] Eve Stenson. "Fields, forces, and flows: What laboratory experiments reveal about the dynamics of arched plasma structures". PhD thesis. Caltech, 2012. URL: http://resolver.caltech.edu/CaltechTHESIS:06102012-025123301.

[16] Quoc Bao N. Ha. "Plasma loop and strapping field dynamics: reproducing solar eruptions in the laboratory". PhD thesis. Caltech, 2016. URL: http://resolver.caltech.edu/CaltechTHESIS:07162015-193957726.

[17] Auna Louise Moser. "Dynamics of magnetically driven plasma jets: An instability of an instability, gas cloud impacts, shocks, and other deformations". PhD thesis. Caltech, 2012. URL: http://resolver.caltech.edu/CaltechTHESIS:04132012-150652134.

[18] Gunsu Soonshin Yun. "Dynamics of Plasma Structures Interacting with External and Self-Generated Magnetic Fields". PhD thesis. Caltech, 2008. URL: http://resolver.caltech.edu/CaltechETD:etd-07242007-162442.

[19] Xiang Zhai and Paul M. Bellan. "An earth-isolated optically coupled wideband high voltage probe powered by ambient light". In: *Review of Scientific Instruments* 83.10 (2012), p. 104703. DOI: 10.1063/1.4757112.

[20] Xiang Zhai. "Experimental, Numerical and Analytical Studies of the MHD-driven plasma jet, instabilities and waves". PhD thesis. Caltech, 2015. URL: http://resolver.caltech.edu/CaltechTHESIS:06092015-162916583.

[21] Paul M. Bellan. "Why current-carrying magnetic flux tubes gobble up plasma and become thin as a result". In: *Physics of Plasmas* 10.5 (2003), pp. 1999–2008. DOI: 10.1063/1.1558275.

[22] J.A. Klimchuk. "Cross-Sectional Properties of Coronal Loops". In: *Solar Physics* 193.1 (2000), pp. 53–75. ISSN: 1573-093X. DOI: 10.1023/A:1005210127703.

[23] M. C. López Fuentes, J. A. Klimchuk, and P. Dèmoulin. "The Magnetic Structure of Coronal Loops Observed by TRACE". In: *The Astrophysical Journal* 639.1 (2006), p. 459. DOI: `10.1086/499155`.

[24] Joseph E. Plowman, Charles C. Kankelborg, and Dana W. Longcope. "Coronal Loop Expansion Properties Explained Using Separators". In: *The Astrophysical Journal* 706.1 (2009), p. 108. DOI: `10.1088/0004-637X/706/1/108`.

[25] Markus J. Aschwanden and Richard W. Nightingale. "Elementary Loop Structures in the Solar Corona Analyzed from TRACE Triple-Filter Images". In: *The Astrophysical Journal* 633.1 (2005), p. 499. URL: `http://stacks.iop.org/0004-637X/633/i=1/a=499`.

[26] G. J. D. Petrie. "Coronal Loop Widths and Pressure Scale Heights". In: *The Astrophysical Journal* 649.2 (2006), p. 1078. DOI: `10.1086/506905`.

[27] P. C. H. Martens. "Scaling Laws and Temperature Profiles for Solar and Stellar Coronal Loops with Non-uniform Heating". In: *The Astrophysical Journal* 714.2 (2010), p. 1290. DOI: `10.1088/0004-637X/714/2/1290`.

[28] Harry P. Warren, Amy R. Winebarger, and John T. Mariska. "Evolving Active Region Loops Observed with the Transition Region and Coronal explorer. II. Time-dependent Hydrodynamic Simulations". In: *The Astrophysical Journal* 593.2 (2003), p. 1174. DOI: `10.1086/376678`.

[29] C. Litwin and R. Rosner. "Coronal Scale-Height Enhancement by Magnetohydrodynamic Waves". In: *The Astrophysical Journal Letters* 506.2 (1998), p. L143. DOI: `10.1086/311656`.

[30] A. Malanushenko and C. J. Schrijver. "On the Anisotropy in Expansion of Magnetic Flux Tubes in the Solar Corona". In: *The Astrophysical Journal* 775, 120 (Oct. 2013), p. 120. DOI: `10.1088/0004-637X/775/2/120`. arXiv: `1307.3440 [astro-ph.SR]`.

[31] Markus J. Aschwanden, Richard W. Nightingale, and David Alexander. "Evidence for Nonuniform Heating of Coronal Loops Inferred from Multithread Modeling of TRACE Data". In: *The Astrophysical Journal* 541.2 (2000), p. 1059. URL: `http://stacks.iop.org/0004-637X/541/i=2/a=1059`.

[32] Durgesh Tripathi et al. "Observations of Plasma Upflow in a Warm Loop with Hinode/EIS". In: *The Astrophysical Journal Letters* 754.1 (2012), p. L4. URL: `http://stacks.iop.org/2041-8205/754/i=1/a=L4`.

[33] Hui Tian et al. "Persistent Doppler Shift Oscillations Observed with Hinode/EIS in the Solar Corona: Spectroscopic Signatures of Alfvénic Waves and Recurring Upflows". In: *The Astrophysical Journal* 759.2 (2012), p. 144. URL: `http://stacks.iop.org/0004-637X/759/i=2/a=144`.

[34] K. Ahn et al. "Patterns of Flows in an Intermediate Prominence Observed by Hinode". In: *The Astrophysical Journal* 721 (Sept. 2010), pp. 74–79. DOI: `10.1088/0004-637X/721/1/74`.

[35] S. Parenti. "Solar Prominences: Observations". In: *Living Reviews in Solar Physics* 11, 1 (Dec. 2014), p. 1. DOI: `10.12942/lrsp-2014-1`.

[36] Caroline E. Alexander et al. "Anti-parallel EUV Flows Observed along Active Region Filament Threads with Hi-C". In: *The Astrophysical Journal Letters* 775.1 (2013), p. L32. URL: `http://stacks.iop.org/2041-8205/775/i=1/a=L32`.

[37] X.-L. Yan et al. "Fine-scale structures and material flows of quiescent filaments observed by the New Vacuum Solar Telescope". In: *Research in Astronomy and Astrophysics* 15, 1725 (Oct. 2015), p. 1725. DOI: `10.1088/1674-4527/15/10/009`. arXiv: `1502.03546 [astro-ph.SR]`.

[38] Boris Filippov et al. "Solar Magnetic Flux Ropes". In: *Journal of Astrophysics and Astronomy* 36.1 (2015), pp. 157–184. ISSN: 0973-7758. DOI: `10.1007/s12036-015-9321-5`.

[39] S. C. Hsu and P. M. Bellan. "A laboratory plasma experiment for studying magnetic dynamics of accretion discs and jets". In: *MNRAS* 334 (Aug. 2002), pp. 257–261. DOI: `10.1046/j.1365-8711.2002.05422.x`.

[40] Hui Li et al. "Modeling the large-scale structures of astrophysical jets in the magnetically dominated limit". In: *The Astrophysical Journal* 643.1 (2006), p. 92. DOI: `10.1086/501499`.

[41] Xiang Zhai et al. "Three-dimensional MHD simulation of the Caltech plasma jet experiment: First results". In: *The Astrophysical Journal* 791.1 (2014), p. 40. DOI: `10.1088/0004-637X/791/1/40`.

[42] E. V. Stenson and P. M. Bellan. "Magnetically Driven Flows in Arched Plasma Structures". In: *Phys. Rev. Lett.* 109 (7 Aug. 2012), p. 075001. DOI: `10.1103/PhysRevLett.109.075001`.

[43] John F. Hansen, S. K. P. Tripathi, and Paul M. Bellan. "Co- and counter-helicity interaction between two adjacent laboratory prominences". In: *Physics of Plasmas* 11.6 (2004), pp. 3177–3185. DOI: `10.1063/1.1724831`.

[44] Paul M. Bellan. "Thermal instability of electrolytic capacitor bank used for gas puff valve". In: *Review of Scientific Instruments* 73.8 (2002), pp. 2900–2905. DOI: `http://dx.doi.org/10.1063/1.1488677`.

[45] A. Kramida et al. NIST Atomic Spectra Database (ver. 5.3), [Online]. Available: `http://physics.nist.gov/asd` [2016, October 12]. National Institute of Standards and Technology, Gaithersburg, MD. 2015.

[46] S. You, G. S. Yun, and Paul M. Bellan. "Dynamic and Stagnating Plasma Flow Leading to Magnetic-Flux-Tube Collimation". In: *Phys. Rev. Lett.* 95 (4 July 2005), p. 045002. DOI: `10.1103/PhysRevLett.95.045002`.

[47] K. G. Puschmann, B. Ruiz Cobo, and V. Martínez Pillet. "The Electrical Current Density Vector in the Inner Penumbra of a Sunspot". In: *The Astrophysical Journal Letters* 721.1 (2010), p. L58. URL: http://stacks.iop.org/2041-8205/721/i=1/a=L58.

[48] D. Orozco Suárez, A. Asensio Ramos, and J. Trujillo Bueno. "The magnetic field configuration of a solar prominence inferred from spectropolarimetric observations in the He I 10 830 A triplet". In: *A&A* 566 (June 2014). DOI: 10.1051/0004-6361/201322903. arXiv: 1403.7976 [astro-ph.SR].

[49] Shengtai Li and Hui Li. *Los Alamos National Lab*. Tech. rep. LA-UR-03-8935, 2003.

[50] M. Tokman and Paul M. Bellan. "Three-dimensional Model of the Structure and Evolution of Coronal Mass Ejections". In: *The Astrophysical Journal* 567.2 (2002), p. 1202. DOI: 10.1086/338699.

[51] Gunsu S. Yun and Paul M. Bellan. "Plasma tubes becoming collimated as a result of magnetohydrodynamic pumping". In: *Physics of Plasmas* 17.6, 062108 (2010). DOI: http://dx.doi.org/10.1063/1.3437075.

[52] James Simpson et al. "Simple Analytic Expressions for the Magnetic Field of a Circular Current Loop". In: *NASA technical documents* (2001).

[53] John F. Hansen and Paul M. Bellan. "Experimental Demonstration of How Strapping Fields Can Inhibit Solar Prominence Eruptions". In: *The Astrophysical Journal Letters* 563.2 (2001), p. L183. DOI: 10.1086/338736.

[54] Bao N. Ha and Paul M. Bellan. "Laboratory demonstration of slow rise to fast acceleration of arched magnetic flux ropes". In: *Geophysical Research Letters* 43.18 (2016), pp. 9390–9396. ISSN: 1944-8007. DOI: 10.1002/2016GL069744.

[55] L. Arnold et al. "Three-dimensional magnetohydrodynamical simulation of expanding magnetic flux ropes". In: *Physics of Plasmas* 15.4 (2008), p. 042106. DOI: 10.1063/1.2903904.

[56] C. E. Myers et al. "Laboratory study of low-β forces in arched, line-tied magnetic flux ropes". In: *Physics of Plasmas* 23.11 (2016), p. 112102. DOI: 10.1063/1.4966691.

[57] SKP Tripathi and W Gekelman. "Dynamics of an Erupting Arched Magnetic Flux Rope in a Laboratory Plasma Experiment." In: *Solar Physics* 286.2 (2013), pp. 479–492. ISSN: 00380938. DOI: 10.1007/s11207-013-0257-0.

[58] F. Suzuki-Vidal et al. "Interaction of radiatively cooled plasma jets with neutral gases for laboratory astrophysics studies". In: *High Energy Density Physics* 9.1 (2013), pp. 141–147. ISSN: 1574-1818. DOI: http://doi.org/10.1016/j.hedp.2012.11.003.

[59]   R. Raman et al. "Design and operation of a fast electromagnetic inductive massive gas injection valve for NSTX-U". In: *Review of Scientific Instruments* 85.11 (2014), 11E801. DOI: `10.1063/1.4885545`.

[60]   Keith T. K. Loebner, Thomas C. Underwood, and Mark A. Cappelli. "A fast rise-rate, adjustable-mass-bit gas puff valve for energetic pulsed plasma experiments". In: *Review of Scientific Instruments* 86.6 (2015), p. 063503. DOI: `10.1063/1.4922522`.

[61]   T. Onchi et al. "Design and implementation of fast charging circuit for repetitive compact torus injector". In: *Fusion Engineering and Design* 89.11 (2014), pp. 2559–2565. ISSN: 0920-3796. DOI: `http://doi.org/10.1016/j.fusengdes.2014.06.019`.

[62]   María M. Milanese et al. "Fast valve and nozzle for gas-puff operation of dense plasma focus". In: *Review of Scientific Instruments* 77.3 (2006), p. 036106. DOI: `10.1063/1.2169535`.

[63]   H Soltwisch et al. "FlareLab: early results". In: *Plasma Physics and Controlled Fusion* 52.12 (2010), p. 124030. DOI: `10.1088/0741-3335/52/12/124030`.

[64]   Jimmy Yee. "Experimental investigations in spheromaks: injection into a tokamak and formation in an unbounded environment". PhD thesis. Caltech, 1999. URL: `http://resolver.caltech.edu/CaltechETD:etd-08302005-134459`.

[65]   A.F. Ismail, K. Khulbe, and T. Matsuura. *Gas Separation Membranes: Polymeric and Inorganic*. Springer International Publishing, 2015. ISBN: 9783319010953. URL: `https://books.google.com/books?id=n2u6CAAAQBAJ`.

[66]   Scott Matteucci et al. "Transport of Gases and Vapors in Glassy and Rubbery Polymers". In: *Materials Science of Membranes for Gas and Vapor Separation*. John Wiley & Sons, Ltd, 2006, pp. 1–47. ISBN: 9780470029039. DOI: `10.1002/047002903X.ch1`.

[67]   J Tenfelde et al. "On the relevance of magnetohydrodynamic pumping in solar coronal loop simulation experiments". In: *Physics of Plasmas* 19.7 (2012), p. 072513. DOI: `10.1063/1.4737581`.

[68]   F Mackel et al. "Evolution of plasma loops in a semi-toroidal pinch experiment". In: *Physics of Plasmas* 22.4 (2015), p. 042502. DOI: `10.1063/1.4916506`.

[69]   Mackel. "Dynamic behaviour of magnetic flux tubes in laboratory simulations of solar flares". PhD thesis. Ruhr-Universität Bochum, 2014.

[70]   Spiros Patsourakos and Jean-Claude Vial. "SOHO Contribution to Prominence Science". In: *Solar Physics* 208.2 (2002), pp. 253–281. ISSN: 1573-093X. DOI: `10.1023/A:1020510120772`.

[71] I. Arregui and R. Soler. "Model comparison for the density structure along solar prominence threads". In: *Astronomy and Astrophysics* 578, A130 (June 2015), A130. DOI: 10.1051/0004-6361/201525720. arXiv: 1505.03448 [astro-ph.SR].

[72] N. Labrosse et al. "Physics of Solar Prominences: I- Spectral Diagnostics and Non-LTE Modelling". In: *Space Science Review* 151 (Apr. 2010), pp. 243–332. DOI: 10.1007/s11214-010-9630-6. arXiv: 1001.1620 [astro-ph.SR].

[73] Chaowei Jiang et al. "Formation and Eruption of an Active Region Sigmoid. I. A Study by Nonlinear Force-free Field Modeling". In: *The Astrophysical Journal* 780.1 (2014), p. 55. DOI: 10.1088/0004-637X/780/1/55.

[74] Satoshi Inoue. "Magnetohydrodynamics modeling of coronal magnetic field and solar eruptions based on the photospheric magnetic field". In: *Progress in Earth and Planetary Science* 3.1 (2016), p. 19. ISSN: 2197-4284. DOI: 10.1186/s40645-016-0084-7.

[75] P. Heinzel and U. Anzer. "Magnetic Dips in Prominences". In: *Solar Physics* 184.1 (1999), pp. 103–111. ISSN: 1573-093X. DOI: 10.1023/A:1005098704665.

[76] S. Gunár et al. "Non-linear force-free magnetic dip models of quiescent prominence fine structures". In: *Astronomy and Astrophysics* 551, A3 (Mar. 2013), A3. DOI: 10.1051/0004-6361/201220597.

[77] S. K. Antiochos, P. J. MacNeice, and D. S. Spicer. "The Thermal Nonequilibrium of Prominences". In: *The Astrophysical Journal* 536.1 (2000), p. 494. DOI: 10.1086/308922.

[78] M. Nakamura, Y. Uchida, and S. Hirose. "Production of wiggled structure of AGN radio jets in the sweeping magnetic twist mechanism". In: *New Astronomy* 6.2 (2001), pp. 61–78. ISSN: 1384-1076. DOI: http://dx.doi.org/10.1016/S1384-1076(01)00041-0.

[79] S. C. Hsu and P. M. Bellan. "Experimental Identification of the Kink Instability as a Poloidal Flux Amplification Mechanism for Coaxial Gun Spheromak Formation". In: *Phys. Rev. Lett.* 90 (21 May 2003), p. 215002. DOI: 10.1103/PhysRevLett.90.215002.

[80] K. Saito and C. L. Hyder. "A Concentric Ellipse Multiple-Arch System in the Solar Corona". In: *Solar Physics* 5 (Sept. 1968), pp. 61–86. DOI: 10.1007/BF00147121.

[81] T. G. Forbes et al. "CME Theory and Models". In: *Space Science Reviews* 123.1 (Mar. 2006), pp. 251–302. ISSN: 1572-9672. DOI: 10.1007/s11214-006-9019-8.

[82] P. F. Chen. "Coronal Mass Ejections: Models and Their Observational Basis". In: *Living Reviews in Solar Physics* 8.1 (Apr. 2011), p. 1. ISSN: 1614-4961. DOI: 10.12942/lrsp-2011-1.

[83] James Chen. "Physics of erupting solar flux ropes: Coronal mass ejections (CMEs)—Recent advances in theory and observation". In: *Physics of Plasmas* 24.9 (2017), p. 090501. DOI: 10.1063/1.4993929.

[84] J. Chen. "Effects of toroidal forces in current loops embedded in a background plasma". In: *The Astrophysical Journal* 338 (Mar. 1989), pp. 453–470. DOI: 10.1086/167211.

[85] A. S. Savcheva et al. "Photospheric Flux Cancellation and the Build-up of Sigmoidal Flux Ropes on the Sun". In: *The Astrophysical Journal* 759.2 (2012), p. 105. DOI: 10.1088/0004-637X/759/2/105.

[86] B. J. Lynch et al. "Observable Properties of the Breakout Model for Coronal Mass Ejections". In: *The Astrophysical Journal* 617.1 (2004), p. 589. DOI: 10.1086/424564.

[87] B. C. Low and J. R. Hundhausen. "Magnetostatic structures of the solar corona. 2: The magnetic topology of quiescent prominences". In: *The Astrophysical Journal* 443 (Apr. 1995), pp. 818–836. DOI: 10.1086/175572.

[88] Sarah Gibson. "Coronal Cavities: Observations and Implications for the Magnetic Environment of Prominences". In: *Solar Prominences*. Cham: Springer International Publishing, 2015, pp. 323–353. ISBN: 978-3-319-10416-4. DOI: 10.1007/978-3-319-10416-4_13.

[89] D. Maričić, B. Vršnak, and D. Roša. "Relative Kinematics of the Leading Edge and the Prominence in Coronal Mass Ejections". In: *Solar Physics* 260 (Nov. 2009), pp. 177–189. DOI: 10.1007/s11207-009-9421-y.

[90] D. J. Schmit et al. "Prominence Mass Supply and the Cavity". In: *The Astrophysical Journal* 779, 156 (Dec. 2013), p. 156. DOI: 10.1088/0004-637X/779/2/156. arXiv: 1311.2382 [astro-ph.SR].

[91] D. Schmit and S. Gibson. "The Formation of a Cavity in a 3D Flux Rope". In: *Nature of Prominences and their Role in Space Weather*. Ed. by B. Schmieder, J.-M. Malherbe, and S. T. Wu. Vol. 300. IAU Symposium. Jan. 2014, pp. 147–150. DOI: 10.1017/S1743921313010880. arXiv: 1311.2384 [astro-ph.SR].

[92] J. Fuller et al. "Observing the Unobservable? Modeling Coronal Cavity Densities". In: *The Astrophysical Journal* 678.1 (2008), p. 515. DOI: 10.1086/533527.

[93] J. Fuller and S. E. Gibson. "A Survey of Coronal Cavity Density Profiles". In: *The Astrophysical Journal* 700.2 (2009), p. 1205. DOI: 10.1088/0004-637X/700/2/1205.

[94] S. E. Gibson et al. "Three-dimensional Morphology of a Coronal Prominence Cavity". In: *The Astrophysical Journal* 724 (Dec. 2010), pp. 1133–1146. DOI: 10.1088/0004-637X/724/2/1133.

[95]   B. C. Forland et al. "Coronal Cavity Survey: Morphological Clues to Erup-
         tive Magnetic Topologies". In: *Solar Physics* 288 (Dec. 2013), pp. 603–615.
         DOI: 10.1007/s11207-013-0361-1.

[96]   Pakorn Wongwaitayakornkul et al. "Apex Dips of Experimental Flux Ropes:
         Helix or Cusp?" In: *The Astrophysical Journal* 848.2 (2017), p. 89. DOI:
         10.3847/1538-4357/aa8990.

[97]   B. Kliem and T. Török. "Torus Instability". In: *Physical Review Letters*
         96.25, 255002 (June 2006), p. 255002. DOI: 10.1103/PhysRevLett.96.
         255002. eprint: physics/0605217.

[98]   George C. Vlases. "Experiments in a Cylindrical Magnetic Shock Tube".
         PhD thesis. Caltech, 1963. URL: http://resolver.caltech.edu/
         CaltechTHESIS:10092012-110749746.

[99]   Alan Lowell Hoffman. "Magnetohydrodynamic shock production and cur-
         rent sheet diffusion". PhD thesis. Caltech, 1967. URL: http://resolver.
         caltech.edu/CaltechETD:etd-12292005-135853.

[100]   Carl Greifinger and Julian D Cole. "On cylindrical magnetohydrodynamic
         shock waves". In: *The Physics of Fluids* 4.5 (1961), pp. 527–534. DOI:
         10.1063/1.1706358.

[101]   T. G. Forbes. "A review on the genesis of coronal mass ejections". In: *Journal
         of Geophysical Research: Space Physics (1978–2012)* 105.A10 (Oct. 2000),
         pp. 23153–23165. ISSN: 2156-2202. DOI: 10.1029/2000JA000005.

[102]   T. Török and B. Kliem. "The evolution of twisting coronal magnetic flux
         tubes". In: *Astronomy and Astrophysics* 406 (Aug. 2003), pp. 1043–1059.
         DOI: 10.1051/0004-6361:20030692.

[103]   C. Delannée et al. "A New Model for Propagating Parts of EIT Waves: A
         Current Shell in a CME". In: *Solar Physics* 247.1 (Jan. 2008), pp. 123–150.
         DOI: 10.1007/s11207-007-9085-4.

[104]   Xiaozhou Zhao et al. "Formation and Initiation of Erupting Flux Rope
         and Embedded Filament Driven by Photospheric Converging Motion". In:
         The Astrophysical Journal 841.106 (2017), 21pp. DOI: 10.3847/1538-
         4357/aa7142.

[105]   T. Amari et al. "Coronal Mass Ejection Initiation: On the Nature of the Flux
         Cancellation Model". In: *Astrophysical Journal Letters* 717 (July 2010),
         pp. L26–L30. DOI: 10.1088/2041-8205/717/1/L26. arXiv: 1005.4669
         [astro-ph.SR].

[106]   Bernhard Kliem et al. "Rapid CME Cavity Formation and Expansion". In:
         American Astronomical Society Meeting Abstracts# 224. Vol. 224. 2014.

[107]   Carl Greifinger and Julian D. Cole. "On Cylindrical Magnetohydrodynamic
         Shock Waves". In: *The Physics of Fluids* 4.5 (1961), pp. 527–534. DOI:
         10.1063/1.1706358.

[108]   D. J. F. Maia et al. "The Radio-Coronal Mass Ejection Event on 2001 April 15". In: *The Astrophysical Journal* 660 (May 2007), pp. 874–881. DOI: 10.1086/508011.

[109]   T. S. Bastian et al. "The Coronal Mass Ejection of 1998 April 20: Direct Imaging at Radio Wavelengths". In: *The Astrophysical Journal Letters* 558 (Sept. 2001), pp. L65–L69. DOI: 10.1086/323421.

[110]   A. Vourlidas et al. "Comprehensive Analysis of Coronal Mass Ejection Mass and Energy Properties Over a Full Solar Cycle". In: *The Astrophysical Journal* 722.2 (2010), p. 1522. DOI: 10.1088/0004-637X/722/2/1522.

[111]   Y.-M. Wang and G. Stenborg. "Spinning Motions in Coronal Cavities". In: *The Astrophysical Journal Letters* 719.2 (2010), p. L181. DOI: 10.1088/2041-8205/719/2/L181.

[112]   Xing Li et al. "A Solar Tornado Observed by AIA/SDO: Rotational Flow and Evolution of Magnetic Helicity in a Prominence and Cavity". In: *The Astrophysical Journal Letters* 752.2 (2012), p. L22. DOI: 10.1088/2041-8205/752/2/L22.

[113]   D. J. Schmit et al. "Prominence Mass Supply and the Cavity". In: *The Astrophysical Journal* 779, 156 (Dec. 2013), p. 156. DOI: 10.1088/0004-637X/779/2/156. arXiv: 1311.2382 [astro-ph.SR].

[114]   J. B. Dove et al. "A Ring of Polarized Light: Evidence for Twisted Coronal Magnetism in Cavities". In: *The Astrophysical Journal Letters* 731.1 (2011), p. L1. DOI: 10.1088/2041-8205/731/1/L1.

[115]   Urszula Bąk-Stęślicka et al. "The Magnetic Structure of Solar Prominence Cavities: New Observational Signature Revealed by Coronal Magnetometry". In: *The Astrophysical Journal Letters* 770.2 (2013), p. L28. DOI: 10.1088/2041-8205/770/2/L28.

[116]   PW Schuck. "The photospheric energy and helicity budgets of the flux-injection hypothesis". In: *The Astrophysical Journal* 714.1 (2010), p. 68. DOI: 10.1088/0004-637X/714/1/68.

[117]   Kil-Byoung Chai, Xiang Zhai, and Paul M. Bellan. "Extreme ultra-violet burst, particle heating, and whistler wave emission in fast magnetic reconnection induced by kink-driven Rayleigh-Taylor instability". In: *Physics of Plasmas* 23.3 (2016), p. 032122. DOI: 10.1063/1.4944390.

[118]   Paul M. Bellan. "Revised single-spacecraft method for determining wave vector k and resolving space-time ambiguity". In: *Journal of Geophysical Research: Space Physics* 121.9 (2016), pp. 8589–8599. ISSN: 2169-9402. DOI: 10.1002/2016JA022827.

[119]   Daniel J. Gershman et al. "Wave-particle energy exchange directly observed in a kinetic Alfvén-branch wave". In: *Nature Communications* 8 (2017), p. 14719. DOI: 10.1038/ncomms14719.

[120] E. E. Fenimore and T. M. Cannon. "Coded aperture imaging with uniformly redundant arrays". In: *Appl. Opt.* 17.3 (Feb. 1978), pp. 337–347. DOI: `10.1364/AO.17.000337`.

[121] R. H. Dicke. "Scatter-Hole Cameras for X-Rays and Gamma Rays". In: *The Astrophysical Journal, Letters* 153 (Aug. 1968), p. L101. DOI: `10.1086/180230`.

[122] L. Mertz and NO Young. "Fresnel transformations of images". In: *SPIE Milestone Series* 128 (1996), pp. 44–49.

[123] Roberto Accorsi. "Design of a near-field coded aperture cameras for high-resolution medical and industrial gamma-ray imaging". PhD thesis. MIT, May 2001. URL: `http://hdl.handle.net/1721.1/8684`.

[124] Alireza Talebitaher et al. "Imaging of Plasma Focus Fusion by Proton Coded Aperture Technique". English. In: *Journal of Fusion Energy* 31.3 (2012), pp. 234–241. ISSN: 0164-0313. DOI: `10.1007/s10894-011-9462-8`.

[125] M. E. Gehm et al. "Static two-dimensional aperture coding for multimodal, multiplex spectroscopy". In: *Applied Optics* 45 (May 2006), pp. 2965–2974. DOI: `10.1364/AO.45.002965`.

[126] A. Haboub et al. "Coded aperture imaging for fluorescent x-rays". In: *Review of Scientific Instruments* 85.6 (2014). DOI: `10.1063/1.4882337`.

[127] Leonard D. Baumert. *Digital Communications with Space Applications: Appendix 2*. Englewood Cliffs, NJ: Prentice-Hall Inc., 1964.

[128] E. D. Nelson and M. L. Fredman. "Hadamard Spectroscopy". In: *J. Opt. Soc. Am.* 60.12 (Dec. 1970), pp. 1664–1669. DOI: `10.1364/JOSA.60.001664`.

[129] Roberto Accorsi, Francesca Gasparini, and Richard C Lanza. "Optimal coded aperture patterns for improved {SNR} in nuclear medicine imaging". In: *Nuclear Instruments and Methods in Physics Research Section A: Accelerators, Spectrometers, Detectors and Associated Equipment* 474.3 (2001), pp. 273–284. DOI: `10.1016/S0168-9002(01)01326-2`.

[130] Deepak Kumar and Paul M. Bellan. "Nonequilibrium Alfvénic Plasma Jets Associated with Spheromak Formation". In: *Phys. Rev. Lett.* 103 (10 Sept. 2009), p. 105003. DOI: `10.1103/PhysRevLett.103.105003`.

[131] Yen-Wei Chen and Keisaku Kishimoto. "Tomographic resolution of uniformly redundant arrays coded aperture". In: *Review of Scientific Instruments* 74.3 (2003), pp. 2232–2235. DOI: `http://dx.doi.org/10.1063/1.1537860`.

[132] A. L. Moser and P. M. Bellan. "Magnetic reconnection from a multiscale instability cascade". In: *Nature* 482 (Feb. 2012), pp. 379–381. DOI: `10.1038/nature10827`.

[133]   Paul M. Bellan. *Fundamentals of Plasma Physics*. The Edinburgh Building, Cambridge CB2 8RU, UK: Cambridge University Press, 2006. ISBN: 978-0-521-82116-2.

[134]   Friedrich Paschen. "Ueber die zum Funkenübergang in Luft, Wasserstoff und Kohlensäure bei verschiedenen Drucken erforderliche Potentialdifferenz". In: *Annalen der Physik* 273.5 (1889), pp. 69–96. ISSN: 1521-3889. DOI: 10.1002/andp.18892730505.

[135]   John S. Townsend. *The Theory of Ionization of Gases by Collision*. 23 Murray Street, New York: D. Van Nostrand Company, 1910.

[136]   *scipy.interpolate.griddata*. Enthought. 2016. URL: http://docs.scipy.org/doc/scipy-0.17.0/reference/generated/scipy.interpolate.griddata.html (visited on).

A p p e n d i x   A

PLASMA PHYSICS 101

This appendix covers the basic topics in plasma theory relevant to understanding the subject matter of this thesis. These topics are the quantitative definition of plasmas (Debye shielding), the three basic plasma descriptions (particle, two-fluid, single-fluid), and several aspects of the single-fluid description also known as magnetohydrodynamics or MHD (frozen-in flux, $\mathbf{J} \times \mathbf{B}$ force). Understanding these various descriptions is important because many problems in plasma physics involve dynamics at multiple length and time scales (e.g. ion scales, electron scales, and the system scale). This multi-scale nature is in part due to the large mass ratio $m_i/m_e = 1823M$ between ions and electrons where M is the ion atomic weight.

It is expected that the reader is reasonably familiar with Maxwell's equations, vector calculus, differential equations, statistical mechanics, and classical mechanics. More in-depth explanations of these topics can be found in plasma textbooks [133].

A.1 Quantitative definition of plasma

Although plasma physics is usually defined as the study of ionized gases, there is an additional condition necessary for an ionized gas to be considered a plasma. This condition is that the gas must be of sufficient density and temperature to exhibit collective, statistically relevant behavior. In other words, one electron does not a plasma make. The threshold for this collective behavior is characterized by the electrostatic shielding or screening length scale of an ionized gas, also known as the Debye length λ_D. If an ionized gas spans many Debye lengths ($L \gg \lambda_D$), it can be considered a plasma.

The Debye length for a given ionized gas is determined by the temperature and density of each charged species, denoted by σ (e.g. ions $\sigma = i$, electrons $\sigma = e$),

$$\lambda_\sigma^2 = \frac{\epsilon_0 \kappa T_\sigma}{n_\sigma q_\sigma^2} \tag{A.1}$$

$$\frac{1}{\lambda_D^2} = \sum_\sigma \frac{1}{\lambda_\sigma^2}. \tag{A.2}$$

Denser plasmas have a stronger shielding effect and thinner shielding layers or sheaths. Due to this shielding property, electric fields cannot exist in steady-state

plasmas on length scales larger than a few Debye lengths. Table A.1 shows the density, temperature and Debye lengths for a wide range of plasmas. These lengths are significant because they define a minimum length scale for plasma

	n	T	λ_D	l_{mfp}	L
units	m^{-3}	eV	m	m	m
Solar corona (loops)	10^{15}	100	10^{-3}	10^5	10^8
Solar wind (near Earth)	10^7	10	10	10^{11}	10^{11}
Magnetosphere (tail lobe)	10^4	10	100	10^{14}	10^8
Mag. fusion (tokamak)	10^{20}	10^4	10^{-4}	10^4	10
Lab plasma (dense)	10^{20}	5	10^{-6}	10^{-2}	10^{-1}
Lab plasma (diffuse)	10^{16}	5	10^{-4}	10	10^{-1}

Table A.1: Comparison of plasma parameters (density n, temperature T, Debye length λ_D, collisional mean-free-path l_{mfp}, and system length scale L) in different regimes. Adapted from [133]

A.2 Particle description

When a plasma passes the Debye threshold, it has a statistically significant number of particles at each position and can be described by a velocity distribution function, $f_\sigma(\mathbf{x}, \mathbf{v}, t)$. This function characterizes the distribution of particle velocities $\mathbf{v}$ at all locations $\mathbf{x}$ as a function of time. This distribution description is called plasma kinetic theory and it evolves according to the Vlasov equation,

$$\frac{\partial f_\sigma}{\partial t} + \mathbf{v} \cdot \nabla f_\sigma + \nabla_v \cdot (\mathbf{a} f_\sigma) = C \tag{A.3}$$

where $\mathbf{v}$ is velocity, $\mathbf{a} = (q_\sigma/m_\sigma)(\mathbf{E} + \mathbf{v} \times \mathbf{B})$ is the Lorentz force, and C is a collision operator. This description is necessary to describe plasma where fluid descriptions break down (e.g. where the particle velocity distribution is far from Maxwellian). Although it provides an excellent description of plasma behavior (given a reasonable collision operator), it is too costly to simulate at macroscopic scales. However, at macroscopic length and time scales, non-Maxwellian effects tend to average to zero and fluid descriptions are generally valid. Figure A.1 show the relevant length and time scales for the particle and fluid descriptions.

A.3 Two-fluid approximation

The next simplest model is the two-fluid approximation which models plasma as a pair of superimposed electron and ion fluids. This description takes an average of the particle velocities at a given position to obtain a fluid center-of-mass velocity
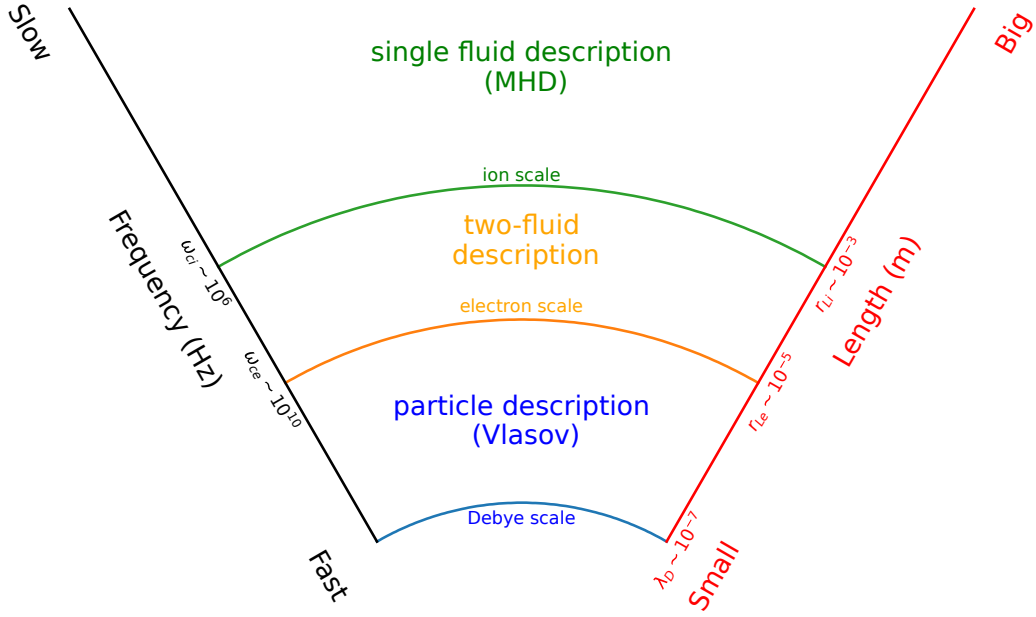
Figure A.1: Diagram of the frequency and length scales where different plasma descriptions are commonly used. Larmor radii and cyclotron frequencies are listed for a typical laboratory hydrogen plasma with B=0.06 T, n=10^{21} m^{-3}, and T=2 eV. Additional length and frequency scales are provided in section 1.2.

$\mathbf{u}_\sigma$ and a density n_σ for each species,

$$n_\sigma(\mathbf{x}, t) = \int f_\sigma(\mathbf{x}, \mathbf{v}, t) \, d^3 v \tag{A.4}$$

$$\mathbf{u}_\sigma(\mathbf{x}, t) = \frac{1}{n_\sigma(\mathbf{x}, t)} \int \mathbf{v} f_\sigma(\mathbf{x}, \mathbf{v}, t) \, d^3 v \tag{A.5}$$

This approximation results in the following set of equations:

- Continuity equation for each species

$$\frac{\partial n_\sigma}{\partial t} + \nabla \cdot (n_\sigma \mathbf{u}_\sigma) = 0, \tag{A.6}$$

- Equation of motion for each species

$$n_\sigma m_\sigma \frac{D\mathbf{u}_\sigma}{Dt} = n_\sigma q_\sigma (\mathbf{E} + \mathbf{v} \times \mathbf{B}) - \nabla P_\sigma - \mathbf{R}_{\sigma\alpha} \tag{A.7}$$

where $\mathbf{R}_{\sigma\alpha}$ is the interspecies collisional drag.

- Equation of state for each species

Equation of state	Name
$P_\sigma \propto n_\sigma^\gamma$	adiabatic
$P_\sigma = n_\sigma \kappa T_\sigma,\ T_\sigma$=constant	isothermal

- Maxwell's equations

$$\nabla \cdot \mathbf{E} = \frac{1}{\epsilon_0} \sum_\sigma n_\sigma q_\sigma \tag{A.8}$$

$$\nabla \cdot \mathbf{B} = 0 \tag{A.9}$$

$$\nabla \times \mathbf{E} = -\frac{\partial \mathbf{B}}{\partial t} \tag{A.10}$$

$$\nabla \times \mathbf{B} = \mu_0 \sum_\sigma n_\sigma q_\sigma \mathbf{u}_\sigma + \mu_0 \epsilon_0 \frac{\partial \mathbf{E}}{\partial t} \tag{A.11}$$

It is this two fluid description that will be used in Chapter 8 to characterize measurements of plasma wave modes.

A.4 Magnetohydrodynamics (MHD)

Magnetohydrodynamics (MHD) is the simplest, most used approximation of plasma behavior. It is a mass weighted average of two-fluid equations and describes the plasma as a single conductive fluid with no net charge. This approximation is valid for slow, large scale phenomenon. Quantitatively this means that MHD can only resolve dynamics slower the the ion cyclotron frequency $\omega \ll q_i B/m_i$, at length scales which are longer than the ion skin depth, $L \gg \sqrt{\frac{m_i}{\mu_0 n_i q_i^2}}$.

The standard set of MHD equations is as follows:

- Continuity equation

$$\frac{\partial \rho}{\partial t} + \nabla \cdot (\rho \mathbf{U}) = 0, \tag{A.12}$$

- Equation of motion

$$\rho \frac{D\mathbf{U}}{Dt} = \mathbf{J} \times \mathbf{B} - \nabla P \tag{A.13}$$

- Equation of state for each species

Equation of state	Name
$P \propto \rho^\gamma$	adiabatic
$P = \rho \kappa T / m_i,\ T$=constant	isothermal
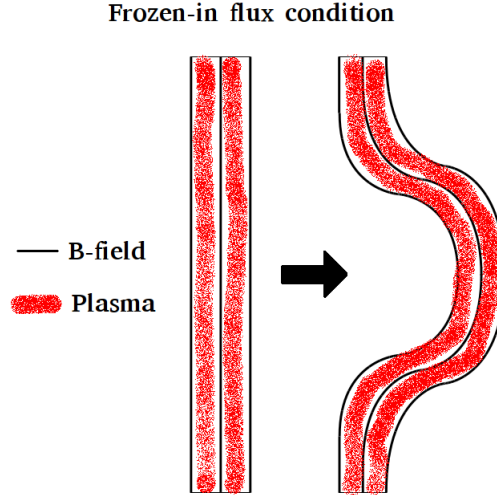
Figure A.2: Illustration of the frozen-in flux property of ideal MHD ($\eta = 0$). The motion of the plasma induces internal currents such that the magnetic flux convects with the plasma motion.

- Maxwell's equations

$$\nabla \cdot \mathbf{E} = 0 \tag{A.14}$$

$$\nabla \cdot \mathbf{B} = 0 \tag{A.15}$$

$$\nabla \times \mathbf{E} = -\frac{\partial \mathbf{B}}{\partial t} \tag{A.16}$$

$$\nabla \times \mathbf{B} = \mu_0 \mathbf{J} \tag{A.17}$$

- Ohm's law

$$\mathbf{E} + \mathbf{U} \times \mathbf{B} = \eta \mathbf{J} \tag{A.18}$$

where $\rho = \sum_\sigma m_\sigma n_\sigma$, $\mathbf{U} = \sum_\sigma m_\sigma n_\sigma \mathbf{u}_\sigma$, $\mathbf{J} = \sum_\sigma n_\sigma q_\sigma \mathbf{u}_\sigma$, and η is the electrical resistivity.

Ideal MHD and frozen-in flux

In many plasma systems, the resistivity η is negligible and the plasma can be treated as a superconducting gas. This assumption $\eta \sim 0$ is called "Ideal MHD" and exhibits the so-called frozen-in flux condition. This condition preserves the magnetic flux of a given fluid element in motion; in other words, the magnetic flux convects with the fluid motion (Fig. A.2). This property can be demonstrated by taking the curl

of Eq. A.18 giving the induction equation,

$$\frac{\partial \mathbf{B}}{\partial t} = \nabla \times (\mathbf{U} \times \mathbf{B}) - \frac{\eta}{\mu_0} \nabla^2 \mathbf{B}. \tag{A.19}$$

The second term is easily recognized as a diffusion term related to the plasma resistivity. If this term is ignorable, then the magnetic flux $\Phi(t)$ through any closed contour $C(t)$ with surface $S(t)$ moving with the plasma velocity, is constant,

$$\Phi(t) = \int_{S(t)} \mathbf{B} \cdot d\mathbf{s} \tag{A.20}$$

$$\frac{D\Phi}{Dt} = \int_{S(t)} \frac{\partial \mathbf{B}}{\partial t} \cdot d\mathbf{s} - \oint_{C(t)} \mathbf{U} \times \mathbf{B} \cdot d\mathbf{l} \tag{A.21}$$

$$= \int_{S(t)} \left[\frac{\partial \mathbf{B}}{\partial t} - \nabla \times (\mathbf{U} \times \mathbf{B}) \right] \cdot d\mathbf{s} \tag{A.22}$$

$$= 0. \tag{A.23}$$

For those familiar with fluid dynamics, rearrangement of Eq. A.19 using vector identities gives,

$$\frac{D\mathbf{B}}{Dt} = (\mathbf{B} \cdot \nabla)\mathbf{U} - \mathbf{B}(\nabla \cdot \mathbf{U}) - \frac{\eta}{\mu_0} \nabla^2 \mathbf{B}, \tag{A.24}$$

which matches the conventional form of the vorticity transport equation.

The $\mathbf{J} \times \mathbf{B}$ force

The plasmas in this thesis are mainly driven by magnetic forces rather than pressure forces $\mathbf{J} \times \mathbf{B}/\nabla P \geq 1$. This does not imply that pressure can be ignored but it is important to give special attention to the $\mathbf{J} \times \mathbf{B}$ force. Several common approaches to understanding this force are described below to give some intuition for magnetically dominated motion.

1. **Recast in terms of the magnetic field**: this most popular representation decomposes the $\mathbf{J} \times \mathbf{B}$ force into a magnetic tension and magnetic pressure force,

$$\mathbf{J} \times \mathbf{B} = \frac{1}{\mu_0} \left[-\nabla_\perp \left(\frac{B^2}{2} \right) + B^2 \kappa \right], \tag{A.25}$$

$$\kappa = \hat{B} \cdot \nabla \hat{B} = -\hat{R}/R, \tag{A.26}$$

where R is the local radius of curvature of the magnetic field and $\nabla_\perp$ is the gradient component perpendicular to the local magnetic field. These pressure and tension forces are written in such a way to exclude components parallel to $\mathbf{B}$ as such components must inevitably cancel.

2. **Parallel currents attract, anti-parallel currents repel**: This view recasts the force as the interaction of various currents. This requires knowledge of where all currents are flowing including those outside the domain of interest. For a given current path with total current I, the force on a given cross-section can be described like the magnetic force on a wire,

$$\int_S \mathbf{J} \times \mathbf{B} \cdot d\mathbf{S} = I \, d\hat{r} \times \mathbf{B}. \tag{A.27}$$

3. **Gradient of magnetic energy**: Due to the frozen-in flux condition of most plasmas of interest, the magnetic flux Φ in a plasma tends to be well conserved over time. However, even when flux is conserved, the total magnetic energy can still decrease. The magnetic energy of a closed current can be expressed as,

$$W = \frac{1}{2} \int_V \mathbf{A} \cdot \mathbf{J} \, d^3 r = \frac{\Phi^2}{2L} \tag{A.28}$$

where $L = \Phi/I$ is the system inductance. Consequently, magnetic forces act to increase system inductance subject to the constraint of constant Φ,

$$\mathbf{F}_{\text{mag}} \sim -\frac{\Phi^2}{2} \nabla \left(\frac{1}{L} \right). \tag{A.29}$$
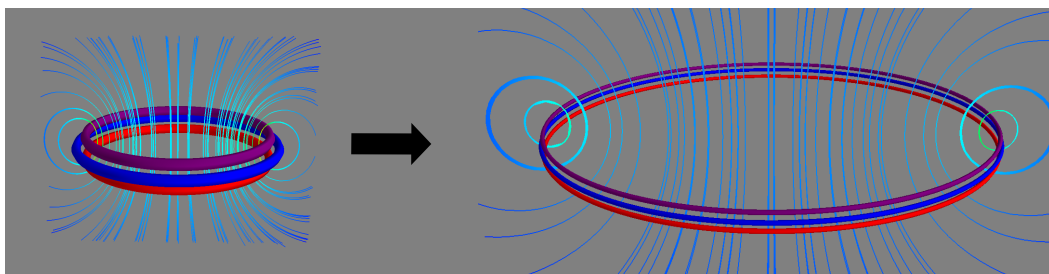
Figure A.3: Evolution of three circular current channels with parallel currents. Magnetic forces tend to both collimate parallel currents (minor radius pinches) as well as expand the loop major radius (hoop force).

Figure A.3 displays the evolution of three circular current loops with parallel current. The $\mathbf{J} \times \mathbf{B}$ force collimates the minor radius (pinch effect) as well as expands the major radius (hoop force). In this system, recasting the force in terms of the magnetic pressure and tension gives little insight since the magnetic tension and pressure exactly cancel everywhere except inside the current paths. Consequently

the relative direction and magnitude of the sum of the two forces are difficult to determine without detailed calculation.

Conversely, thinking of the system in terms of currents provides a much more intuitive understanding. The parallel currents attract, collimating the minor radius, and the anti-parallel currents on opposite sides of the circles repel, expanding the major radius.

Energy considerations also can also explain the evolution in simple terms: narrowing the minor radius and expanding the major radius both increase inductance, moving the system to a lower energy state.

Each of these perspectives can provide insight in different circumstances and this thesis will attempt to explain the relevant plasma dynamics using the most intuitive representation for each situation.

A.5 Plasma scales

For different approximations, including MHD, it is important to know if a process is fast or slow, and whether it is macroscopic or microscopic. These determinations are made with respect to certain frequencies and length scales.

- **Cyclotron frequencies**: frequency with which a given species, σ, orbits the local magnetic field. Particle cyclotron motion is often described as perpendicular motion (i.e. perpendicular relative to the local magnetic field).

$$\omega_{c\sigma} = \frac{q_\sigma |B|}{m_\sigma}$$

- **Plasma frequencies**: frequency at which global plasma oscillations are supported by the electrostatic restoring force of the local charge density. Electromagnetic waves with frequency lower than the electron plasma frequency are reflected (e.g. mirrors, radio reflection from ionosphere).

$$\omega_{p\sigma} = \sqrt{\frac{n_\sigma q_\sigma^2}{\epsilon_0 m_\sigma}}$$

- **Debye length**: smallest length scale over which ionized gas can be considered a plasma.

$$\lambda_\sigma = \sqrt{\frac{\epsilon_0 \kappa T_\sigma}{n_\sigma q_\sigma^2}}$$

- **Larmor Radii**: cyclotron (also known as Larmor) orbit radius

$$r_{L\sigma} = \frac{\sqrt{\kappa T_\sigma / m_\sigma}}{|\omega_{c\sigma}|}$$

- **Ion Skin Depth**: this is the length scale below which MHD breaks and ion and electron motion is decoupled.

$$\frac{c}{\omega_{pi}} = c\sqrt{\frac{\epsilon_0 m_i}{n_i q_i^2}}$$

- **Thermal velocity**: particle thermal velocity

$$v_{T_\sigma} = \sqrt{\frac{2\kappa T_\sigma}{m_\sigma}}$$

- **Ion acoustic velocity**: the sound speed in ionized gas. Depends both on electron temperature and ion mass.

$$c_s = \sqrt{\frac{\kappa T_e}{m_i}}$$

- **Alfvén velocity**: the characteristic velocity of Alfvén waves, the normal modes of MHD.

$$v_A = \frac{B}{\sqrt{\mu_0 \rho}}$$

A p p e n d i x B

EXPERIMENTAL CONSIDERATIONS

B.1   Discussion of plasma breakdown

Previous fast ion gauge measurements [17], have demonstrated that the neutral background density before breakdown is approximately distributed around each footpoint in an exponential cone:

$$n_{\text{footpoint}} = n_0 (\frac{\beta}{z + \beta})^2 \exp\left(-\frac{\alpha r^2}{(z + \beta)^2}\right) \tag{B.1}$$

where $n_0 \approx 10^{22}$ m^{-3}, $\beta = 1$cm, and $\alpha = 1$ (corresponding to a 45° cone angle). Computing the sum of two footpoints spaced 0.25 m apart, we expect the density to be $\sim 10^{19}$ m^{-3} near the loop apex.

Given the measured initial conditions: $n_{neutral} \sim 10^{19}$ m^{-3}, $d = 0.25$ m (electrode separation), $V = 3$ kV, and $T = 300$ K, we find that the pressure-density product, $P \cdot d \approx 0.01$ Torr-cm falls well below the minimum Paschen criterion for Argon ($\sim$0.25 Torr-cm). Now, given this violation, it is clear that either the measured density or the Paschen criterion is lacking. In this case, it is the Paschen criterion which is lacking as it is unsuited to evaluate highly non-uniform gas distributions and non-parallel-plate geometries.

To remedy this, we develop a more fundamental criterion for breakdown: calculating the conditions under which the average electron ionizes at least one atom between anode and cathode [134, 135]:

$$\text{number atoms ionized} = \int_0^d \alpha \, dl \geq 1, \tag{B.2}$$

$$\alpha = \frac{1}{\lambda_e} e^{-\frac{E_{\text{ionize}}}{q|\mathbf{E}|\lambda_e}} = n\sigma e^{-\frac{15n\sigma}{|\mathbf{E}|}}, \tag{B.3}$$

where α represents the number of ionizations per unit length, λ_e is the mean free path, E_{ionize} is the ionization energy (Argon:15 eV), $|\mathbf{E}|$ is the electric field, σ is the atom cross section (Argon:10^{-20} m^2), and d is the path length.

If we now integrate Equation B.2 over the observed breakdown path, our measured densities do satisfy this more fundamental breakdown criterion due to the high densities present at the footpoints. We find that at 3 kV, we expect average ionization

of 1.3 atoms per e^- down to 0.92 atoms per e^- at 1 kV. This agrees with the experimentally observed breakdown limit of around 1 kV for the standard neutral gas settings.
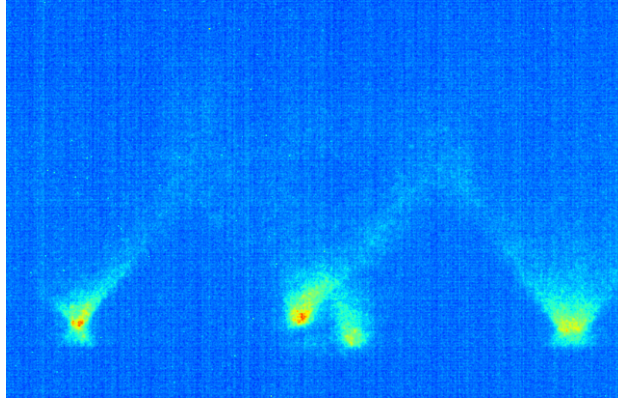

Figure B.1: Visible light image (20ns exposure) at breakdown. Pattern of strong footpoint ionization with conical structure is clearly visible.

B.2 Magnetic Field measurements from Bao's Hall Probes

A former Bellan graduate student, Bao Ha, built a set of Hall effect probes to measure low frequency magnetic fields ($<$ 10 kHz) such as the background magnetic fields produced by the solenoids beneath each electrode. This mapping is necessary because the Bdot probe array does not measure the constant background field. The initial plan was to use all 6 viable Hall probes to measure the magnetic field of the double loop setup. Unfortunately, the VME did not trigger all chips simultaneously when set to a sampling rate less than 100MHz. As a result, only one probe was used (Probe E) and the data was taken with the large oscilloscope.

Data collection

The data was taken in a 2D fashion assuming that the remaining dimension could be interpolated using cylindrical symmetry. The x-direction was vertical, the y-direction was away from the VME, and the z-direction was towards the gun. Only the top solenoid of loop A was measured. The data was taken in the plane corresponding to (x=-1in as defined by the plastic mounting system for the sensors). 8 y-positions and 4 x-positions were measured for a total of 32 core positions for a bank voltage of 200V.

Fitting solenoid position

Additional data was taken at z=0 (electrode plane) to determine the position of the electrode [Figures B.2,B.3] relative to the measuring coordinate system.
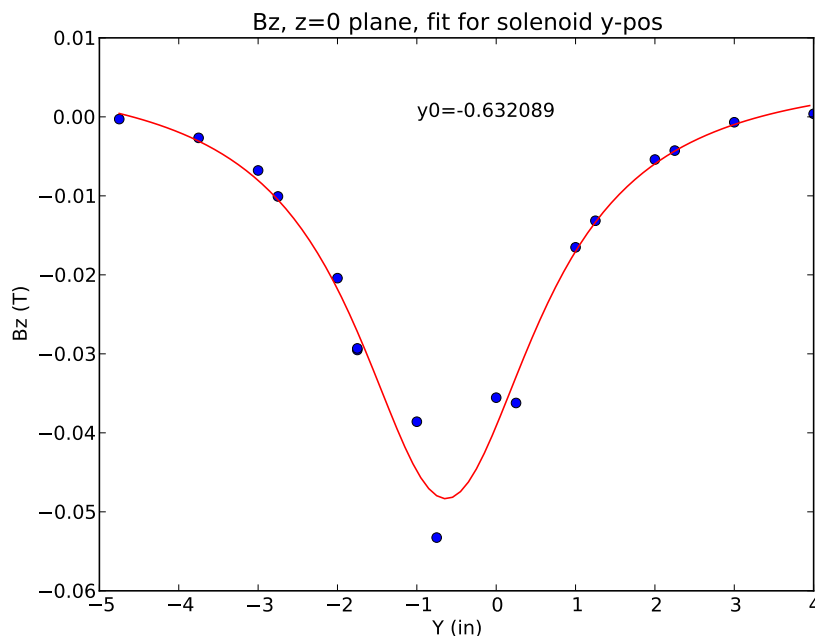

Figure B.2: Fit for solenoid y-position

Magnetic field measurements

After fitting the solenoid position, the data was converted to cylindrical coordinates and symmetry around the solenoid axis was assumed. With these data, we can plot field components in the (r,z) plane [Figures B.4,B.5,B.6]

Scaling with bank voltage

Additional shots at z=0 were also taken at 50V and 100V to determine scaling of field with bank voltage. Since these were only taken at 2 locations, the calculation is fairly rough.

z=0 in, r=1.6 in (200V/100V: 1.77), (100V/50V: 1.66)

z=0 in, r=-1.3 in (200V/100V: 1.23), (100V/50V: 1.45)

These ratios imply that background B-field scales like:

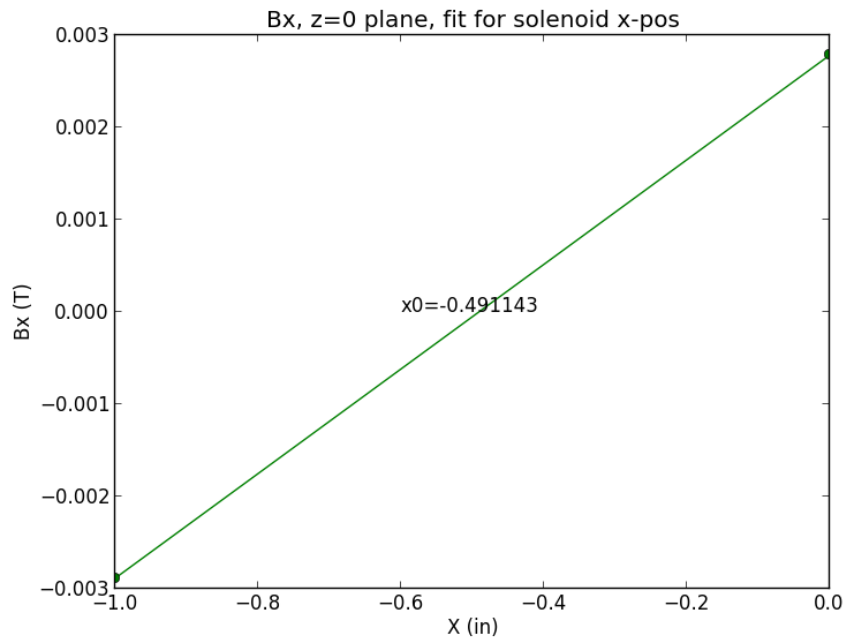$$B \propto 1.5^{\log_2(\frac{V}{V_0})}. \tag{B.4}$$

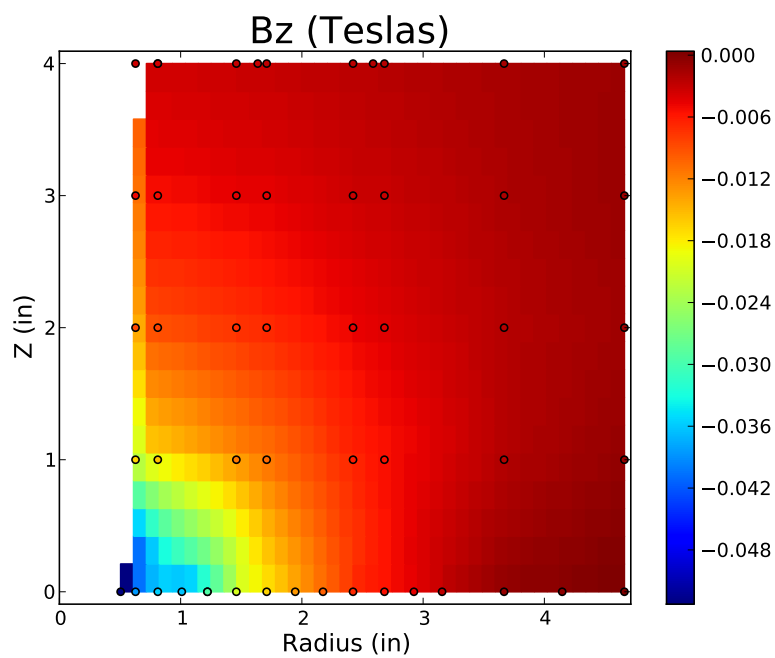Figure B.3: Fit for solenoid x-position
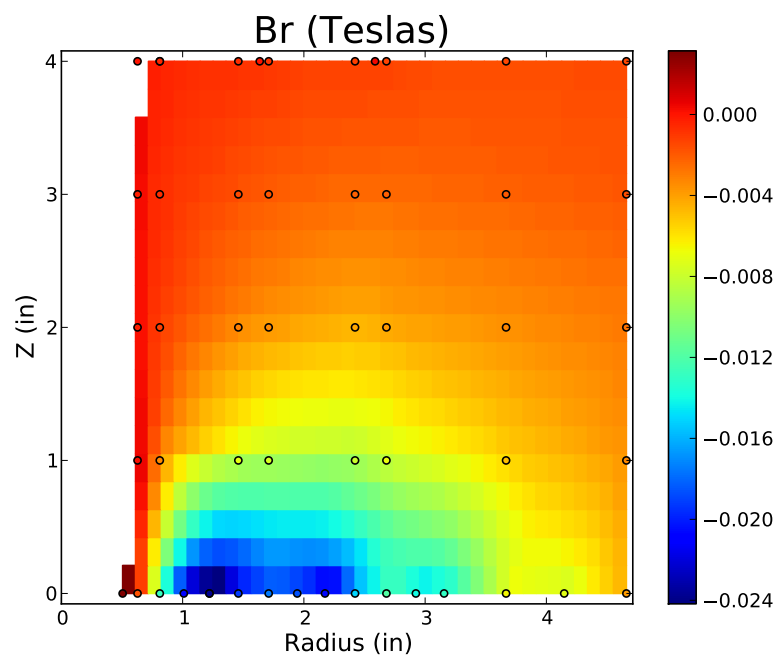

Figure B.4: Axial magnetic field plotted in (r,z) plane

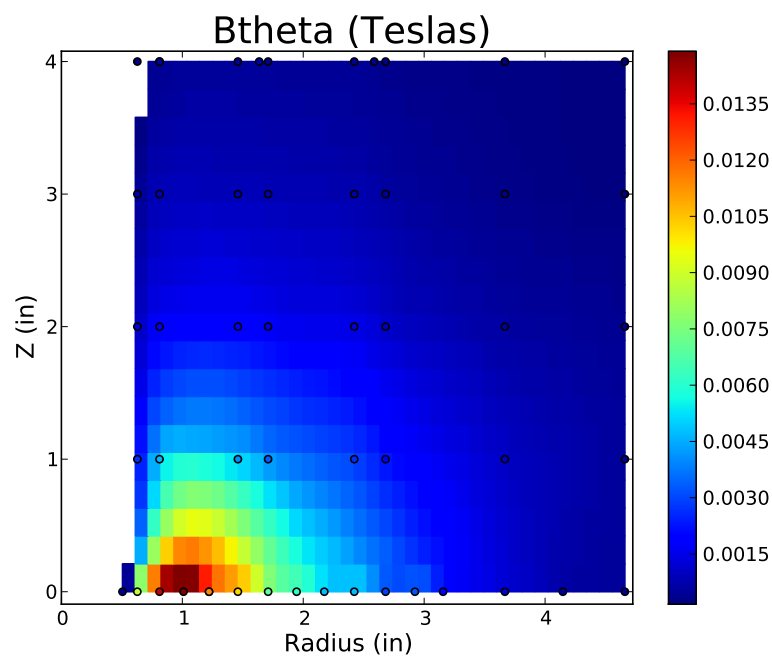Figure B.5: Radial magnetic field plotted in (r,z) plane

Figure B.6: Toroidal magnetic field plotted in (r,z) plane

A p p e n d i x   C

SUPPLEMENTAL INFORMATION FOR CHAPTER 3

This supplement covers supporting information not included in Chapter 3. These sections discuss, (1) how the axis of the flux ropes was defined, (2) a quantitative comparison of axial forces with theory, (3) temperature measurements from spectroscopic line ratios, (4) a derivation of the internal pressure of a flared current channel, and (5) a discussion of how current is distributed between the four electrodes in the double loop experiment.

C.1   Axial cross-sections

The process of acquiring cross-sections perpendicular to the loop axis first requires the axis to be defined. As mentioned in Chapter 3, the current axis was chosen as the loop axis as it was more consistent and more localized than the magnetic axis. These two axes are not coincident due to the arched geometry and the small aspect ratio of the current density ($R/r < 3$). This offset of the magnetic axis to a larger radius than the current axis is another manifestation of the hoop force.

The tracking procedure follows the local maximum of the current density along the loop. The axial direction was defined by the average direction of the current across a cross-section. After defining both the axis location and direction, perpendicular cross-sections were taken at 1 cm intervals along the loop axis. Cross-section values for **B** and **J** were interpolated using Delauney triangulation [136] from the 3D dataset.

For the majority of the loop length, the current cross-sections have a 2D Gaussian cross-section. Figure C.1 shows that the contours of the Gaussian fit and the data are nearly coincident. Consequently, the following section will use this symmetry to quantitatively compare the analytic theory with the measured forces.

C.2   Quantitative comparison of axial forces

To quantitatively compare the magnitude of these 3D forces with the axisymmetric theory requires a reduction to one dimension. In this reduction, the compared quantity is the integral of the axial force over the cross-section:

$$F_s[N/m] = \int_S (\mathbf{J} \times \mathbf{B}) \cdot d\mathbf{S} \tag{C.1}$$
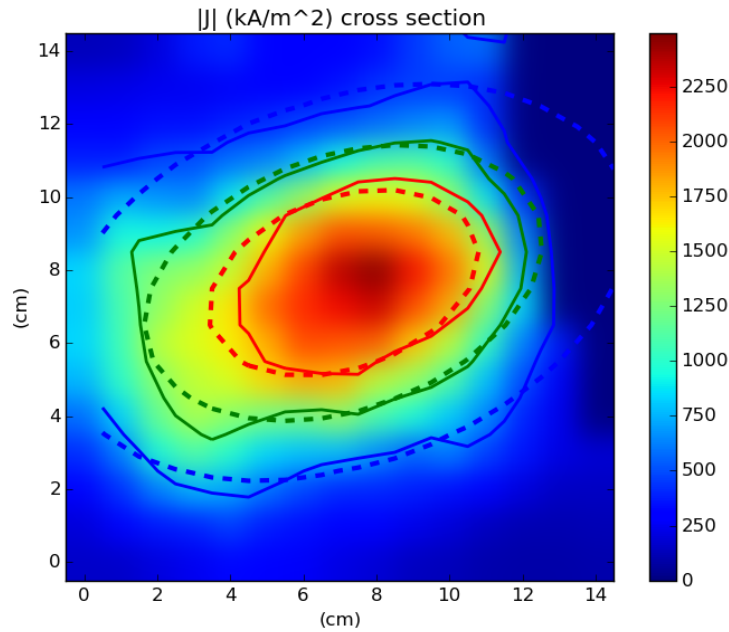
Figure C.1: Plot of current density cross-section and 2D Gaussian fit. Equivalent contours from the Gaussian fit and the current density are plotted in dotted and solid lines, respectively (red:90%, green:75%, blue:50%). Discontinuous region in upper right corner is outside the data region.

These integrated values (force-per-length) are compared against the forces predicted for an axisymmetric current channel with the same minor radius, $\sigma(s)$, and a Gaussian current cross-section.

$$J(r) = \frac{I}{(2\pi\sigma^2)}e^{-\frac{r^2}{2\sigma^2}}, \tag{C.2}$$

$$B_\theta(r) = \frac{\gamma(r)I\mu_0}{2\pi r}, \tag{C.3}$$

$$\gamma(r) = 1 - e^{\frac{-r^2}{2\sigma^2}}, \tag{C.4}$$

where s is the distance along the axis, I is the total current, r is the distance from the loop axis, and $\gamma(r)$ is the fraction of total current inside radius r. Solving for the magnetic forces gives:

$$f_{\hat{s}}[N/m^3] = \frac{I^2\mu_0}{4\pi^2\sigma^3}\gamma(1-\gamma)\frac{d\sigma}{ds} \tag{C.5}$$

Integrating Eq. C.5 over the cross-section, gives the axial magnetic-force-per-length:

$$F_{\hat{s}}[N/m] = \frac{I^2\mu_0}{4\pi\sigma}\frac{d\sigma}{ds}. \tag{C.6}$$

Plotting the measured axial magnetic-force-per-length against Eq. C.6 over a range of currents (Figure C.2) shows good agreement. This comparison demonstrates two properties. First, the axisymmetric theory can accurately predict the relevant axial forces of a asymmetric 3D structure simply from the loop minor radius. Second, it validates the assumption in Ref. [21] that forces from perturbing the background field ($-J_\theta B_r$) are negligible compared to the forces due to flared current ($J_r B_\theta$).
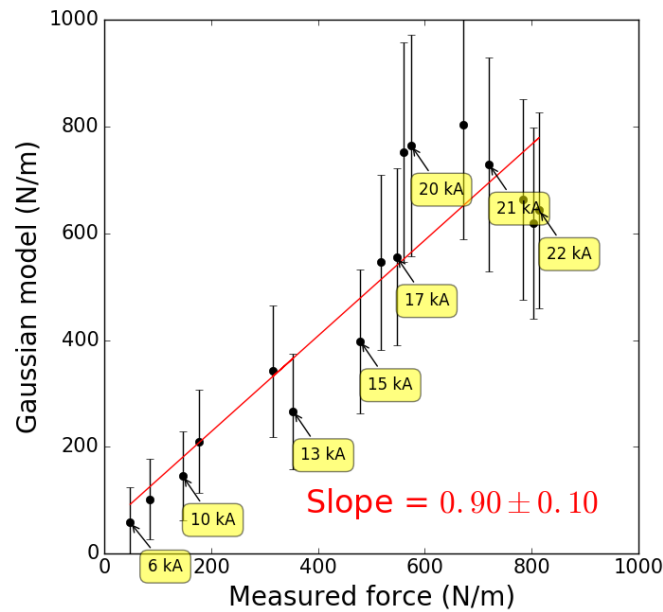

Figure C.2: Plot of axial force per length at footpoints versus Eq. C.6 for current range 0-22 kA. Yellow labels indicate total current. Good agreement with Eq.C.6 shows that axial forces due to perturbation of the background field ($-J_\theta B_r$) are negligible.

C.3 Temperature Measurement

Spectroscopic measurements of the Argon plasma (Fig. C.3) in the lab experiment along 12 lines of sight indicate a constant temperature between 1.92-2.02 eV. Temperature is bounded by matching observed lines to Saha/LTE spectra for Argon [45]. Since line ratios remain constant in time and space, it is expected that the plasma can be modeled as isothermal.

C.4 Pressure Integration

A model for the internal pressure of a flared current channel is developed from the assumption of radial force balance:
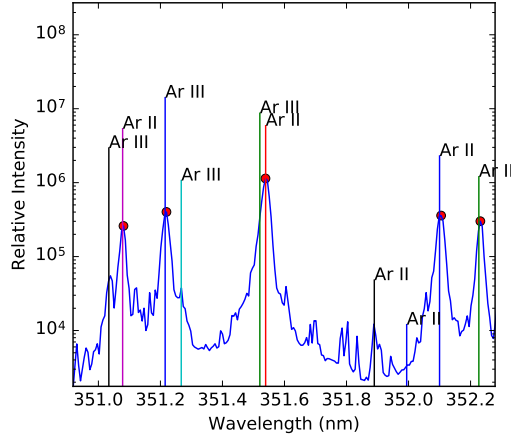
Figure C.3: Sample spectrum around 351.5 nm. Line ratios of Ar II and Ar III predict a temperature between 1.92 and 2.02 eV.

$$
\begin{aligned}
0 &= \hat{r} \cdot (\vec{J} \times \vec{B} - \vec{\nabla} P) \\
&= J_\theta B_s - J_s B_\theta - \frac{\partial P}{\partial r}
\end{aligned}
\tag{C.7}
$$

The $J_\theta B_s$ term is associated with the magnetic pressure of the axial field resisting radial compression. We omit this term here for clarity. However, this term is important as it reduces the equilibrium internal pressure of the current channel.

Using the flared current channel model from Chapter 3:

$$
B_\theta(r) = \frac{\gamma(r) I \mu_0}{2\pi r},
\tag{C.8}
$$

$$
\begin{aligned}
J_s B_\theta &= \frac{B_\theta}{\mu_0 r} \frac{\partial}{\partial r}(r B_\theta) \\
&= \left(\frac{I}{2\pi}\right)^2 \frac{\mu_0}{r^2} \gamma(r) \frac{\partial \gamma}{\partial r},
\end{aligned}
\tag{C.9}
$$

so,

$$
\frac{\partial P}{\partial r} = -\left(\frac{I}{2\pi}\right)^2 \frac{\mu_0}{r \sigma^2} \gamma(r)(1 - \gamma(r)).
\tag{C.10}
$$

Integrating this force from infinity to zero gives a pressure distribution:

$$
P(r) = -\left(\frac{I}{2\pi}\right)^2 \frac{\mu_0}{2\sigma^2} W(r),
\tag{C.11}
$$

where,

$$W(r) = \text{Ei}\left(\frac{-r^2}{\sigma^2}\right) - \text{Ei}\left(\frac{-r^2}{2\sigma^2}\right), \tag{C.12}$$

and 'Ei' is the exponential integral:

$$\text{Ei}(x) = \int_{-\infty}^{x} \frac{e^t}{t}\, dt. \tag{C.13}$$

Consequently the vertical pressure gradient is:

$$-\frac{\partial P}{\partial s} = \left(\frac{\mu_0 I^2}{4\pi^2 \sigma^3} \frac{\partial \sigma}{\partial s}\right)(\gamma(\gamma - 1) + W(r)), \tag{C.14}$$

adding the magnetic forces,

$$J_s B_\theta = \frac{I^2 \mu_0}{4\pi^2 \sigma^3} \frac{d\sigma}{ds} \gamma(1 - \gamma), \tag{C.15}$$

we get the total axial force density:

$$J_s B_\theta - \frac{\partial P}{\partial s} = \left(\frac{\mu_0 I^2}{4\pi^2 \sigma^3} \frac{\partial \sigma}{\partial s}\right) W(r). \tag{C.16}$$

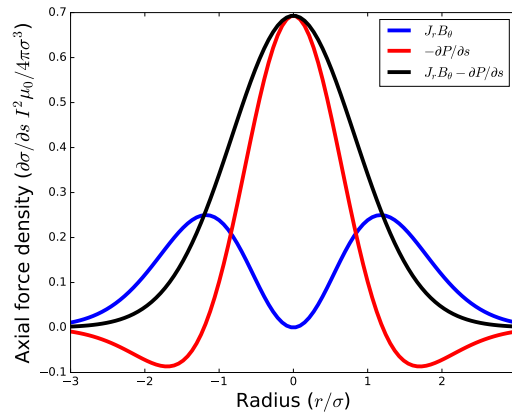Figure C.4 plots the separate magnetic and pressure terms for axial force density.

Figure C.4: Plot of theoretical axial forces from a flared current channel in radial equilibrium.

The axial pressure gradient calculated here represents an upper bound due to the omission of the $J_\theta B_s$ term. In the experiment, the $J_\theta B_s$ term offsets a large fraction (0.5-0.9) of the pinch force, resulting in 2-10 times lower internal pressure than a system without axial field. This reduces axial pressure gradients by the same factor (2-10) but does not affect the axial magnetic forces. Consequently, the experimental axial-force-density has a much flatter profile.

C.5 Bifurcation of current

Current streamlines were constructed from the 3D B-field measurements detailed in Chapter 3. These streamlines characterize the flow of current in the measured 3D region and show that the two loops are initially merged during breakdown and remain so over the course of the evolution. Figure C.5 shows the additional current paths, a short middle path and a long overarching path, in this merged configuration.
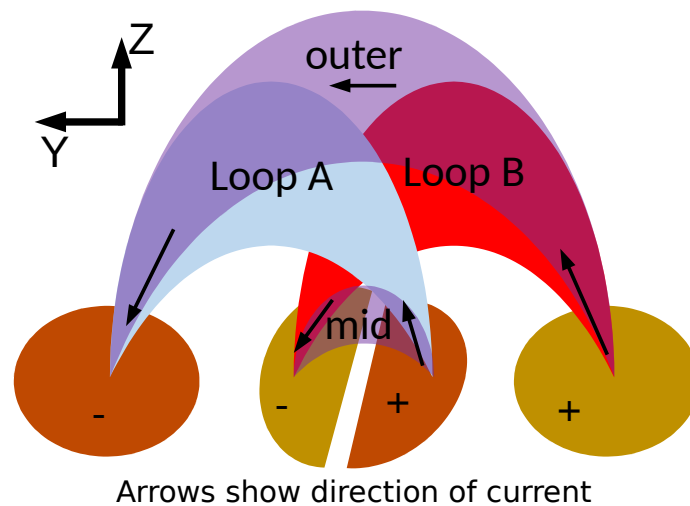

Figure C.5: Diagram of current paths in merged configuration. In addition to the two loops A and B, there is a short middle path and an overarching outer path.

Figure C.6 shows the quantitative breakdown at three times of the current bifurcation from the negative electrode on loop B. For these plots, the current streamlines were seeded over the electrode surface and classified as either part of the middle path or the main loop B path by their termination location. The net current associated with each streamline was assumed to be proportional to the current density at the seeding location on the electrode. Summing the contributions of streamlines along both paths, gives an estimate of nearly equal bifurcation (50/50) which remains relatively constant over time.
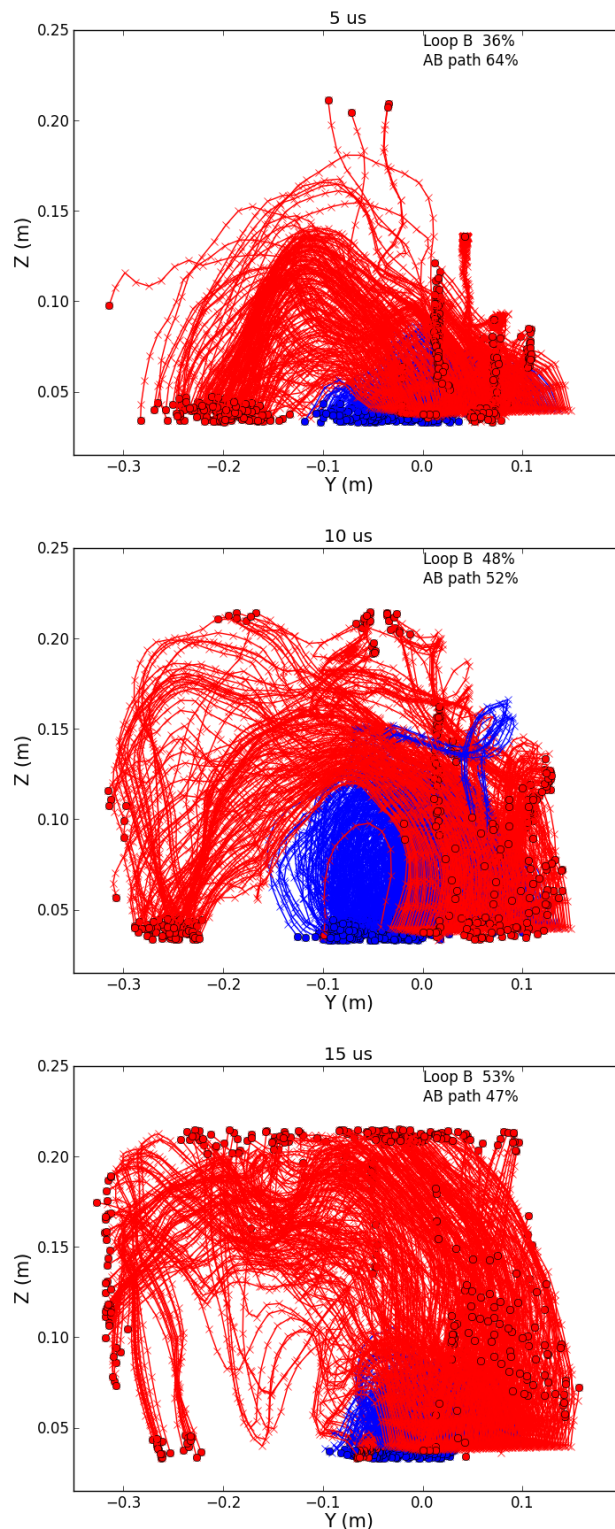
Figure C.6: Plot of current bifurcation from the lower loop negative electrode. Current density streamlines are classified as part of the main loop B or the shorter mid path (AB) based on their termination locations. The bifurcation is nearly constant at about 50%.

HIGH-RESOLUTION $\dot{B}$-PROBE ARRAY

This appendix will describe the design and calibration of the $\dot{B}$-probe array used in Chapter 3. This probe was designed with printed circuit board (PCB) surface mount technology to minimize construction time and improve uniformity. The probe has a linear spatial resolution of 1 cm which is double the resolution of other magnetic probes in the lab. This higher spatial resolution was necessary to properly measure the 3D current density which was integral to the results presented in Chapter 3.

D.1 Design

The purpose of the magnetic probe array is to measure the three components of the vector magnetic field at multiple positions along an axis.

Printed Circuit Board Array

For this array, the field along a given direction at a given location is measured using a small 5.6 μH surface-mount inductor (Coilcraft Part #1008CS-562XJE_, Figure D.1a). The large inductance of these coils gives a large output signal but limits their frequency response to ~ 1 MHz and below.

A single array structure is composed of two 3 mm wide PCB strips mounted at 90° to each other. One strip contains nine sets of two perpendicular coils at 1 cm spacing
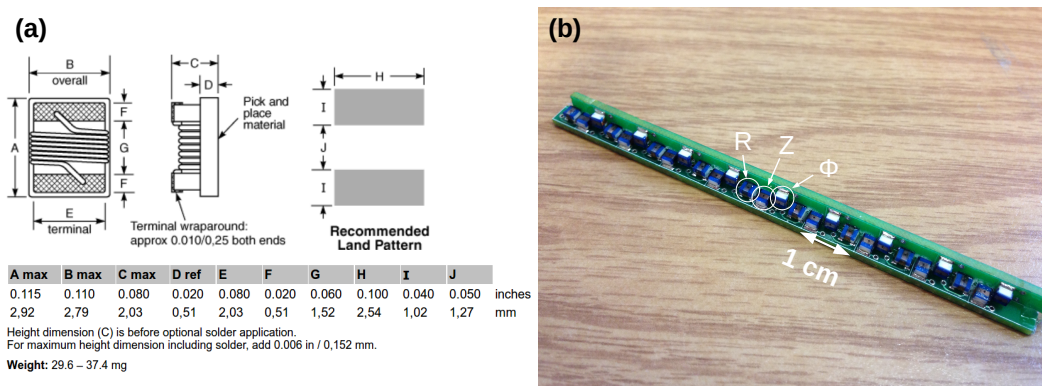

Figure D.1: (a) Mechanical drawing of single surface mount coil. (b) Image of 27 channel PCB $\dot{B}$-probe array.
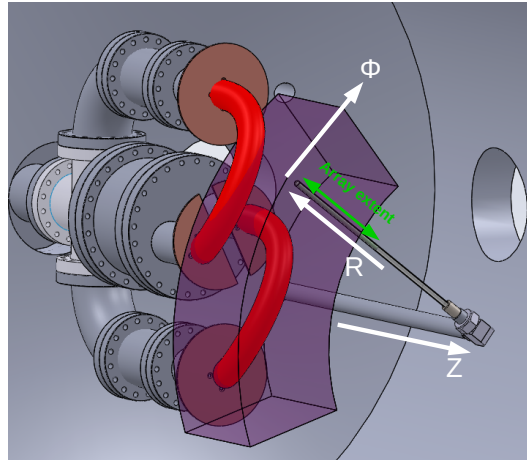
Figure D.2: Cylindrical coordinate system for probe array relative to mounting structure. The purple annular region represents the spatial positions accessible to the probe via translation and rotation.

and the other strip contains nine coils spaced every 1 cm as shown in Figure D.1b. This gives a 1 cm resolution at nine positions for measurement of the field along each perpendicular axis. Two of these 27 channel arrays were used in the final probe design for a total of 57 channels in eighteen 3-axis clusters.

All of the surface mount elements were soldered simultaneously in a toaster oven. This process involves putting small amounts of solder paste on all of the individual solder pads, placing each inductor element on top of a pair of pads, and then baking all the arrays in the toaster oven at 450° for about 4 minutes. The surface tension of the solder when it melts aligns each element with its solder pads resulting in highly uniform orientations.

Due to the cylindrical symmetry of the probe mounting, the axes are labeled as follows,

- **R**: the direction of the probe axis

- Φ: the direction of probe rotation

- **Z**: the direction of probe translation
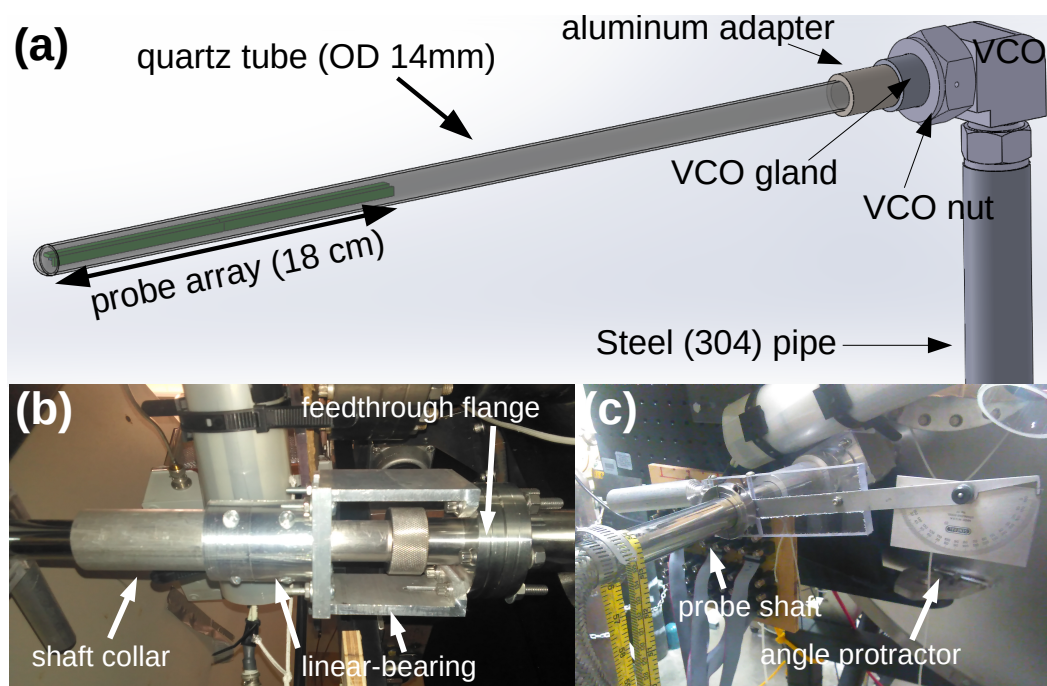
These axes are visualized in Figure D.2.

Figure D.3: (a) Interior parts of vacuum assembly for magnetic probe array (b) Exterior vacuum parts (c) Probe angle measurement using protractor.

Vacuum mounting

The vacuum mounting is similar to the other magnetic probes in the lab. The array is contained within a quartz tube (14 mm outer diameter, 12 mm inner diameter) which is closed at one end. The open end of the tube is attached to a Swagelok VCO gland (SS-12-VCO-3) using vacuum epoxy (Torr Seal) and an aluminum adapter. This gland attaches to a 90° angle bend VCO (SS-12-VCO-9) using a VCO female nut (SS-12-VCO-1). The free end of the 90° VCO angle is welded to a 6 foot long, 1 in outer diameter steel pipe (stainless steel alloy 304). This assembly is shown in Figure D.3a.

The stainless steel tube exits the chamber through a 2.75" Conflat feedthrough. This flange also has an attached linear bearing for support and ensure smooth translation and rotation of the axis. A shaft collar is also needed to prevent the setup from being sucked into the vacuum chamber. It is recommended for future probes to purchase the shaft collar and linear bearing rather than machining them as it is difficult to get all the tolerances correct.
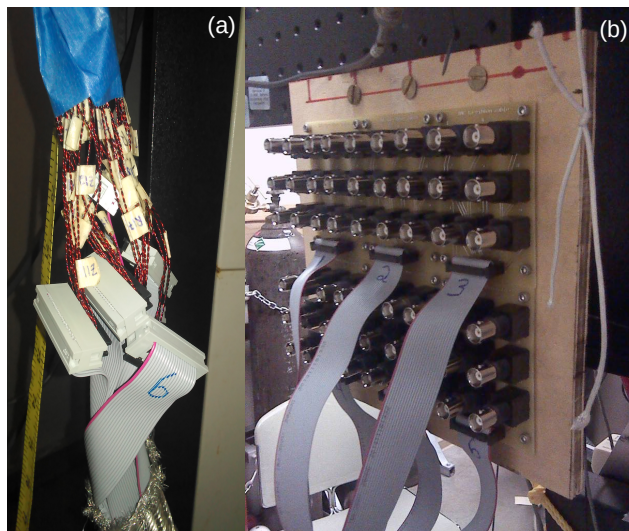
Figure D.4: (a) Image of twisted-pair magnet wires attaching to ribbon cables (b) Image of ribbon-cable-to-BNC adapter boards.

Cabling

Each coil is connected to a length of twisted-pair magnet wire (AWG 27, 0.375 mm diameter). These twisted pairs are then connected to ribbon cables via bladed crimp fittings (Figure D.4a). The ribbon cables then plug into PCB boards which connect individual channels to BNC cables (Figure D.4b). These ribbon cable connectors provide an easy detachment point if the probe needs to be removed from the chamber. Also, the ribbon connectors terminate sets of cables simultaneously without stripping or soldering, which allowed a significant reduction in manual labor.

D.2 Calibration

The calibration of the probe was conducted in-situ using a custom Helmholtz coil. This coil has N=10, R=17 mm with perpendicular holes for alignment along each axis. The current through the coil is measured with a 0.43 Ω resistor in parallel with the coils.

The calibration procedure consisted of applying 0.7 MHz oscillating field to each channel along all three perpendicular axes. The voltage amplitude for each field direction (R, Φ, Z) is recorded for each channel. The matrix of amplitudes for each cluster is then inverted to acquire a calibration matrix as shown in Auna's thesis [17]. This calibration file is located in the group server:

Figure D.5: Image of Helmholtz coil (N=10, R=17 mm) used for calibration of probe array. The coil is wound on a machined plastic cylinder with a 14 mm axial hole and a 14 mm perpendicular hole for calibrating the other two axes.

```
\\flux\public\data\croft\calibrations\bdot_v2_calibration_matrix.txt
```

```
 #cluster 1
6.931971e-05,2.280898e-06,-1.784141e-06
2.545543e-06,-8.178870e-06,-6.689360e-05
3.239601e-06,-7.717792e-05,1.650782e-05
#cluster 2
-7.033042e-05,1.228048e-06,-8.777862e-07
-3.792115e-06,-1.183214e-05,-6.582754e-05
-2.035724e-06,-6.681623e-05,1.507158e-05
#cluster 3
-6.994532e-05,-3.133043e-06,-1.524791e-06
-4.867825e-06,1.327051e-05,-6.642862e-05
-1.489208e-06,6.810366e-05,1.430509e-05
#cluster 4
7.109242e-05,-1.403789e-06,-4.916504e-07
5.535473e-06,1.245848e-05,6.619422e-05
1.514296e-06,6.809750e-05,-1.433927e-05
#cluster 5
-6.975625e-05,-1.099918e-06,7.548406e-07
-5.976776e-06,1.049402e-05,6.642589e-05
```

-2.920835e-06,6.918405e-05,-1.379752e-05
#cluster 6
-6.986844e-05,6.158665e-07,5.209423e-07
-4.180235e-06,-9.200068e-06,6.617970e-05
-2.799661e-06,-6.865882e-05,-1.546462e-05
#cluster 7
-6.954115e-05,-1.825965e-06,-7.506254e-07
-4.093920e-06,7.469317e-06,-6.845870e-05
-4.104451e-06,6.881023e-05,2.115268e-05
#cluster 8
-6.981198e-05,1.703176e-06,-6.477696e-07
-7.325473e-06,-8.707596e-06,-6.779221e-05
-2.243123e-06,-6.529238e-05,1.487616e-05
#cluster 9
6.962836e-05,2.790980e-06,1.272197e-06
3.339564e-06,-1.158637e-05,6.699374e-05
3.863279e-06,-6.546127e-05,-1.685915e-05
#cluster 10
-6.787340e-05,-9.372418e-07,3.386524e-06
4.535572e-06,4.920207e-05,4.667388e-05
-7.439067e-07,-4.603437e-05,4.821460e-05
#cluster 11
-7.078151e-05,5.657038e-07,-2.882804e-06
3.970911e-06,-5.233124e-05,-4.467293e-05
-6.637705e-07,4.551207e-05,-4.759615e-05
#cluster 12
6.950274e-05,8.756956e-07,2.245998e-07
-2.352052e-06,5.188650e-05,4.673847e-05
2.433470e-06,-4.575120e-05,4.787597e-05
#cluster 13
7.052922e-05,-3.024421e-06,9.772170e-07
-3.573537e-06,-5.042790e-05,-4.618671e-05
-1.681535e-06,4.560177e-05,-4.895451e-05
#cluster 14
7.031290e-05,-2.033676e-06,-1.094625e-06
-5.021137e-06,-4.950097e-05,-4.741425e-05

-7.261562e-07,4.792218e-05,-5.012283e-05
#cluster 15
6.995045e-05,-1.446403e-06,6.391197e-07
-4.060683e-06,-4.918977e-05,4.474813e-05
-5.562666e-07,4.617371e-05,4.805713e-05
#cluster 16
-6.992290e-05,-6.204385e-07,-3.306483e-06
6.725334e-06,-4.984008e-05,-4.492627e-05
3.201034e-06,4.583280e-05,-4.851451e-05
#cluster 17
-7.051448e-05,-6.208052e-07,8.706897e-07
3.777682e-06,-5.139477e-05,4.317005e-05
-1.408425e-06,4.534024e-05,4.943133e-05
#cluster 18
6.975948e-05,-2.463094e-07,-1.945683e-06
-5.381909e-06,5.646957e-05,-4.990794e-05
-1.280065e-06,-4.409998e-05,-5.012522e-05

A p p e n d i x   E

3D VISUALIZATIONS

Since so much of this thesis was devoted to 3D effects, a form of visualizing these complex data sets was needed. The tool of choice for these 3D visualizations was the Mayavi2 python library. This library is essentially a simple, scriptable python wrapper for the uber-complex VTK (Visualization Tool Kit). The library has two dependencies:

1. VTK

2. A GUI toolkit, either PyQt4, PySide, PyQt5 or wxPython.

So, at the time of this writing, it is fairly simple to install on Windows/Mac/Linux. At present, binary packages for Mayavi2 are only available for Python 2.7 but will likely become available for Python 3.x soon.

E.1   Implementation

A larger-than-minimal working example is available at my github for the 3D B-field data shown in Chapter 3. This example implements the essential steps in forming a 3D visualization from experimental data,

1. Save irregular or gridded data of a 3D quantity into a scriptable format (i.e. comma separated values)

2. Interpolate data onto a cartesian grid using Delauney triangulation (see get_rect_grid function in this library file)

3. Place the gridded data into the Mayavi scalarfield and vectorfield objects

4. Plot different representations of the data (surfaces, streamlines, vector fields, etc.)

The resulting visualization is a zoomable, rotatable, window with a reasonably user-friendly graphical user interface (GUI). This GUI allows the user to change all features of the visualization including visibility, colormaps, streamline seed positions (press 'i'), etc..

E.2   Tips and Tricks

The Mayavi2 documentation for scripting is suitable for basic operations but lacks depth. For more advanced scripting control of the visualization there is a simple feature called "record" in the GUI which appears as a toolbar button that resembles a stop sign. This feature will record and display the scripting equivalent of any changes to the visualization made in the GUI. This allows complex changes made with the GUI to be recorded as a script so that the visualization can be easily reproduced.

E.3   Making movies from image sequences

The most reliable program for making movies from sequences of images was "ffmpeg". This is a powerful scripting command with many slicing, splicing, and compilation options for videos. However, for making movies from an image sequence, I used the following command,

```
ffmpeg -r 2 -i rc%04d.png -c:v libx264 -pix_fmt yuv420p slides.mp4
```

This command compiles images named with the convention "rc%04d.png" (i.e. rc0007.png) at a framerate of 2 Hz (the number after **-r**) into a file named **slides.mp4**.

The following movies were made using image sequences generated with Mayavi and compiled using ffmpeg:

- Doubleloop firing sequence and evolution

- Time dependent 3D Bfield streamlines, current density isosurfaces, and JxB vectors

WAVEPROBE SUPPLEMENTAL

F.1   Review of previous wave polarization measurements

A former student from the Bellan group identified whistler waves in the jet from measurements of circularly polarized magnetic oscillations. One of the primary shots from this analysis was #17012, shown in Figure F.1.

However, after re-examining the data, there are two major issues with the analysis identifying circular polarization.

1. The high frequncy components of the signal are completely in phase with the significant common mode noise.

2. The narrow band filtering method used to isolate particular frequencies also produces circular polarization from random noise.

The first issue is visible in the raw data of shot #17012 shown in Figure F.2. Since the high frequency components of the signal are in phase with the common mode noise, it is likely that they are simply uncancelled noise rather than magnetic waves.
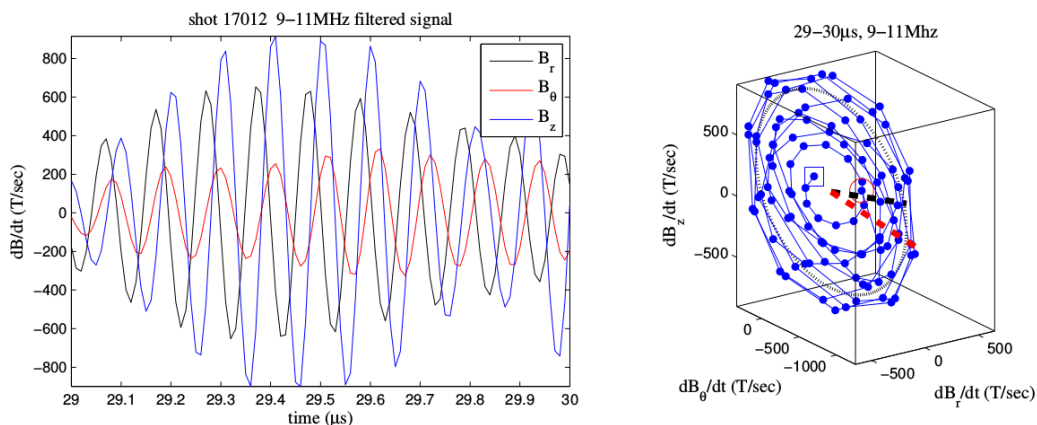

Figure F.1: (Left) Filtered data (9-11 MHz) from shot 17012, 29-30 μs. (Right) Hodogram of filtered B-field oscillations.
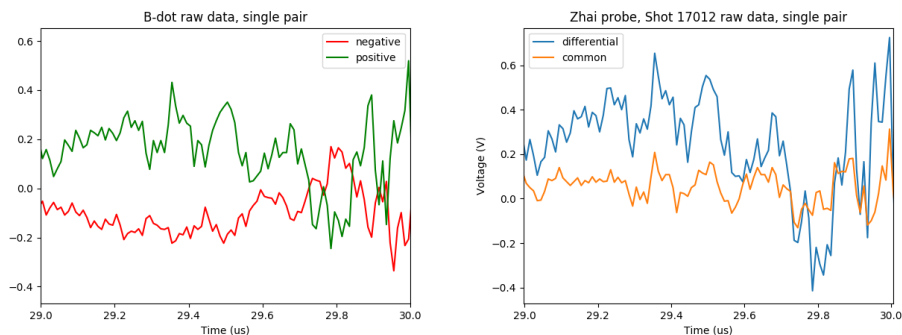
Figure F.2: (Left) Raw B_z data from each coil in z-axis pair, shot #17012. (Right) Differential and common signals from same shot. This is the raw data for the plots in Figure F.1.
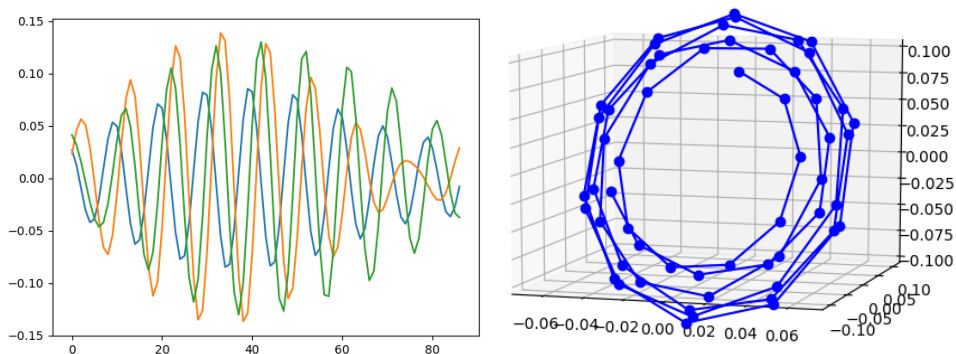

Figure F.3: (Left) Filtered white noise (9-11 MHz). (Right) Hodogram of filtered noise

The second issue is more subtle. The narrow band filter 9-11 MHz used to isolate a particular frequency can also create artificial polarization. This can be demonstrated by applying the same narrow band filters to random noise. The resulting signals are always sinusoids of nearly 10 MHz with slowly varying phase. Given a long enough time series, the signal is guaranteed to be circularly polarized for segments of time when the three components (B_r, B_θ, B_z) drift out of phase. Figure F.3 shows a plot of white noise filtered using a 9-11 MHz window with associated hodogram.

This issue was discovered after applying the technique to the quadprobe data and getting circular polarization in different directions for each probe (Figure F.4).

Lastly, as can be seen by comparing Figures F.1 and F.2, the raw data and the filtered data look very different. The oscillations visible in the raw data have roughly 5-6
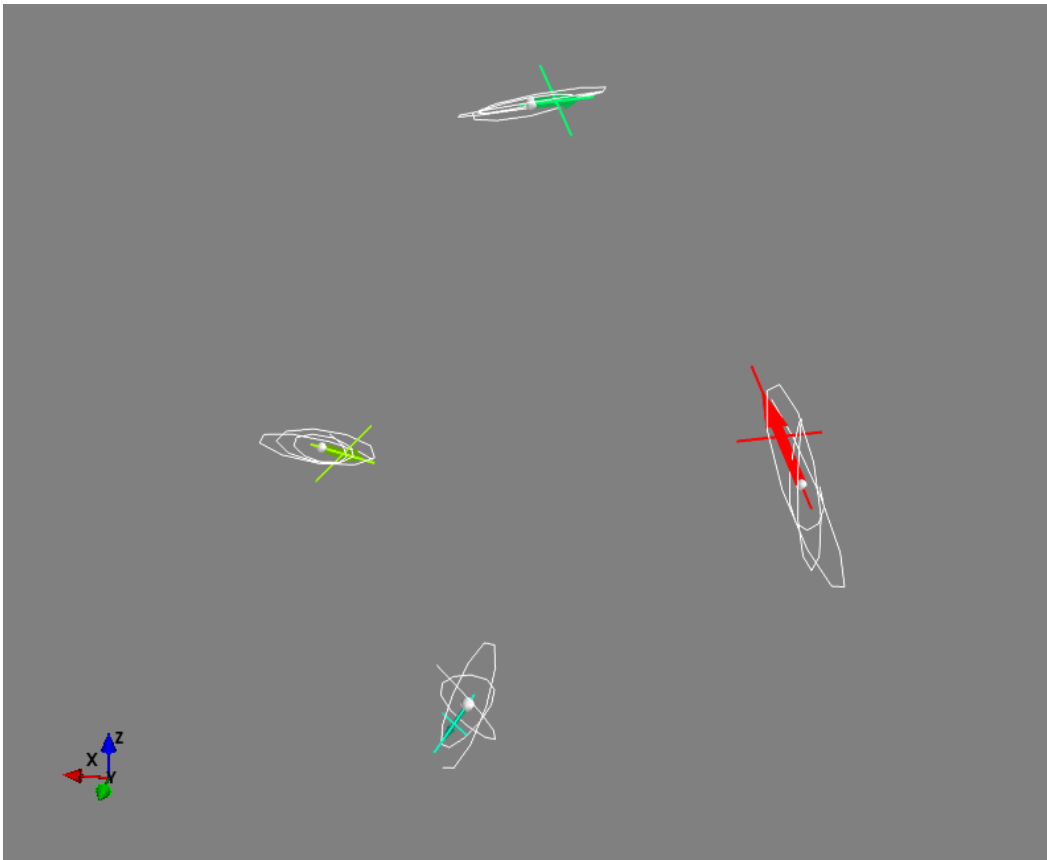
Figure F.4: Plot of quadprobe hodograms shot #20164 (26-32 μs) after applying narrow band filters. All the circular polarizations are in different directions indicating an incoherent signal.

periods over the 1 μs window, implying a core frequency of 5-6 MHz. Consequently, it is not appropriate to apply a 9-11 MHz filter.

In summary, it is believed that previous measurements of circular polarization are the artifact of narrow band filtering and significant common mode noise.

F.2 Tetrahedron geometry

The tetrahedral positions can be quantified by specifying an origin and a side length. To simplify calculations, the origin is chosen to be the center of the tetrahedron and the side length is specified as $a\sqrt{3}$, where a is the radial distance from the center of a face to the corners of that face. This odd choice of units is motivated by the probe construction where the spacing is set by the vacuum flange hole positions which have a radial spacing of a =0.5"=12.7 mm.

The probe axis is taken to be the z-axis and one probe is aligned with the x-axis. This gives the following four probe positions:

$$\mathbf{R} = \begin{pmatrix} 0 & 0 & \frac{-3a}{\sqrt{8}} \\ a & 0 & \frac{a}{\sqrt{8}} \\ -a/2 & \frac{a\sqrt{3}}{2} & \frac{a}{\sqrt{8}} \\ -a/2 & -\frac{a\sqrt{3}}{2} & \frac{a}{\sqrt{8}} \end{pmatrix}$$

F.3 Solving for B, J

This section provides the first order interpolation of the B and J vectors at the center of four measurement positions.

The approach is to write each scalar component of the vector B-field of each measurement position as a Taylor expansion of the value at the tetrahedron center, $\mathbf{B_c}$:

$$\mathbf{B}_i = \mathbf{B}_c + (\vec{\nabla}\mathbf{B_c}) \cdot \mathbf{R}_i, \tag{F.1}$$

where the i subscript denotes a probe location. The following shows this equation written out for the B_x-component,

$$\begin{pmatrix} B_{0x} \\ B_{1x} \\ B_{2x} \\ B_{3x} \end{pmatrix} = \begin{pmatrix} 1 & 0 & 0 & \frac{-3a}{\sqrt{8}} \\ 1 & a & 0 & \frac{a}{\sqrt{8}} \\ 1 & -a/2 & \frac{a\sqrt{3}}{2} & \frac{a}{\sqrt{8}} \\ 1 & -a/2 & -\frac{a\sqrt{3}}{2} & \frac{a}{\sqrt{8}} \end{pmatrix} \begin{pmatrix} B_{cx} \\ \frac{\partial B_{cx}}{\partial x} \\ \frac{\partial B_{cx}}{\partial y} \\ \frac{\partial B_{cx}}{\partial z} \end{pmatrix} \tag{F.2}$$

This equation can be inverted to recover the center value and derivatives,

$$\begin{pmatrix} B_{cx} \\ \frac{\partial B_{cx}}{\partial x} \\ \frac{\partial B_{cx}}{\partial y} \\ \frac{\partial B_{cx}}{\partial z} \end{pmatrix} = \begin{pmatrix} \frac{1}{4} & \frac{1}{4} & \frac{1}{4} & \frac{1}{4} \\ 0 & \frac{2}{3a} & \frac{-1}{3a} & \frac{-1}{3a} \\ 0 & 0 & \frac{1}{a\sqrt{3}} & \frac{-1}{a\sqrt{3}} \\ \frac{-1}{a\sqrt{2}} & \frac{1}{a3\sqrt{2}} & \frac{1}{a3\sqrt{2}} & \frac{1}{a3\sqrt{2}} \end{pmatrix} \begin{pmatrix} B_{0x} \\ B_{1x} \\ B_{2x} \\ B_{3x} \end{pmatrix} \tag{F.3}$$

The other components can be solved in the same manner. The current density can then be calculated from the various derivatives,

$$J_x = \partial B_z/\partial y - \partial B_y/\partial z$$
$$J_y = \partial B_x/\partial z - \partial B_z/\partial x$$
$$J_z = \partial B_y/\partial x - \partial B_x/\partial y$$

F.4 Wave pulses

This section has two figures showing wave probe measurements from different shots. Figure F.5 shows plots of six representative shots where there was visible tearing of the jet axis in fast camera images. Figure F.6 shows plots of six representative shots where there was no visible tearing of the jet axis in fast camera images. The measurements show a clear high frequency pulse during the tearing shots and no pulse in the shots without visible tearing.
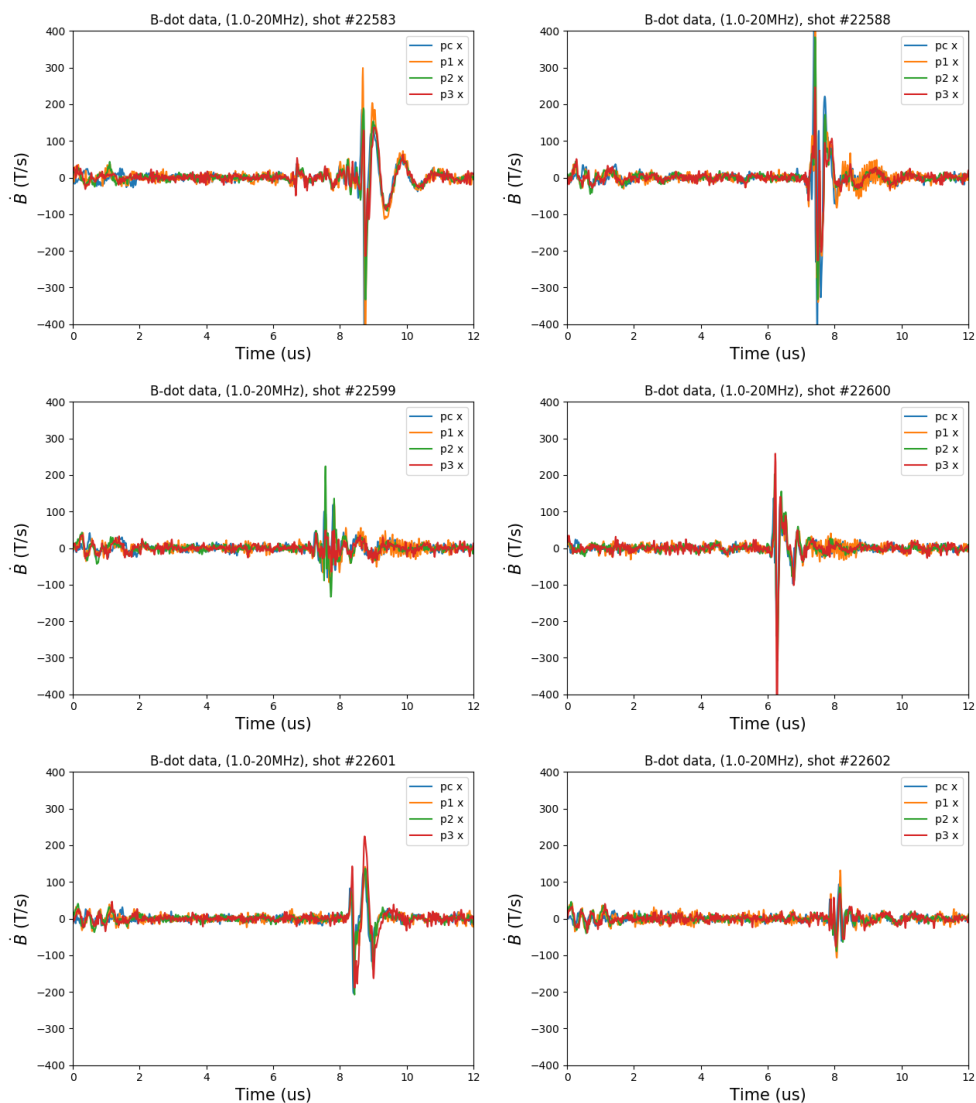

Figure F.5: Plots of filtered (1-20 MHz) B_x component waveprobe signals for shots with visible tearing of jet axis (22583, 22588, 22599, 22600, 22601, and 22602).
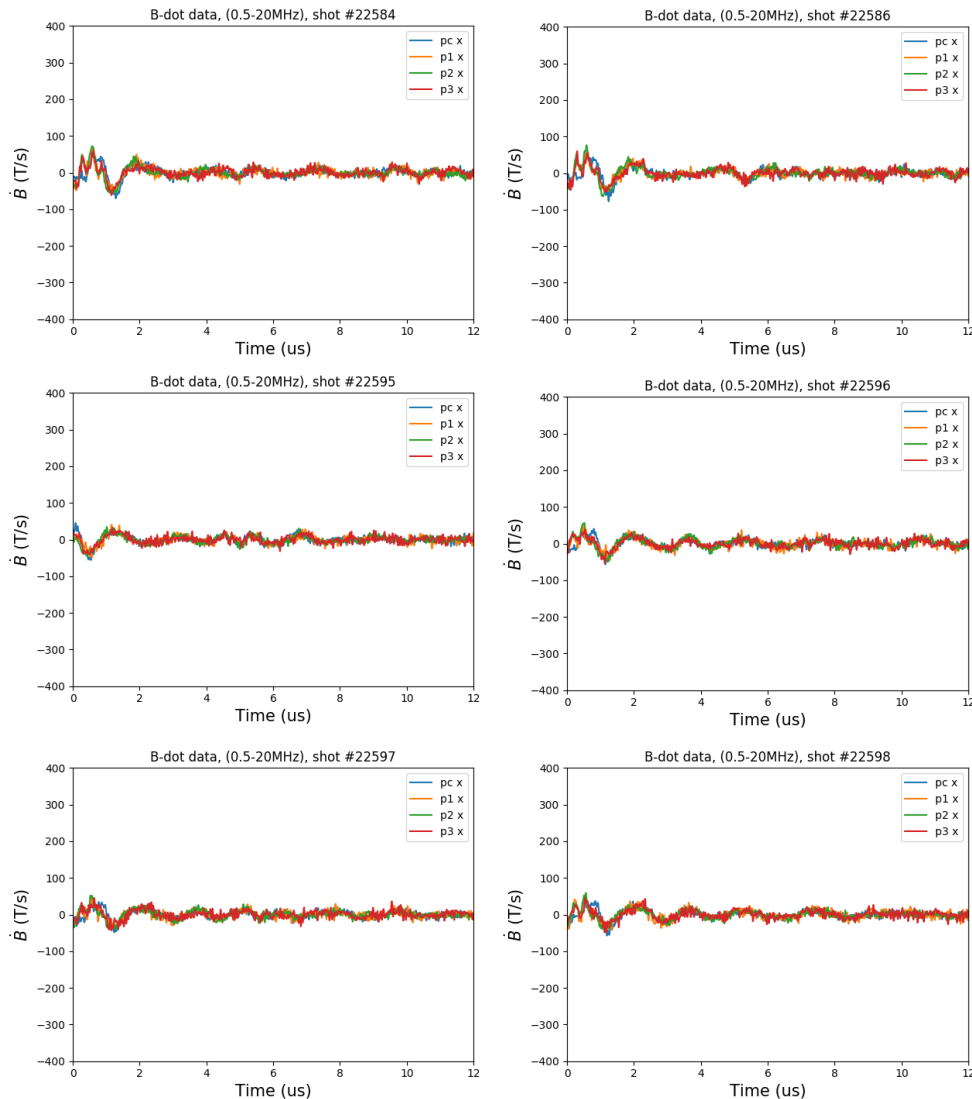
Figure F.6: Plots of filtered (1-20 MHz) B_x component waveprobe signals for shots without visible tearing of jet axis (22584, 22586, 22595, 22596, 22597, and 22598).

F.5   Dispersion plots

This section has two figures showing dispersion relations calculated from Eq. 8.7. Figure F.7 shows dispersion relations calculated from four different time windows from shot #22600. This figure clearly shows a improved correlation with the whistler dispersion relationship during the wave pulse time window. Figure F.8 shows plots of dispersion relations calculated from the wave pulse time window for four different shots. Although shot #22600 has the best agreement with the theoretical whistler dispersion relation, all the shots show a consistent direction ($-\hat{z}$) and comparable wavelengths (8-16 cm) in the 5-10 MHz range corresponding to the wavepulses.
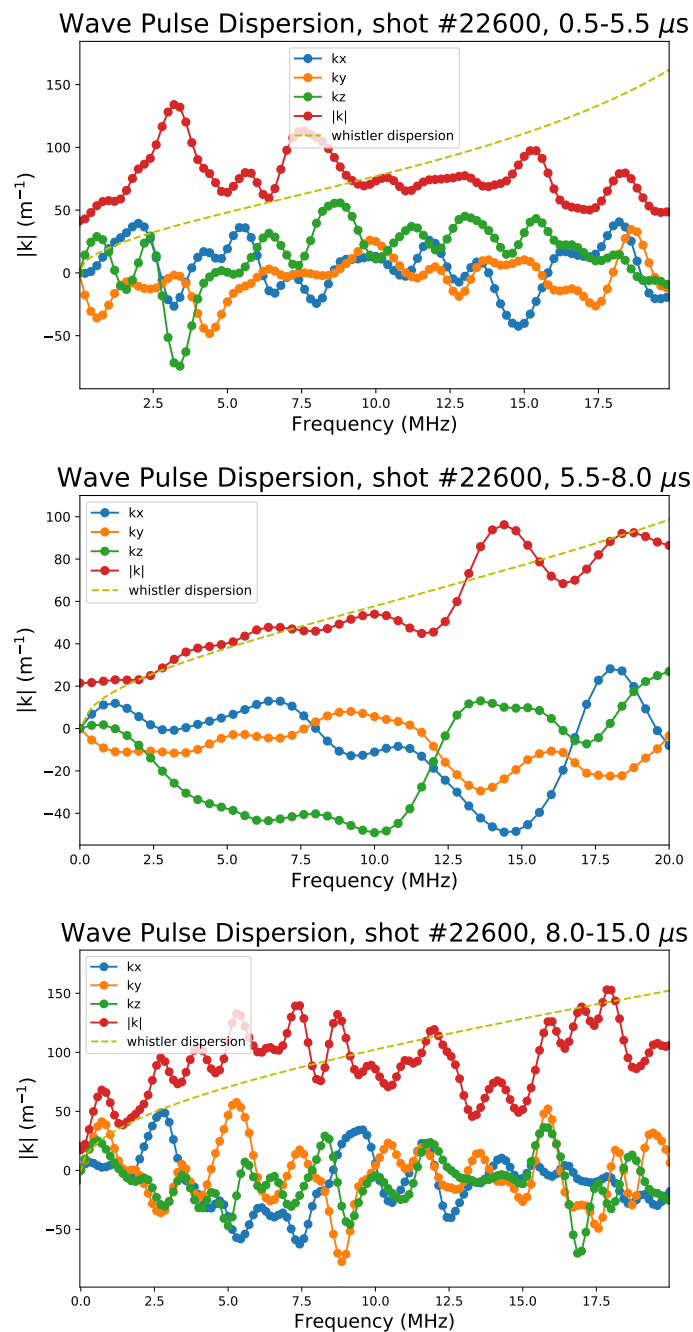
Figure F.7: Dispersion plots for different time periods in shot #22600. The plots show that only the wave pulse time period (5.5-8 μs) shows good agreement with the whistler dispersion relation. Theoretical whistler dispersion is plotted for background parameters $|\mathbf{B}| = 0.0015$ T, $n = 3 \cdot 10^{17}$ m^{-3}.
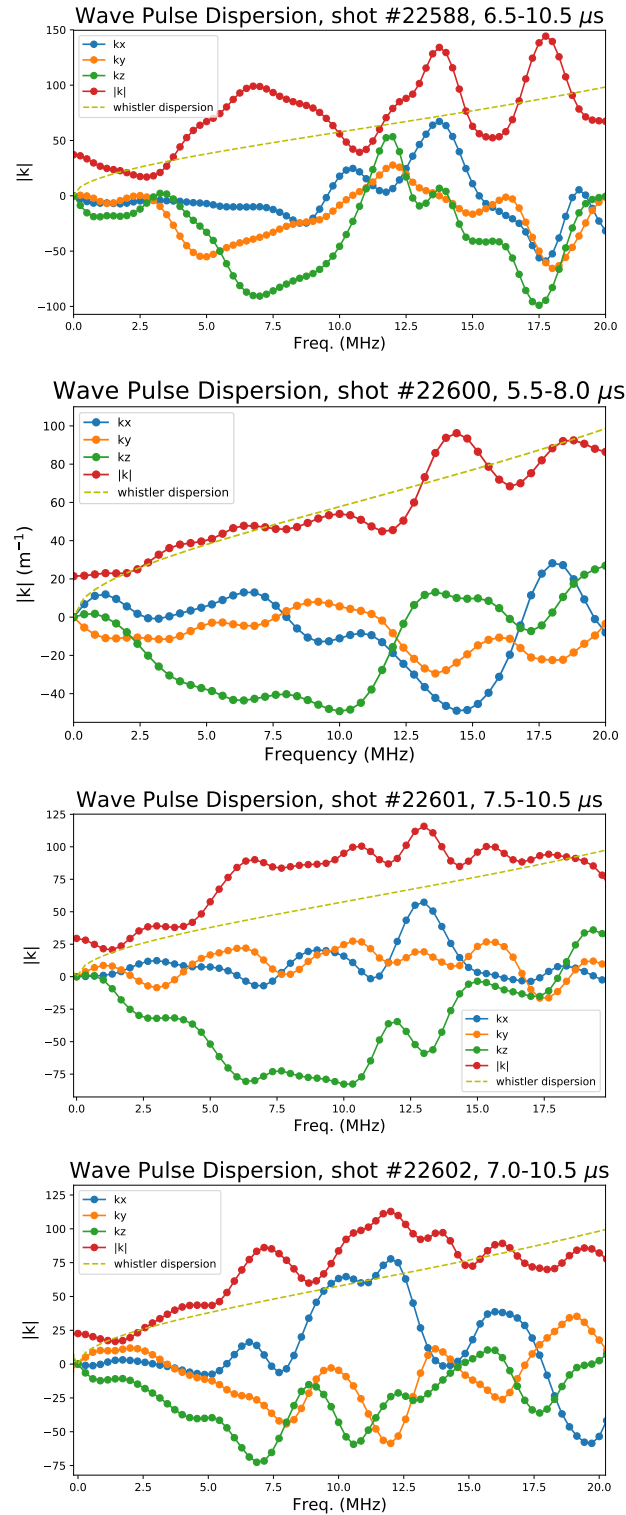
Figure F.8: Dispersion relation plotted for multiple shots. All the shots have reasonable agreement with the whistler dispersion relation and show propagation mainly in the $-\hat{z}$ direction. Theoretical whistler dispersion is plotted for background parameters $|\mathbf{B}| = 0.0015$ T, $n = 3 \cdot 10^{17}$ m^{-3}.